

Study of induced radioactivity in proton accelerator facilities

Inauguraldissertation

der Philosophisch-naturwissenschaftlichen Fakultät
der Universität Bern

vorgelegt von

Francesco Paolo La Torre

von Monte S. Angelo, Italia

Leiter der Arbeit:

Prof. Dr. Antonio Ereditato

Albert Einstein Center for Fundamental Physics

Laboratorium für Hochenergiephysik

Physikalisches Institut

Dr. Marco Silari

CERN - European Organization for Nuclear Research



Study of induced radioactivity in proton accelerator facilities

Inauguraldissertation

der Philosophisch-naturwissenschaftlichen Fakultät
der Universität Bern

vorgelegt von

Francesco Paolo La Torre

von Monte S. Angelo, Italia

Leiter der Arbeit:

Prof. Dr. Antonio Ereditato
Albert Einstein Center for Fundamental Physics
Laboratorium für Hochenergiephysik
Physikalisches Institut

Dr. Marco Silari
CERN - European Organization for Nuclear Research

Von der Philosophisch-naturwissenschaftlichen Fakultät angenommen.

Bern, 28.02.2014

Der Dekan
Prof. Dr. Silvio Decurtins

Contents

Introduction	1
1 Proton accelerators	5
1.1 Historical overview	5
1.2 Linear accelerators	6
1.3 Circular accelerators	8
1.3.1 Cyclotrons	9
1.3.2 Synchro-cyclotrons	11
1.3.3 Synchrotrons	12
2 Induced radioactivity in proton accelerators	15
2.1 Properties of induced radioactivity	15
2.2 The activation formula	16
2.3 Nuclear interactions	19
2.4 Principal radionuclides produced	22
2.4.1 Activation of structural materials	25
3 Simulation codes and analytical models	29
3.1 Methods for predicting induced radioactivity	29
3.2 The FLUKA radiation transport code	31
3.3 The JEREMY analytical model	34
4 Application to a specific case: the CERN 600 MeV synchro-cyclotron	37

4.1	The CERN 600 MeV synchro-cyclotron	37
4.2	Specific activity in concrete samples	39
4.3	Prediction of residual radioactivity in the walls	47
4.4	Results and discussion	50
5	Activation experiments	61
5.1	Irradiation at the CERF facility	62
5.1.1	The Ionization Chamber (IC)	64
5.1.2	Estimation of the calibration factor	65
5.2	The activation foil technique	67
5.2.1	Theoretical basis	67
5.2.2	The $^{27}\text{Al}(p,3pn)^{24}\text{Na}$ reaction	68
5.2.3	The $^{nat}\text{Cu}(p,x)^{24}\text{Na}$ reaction	73
5.2.4	Experiments	74
5.2.5	IC calibration factor	76
5.2.6	Discussion	79
5.3	Activation of copper and iron samples	81
5.3.1	Theory	81
5.3.2	Experimental set-up	82
5.3.3	Results	83
5.4	Activation of soil-shield samples	84
5.4.1	Soil samples	86
5.4.2	H4IRRAD facility and irradiation set-up	87
5.4.3	FLUKA simulations and experimental results	88
5.4.4	Leaching procedure	91
5.4.5	Data analysis	94
5.4.6	Fraction of radioactivity leached into the water	96
6	Prediction of the induced radioactivity for the future CERN Linac4 accelerator	101
6.1	The Linac4 injector	102
6.2	Prediction of induced radioactivity in machine components	103

6.2.1	FLUKA calculations	104
6.2.2	Induced Radioactivity	111
6.3	Estimation of residual dose rates	121
6.3.1	Drift Tube Linac (DTL)	121
6.3.2	Cell Coupled Drift Tube Linac (CCDTL)	121
6.3.3	Pi-Mode accelerating structure (PIMS)	123
6.4	Discussion	125
Conclusions		129
APPENDIX		133
A Residual radioactivity at the CERN 600 MeV synchro- cyclotron		135
B Monitoring reactions for the calibration of high-energy mixed hadron beams		147
C Spallation cross sections for ^{nat}Fe and ^{nat}Cu targets for 120 GeV/c protons and pions		159
D Long-term residual radioactivity in an intermediate- energy proton linac		169
List of Tables		182
List of Figures		185
Bibliography		187

Introduction

Particle accelerators are used in a wide variety of fields, ranging from the basic research to medical and industrial applications. It has been estimated that more than 30000 particle accelerators are in operation worldwide today [1]. Facilities normally undergo upgrade and maintenance in the course of their operating period generating important amounts of activated components and radioactive waste. Furthermore, all of them will require decommissioning at the end of their life cycle. Hence, a careful study of the processes governing the amount of radioactivity induced in an accelerator at any one time is of the utmost importance.

Operating an accelerator leads to nuclear activation of the surrounding material due to particle interactions in accelerator components, beam transfer line elements and shielding structures. Induced radioactivity can be produced at all accelerator facilities capable of generating particles above the reaction threshold of the activation process of interest. The final activation level will depend on several factors, such as the type of accelerator, the beam energy and intensity, the radiological history of the machine, the composition of materials and their location with respect to beam losses. In addition, activation occurs in the structural material enclosing the accelerators and may be even produced outside the accelerator enclosure, primarily in adjacent groundwater and soils. The higher the beam energy, the higher the maximum energy of the secondary radiation, the deeper the induced activity in the shielding walls of the facility. Material activation constitutes a permanent hazard to the staff and imposes serious restrictions on accessibility to

the activated equipment for purposes of operation, maintenance, repairs and decommissioning after the final shutdown. This is why the induced radioactivity at accelerator installations has become one of the major challenges that radiation protection faces.

The purpose of this thesis work is to study nuclear activation processes applied to three selected cases: the first CERN accelerator; materials currently used in accelerator and shielding structures; the forthcoming Linac4 injector under installation at CERN. Experimental measurements, Monte Carlo and analytical techniques were used to quantify the radioactivity produced. The results of this work will make possible a better choice of materials in terms of reducing activation in future accelerator facilities and allow more exact and extensive calculations of radioactivity induced in accelerators.

This thesis is structured in six chapters. The first chapter provides an overview of the physics of proton accelerators of direct interest for the studies conducted in this work. Some general features, specifications and parameters of the accelerators are also presented.

The second chapter contains a short review of the physics underlying the main mechanisms of induced radioactivity at medium and high-energy proton accelerators.

The third chapter presents the FLUKA Monte Carlo code and the analytical model JEREMY, the tools used to estimate the residual radioactivity in the accelerator facilities and materials studied in this work.

The assessment of the consequences of current and future activation of accelerators asks for a detailed study of the radiological status of shutdown facilities. The 600 MeV synchro-cyclotron (SC) is the first accelerator that came into operation at CERN and was operated for 33 years. In chapter 4, I introduce the results of the residual radioactivity measurements in the SC shielding walls and their comparison with calculated values. For this purpose I performed detailed in-situ investigations of the activation of shielding material and of the structural parts of the machine itself and its surrounding technical infrastructure. For the first time, the reliability of the FLUKA and

JEREMY codes in predicting radionuclides produced in concrete walls was tested over such a broad irradiation scenario.

In the first part of chapter 5, I describe the facilities I used for the activation studies and the calibration of the beam monitor. CERF and H4IRRAD are two facilities installed in the secondary beam lines of the CERN Super Proton Synchrotron (SPS). I calibrated the beam monitor by the aluminium foil activation technique via the $^{27}\text{Al}(p,x)^{24}\text{Na}$ nuclear reaction. Although this method has been used in the past, for the first time the contribution of the competing reaction $^{27}\text{Al}(n,\alpha)^{24}\text{Na}$ and the recoil nuclei effect in the aluminium foils were taken into account and carefully quantified for a more precise calibration. Furthermore, the $^{nat}\text{Cu}(p,x)^{24}\text{Na}$ reaction as a promising reaction for beam monitoring was employed. The experimental results and the advantages of this new monitor reaction are also presented. Therefore, I describe the activation experiment carried out to calculate the cross sections of proton- and pion-induced spallation reactions on copper and iron samples. The cross sections for the productions of 14 radioisotopes in ^{nat}Cu and 16 radioisotopes in ^{nat}Fe targets are shown. The second part of the chapter is dedicated to the study of the activation of the soil-shield samples. In particular, I investigated the mechanism and the probability that the radioactivity produced in soil and groundwater may transfer from the site of activation to the environment. Two techniques were used to quantify the amount of radioactivity leaching in the groundwater.

Exposure of personnel and activation of components can be minimized by a suitable engineering design and right choice of materials at the design stage of the facility, provided reliable tools or techniques are available to predict activation of various accelerator parts. Chapter 6 is dedicated to the predictions of induced radioactivity in the Linac4, the new 160 MeV proton injector under installation at CERN for the LHC high-luminosity operation. In this chapter I discuss the FLUKA simulations I carried out to estimate induced radioactivity and residual dose rates in the main linac components after 30 years of foreseen operation. The results of my work will be used

as guidelines for similar studies aimed at future intermediate-energy proton accelerators.

I have been author of several reports and publications summarizing the work mentioned above.

1. P. Carbonez, F.P. La Torre, R. Michaud and M. Silari, *Residual radioactivity at the CERN 600 MeV synchro-cyclotron*, Nuclear Instruments and Methods in Physics Research A 694 (2012) 234-245.
2. A.Ferrari, F.P. La Torre, G.P. Manessi, F. Pozzi and M. Silari, *Monitoring reactions for the calibration of high-energy mixed hadron beams*, submitted to: Physical Review Special Topics - Accelerators and Beams, Ref. ZN10088 (2014).
3. A. Ferrari, F.P. La Torre, G.P. Manessi, F. Pozzi and M. Silari, *Spallation cross sections for ^{nat}Fe and ^{nat}Cu targets for 120 GeV/c protons and pions*, submitted to: Physical Review C, Ref. CN10349 (2014).
4. J. Blaha, F.P. La Torre, M. Silari and J. Vollaire, *Long-term residual radioactivity in an intermediate-energy proton linac*, submitted to: Nuclear Instruments and Methods in Physics Research A, Ref. NIMA-D-13-01100 (2013).

These publications are reprinted in the Appendix. I am the corresponding author of papers 1 and 4, since the major work for these publications was done by myself in the framework of my PhD thesis.

Chapter 1

Proton accelerators

This chapter provides a short review of the principles of proton accelerators of direct interest for the studies conducted in this work. Some general features, specifications and parameters of the accelerators are also presented.

1.1 Historical overview

From the discovery of artificial radioactive transformations up to the construction of the first particle accelerators, nuclear physics had at its disposal only natural sources of high-energy elementary particles. These sources were isotopes of natural radioactive elements emitting α -particles. Nuclear research was therefore confined to bombardment of elements with one type of particle and at relatively low energies. Another major obstacle to the development of nuclear research was the low yield of reactions initiated by particles from natural sources. Experimental physics was confronted with the task of building devices which could produce particles with energies initially comparable with those of the same particles from natural sources and then with much higher energies and intensities.

The first accelerators in the early 1930's utilized direct voltage to accelerate ions to energies of a few hundred keV. In the electrostatic accelerators, the particles were accelerated by applying a voltage difference, constant in

time, whose value fixes the value of the final energy of particles. In this device the large potential difference is obtained from electrostatic charge stored on the outer surface of a conducting sphere of large radius. The Van de Graaff and the Cockcroft-Walton accelerators belong to this class. By using this kind of machines, Cockcroft and Walton were able to accelerate protons to bombard a lithium target, resulting in the first induced nuclear disintegrations in 1932 [2]. This was the first time that charged particles artificially accelerated had been used to trigger a nuclear reaction.

The next stage in the development of particle accelerators was the invention of cyclic accelerators. In these machines the accelerating voltage corresponds to a small fraction of the value of the final energy attained by the particles. This is obtained by applying the accelerating voltage to the same particle a large number of times. One obtains a process of gradual acceleration which is not limited by the maximum voltage drop existing in the machine.

The various types of accelerators differ essentially in the way the electric field is produced and how it acts on the particles to be accelerated. Depending on the trajectories of the particles, that can be straight or curved, we have linear or circular accelerators. In the first kind, the particles move in a straight line, passing once through each accelerating gap in the process of acceleration (linacs); in the second, the particles move in a circle or spiral, accomplishing a cyclical motion and passing many times through the same accelerating gaps. Depending on the details of the acceleration process, we can have cyclotrons, synchro-cyclotrons and synchrotrons.

1.2 Linear accelerators

In linear accelerators (called "linacs") the particles are accelerated by definition along approximately straight trajectories. The particles move along the axis of a structure with cylindrical symmetry, along which the accelerating fields are also made to propagate. The accelerating structures allow a

continuous transfer of energy to the particles from the electromagnetic waves and can be obtained either from resonant cavities or from waveguides. The simplest linear accelerator consists of a series of cylindrical electrodes, called drift tubes, arranged along the beam axis and connected with alternating polarity to a radiofrequency (RF) supply. The first design of such an accelerator was accomplished by Wideröe in 1929, followed in 1931 by Sloan and Lawrence [3]. Figure 1.1 shows the schematic of Wideröe's idea for a linear accelerator. The generator delivers a high-frequency alternating voltage of the form $V(t) = V_{pk} \sin(\omega t)$, where V_{pk} is the peak voltage. The RF accelerating voltage applied successively to adjacent drift tubes causes the particle energy to increase when they pass through the gaps between two consecutive drift tubes. At transit through the n -th drift tube, the particle of charge q receives an increase of energy

$$\Delta E_n = nqV_0 = nqV_{pk} \sin \varphi_0 \quad (1.1)$$

where V_0 is the voltage drop across the gap at the instant of the particle transit and φ_0 is the corresponding average RF phase in the gap. After the n -th drift tube the energy E_n is reached, which for a particle of mass m corresponds to a velocity

$$v_n = \sqrt{\frac{2E_n}{m}} \quad (1.2)$$

assuming non-relativistic velocities ($v \ll c$). It is clear that the energy is proportional to the number of stages n traversed by the particles and the particle velocity increases from one stage to the next one. In addition, since the frequency of the alternating voltage must remain constant for all the tubes, this means that the downstream drift tubes and gaps have to get longer as the particles get faster.

In principle, there is no limit to the energy to which particles can be accelerated using this kind of machine. Of course, the higher the final energy of the particles, the longer has to be the machine or the higher the RF frequency. So, the ultimate energy is limited by availability of space and in

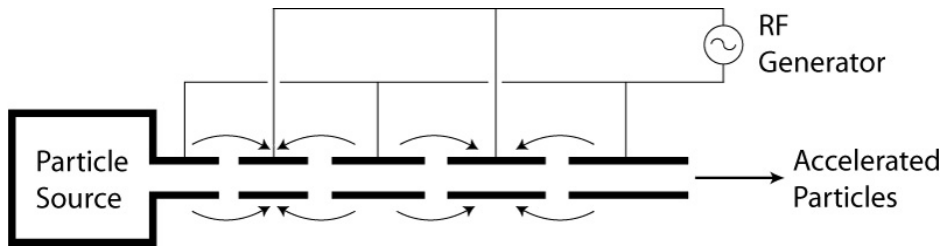


Figure 1.1: Schematic diagram of the drift-tube type of linear accelerator. The arrows at the gaps show the direction of the electric field.

order to avoid that the accelerator gets too long, very high frequencies are used. Linacs consisting of a succession of drift tubes, where the acceleration only occurs in the gaps between tubes are called discontinuous accelerators. They are mainly used to accelerate protons and heavy ions. This is the case of the new CERN linear accelerator, the Linac4, that will replace the old Linac2 as proton injector of the CERN accelerator complex. Further details will be presented in chapter 6.

Another important method to accelerate particles is to have electromagnetic waves propagating inside the accelerating structure. If the electric field at the point occupied by a moving particle on the average has the direction of the particle motion and if certain phase relations are satisfied, then the particles can receive energy from the electromagnetic wave. These types of machines which make use of waveguides to propagate electromagnetic waves together with the particles are called continuous accelerators. Linear electron accelerators belong to this type.

1.3 Circular accelerators

In order to reach higher energies and reduce size and cost of the machine, it is desirable to drive particles around a circular path using the same accelerating structure many times. In circular accelerators particles are accelerated by a RF electric field but instead of moving along a straight line as in linacs they move along a nearly spiral or circular path, guided by a magnetic field

perpendicular to the orbital plane.

1.3.1 Cyclotrons

The first circular accelerator was the cyclotron, proposed by Lawrence and Livingstone in 1930. Two years later, they built the first cyclotron suitable for experiments, with a peak energy of 1.2 MeV [4].

A cyclotron consists of a flat accelerating chamber, housing two or more hollow electrodes called "dees", as in the first cyclotrons they were D-shaped. A radiofrequency voltage is applied between the electrodes, so that there is an alternating electric field in the gap, but no field inside the dees. The vacuum chamber is placed between the pole expansions of a large magnet which produces a constant and almost uniform magnetic field perpendicular to the plane of the dees. Figure 1.2 shows the original cyclotron concept [5]. The accelerated ions moving in a constant uniform magnetic field, perpendicular to the initial velocity, are subject only to the Lorentz force $\mathbf{F}_L = q\mathbf{v} \times \mathbf{B}$, where q and \mathbf{v} are the charge and the velocity of the particle and \mathbf{B} is the magnetic field induction. The charged particles experiences a force transverse to their motion as well as to the direction of the magnetic field, the intensity of which is proportional to the velocity of the (non-relativistic) particle and to the field

$$F = qvB \quad (1.3)$$

Hence the centripetal force which the particles will experience is given by

$$\frac{mv^2}{R} = qvB \quad (1.4)$$

If the magnet produces a strong enough uniform field, the particle moving perpendicular to the field will follow a circular path of constant radius R

$$R = \frac{mv}{qB} \quad (1.5)$$

The time T required to travel one orbit of radius R with constant velocity v

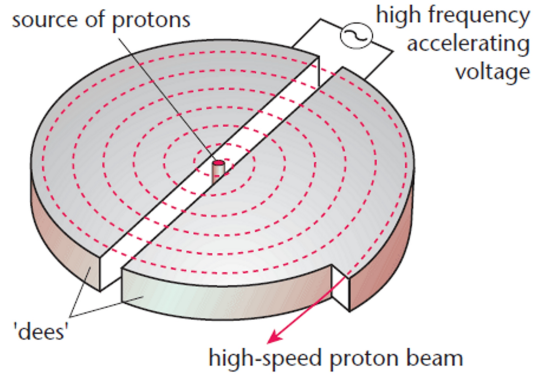


Figure 1.2: Schematic diagram illustrating the operation of the classical cyclotron; the magnetic field (not shown) is perpendicular to the plane of drawing.

is

$$T = \frac{2\pi R}{v} = \frac{2\pi m}{qB} \quad (1.6)$$

The revolution frequency for a non-relativistic particle, also called "cyclotron frequency" is then given by

$$f = \frac{1}{T} = \frac{qB}{2\pi m} \quad (1.7)$$

In conventional cyclotrons, the cyclotron frequency is usually around 10 MHz for an RF power of around 100 kW [4]. Accelerated particles are emitted from an ion source located in the centre of the machine, between the two poles. Starting from the source, the particles travel in orbits which are bent by the magnetic field. As their circular path passes through the gap between the two dees they are accelerated. If in the meantime the RF polarity is reversed, when the ions turn around and return to the first dee they are again accelerated. Therefore, the particles are repeatedly accelerated each time they cross the gap. The orbital radius is initially small since the velocity is small and as the particles accelerate, they spiral out to a larger radius. The particles are then extracted, moved out of the magnetic field and channeled out of the cyclotron. If the particles are extracted at a radius R_f , from

expression (1.5)

$$R_f = \frac{mv_f}{qB} \quad (1.8)$$

where v_f is the velocity of the particle at extraction. The final energy of the particle when extracted is then given by

$$E_f = \frac{1}{2}mv_f^2 = \frac{(qRB)^2}{2m} \quad (1.9)$$

The final energy is inversely proportional to the mass of the particle and directly proportional to the square of the radius of extraction and to the square of the magnetic field. High energies require high magnetic fields or large orbital radii, which require increasing the diameter of the pole expansions. Moreover, the condition for the validity of the classical approximation for the cyclotron frequency given by equation (1.7), limits the maximum energy to a few percent of the rest energy of the particles [6, 7].

1.3.2 Synchro-cyclotrons

The orbital or cyclotron frequency of a relativistic particle is given by

$$f_R = \frac{qB}{2\gamma\pi m_0} \quad (1.10)$$

where m_0 is the invariant rest mass of the particle, γ is the relativistic factor given by $\gamma = 1/(1 - \beta^2)^{1/2}$ and $\beta = v/c$ is the ratio between the velocity of the particle v and the light c . The relativistic increase in effective mass, as the particles approach the velocity of light, causes the particles to slow down in their orbit relative to the applied frequency and fall out of resonance with the accelerating voltage so they do not get accelerated anymore and are eventually decelerated. If the frequency of the RF system is decreased gradually to be synchronous with the particle velocity as the particle becomes relativistic, much higher energies can be reached. Accurate tuning of the frequency modulation creates higher particle stability and the particle losses in each orbit are reduced. This principle is employed in the synchro-cyclotron,

a variant of the cyclotron which overcomes the energy limit of the latter. On the whole the construction of the synchro-cyclotron is similar to the cyclotron except for the modulated frequency of the RF supply.

In a synchro-cyclotron the particles are not distributed along the whole trajectory as in a cyclotron, but they may only be accelerated in short pulses, because the RF can only "pick up" a bunch at the time from the source and has to guide it through the entire acceleration process until extraction. The bunches leave the source at a rate equal to the rate of frequency modulation and so the beam produced by the machine is pulsed at the same rate, leading to a large reduction of the average beam intensity with respect to the cyclotron. On the other hand, an important advantage offered by the synchro-cyclotron is that since the orbit stability is greater, the particles carry out a much greater number of turns and thus it is possible to use a much lower accelerating voltage.

One of the most important and fruitful accelerators in the history of the particle physics was the CERN's 600 MeV synchro-cyclotron (SC). Its construction was started in 1955, applying all the lessons learnt in the previous accelerators. Unsurprisingly, the machine achieved its target energy immediately after commissioning in 1957. One year later, in 1958, the SC made one of the most important discoveries in physics by demonstrating the decay of pions into electrons and thereby confirmed the theory of weak interaction force. More details will be discussed in Chapter 4.

The limit to the energy which can be obtained is given essentially by the technical limit to the size and cost of the magnet that can be built in practice.

1.3.3 Synchrotrons

The principle of the synchrotron was developed independently in 1945 by Veksler in the Soviet Union and by McMillan at the University of California. In a synchrotron, particles are accelerated by a RF voltage in a rising magnetic field, following a circular orbit with constant radius R rather

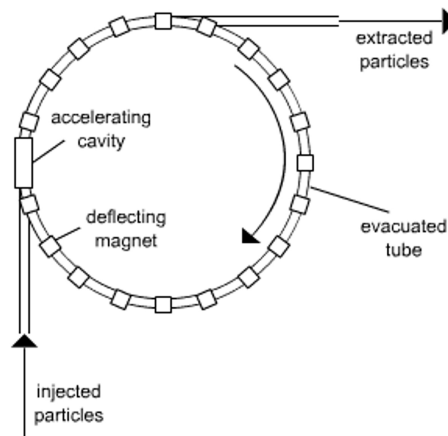


Figure 1.3: Basic layout of the synchrotron. The particle trajectory is controlled by bending magnets with homogeneous field, while the beam focusing is performed by specially designed magnets. The acceleration take place in one or more short RF structures.

than a spiral (Figure 1.3). Contrary to the cyclotron, the synchrotron requires a magnetic field only in the region of the circular orbit along which particles are accelerated. The vacuum chamber containing the particles is torus-shaped and the volume is also small enough to permit easier pump down to ultrahigh vacuum. Hence the electromagnets only have to provide the field in the beam tube. The annular magnets consist of two ring-shaped pole pieces and the magnetic circuit is usually closed by a vertical iron yoke. Their weight increases only linearly and not as a square of the orbit radius, as in cyclotrons. This makes it feasible to obtain much larger magnetic field required for much larger particle energies [2]. Alternatively, it is possible to reach high particle energies with a limited magnetic field, but with a large orbit radius. The diameters of orbits in modern synchrotrons for very high energies can reach thousands of meters: the CERN Large Hadron Collider (LHC) with its 27-kilometre ring of superconducting magnets is the world's largest and most powerful particle accelerator.

In the synchrotron, the actual acceleration of particles is accomplished with gaps (resonators) operating with an RF electric field, obtained by exciting stationary electromagnetic waves in a resonant cavity through which

the particles pass. In proton synchrotrons, the velocity of the accelerated protons usually changes within relatively wide limits during the acceleration cycle. For this reason, the rate of change of frequency must also be synchronized with the rate of change of the magnetic field. These requirements in a proton synchrotron introduced significant engineering challenges in the design of the RF modules, and in the design of an oscillator that could handle high frequencies. As a consequence, acceleration of protons in a synchrotron was not successfully performed until 1952, five years after the first electron synchrotron was in operation.

Only the particles which find the right value of the electric field in the cavity can be accelerated; therefore the operation of this machine is also pulsed with the period of the magnetic field and the accelerated particles are bunched. In order to avoid too wide a range of modulation of the radio frequency, the particles are usually injected into the machine after being pre-accelerated by means of an auxiliary accelerator called the "injector". For example the CERN's accelerator complex consists of a number of accelerating structures used as pre-injector for the LHC, with the aim of boost the energy of the particles along the way. The Super Proton Synchrotron is the second-largest machine in CERN's accelerator complex. Measuring nearly 7 kilometres in circumference, it provide up to 450 GeV energy beam for the Large Hadron Collider (LHC) as well as for many experimental facilities like H4IRRAD and CERF in the CERN North Experimental Area, used in this thesis work. These irradiation facilities will be presented in chapter 5.

Chapter 2

Induced radioactivity in proton accelerators

When materials at accelerators are exposed to stray radiation, they become radioactive decaying by gamma-rays, beta particles and rarely neutrons. This radioactivity induced by the radiation produced during the operation of the accelerator remains after the latter has stopped running, often for several years. It constitutes a permanent hazard to the staff and imposes serious restrictions on accessibility to the activated equipment for purposes of operation, maintenance, repairs and decommissioning after the shutdown. This chapter briefly describes the production mechanisms of induced radioactivity at high-energy proton accelerators. It provides a short review of the basic principles involved in activation processes and lists the principal radioactive isotopes generated in accelerator environment and its surrounding structures.

2.1 Properties of induced radioactivity

If a high-energy hadron interacts with a nucleus, neutrons, protons and other nuclear fragments may be emitted, converting the struck nucleus to that of a different isotope, most probably of a different element, which has a

high probability of being radioactive. Some of the secondary particles emitted in an interaction may have sufficient energy to undergo further interactions and cause additional activation, thus creating a nuclear particle cascade. In this process, many nuclei are produced in excited states and de-excite by emitting neutrons, charged particles or fragments (that can also in turn be in an excited state) in a so called "evaporation" process, or they may de-excite by emitting gamma-ray. The hadron cascade continues to produce radionuclides until their energies of the particles drop below the thresholds for the nuclear reactions involved or, in the case of exothermic reactions, until they are captured.

Although the overall amount of radioactivity induced in an accelerator will depend on the primary beam loss (type, energy and number of lost particles), the probability of producing a particular isotope will depend on the composition of the material struck, the spectrum of secondaries produced and the production cross section of the isotope concerned. The amount of a radioactive isotope present at any given time will also depend on the isotope half-life and the time that the accelerator has been in operation, as well as on the time that the activity has had to decay since operation stopped. Hence the estimation of induced radioactivity in an accelerator is a very complex process.

2.2 The activation formula

In principle, induced radioactivity can be produced at all accelerators capable of generating particles above the reaction threshold of the activation process of interest. When the accelerated beam strikes a nucleus, the resulting nuclear reactions can convert it into a different nuclide, which may or may not be radioactive.

The most simple activation situation at accelerators is that of the steady irradiation of some material by a spatially uniform flux density of particles that begins at time $t = 0$ and continues at a constant rate for an irradiation

period that ends at $t = t_i$. This is followed by a decay period called the cooling time, t_c , a period of time that begins at $t = t_i$ and ends at $t = t_i + t_c$. For this simple situation, self-absorption of the hadrons by the target is ignored, as is the fact that a whole energy spectrum of particles might be incident. Thus the process of producing the radioactivity is characterized by a single average cross section value, σ . In the more complicated generalized situations the value of this cross section must be obtained from averaging over the energy spectra of the incident particles [8].

The number of atoms of the radionuclide of interest per unit volume will thus be governed by the following equation during the irradiation period:

$$\frac{dn(t)}{dt} = -\lambda n(t) + N\sigma\phi \quad (2.1)$$

where $n(t)$ is the number density of atoms (cm^{-3}) of the radionuclide of interest at time t , λ is the decay constant (s^{-1}), N is the number density of "target" atoms (cm^{-3}), σ is the production cross section (cm^2), ϕ is the flux density ($\text{cm}^{-2}\text{s}^{-1}$) of the incident particles. On the right hand side of the above equation, the first term represents the loss of radionuclides through decay during the irradiation while the second term represents the build-up of radionuclides through the production reaction under consideration. The equation has the following solution for $0 < t < t_i$:

$$n(t) = \frac{N\sigma\phi}{\lambda} \{1 - \exp(-\lambda t)\} \quad (2.2)$$

The specific activity induced in the material as a function of time during the irradiation is given by $a(t) = \lambda n(t)$, hence

$$a(t) = N\sigma\phi \{1 - \exp(-\lambda t)\} \quad (\text{Bq cm}^{-3}) \quad \text{for } 0 < t < t_i \quad (2.3)$$

At the instant of completion of the irradiation ($t = t_i$), the specific activity

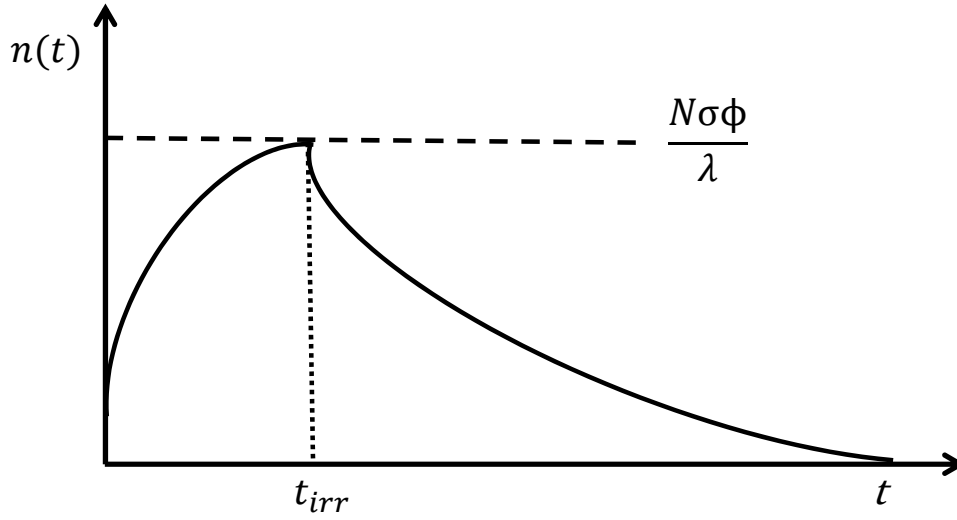


Figure 2.1: Radioisotope build-up and decay over time [9].

will be given by

$$a(t_i) = N\sigma\phi \{1 - \exp(-\lambda t_i)\} \text{ (Bq cm}^{-3}\text{)} \quad (2.4)$$

so that the specific activity as a function of time is characterized by a buildup from zero to the saturation value equal to $N\sigma\phi$ for an infinitely long irradiation. After the irradiation has ceased ($t > t_i$), the specific activity as a function of the cooling time, $t_c = t - t_i$, will obviously decay exponentially and be given by the activation equation:

$$a(t_c) = N\sigma\phi \{1 - \exp(-\lambda t_i)\} \{\exp(-\lambda t_c)\} \text{ (Bq cm}^{-3}\text{)} \quad (2.5)$$

The number of radioactive nuclei produced during the irradiation as a function of time is plotted in Figure 2.1. In more complex cases, where a spectrum of energies is involved, more complex integrations need to be performed.

2.3 Nuclear interactions

At intermediate energies (from a few MeV up to about 50 MeV) various types of nuclear reactions are involved. The particles entering the nucleus are capable of knocking out one or more nucleons, or even a part or fragment of the target nucleus. For instance, with proton induced reactions we find, with increasing energy, first (p,n), (p,np), (p,2n), (p, α) and so forth, in which a neutron, a proton and neutron, two neutrons and an alpha particle (helium nucleus) are expelled. Each of these reactions begins at the threshold energy, which is progressively higher than that of the preceding one.

At still higher energies, the picture gets more complicated. The nucleons struck by the incident particle in the target atom obtain enough energy themselves to travel through the nucleus and to hit other nucleons of the same atom in the same way, thus giving birth to an "intranuclear" cascade of fast nucleons. These nucleons can either escape from the nucleus at some moment or be captured and give up their energy to excite the whole nucleus. A much wider variety of new nuclei can be formed in this way than by the channels previously considered, as a result of the large number of cascade nucleon events which can take place in the nucleus.

Other processes than intranuclear cascades causing spallation or fission are also observed at high energies. Direct ejection of high energy ions or light nuclei, called fragmentation reactions, do not fit in the two-step process outlined and are also observed. Also the production of new particles by high energy nucleons striking other nucleons or target nuclei is a possible role for an incident or an intranuclear cascade particle. As an example, π -mesons are produced by nucleons from 300 MeV upwards, K-mesons from 1 GeV, nucleons and antinucleons from 4.5 GeV. Among these newly generated particles, the π -mesons, nucleons and antinucleons are able to develop intranuclear cascades in their turn, and eventually π -mesons and antinucleons can transfer their total energy to nucleons in the target nucleus, thus making the number of all possible products from the nuclear reaction still larger. Clearly there cannot be a theory or a formula to cover this whole set of phenomena. This

is what makes predictions in the field of induced activity rather intricate and difficult.

For high-energy proton and ion accelerators, neglecting secondary reactions and restricting to few- and multi-nucleon transfer reactions can become a serious deficiency in the accuracy of estimation of induced radioactivity, because of the rise in importance of such processes as spallation. Below a kinetic energy of about 40 MeV only few-nucleon transfer reactions are available. As the energy of the incident particle increases, the number of possible reaction channels increases, with a corresponding increase in the number of radionuclides produced. An example of this is shown in Fig. 2.2 for the case of bismuth when bombarded by protons. The number of radionuclides increases with increasing proton energy. At 40 MeV, only few nucleon transfer reactions are available, while at 3 GeV the entire periodic table is essentially available for the production of nuclei lighter than the target. The variety of radionuclides that can be produced increases as the bombarding energy increases, because more reaction thresholds are exceeded [10]. As a general rule, at high energies one must consider that all radionuclides in the periodic table that have mass numbers lower than that of the material exposed to the flux of hadrons may be produced. Of course, many of these are of little significance due to their short half-life and small production cross sections. In fact, the cross sections for producing specific radionuclides are often nearly independent of the target element [11]. The spallation reaction is the most important kind of reaction, apart from fission for heavy elements, if an element is irradiated with high energy particles. This is a violent inelastic interaction in the nucleus resulting in the emission of various kinds and numbers of light particles and fragments and leaving behind a reaction product that is generally radioactive. The effect of all these different spallation products must be summed up if one wants to make an estimate of the total induced radioactivity. An important factor entering such estimates is evidently the production cross section of the various spallation products. The nuclear cross section for such a reaction approaches the geometric cross

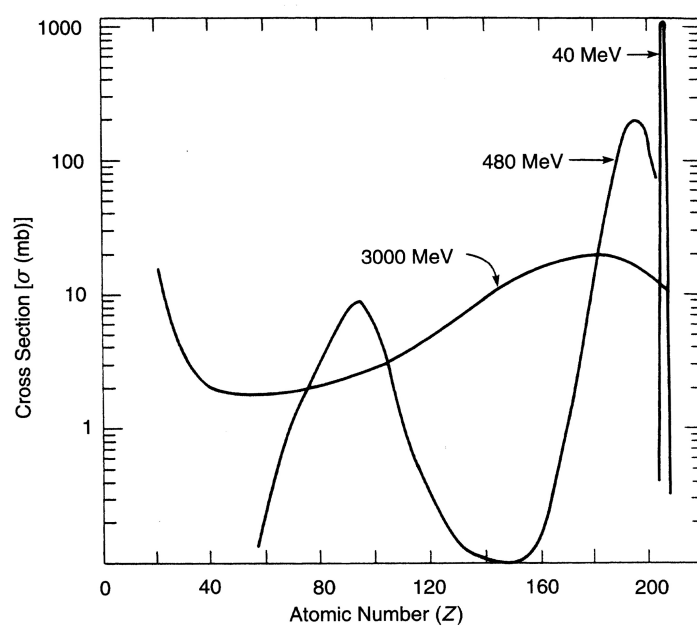


Figure 2.2: Mass-yield curves (cross section versus Z) for the bombardment of bismuth by protons of the indicated energies [12].

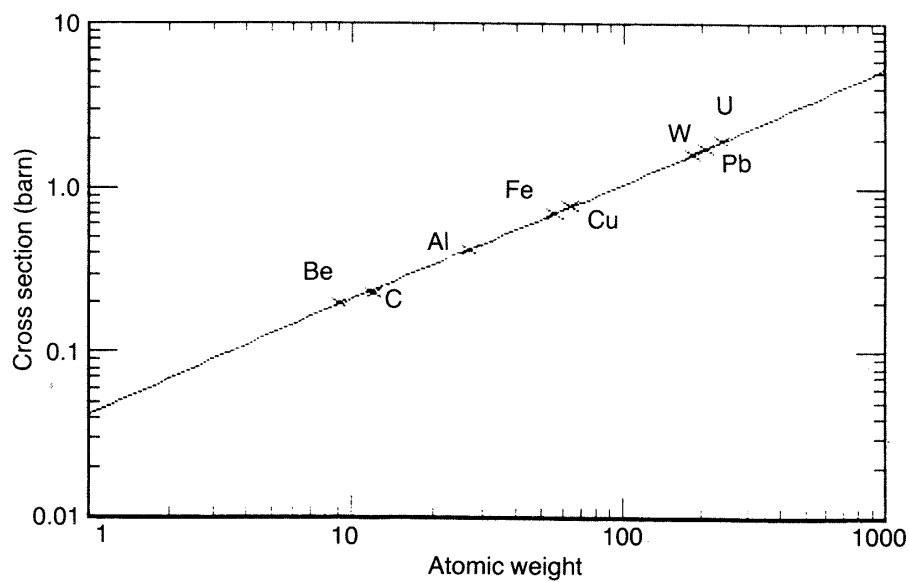


Figure 2.3: The nuclear inelastic cross section as a function of atomic weight of the target nucleus in units of barns [13].

section of the nucleus at high particle energies. A review of nuclear interaction cross section suggests an empirical dependence of the interaction cross section, σ , on the atomic mass of the target nucleus A

$$\sigma = 42 A^{2/3} \times 10^{-3} \text{ (barn)} \quad (2.6)$$

which is a good approximation for the cross section for an inelastic collision by a hadron of energy greater than about 120 MeV [14]. The formula is valid for proton or neutron induced spallation. This cross section is plotted in units of barns (1 barn = 10^{-24} cm²) as a function of atomic weight of the target nucleus in Fig. 2.3. High-energy particle nuclear interaction cross sections for common target materials are listed in Table 2.1.

For very heavy targets, with mass above about 200, the usefulness of the formula is limited, because of the competition with fission which will depress the spallation yields. In addition, although the formula does not contain any explicit cut-off, it is clear that it should not be used below the threshold for the reaction under consideration.

2.4 Principal radionuclides produced

The isotope remaining after an interaction by a high energy particle with a nucleus can have an atomic weight of anything up to that of the target nucleus (or even higher in the case of a capture reaction). The probability of producing a particular isotope in a given target material, or the isotope production cross section, depends on the energy (and charge) of the incident hadron. The relative importance of a particular isotope from the point of view of its contribution to the dose rate depends on its half-life and on the radiation emitted when it decays. The common isotopes typically found in high energy accelerator installations are listed in Table 2.2 together with their half-lives and decay modes. Approximate cross-sections for the production of these radionuclides by protons at the high energy limit and approximate thresholds for selected radionuclides are also provided where available [15].

Table 2.1: Cross sections for high-energy particle interactions in various target and shielding materials [13].

Material	Inelastic Cross Section (barn)	Nominal density (g cm ⁻³)
Beryllium	0.20	1.8
Graphite	0.23	2.0
Water	- -	1.0
Concrete	- -	2.35
Earth	- -	1.8
Aluminium	0.42	2.7
Barytes	- -	3.2
Iron	0.70	7.4
Copper	0.78	8.9
Tungsten	1.61	19.3
Platinum	1.78	21.4
Lead	1.77	11.3
Uranium	1.98	19.0

In Table 2.2 only nuclides with half-lives longer than 1 day are listed. Also, all "pure" β^- (electron) emitters, i.e. those radionuclides that emit no γ -rays in their decays, are not listed. β^+ (positron) emitters are included due to the generation of the pairs of 0.511 MeV photons resulting from annihilation of the positrons with electrons in matter. These photons have to be included as part of the average gamma radiation emitted in the decay of the isotope and makes a significant contribution to the gamma dose rate from activated accelerator components. The radioactive isotopes may also decay through isomeric transition (IT), e.g. the metastable (isomeric-)state of ⁴⁴Sc, or by capturing an orbiting electron (EC). The daughter nucleus resulting from the latter decay may de-excite by emitting gamma radiation as well as the characteristic X-rays of the new atom.

A large range of different isotopes will normally be present in radioactivity induced by high energy particle spallation reactions, each isotope having its characteristic half-life and radiation emission. Providing there are enough isotopes present, then the average properties of the isotopes concerned will

Table 2.2: Medium- and long-lived radionuclides commonly identified in materials irradiated around accelerators (adapted from [10, 15, 16]).

Material	Isotope	Threshold (MeV)	Half-life	Cross Section (mb)	Decay mode
Plastics & Oils	^3H	11	12.33 y	10	β^-
	^7Be	2	53.22 d	10	EC
Al	as above plus ^{22}Na	30	2.60 y	10	β^+
Iron	as above plus $^{44\text{m}}\text{Sc}$		2.44 d		IT
	^{46}Sc		83.8 d		β^-
	^{47}Sc		3.35 d		β^-
	^{48}Sc		1.82 d		β^-
	^{48}V	20	15.97 d	6	β^+
	^{51}Cr	30	27.7 d	6	EC
	^{52}Mn	20	5.59 d	30	β^+
	^{54}Mn	30	312.1 d	30	EC
	^{55}Fe		2.74 y		EC
	^{59}Fe		44.5 d		β^-
	^{56}Co	5	77.2 d	30	β^+
	^{57}Co	30	271.7 d	30	EC
^{58}Co	30	70.9 d	25	β^+	
St.Steel	as above plus ^{59}Ni		75 y		EC
	^{60}Co	30	5.27 y	15	β^-
Copper	as above plus ^{63}Ni		100 y		β^-
	^{65}Zn		243.7 d	100	EC

be sufficient for determining the "average" amounts of induced activity and resulting dose rates. Examination of the isotope charts suggests that on average there are 1.5 γ -photons of mean energy 0.8 MeV emitted per decay of isotopes of half-life between 10 minutes and 2 years and of mass less than about 60 on the atomic weight scale. In addition, in about 25% of the decays the daughter nucleus is also likely to be radioactive, making the effective average photon emission per decay of an induced radioactive isotope in medium atomic number materials equivalent to 1.9 photons of mean energy 0.8 MeV. Beta particles or positrons are emitted in about 75% of the decays with an "average" maximum energy in the region of 1.8 MeV. Again, if 25% of the daughter isotopes are also radioactive and the average energy of a beta particle or positron is 30% of the maximum, then the average beta or positron energy emitted per radioisotope decay will be 0.5 MeV [13].

Fig. 2.4 plots the number of radionuclides as a function of half-life, $t_{1/2}$, that have half-lives less than that particular half-life for several choices of atomic mass number, A . This corresponds to the distribution of radionuclides that could be produced in a target of mass number A irradiated by high energy hadrons. The straight broken lines drawn in the figure are an attempt at linearization over this range. As one can see, these cumulative distributions are well-described for values of half-life between about 10^{-3} and 10^3 days by a function of the following form:

$$N(t_{1/2}) = a + b \ln(t_{1/2}) \quad (2.7)$$

where $N(t_{1/2})$ is the number of radionuclides with half-lives less than the value of $t_{1/2}$ and a and b are fitting parameters.

2.4.1 Activation of structural materials

During accelerator operation, radiation is produced when the beam interacts with targets and other accelerator materials. Secondary radiation (e.g. neutrons, muons and photons) generates additional radiation through atomic

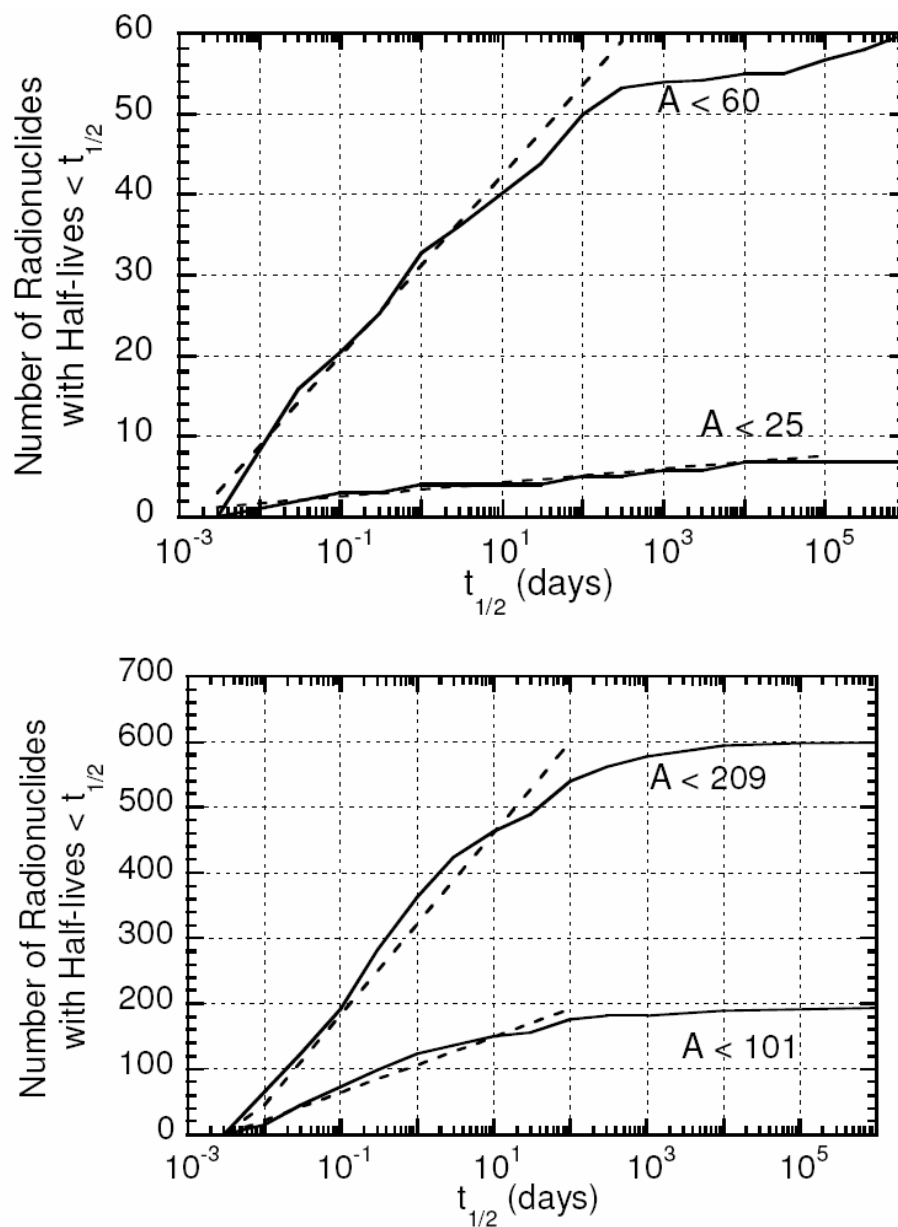


Figure 2.4: Total number of isotopes having half-lives up to a given half-life as a function of the logarithm of this half-life for target mass numbers less than those indicated [8].

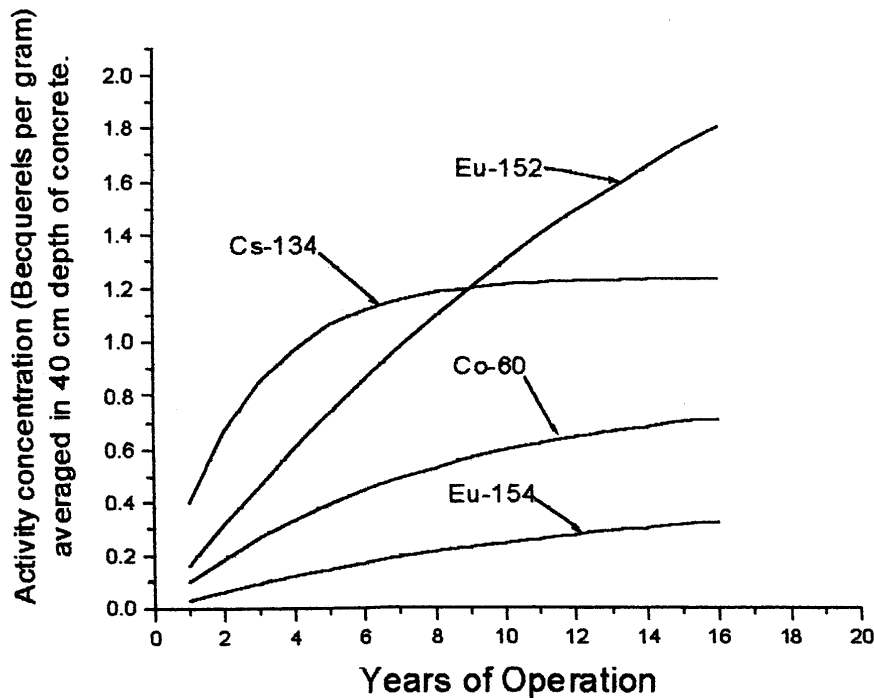
or nuclear interactions, including hadronic and electromagnetic cascades.

Experience to date at high-energy accelerators indicates that the dominant radiological impact on the environment is in the form of prompt radiation [16]. Muons, neutrons and photons dominate the prompt radiation field affecting the environment in the vicinity of the accelerator. Of these three components, neutrons are usually the most important. Neutron fields are quite complicated because neutrons are produced in a variety of reactions and span a wide energy range. They are not affected by the Coulomb barrier of nuclei, so they will not be repelled by the electrostatic charge of the target nucleus and can react at any energy, producing radioactive nuclides. Neutron capture dominates for thermal neutrons, while with increasing energy reactions of type (n,p), (n,np), (n,2p), (n, α) and so forth, occur. High-energy neutrons cause spallation reactions that can produce any nuclide lighter than the target nucleus. Thermal neutrons may cause significant induced radioactivity over and above that caused by spallation reactions on account of the high capture cross section of some materials for thermal neutrons. These radionuclides build-up over time from (n, γ) capture reactions, e.g. on trace amounts of stable Europium, Cobalt and Cesium which are present in concrete in concentrations of a few parts per million or less by weight. The activity concentration of these radionuclides as a function of accelerator operating time is shown in Figure 2.5.

There are many elements in concrete that become activated when irradiated by neutrons from a cyclotron target. Fortunately, only a few of the resulting radioisotopes are long-lived. These are identified in Table 2.3. Normal concrete is more than 50% by weight oxygen and contains about 30% silicon, together with various other elements. Activation of oxygen does not contribute significantly to the long-lived induced activity and activation of Si is not very different from that of aluminium. The use of heavy concrete containing barium in target area means a production of long-lived radioactive isotopes. Long-term irradiation of barytes concrete shows the presence of significant quantities of ^{133}Ba and ^{137}Cs .

Table 2.3: Medium- and long-lived activation products in concrete and barytes concrete (derived from [17] and [18]).

Isotope	Candidate Production Mechanism	Half-life
^{22}Na	$^{23}\text{Na}(n,2n)^{22}\text{Na}$, $^{23}\text{Na}(\gamma,n)^{22}\text{Na}$ $^{27}\text{Al}(n,x)^{22}\text{Na}$, $^{27}\text{Al}(p,x)^{22}\text{Na}$ $^{28}\text{Si}(n,x)^{22}\text{Na}$, $^{28}\text{Si}(p,x)^{22}\text{Na}$	2.6 y
^{45}Ca	$^{45}\text{Sc}(n,p)^{45}\text{Ca}$, $^{44}\text{Ca}(n,\gamma)^{45}\text{Ca}$	162.3 d
^{46}Sc	$^{45}\text{Sc}(n,\gamma)^{46}\text{Ca}$	83.8 d
^{54}Mn	$^{54}\text{Fe}(n,p)^{54}\text{Mn}$, $^{55}\text{Mn}(n,2n)^{54}\text{Mn}$	313 d
^{60}Co	$^{59}\text{Co}(n,\gamma)^{60}\text{Co}$	5.27 y
^{127}Xe	$^{126}\text{Xe}(n,\gamma)^{127}\text{Xe}$	36 d
^{131}Ba	$^{130}\text{Ba}(n,\gamma)^{131}\text{Ba}$	11.5 d
^{133}Ba	$^{132}\text{Ba}(n,\gamma)^{133}\text{Ba}$, $^{133}\text{Cs}(p,n)^{133}\text{Ba}$	10.52 y
^{134}Cs	$^{133}\text{Cs}(n,\gamma)^{134}\text{Cs}$, $^{134}\text{Ba}(n,p)^{134}\text{Cs}$	2.06 y
^{136}Cs	$^{135}\text{Cs}(n,\gamma)^{136}\text{Cs}$	13 d
^{137}Cs	$^{137}\text{Ba}(n,p)^{137}\text{Cs}$, $^{136}\text{Ba}(n,\gamma)^{137\text{m}}\text{Ba}$	30.1 y
^{152}Eu	$^{151}\text{Eu}(n,\gamma)^{152}\text{Eu}$	13.5 y
^{154}Eu	$^{153}\text{Eu}(n,\gamma)^{154}\text{Eu}$	8.59 y

**Figure 2.5:** Build-up of long-term, neutron-induced activity in concrete [17].

Chapter 3

Simulation codes and analytical models

The present chapter presents an introduction to the Monte Carlo methods and to the role of random numbers used to calculate approximate solutions to mathematical or physical problems. It follows a description of the cascade code FLUKA with an overview of the physical models it uses, underlying those aspects important for the present work. The analytical code JEREMY, a tool to estimate residual radioactivity in accelerator facilities and materials, is also presented.

3.1 Methods for predicting induced radioactivity

The analytical formulation through differential equations of various physical problems, like those handled in the present work, e.g. particles transport or radiation interaction with matter, is complicated and, in the most complex cases, impossible. Usually it takes some approximations to build a reasonable analytical formulation of the problem. As an alternative, numerical, and consequently, approximated solutions can be found, but their determination is heavily affected by the accuracy of the method itself.

Monte Carlo methods have a completely different approach. They use random sampling to calculate approximate solutions to a mathematical or physical problem. Often, the complex mathematics needed in many analytical applications can be avoided entirely by simulations. Thus, Monte Carlo methods provide extremely powerful ways to address realistic problems that cannot be solved by analytic techniques. A typical application is the simulation of random processes like, for example, particle-transport methods [19].

Monte Carlo approaches the solution of transport equations without trying to solve all the differential equations describing the problem, but by making a virtual (mathematical) experiment similar to the real one. Every single physical event of the cascade is simulated and the particle stories are tracked. In order to simulate the history of a particle, a description of each region with its geometrical boundaries and its material composition is required. This information is usually provided through an input file, while an adequate description of the cross sections for each isotope is normally contained in the libraries used by the code. Once each event that may happen to a particle is defined in terms of its associated probability, any required macroscopic physical quantity can be scored at any point of the mathematical experiment.

A typical issue that could affect a Monte Carlo simulation is the choice of the physical models and the accuracy of their implementation. Indeed the better efficiency of one code over another concerns how the balance between accuracy and simulation time is reached. In addition, due to the statistical nature of the Monte Carlo method, the result of the simulation approaches the exact value of the real physics quantity only as the number of events treated approaches infinity. Since an actual calculation does not use an infinite number of particles, but is necessarily truncated after a finite number of events, results must be considered with some judgment.

The significance of the results found using Monte Carlo simulations may be improved by using biasing techniques, e.g. the "Splitting" and the "Russian roulette". With these techniques a different weight is given to those

trajectories and those regions that are supposed to give the greatest contribution to the physical quantity scored. In the present work, these biasing techniques have been used for the estimation of induced radioactivity in the samples irradiated at the CERN H4Irrad beam line, as showed in chapter 5.

3.2 The FLUKA radiation transport code

FLUKA is a general purpose Monte Carlo code capable of simulating particle interaction and transport in matter of about 60 different particles, from TeV energies down to energies of thermal neutrons [20, 21]. FLUKA is one of the very few codes available for radiation protection calculations which is capable to calculate in one and the same simulation proton-proton and heavy ion collisions over a wide range of energies as well as the entire hadronic and electromagnetic particle cascade initiated by secondary particles in any material of accelerator components [22]. This code is integral part of all radiation protection studies for the design and operation of the accelerator facilities at CERN. It therefore comprises all features needed in this area of application.

The capabilities of FLUKA are unique for studies of induced radioactivity, especially with regard to nuclide production, their decay and the transport of residual radiation. Particle cascades by prompt radiation and residual radiation are simulated in parallel based on microscopic models for nuclide production and a solution of the Bateman equations for activity build-up and radioactive decay. The decay radiation and the electromagnetic cascade are marked as such in order to distinguish them from the prompt cascade. This allows the user to apply different transport thresholds and biasing options to residual and prompt radiation and to score them independently. Particle fluence can be multiplied with energy-dependent conversion coefficients to effective dose or ambient dose equivalent at scoring time. Prompt and residual dose equivalent can thus be computed in three-dimensional meshes, the latter for arbitrary user-defined irradiation and cooling profiles.

FLUKA allows detailed calculations of the radionuclide inventory based on theoretical models for nuclear interactions and fragmentation. Their implementation in the code has reached unprecedented detail enabling the user to predict the production of individual radioactive isotopes with high accuracy. This achievement has been quantified in a comprehensive benchmark studies [23–26]. In particular, the capability of FLUKA in predicting induced radioactivity and residual dose rates were extensively benchmarked at the CERF facility, which is one of the experimental facilities where the work discussed in the present study has been performed (see Chapter 5).

These are the reasons why FLUKA was chosen in the present work as Monte Carlo method for predicting induced radioactivity. It presents several important features, some of which are outlined in the following.

Physical models

Several models are employed in FLUKA for the transport of the different groups of particles in different energy range. Isotope production by hadronic interactions (except low-energy neutron interactions) is described in FLUKA by well-tested models, which typically act at different energy scales. They comprise a sophisticated Generalized Intranuclear Cascade model including pre-equilibrium emission for energies below a few GeV, i.e. PEANUT (PreEquilibrium Approach to Nuclear Thermalization); the Glauber-Gribov approach together with the Dual Parton Model describing the high-energy (above several GeV) primary interactions with target nucleons; various mechanisms implemented for evaporation, fragmentation, fission, and de-excitation by gamma emission. Interactions of ions are simulated through interfaces with different codes based on models applicable in certain ranges of energy. The transport of neutrons with energies below 20 MeV is performed by a multi-group algorithm based on evaluated cross section data (ENDF/B, JEF, JENDL, etc.) binned into 260 energy groups, 31 of which are in the thermal energy region. Particularly relevant for water, soil and concrete simulations, low-energy neutron transport is also provided with a

detailed kinematics of elastic scattering on hydrogen nuclei as well as transport of recoil protons.

Multi-fragmentation is not taken into account in FLUKA which might pose limitations to the predictions of intermediate and small-mass isotopes from heavy elements (underestimation of their yield). However, this should have only little influence on integral quantities such as total activity or dose rates, since over and underestimates for single elements tend to cancel or compensate each other.

Combinatorial geometry

The combinatorial geometry used by FLUKA is based on two fundamental concepts: bodies and regions. Bodies are defined as: convex solid bodies, i.e. finite portion of space completely delimited by surfaces of first (planes) or second degree (quadratics); infinite cylinders (circular and elliptical); planes (half-spaces). An advantage of using infinite bodies is that they make input preparation and modification much easier and less error-prone.

Complex objects are defined starting from bodies by using the Boolean operators union, difference and intersection. Each region is not necessarily simply connected, since it can be made of two or more non contiguous parts, but must be of homogeneous material composition. Defining bodies and regions with the combinatorial geometry is not an easy task. FLUKA provides the user with a geometry debugger with the capability of finding undefined points, i.e. points which are not included in any defined region, as well as multiple defined points, i.e. points which are included in more than one region. All the regions are surrounded by an infinitely absorbing material ("blackhole"), which absorbs all the escaping particles.

A repetition capability ("lattice") is available to avoid the multiple description of repetitive structures. Only one module has to be defined, which can be re-iterated as many times as required. This allows defining geometries, containing up to thousands of different regions, by using only a small number of region and body definitions. Various visualization tools have also

been integrated into FLUKA thus making it a very powerful tool with many different capabilities according to the user's need.

3.3 The JEREMY analytical model

JEREMY is an analytical tool which allows calculating induced radioactivity from the fluence spectra of the radiation field generated by the beam loss [27]. The approach chosen for the computation is based on two steps. First, the particle spectra of the radiation environment are calculated via Monte Carlo simulations with codes like FLUKA. Given these fluence spectra as input, the radioactivity build-up and subsequent decay are calculated for each isotopes of interest. The radiological characterization calculated with JEREMY is based on the following assumptions:

- **Irradiation history:** this is a critical input parameter for the computation of the induced radioactivity. In the case of particle accelerators the main source of the induced activity are beam losses. Since the beam loss profile should be more or less constant over time, the assumption of a constant irradiation profile is easily fulfilled for most accelerator components. However, the induced activity for an arbitrary irradiation profile can be computed by first approximating the irradiation profile with an irradiation histogram and then by summing the induced activities over the time slices of constant irradiation. In order to approximate the arbitrary irradiation profile sufficiently well, these time slices have to be chosen fine enough.
- **Known uniform particle spectra:** the spectra of the activating particles composing the radiation field have to be uniform in the activated component for the whole irradiation period. If this is not the case, the irradiation period and/or the activated component must be divided into smaller parts until this condition is met or the remaining non-uniformity is taken into account by treating it as an uncertainty on

the particle spectra. Uncertainties on these spectra can be propagated to the computed induced radioactivity.

- **Uniform and known material composition:** The material composition, i.e. the mass weight fractions of the chemical elements, must be uniform within the activated component. If this is not the case, the sample must be divided into smaller parts until this condition is met or the remaining non-uniformity is taken into account by treating it as an uncertainty on the material composition. Uncertainties on the material composition can be propagated to the computed induced radioactivity.
- **Interaction between the radiation field and the isotopes produced during the irradiation period are not take into account:** this means that the amount of nuclei of the isotopes produced during the irradiation period has to be very small compared to the amount of initial material of the component, which is normally the case.
- **There is no depletion of the initial material due to the interactions with the radiation field:** this means that the amount of nuclei of the isotopes produced during the irradiation period has to be very small compared to the amount of initial material of the component. As a consequence, the capabilities of the JEREMY code to describe breeding reactions are very limited. This constraint is of no practical concern for induced radioactivity in particle accelerators.

The flow of information within the JEREMY code for the computation of the induced activity is shown in Fig. 3.1. The fluence spectra together with the isotope production cross sections yield the so-called activation matrix. The fluence spectra for various secondary particles, mainly p, n, γ , π^+ and π^- , per primary beam particle can be obtained by Monte Carlo simulations with codes like FLUKA. The isotope production cross sections for neutrons below 20 MeV have been extracted from the JEFF 3.1.1 library [28]. The isotope production cross sections for neutrons above 20 MeV as well as for p, n, π^+ and π^- have been calculated with FLUKA. The decay data used in JEREMY

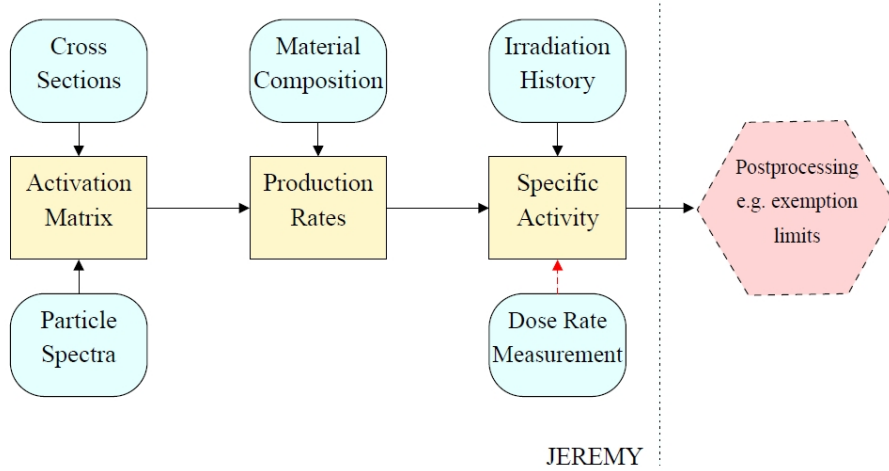


Figure 3.1: Flow of information within the JEREMY code for the computation of the induced activity [29].

has been extracted from the JEFF 3.1.1 library. The idea is to compute the fluence spectra of the particles in the hadronic cascades via Monte Carlo simulation and fold them with the cross sections offline. Taking the material composition of the component into account, the activation matrix can be used to compute the isotope production rates. The isotope production rates together with the irradiation history yield the specific activity. If the absolute scale of the flux of primary particles is not known, the computed specific activity has to be normalised. The measurement of the specific activity of a certain gamma emitter or a dose rate measurement can be used to obtain a proper normalised specific activity.

Standard error propagation assuming Gaussian errors with a given covariance matrix can be used to estimate the uncertainty of the induced activity. For this method, the derivatives with respect to the parameters of interest are required. Another possible way to estimate the uncertainty of the induced activity implemented in JEREMY is to attribute a probability density distribution to every parameter of interest. These probability density distributions are used to perform a Monte Carlo simulation which yields a distribution for the induced activity.

Chapter 4

Application to a specific case: the CERN 600 MeV synchro-cyclotron

The 600 MeV Synchro-cyclotron (SC) was the first accelerator that came into operation at CERN in 1957. It provided beams for CERN's first particle and nuclear physics experiments and was operated until 1990. This chapter presents the results of the measurements that I carried out to evaluate the levels of residual radioactivity after about 20 years of cooling time and their comparison with both analytical and Monte Carlo calculations. The results obtained also serve as indirect validation of the capabilities of FLUKA and JEREMY to correctly predict residual radioactivity with only a very approximate knowledge of the irradiation profile and after a very long cooling time.

4.1 The CERN 600 MeV synchro-cyclotron

The 600-MeV proton synchro-cyclotron (SC) was the very first accelerator designed and built at CERN. The machine started operation in 1957, soon after CERN was founded. A picture of the CERN synchro-cyclotron after



Figure 4.1: The synchro-cyclotron accelerator in its third year of operation (September 1959)

three years of operation is shown in Figure 4.1. Apart from an interruption to undergo a major upgrade in the early 1970s (which included the installation of a new axial ion source, radiofrequency system, magnet coils and vacuum chamber), the accelerator had been in operation for 33 years until it was shutdown in 1990, providing experiments with proton, neutron, muon and pion beams. During its 33 years of operation the accelerator has produced a wealth of physics results.

The building housing the synchro-cyclotron rises up on three levels: the ground floor at the street level housing the top part of the accelerator with the extraction beam lines; the underground level -1 that accommodates the bottom part of the machine; the underground level -2 housing the axial support of the ion source and the hydraulic bearing of the two moving shielded

walls.

The two experimental rooms were decommissioned within a few years after shutdown, whereas the shielded vault housing the accelerator has remained untouched to allow for radioactive decay of its components. The building also served as a storage area for discarded equipment coming from the dismantled experimental areas.

Induced radioactivity at particle accelerators is an important radiation safety issue for sorting out radioactive and conventional waste and for potential free-releasing metallic scrap. The main problem twenty years after shutdown is due to the presence of long-lived radionuclides, their activity concentration (specific activity) and, to a lesser extent, the related dose rate. In view of a partial decommissioning of the accelerator and related equipment, a thorough measurement campaign was conducted to evaluate the levels of residual radioactivity after about 20 years of cooling time [30,31].

4.2 Specific activity in concrete samples

During operation of an accelerator, its building walls and shielding are activated by secondary particles, mainly neutrons, which are produced by nuclear reactions on targets or at beam loss points during acceleration, extraction and transport of particle beams. Although the specific activity of the radioisotopes induced in surrounding materials is generally low, the amount of activated material could be quite large. For evaluation of radioactivity induced in the concrete shields, the residual radioactivity was determined by γ -spectrometry.

A total of 11 concrete cores were taken, 9 of which from the walls and 2 from the SC basement. The cores are distributed as follows: 6 at ground level, where the extraction lines and the machine mid-plane are located (Fig. 4.2); 3 at underground level -1 and 2 at underground level -2. The concrete cores were 50 cm deep and 5 cm in diameter (Fig. 4.3 - a). Each core was cut in slices of about 10 cm thickness (Fig. 4.3 - b). In all, 44 concrete samples

were analyzed.

The main radioisotopes found in concrete are ^{133}Ba , ^{152}Eu , ^{154}Eu , ^{137}Cs , ^{60}Co . ^{133}Ba and ^{137}Cs were detected only in barytes concrete. It is important to point out that the east, north and south walls at the SC ground floor are made of "heavy" barytes concrete, which has good shielding properties, but worst features concerning induced radioactivity. All samples taken from the barytes concrete walls show some residual radioactivity. Figure 4.4 shows two samples of barytes concrete and normal concrete. Barytes concrete, on the left, shows a lighter colour and a more homogeneous structure than the normal one, due to the fine white aggregate of barytes with a density of about 3.5 g/cm^3 , larger than the density of ordinary concrete ($\sim 2.35\text{ g/cm}^3$).

The activation of trace elements (e.g. europium) and of metals in sand yields long-living radionuclides. These are mainly created by neutron capture with high cross sections and by threshold reactions with lower yield. Because of the high ^{151}Eu cross section for thermal neutrons and the long half-life of ^{152}Eu , this radionuclide is present in large quantities in the activated concrete. ^{152}Eu was observed in all concrete samples, without exception, while only 21 samples contain ^{154}Eu . The most probable production reactions are $^{151}\text{Eu}(n,\gamma)^{152}\text{Eu}$ and $^{153}\text{Eu}(n,\gamma)^{154}\text{Eu}$. The several-year half-lives ($t_{1/2}(^{152}\text{Eu})= 13.5\text{ y}$ and $t_{1/2}(^{154}\text{Eu})= 8.6\text{ y}$) and very large capture cross sections for thermal neutrons greatly enhance the sensitivity with which even minute concentrations of Eu in the concrete is revealed after many years of exposure to neutrons.

The presence of the caesium isotopes ^{137}Cs and ^{134}Cs was also detected in barytes concrete. The first radionuclide comes from neutron capture on trace amounts of ^{136}Ba and ^{137}Ba via the $^{136}\text{Ba}(n,\gamma)^{137\text{m}}\text{Ba}$ reaction and the $^{137}\text{Ba}(n,p)^{137}\text{Cs}$ reaction, whereas ^{134}Cs is produced via the $^{134}\text{Ba}(n,p)^{134}\text{Cs}$ reaction and the $^{133}\text{Cs}(n,\gamma)^{134}\text{Cs}$ reaction from trace amounts of ^{134}Ba and ^{133}Cs , respectively. ^{137}Cs was detected in a larger number of samples (29 samples) compared to ^{134}Cs (8 samples). This gap can be explained by the large difference in the half-lives: $t_{1/2}(^{137}\text{Cs})= 30.1\text{ y}$ compared to $t_{1/2}(^{134}\text{Cs})= 2.06\text{ y}$.

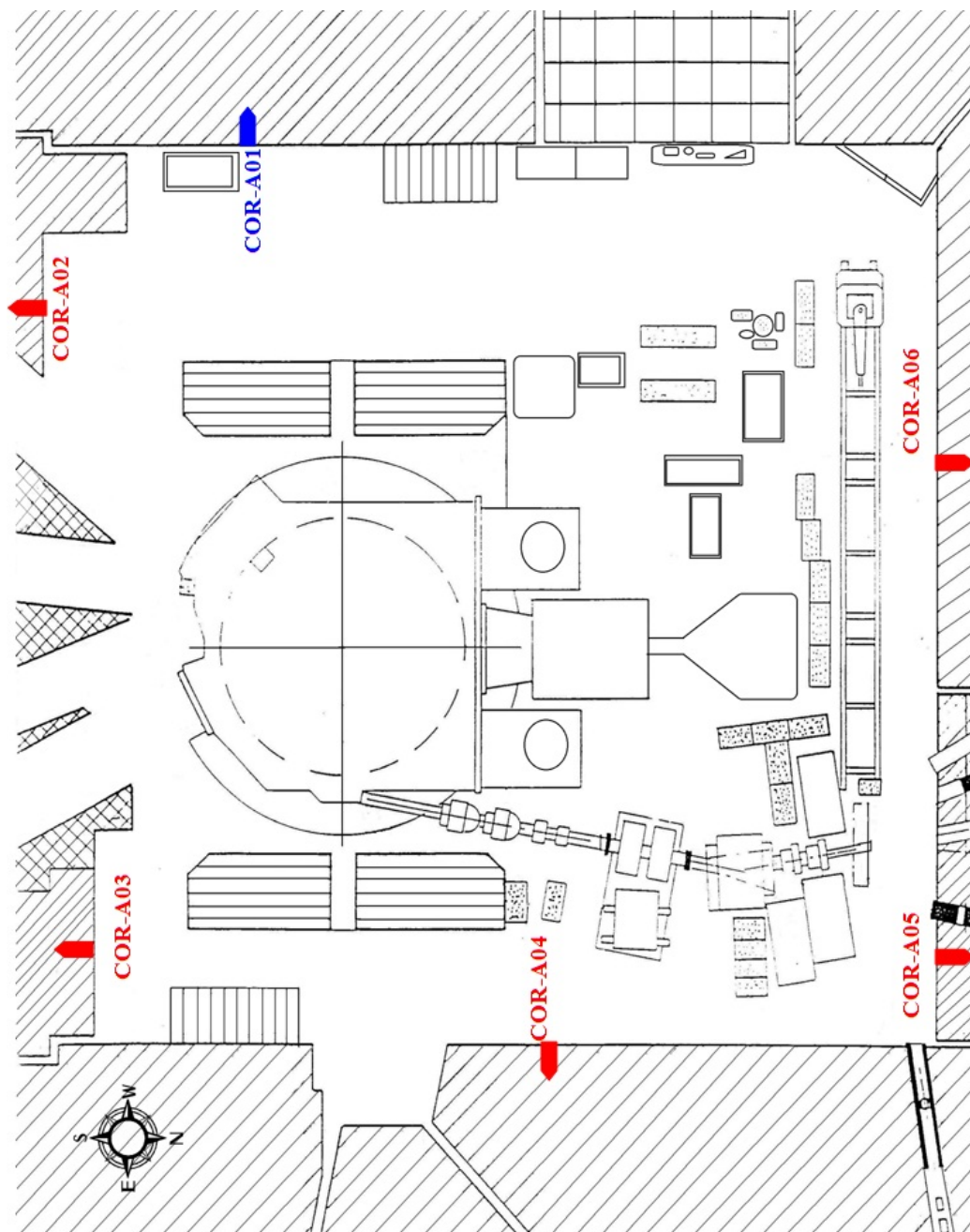


Figure 4.2: Concrete core sampling performed at SC level 0 (ground floor). Concrete samples with a specific activity greater than 1 Bq/g are shown in red, while blue indicates a specific activity lower than 1 Bq/g.



(a) Concrete core



(b) Concrete samples

Figure 4.3: Concrete cores were 50 cm deep and 5 cm in diameter (a). Each core was sliced to 10 cm thickness (b).



Figure 4.4: Comparison between "heavy" barytes concrete (left) and "light" concrete samples (right).

It should be noted that although concrete is typically composed of 1.7% sodium, only a small amount of ^{22}Na was detected, because of its comparatively short half-life ($t_{1/2} = 2.6$ y). It is possible that this radionuclide is produced in $^{23}\text{Na}(n,2n)^{22}\text{Na}$ reactions, but it may also come from the $^{27}\text{Al}(n,2p4n)^{22}\text{Na}$ spallation reaction, a reaction frequently used in activation detectors. A summary of the medium and long-lived activation products in concrete and barytes concrete has been shown in Table 2.3 of chapter 2.

Figures 4.5, 4.6 and 4.7 show the activity depth profiles of the main radionuclides observed in barytes concrete collected from the east, south and north walls, respectively. The most active core was COR-A05, extracted from the north wall, near the proton transfer line. The results of the gamma spectrometry for this sample are given in Tables 4.8 - 4.13. Figure 4.7 indicates that the specific activity of long-lived radionuclides such as ^{133}Ba , ^{137}Cs and ^{60}Co is the highest at a depth of about 35 cm and decreases to a lower level over a depth of 45 cm. The maximum activity is 116 Bq/g for ^{133}Ba . This means that fast neutrons from the beam loss point are slowed down inside the concrete and the thermal neutron component increases up to a depth of

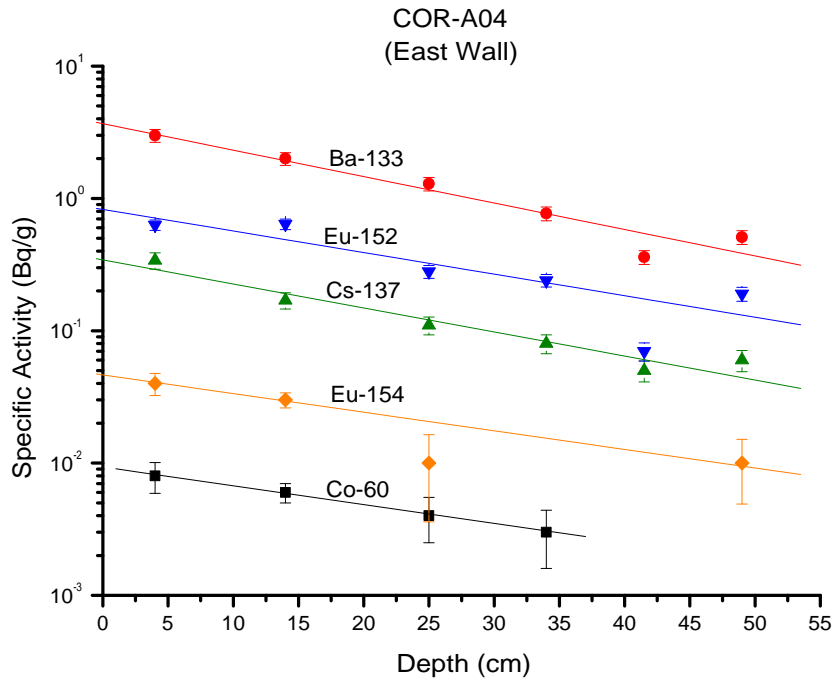


Figure 4.5: Depth profile of the residual radioactivity in the east wall.

about 35 cm. The europium radioisotopes show a more complicated depth profile: a peak at a depth of 15 cm to 20 cm followed by a decrease, then the activity seems to increase again to a maximum value at 45 cm. COR-A05 was the only core where ^{134}Cs and ^{22}Na were detected. ^{134}Cs has a maximum value at the surface and then it seems to stay constant. However, the uncertainty is very large, because of its MDA (Minimum Detectable Activity). The radioactivity of ^{22}Na induced by fast neutrons is the highest at the concrete surface and slowly decreases deep into the wall.

The other graphics plot the activity depth profile of the remaining barytes concrete samples. Only radionuclides induced by thermal neutron capture reactions, which decrease exponentially with depth, were detected. The attenuation curves of ^{152}Eu and ^{137}Cs are close to each other.

COR-A03 in Figure 4.6 shows a peak of ^{60}Co at 30 cm depth, due to a

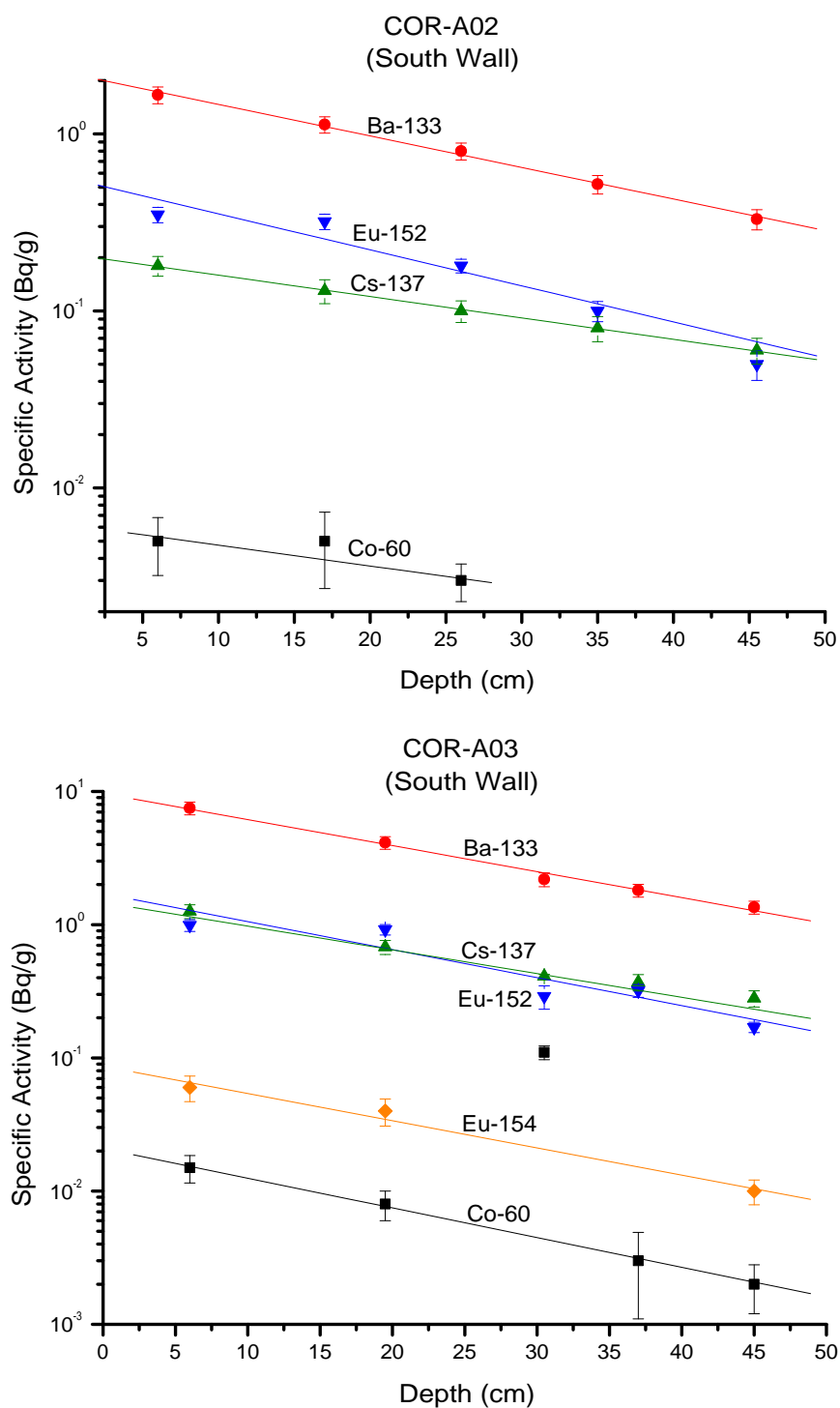


Figure 4.6: Depth profile of the residual radioactivity in the south wall.

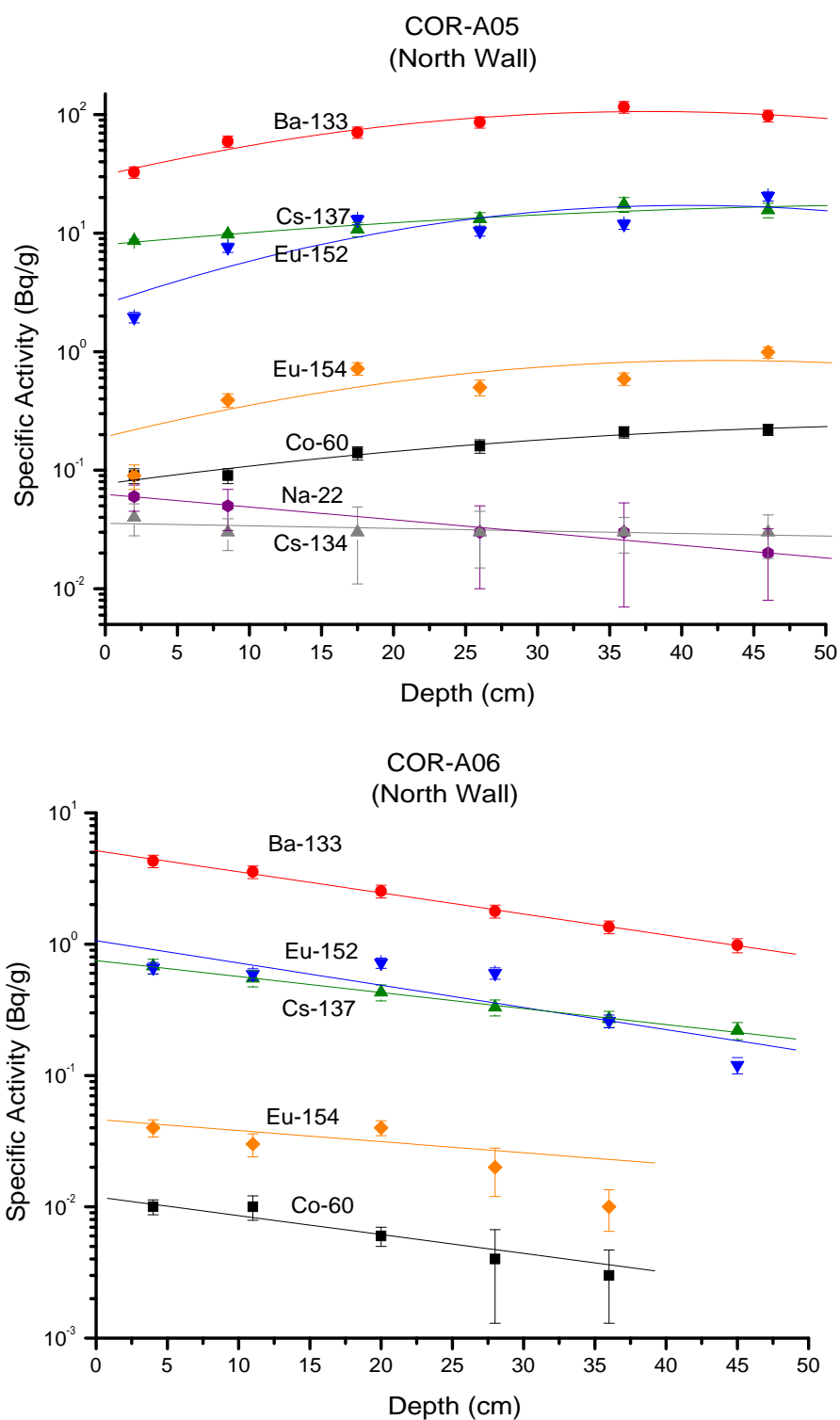


Figure 4.7: Depth profile of the residual radioactivity in the north wall

steel bar in the concrete. Indeed, because the concrete is reinforced with steel bars, some pieces of steel were extracted during the concrete core drilling.

Summarizing, of the 44 concrete samples analyzed, only 24 have at least one radionuclide with a specific activity higher than 1 Bq/g and all of these are made of barytes concrete.

4.3 Prediction of residual radioactivity in the walls

The concentration of the various radionuclides in the core samples was calculated with FLUKA on the basis of a simplified description of the experimental hall. In fact, even if a detailed description of the cyclotron bunker and equipment as it was over the 33 years of operation is not feasible, we will demonstrate that the geometry adopted is good enough to predict with sufficient accuracy the long-lived isotopes in the SC walls (on the proton extraction side). The whole SC hall ($16 \times 17 \times 7 \text{ m}^3$) was modelled together with the 5.5 m thick North, South and East walls made of barite concrete and the 4 m thick West wall made of ordinary concrete. Most of the induced radioactivity in the SC walls was due to the beam losses in the SC extraction system. The low extraction efficiency (see below) depended mainly on beam scattering on the iron septum of the extraction channel, on the losses at the external target, at the exit of the bending magnets and at the entrance of the proton channel wall [32–34]. In order to simulate the overall beam losses that occurred in the extraction system, a 600 MeV proton beam impinging on a $60 \times 100 \times 100 \text{ cm}^3$ steel target was used for the FLUKA simulations. The origin of the coordinate frame of the FLUKA geometry was chosen to be in the centre of the SC hall, the z-axis coinciding with the beam axis and the y-axis pointing up, whereas the steel target was placed around the proton extraction channel, at 5 m distance from the North wall and 3 m from the East wall. Furthermore, a $150 \times 40 \times 100 \text{ cm}^3$ wall made of ordinary concrete was placed between the target and the East wall to simulate the brick wall

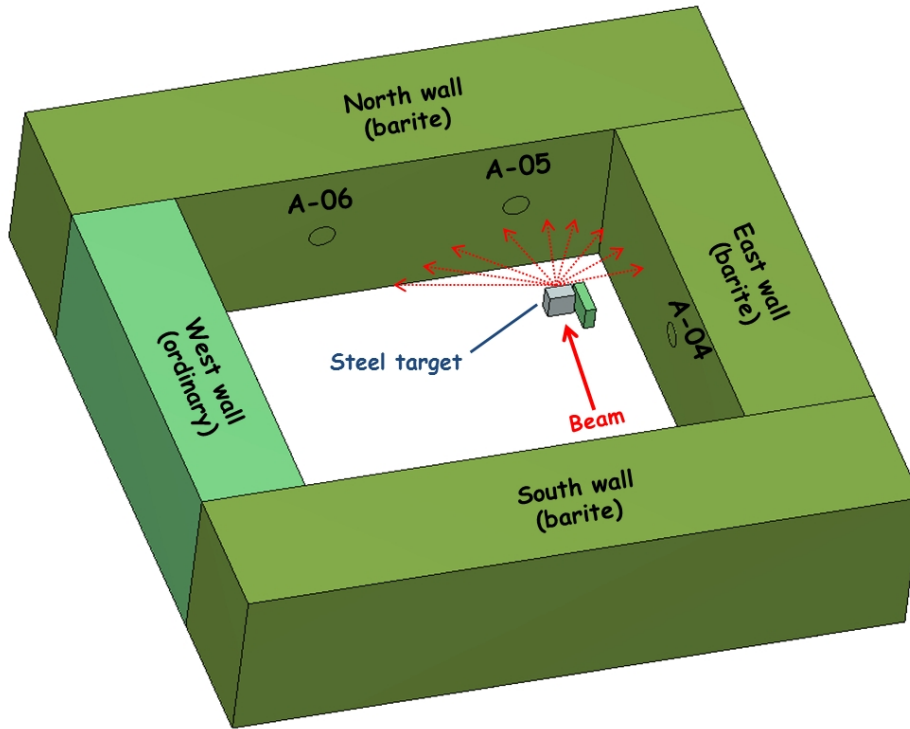


Figure 4.8: Three-dimensional view of the SC geometry used in the FLUKA simulations. The picture was obtained using SimpleGeo [35].

shielding the East side [30]. Figure 4.8 shows the FLUKA geometry used in the simulations.

The elemental composition of the barite concrete used in the simulations is given in Table 4.1. The full hadronic cascade was simulated in the target and in the concrete, including particles backscattered from the walls. The electromagnetic component of the radiation field was disregarded, as its contribution to induced radioactivity is minor as compared to that caused by the hadronic component. Neutrons were transported down to thermal energies; for all other hadrons a threshold of 1 keV was used. Residual nuclei production was treated using the new evaporation model of FLUKA and taking into account heavy fragment evaporation and coalescence mechanism.

The SC performance data were retrieved from the many status reports [36–41]. Above all, Allardyce et al. [39] declared an extraction efficiency ranging

Table 4.1: Composition of the barite concrete wall (density 3.2 g/cm³), in mass fractions.

Element	Ba	O	Ca	Fe	S	Si	H	Al	Na	Mg	Cs	Co	Eu
(Wt-%)	45	40	5	5	2.5	1	0.7	0.5	0.3	0.2	5E-4	1E-4	5E-5

between 5 - 7% for the SC1 and one order of magnitude higher (50 - 70%) for the SC2 after the Improvement Programme. Since the SC1 internal beam current was about 1 μA ($\sim 6.24\text{E}+12$ p/s) and 1.5 μA ($\sim 9.36\text{E}+12$ p/s) for the SC2 (this is an average value versus a nominal value of 10 μA), we calculated a beam loss of 5.8E+12 p/s for the SC1 operational period and 3.12E+12 p/s for the SC2. As from 1978 the SC was used to accelerate heavy ion as well. Since the ion intensity was less than that of protons by a factor of up to 5 [41] and ions were accelerated just for a few years, only the proton beam irradiation profile was considered in the FLUKA simulations.

For each concrete region two types of scoring were used. In one case, the production of residual nuclei and their radioactive decay were performed by FLUKA in the same run. The RESNUCLEi card scored the residual nuclei produced in inelastic interactions, while the radioactive decay was calculated using the RADDECAY, DCYSCORE, DCYTIMES and IRRPROFILE cards, taking into account the decay chains and build-up of isotopes, and the irradiation profile. The data files produced were then post-processed to obtain the specific activity, since the mass of the scored region had to be obtained from its volume and the density of the barite concrete. The USRSUW routine was used to read results in binary form and to compute standard deviations over several runs.

In the second case, FLUKA calculated only the particle spectral fluences that were used as input data into JEREMY. The differential distributions of the energy fluence of protons, pions, neutrons and low-energy ($E < 20$ MeV) neutrons were scored separately for all concrete samples and the results were written into output files (JEREMY input files). The USTSUW routine was used to read the USRTRACK results in binary form from several runs and

to compute statistical uncertainties.

4.4 Results and discussion

This section compares the calculated and measured specific activities for each concrete core. The experimental results [30], the simulation results and their ratios are summarized in Tables 4.2 - 4.7 (for the concrete sample A-04), Tables 4.8 - 4.13 (sample A-05), Tables 4.14 - 4.19 (sample A-06) and in Figure 4.9. The quoted errors include statistical and systematic uncertainties of the gamma spectrometry measurements as well as statistical uncertainties in the FLUKA and JEREMY simulations. It can be observed that, even if the uncertainties in the FLUKA input values (irradiation conditions, geometry, concrete elemental composition, etc.) are quite large, the agreement between calculated and measured activities is rather good, in most cases within a factor of 2.

A rather remarkable agreement is found between the measured and calculated values of residual radioactivity for the A-04 and A-06 samples throughout their thickness (50 cm). At their location in the vault, the particle spectrum is dominated by the thermal neutron component and the residual activity decreases exponentially with depth in the shield.

A different picture is observed for the activity depth profile in the A-05 concrete core, collected where the fast neutron component dominates the particle spectrum. The residual radioactivity in the core surface is particularly well reproduced by the codes, but a striking difference is noted as from a depth of 25 cm in the wall (Figure 4.10 for ^{133}Ba). Here a fast neutron component coming from beam losses not only in the cyclotron extraction channel but also in the bending magnet and in the beam pipes traversing the wall in the A-05 sample area, are slowed down inside the concrete, increasing the thermal neutron component up to a depth of about 35 cm. These particular beam loss conditions were not taken into account in detail in the FLUKA calculations, which can explain the discrepancies observed between measured

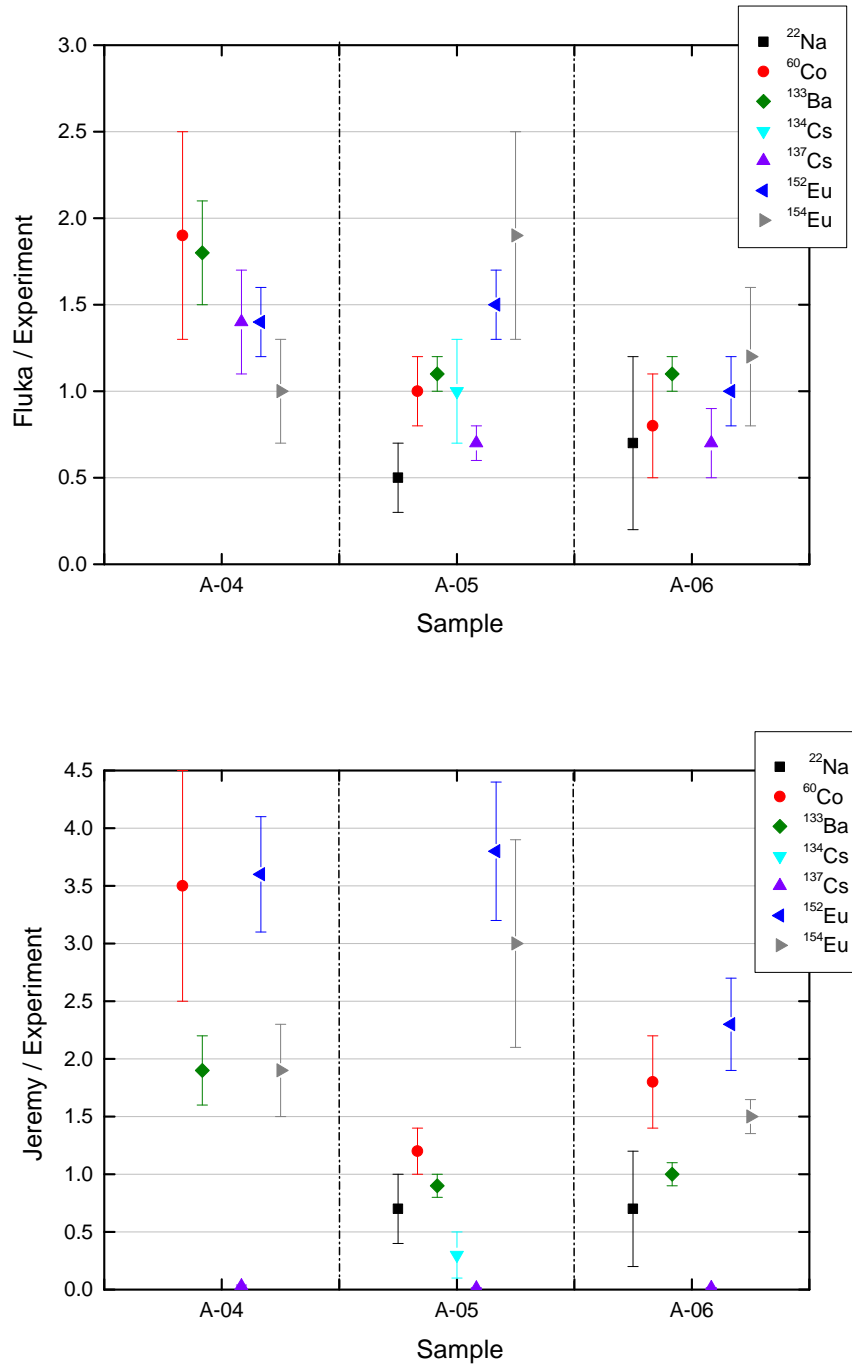


Figure 4.9: Ratios of FLUKA (top) and JEREMY (bottom) over measured specific activities in concrete samples at a wall depth of 5 -10 cm.

and calculated values in the A-05 sample as from a depth of 25 cm.

Residual radioactivity of ^{133}Ba is well described by the codes as shown in Figure 4.10 and Figure 4.11. This radionuclide was measured with high accuracy [30] since it was the most active one and except for the A-05 sample, measured and calculated values are within a factor 2 for both codes. Cesium radionuclides are generally well reproduced by FLUKA, whereas JEREMY underestimates ^{134}Cs and shows very little reliability in the calculation of the residual activity of ^{137}Cs , underestimating it by up to a factor of 100. This could be due to problems with the processing of the JEREMY cross section database [27, 28], which is currently under revision. The predicted values of ^{152}Eu and ^{154}Eu match the measured ones within a factor of 2 for FLUKA and within a factor of 4 for JEREMY. Larger discrepancies can be observed for deeper samples (from a depth of 30 cm). A possible reason is the variable length of the actual samples measured by gamma spectrometry. The FLUKA calculations were performed assuming that all samples had the same dimensions (10 cm thick), whereas the real samples have an average thickness varying from 5 to 15 cm. The remaining isotopes, ^{60}Co and ^{22}Na , are well described by the calculations, in spite of the very low residual radioactivity left after 20 years of cooling. Uncertainties in the elemental composition are expected to be the main reason for the discrepancies.

The complete gamma spectrometry results of the samples and more details on the CERN synchro-cyclotron decommissioning work can be found in Refs. [30, 31, 42, 43] and in the first paper of the Appendix.

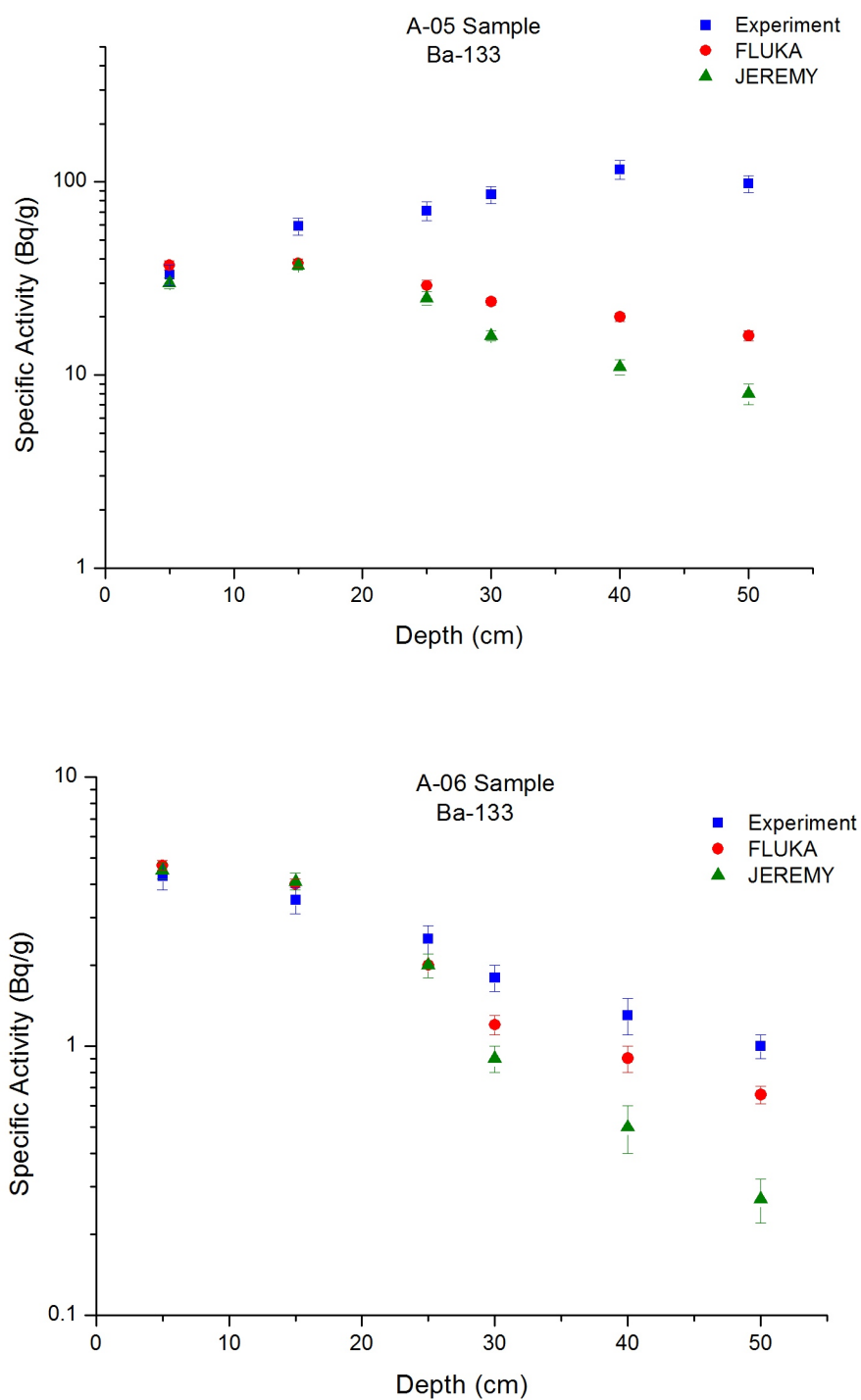


Figure 4.10: Depth profile of the measured and calculated activity of ^{133}Ba in the North wall: A-05 sample (top) and A-06 sample (bottom).

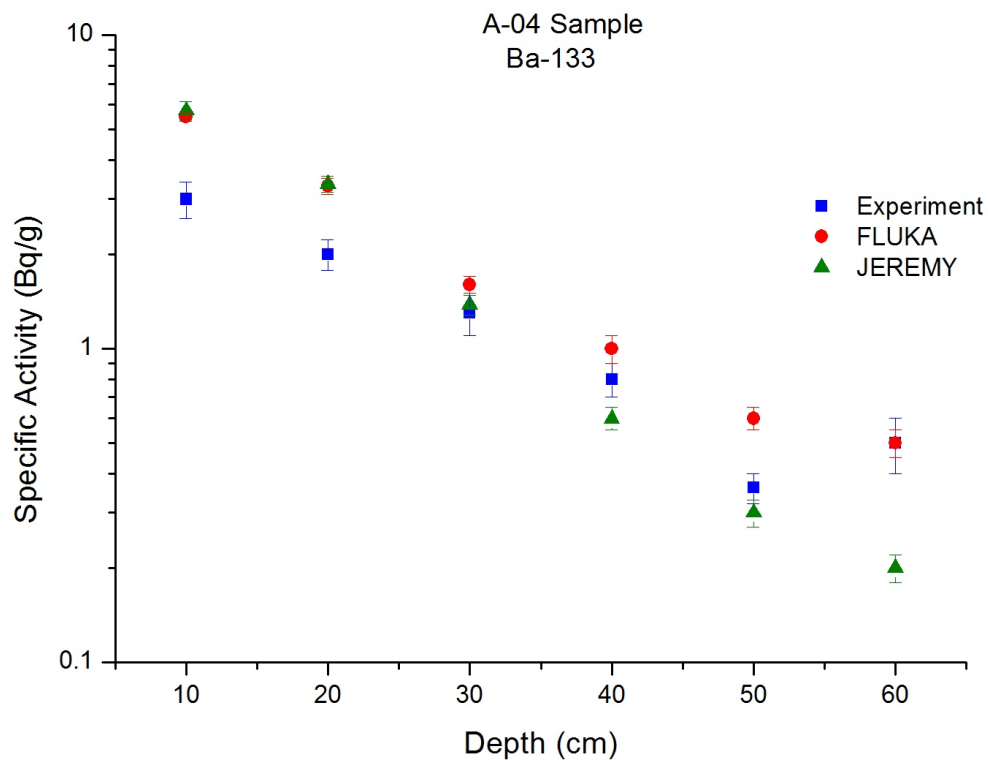


Figure 4.11: Depth profile of the measured and calculated activity of ^{133}Ba in the East wall (A-04 core sample).

Table 4.2: Comparison of calculated and measured specific activity in the A04 sample from 0 to 10 cm depth.

Isotope	$t_{1/2}$ (years)	FLUKA (Bq/g)	JEREMY (Bq/g)	Experiment (Bq/g)	FLU./Exp.	JER./Exp.
^{22}Na	2.6	$0.0010 \pm 3\text{E-}4$	0.003 ± 0.001	< 0.004	/	/
^{60}Co	5.27	0.017 ± 0.004	0.030 ± 0.004	0.009 ± 0.002	1.9 ± 0.6	3.5 ± 1.0
^{133}Ba	10.5	5.5 ± 0.2	5.8 ± 0.4	3.0 ± 0.4	1.8 ± 0.3	1.9 ± 0.3
^{134}Cs	2.06	0.004 ± 0.001	0.002 ± 0.001	< 0.006	/	/
^{137}Cs	30.1	0.46 ± 0.05	0.010 ± 0.002	0.34 ± 0.05	1.4 ± 0.3	0.03 ± 0.01
^{152}Eu	13.5	0.90 ± 0.05	2.3 ± 0.2	0.63 ± 0.06	1.4 ± 0.2	3.6 ± 0.5
^{154}Eu	8.59	0.04 ± 0.01	0.080 ± 0.005	0.04 ± 0.01	1.0 ± 0.3	1.9 ± 0.4

Table 4.3: As in Table 4.2, for the A04 sample from 10 to 20 cm depth.

Isotope	$t_{1/2}$ (years)	FLUKA (Bq/g)	JEREMY (Bq/g)	Experiment (Bq/g)	FLU./Exp.	JER./Exp.
^{22}Na	2.6	$0.0010 \pm 3\text{E-}4$	0.002 ± 0.001	< 0.006	/	/
^{60}Co	5.27	0.006 ± 0.002	0.019 ± 0.003	0.006 ± 0.001	1.1 ± 0.4	3.1 ± 0.6
^{133}Ba	10.5	3.3 ± 0.2	$3.4 \pm .2$	2.0 ± 0.2	1.6 ± 0.2	1.7 ± 0.2
^{134}Cs	2.06	$0.0020 \pm 5\text{E-}4$	$0.0010 \pm 6\text{E-}4$	< 0.003	/	/
^{137}Cs	30.1	0.30 ± 0.04	0.007 ± 0.001	0.17 ± 0.02	1.7 ± 0.3	70.04 ± 0.01
^{152}Eu	13.5	0.65 ± 0.04	1.5 ± 0.2	0.64 ± 0.06	1.0 ± 0.1	2.3 ± 0.3
^{154}Eu	8.59	0.03 ± 0.01	0.045 ± 0.004	0.030 ± 0.004	0.9 ± 0.3	1.3 ± 0.2

Table 4.4: As in Table 4.2, for the A04 sample from 20 to 30 cm depth.

Isotope	$t_{1/2}$ (years)	FLUKA (Bq/g)	JEREMY (Bq/g)	Experiment (Bq/g)	FLU./Exp.	JER./Exp.
^{22}Na	2.6	$0.0010 \pm 3\text{E-}4$	$0.0010 \pm 5\text{E-}4$	< 0.006	/	/
^{60}Co	5.27	0.009 ± 0.003	0.007 ± 0.001	0.004 ± 0.002	2.3 ± 1.2	1.9 ± 0.9
^{133}Ba	10.5	1.6 ± 0.1	1.4 ± 0.1	1.3 ± 0.2	1.2 ± 0.2	1.1 ± 0.2
^{134}Cs	2.06	$0.0010 \pm 3\text{E-}4$	$4\text{E-}4 \pm 2\text{E-}4$	< 0.005	/	/
^{137}Cs	30.1	0.26 ± 0.03	0.05 ± 0.005	0.11 ± 0.02	2.3 ± 0.5	0.04 ± 0.01
^{152}Eu	13.5	0.30 ± 0.03	0.60 ± 0.05	0.28 ± 0.03	1.1 ± 0.2	2.1 ± 0.3
^{154}Eu	8.59	0.009 ± 0.005	0.017 ± 0.006	0.010 ± 0.006	1.1 ± 0.8	1.9 ± 1.2

Table 4.5: As in Table 4.2, for the A04 sample from 30 to 40 cm depth.

Isotope	$t_{1/2}$ (years)	FLUKA (Bq/g)	JEREMY (Bq/g)	Experiment (Bq/g)	FLU./Exp.	JER./Exp.
^{22}Na	2.6	$5\text{E-}4 \pm 2\text{E-}4$	$0.0010 \pm 5\text{E-}4$	< 0.004	/	/
^{60}Co	5.27	0.001 ± 0.001	$0.0030 \pm 5\text{E-}4$	0.003 ± 0.001	0.3 ± 0.3	1.0 ± 0.5
^{133}Ba	10.5	1.0 ± 0.1	0.58 ± 0.05	0.8 ± 0.1	1.3 ± 0.2	0.7 ± 0.1
^{134}Cs	2.06	$8\text{E-}4 \pm 2\text{E-}4$	$2\text{E-}4 \pm 1\text{E-}4$	< 0.005	/	/
^{137}Cs	30.1	0.20 ± 0.03	$0.0030 \pm 5\text{E-}4$	0.08 ± 0.01	2.5 ± 0.5	0.04 ± 0.01
^{152}Eu	13.5	0.15 ± 0.02	0.24 ± 0.02	0.24 ± 0.03	0.6 ± 0.1	1.0 ± 0.1
^{154}Eu	8.59	0.005 ± 0.003	0.007 ± 0.001	0.015 ± 0.007	0.3 ± 0.2	0.5 ± 0.2

Table 4.6: As in Table 4.2, for the A04 sample from 40 to 50 cm depth.

Isotope	$t_{1/2}$ (years)	FLUKA (Bq/g)	JEREMY (Bq/g)	Experiment (Bq/g)	FLU./Exp.	JER./Exp.
^{22}Na	2.6	$5\text{E-}4 \pm 2\text{E-}4$	$7\text{E-}4 \pm 2\text{E-}4$	< 0.005	/	/
^{60}Co	5.27	/	$0.002 \pm 5\text{E-}4$	< 0.004	/	/
^{133}Ba	10.5	0.60 ± 0.05	0.30 ± 0.03	0.36 ± 0.04	1.7 ± 0.3	0.8 ± 0.1
^{134}Cs	2.06	$0.0010 \pm 2\text{E-}4$	$2\text{E-}4 \pm 1\text{E-}4$	< 0.005	/	/
^{137}Cs	30.1	0.13 ± 0.02	$0.0020 \pm 3\text{E-}4$	0.05 ± 0.01	2.8 ± 0.7	0.05 ± 0.02
^{152}Eu	13.5	0.04 ± 0.01	0.12 ± 0.01	0.07 ± 0.01	0.6 ± 0.2	1.7 ± 0.3
^{154}Eu	8.59	/	$0.0030 \pm 5\text{E-}4$	< 0.001	/	/

Table 4.7: As in Table 4.2, for the A04 sample from 50 to 60 cm depth.

Isotope	$t_{1/2}$ (years)	FLUKA (Bq/g)	JEREMY (Bq/g)	Experiment (Bq/g)	FLU./Exp.	JER./Exp.
^{22}Na	2.6	$1\text{E-}4 \pm 1\text{E-}4$	$5\text{E-}4 \pm 2\text{E-}4$	< 0.006	/	/
^{60}Co	5.27	0.001 ± 0.001	$9\text{E-}4 \pm 5\text{E-}4$	< 0.004	/	/
^{133}Ba	10.5	0.50 ± 0.05	0.18 ± 0.02	0.5 ± 0.1	1.0 ± 0.2	0.4 ± 0.1
^{134}Cs	2.06	$5\text{E-}4 \pm 1\text{E-}4$	$4\text{E-}5 \pm 2\text{E-}5$	< 0.005	/	/
^{137}Cs	30.1	0.08 ± 0.02	$0.0020 \pm 4\text{E-}4$	0.06 ± 0.01	1.4 ± 0.4	0.03 ± 0.01
^{152}Eu	13.5	0.04 ± 0.01	0.07 ± 0.02	0.19 ± 0.02	0.20 ± 0.06	0.4 ± 0.1
^{154}Eu	8.59	/	$0.0020 \pm 5\text{E-}4$	0.013 ± 0.007	/	0.2 ± 0.1

Table 4.8: As in Table 4.2, for the A05 sample from 0 to 5 cm depth.

Isotope	$t_{1/2}$ (years)	FLUKA (Bq/g)	JEREMY (Bq/g)	Experiment (Bq/g)	FLU./Exp.	JER./Exp.
^{22}Na	2.6	0.03 ± 0.01	0.04 ± 0.01	0.06 ± 0.02	0.5 ± 0.2	0.7 ± 0.3
^{60}Co	5.27	0.09 ± 0.01	0.11 ± 0.01	0.09 ± 0.01	1.0 ± 0.2	1.2 ± 0.2
^{133}Ba	10.5	37 ± 2	30 ± 2	33 ± 4	1.1 ± 0.1	0.9 ± 0.1
^{134}Cs	2.06	0.04 ± 0.01	0.010 ± 0.005	0.04 ± 0.01	1.0 ± 0.3	0.3 ± 0.2
^{137}Cs	30.1	6.4 ± 0.5	0.07 ± 0.02	8.6 ± 1.2	0.7 ± 0.1	0.010 ± 0.005
^{152}Eu	13.5	3.0 ± 0.2	7.7 ± 0.6	1.9 ± 0.2	1.5 ± 0.2	3.8 ± 0.6
^{154}Eu	8.59	0.19 ± 0.03	0.30 ± 0.03	0.10 ± 0.02	1.9 ± 0.6	3.0 ± 0.9

Table 4.9: As in Table 4.2, for the A05 sample from 5 to 15 cm depth.

Isotope	$t_{1/2}$ (years)	FLUKA (Bq/g)	JEREMY (Bq/g)	Experiment (Bq/g)	FLU./Exp.	JER./Exp.
^{22}Na	2.6	0.020 ± 0.005	0.04 ± 0.01	0.05 ± 0.02	0.4 ± 0.1	0.8 ± 0.4
^{60}Co	5.27	0.10 ± 0.01	0.15 ± 0.02	0.09 ± 0.01	1.1 ± 0.2	1.7 ± 0.3
^{133}Ba	10.5	38 ± 2	37 ± 2	59 ± 6	0.6 ± 0.1	0.6 ± 0.1
^{134}Cs	2.06	0.04 ± 0.01	0.010 ± 0.006	0.03 ± 0.01	1.4 ± 0.5	0.4 ± 0.3
^{137}Cs	30.1	6.0 ± 0.4	0.08 ± 0.01	9.8 ± 1.3	0.6 ± 0.1	0.010 ± 0.005
^{152}Eu	13.5	4.8 ± 0.2	11 ± 1	7.6 ± 0.7	0.6 ± 0.1	1.5 ± 0.2
^{154}Eu	8.59	0.26 ± 0.03	0.38 ± 0.03	0.39 ± 0.05	0.7 ± 0.2	1.0 ± 0.2

Table 4.10: As in Table 4.2, for the A05 sample from 15 to 25 cm depth.

Isotope	$t_{1/2}$ (years)	FLUKA (Bq/g)	JEREMY (Bq/g)	Experiment (Bq/g)	FLU./Exp.	JER./Exp.
^{22}Na	2.6	0.020 ± 0.005	0.04 ± 0.01	< 0.02	/	/
^{60}Co	5.27	0.07 ± 0.01	0.10 ± 0.02	0.14 ± 0.02	0.5 ± 0.1	0.7 ± 0.2
^{133}Ba	10.5	29 ± 2	25 ± 2	71 ± 8	0.40 ± 0.06	0.30 ± 0.05
^{134}Cs	2.06	0.04 ± 0.01	0.006 ± 0.003	0.03 ± 0.02	1.2 ± 0.7	0.2 ± 0.2
^{137}Cs	30.1	5.5 ± 0.4	0.08 ± 0.01	10.8 ± 1.5	0.5 ± 0.1	0.007 ± 0.003
^{152}Eu	13.5	3.1 ± 0.1	7.9 ± 0.7	13 ± 1	0.24 ± 0.04	0.6 ± 0.1
^{154}Eu	8.59	0.19 ± 0.03	0.24 ± 0.03	0.7 ± 0.1	0.30 ± 0.05	0.33 ± 0.07

Table 4.11: As in Table 4.2, for the A05 sample from 25 to 30 cm depth.

Isotope	$t_{1/2}$ (years)	FLUKA (Bq/g)	JEREMY (Bq/g)	Experiment (Bq/g)	FLU./Exp.	JER./Exp.
^{22}Na	2.6	0.020 ± 0.005	0.03 ± 0.01	0.03 ± 0.02	0.7 ± 0.6	1.1 ± 0.9
^{60}Co	5.27	0.03 ± 0.01	0.06 ± 0.01	0.16 ± 0.02	0.20 ± 0.08	0.4 ± 0.1
^{133}Ba	10.5	24 ± 1	16 ± 1	86 ± 9	0.28 ± 0.03	0.18 ± 0.03
^{134}Cs	2.06	0.030 ± 0.05	0.003 ± 0.002	0.03 ± 0.01	1.0 ± 0.5	0.10 ± 0.08
^{137}Cs	30.1	5.2 ± 0.5	0.07 ± 0.01	13.2 ± 1.8	0.40 ± 0.07	0.005 ± 0.001
^{152}Eu	13.5	2.1 ± 0.2	5.0 ± 0.4	10 ± 1	0.20 ± 0.03	0.50 ± 0.08
^{154}Eu	8.59	0.10 ± 0.02	0.15 ± 0.01	0.50 ± 0.07	0.20 ± 0.06	0.3 ± 0.1

Table 4.12: As in Table 4.2, for the A05 sample from 30 to 40 cm depth.

Isotope	$t_{1/2}$ (years)	FLUKA (Bq/g)	JEREMY (Bq/g)	Experiment (Bq/g)	FLU./Exp.	JER./Exp.
^{22}Na	2.6	0.015 ± 0.005	0.03 ± 0.01	0.03 ± 0.02	0.5 ± 0.4	1.0 ± 0.8
^{60}Co	5.27	0.020 ± 0.005	0.04 ± 0.01	0.21 ± 0.03	0.10 ± 0.03	0.2 ± 0.1
^{133}Ba	10.5	20 ± 1	11 ± 1	116 ± 13	0.18 ± 0.02	0.10 ± 0.01
^{134}Cs	2.06	0.03 ± 0.01	0.002 ± 0.001	0.03 ± 0.01	1.0 ± 0.5	0.07 ± 0.05
^{137}Cs	30.1	4.3 ± 0.5	0.06 ± 0.01	17.5 ± 2.4	0.25 ± 0.05	0.004 ± 0.001
^{152}Eu	13.5	1.5 ± 0.1	3.5 ± 0.3	12 ± 1	0.12 ± 0.02	0.30 ± 0.05
^{154}Eu	8.59	0.05 ± 0.01	0.10 ± 0.02	0.6 ± 0.1	0.10 ± 0.03	0.20 ± 0.05

Table 4.13: As in Table 4.2, for the A05 sample from 40 to 50 cm depth.

Isotope	$t_{1/2}$ (years)	FLUKA (Bq/g)	JEREMY (Bq/g)	Experiment (Bq/g)	FLU./Exp.	JER./Exp.
^{22}Na	2.6	0.015 ± 0.005	0.02 ± 0.01	0.02 ± 0.02	0.7 ± 0.8	1.2 ± 1.5
^{60}Co	5.27	0.025 ± 0.005	0.03 ± 0.01	0.22 ± 0.03	0.11 ± 0.03	0.14 ± 0.05
^{133}Ba	10.5	16 ± 1	8 ± 1	98 ± 10	0.17 ± 0.05	0.08 ± 0.02
^{134}Cs	2.06	0.025 ± 0.005	0.002 ± 0.001	0.03 ± 0.01	0.8 ± 0.4	0.05 ± 0.04
^{137}Cs	30.1	3.8 ± 0.2	0.05 ± 0.01	15.7 ± 2.1	0.24 ± 0.04	0.003 ± 0.001
^{152}Eu	13.5	1.1 ± 0.1	2.5 ± 0.2	20.5 ± 2.1	0.05 ± 0.01	0.12 ± 0.03
^{154}Eu	8.59	0.07 ± 0.02	0.08 ± 0.01	1.0 ± 0.1	0.07 ± 0.02	0.08 ± 0.02

Table 4.14: As in Table 4.2, for the A06 sample from 0 to 5 cm depth.

Isotope	$t_{1/2}$ (years)	FLUKA (Bq/g)	JEREMY (Bq/g)	Experiment (Bq/g)	FLU./Exp.	JER./Exp.
^{22}Na	2.6	0.002 ± 0.001	0.002 ± 0.001	0.003 ± 0.002	0.7 ± 0.5	0.7 ± 0.5
^{60}Co	5.27	0.009 ± 0.004	0.020 ± 0.005	0.012 ± 0.002	0.8 ± 0.3	1.8 ± 0.4
^{133}Ba	10.5	4.7 ± 0.2	4.5 ± 0.3	4.3 ± 0.5	1.1 ± 0.1	1.0 ± 0.1
^{134}Cs	2.06	0.003 ± 0.001	0.002 ± 0.001	< 0.003	/	/
^{137}Cs	30.1	0.5 ± 0.1	0.010 ± 0.002	0.7 ± 0.1	0.7 ± 0.2	0.010 ± 0.005
^{152}Eu	13.5	0.7 ± 0.1	1.6 ± 0.2	0.7 ± 0.1	1.0 ± 0.2	2.3 ± 0.4
^{154}Eu	8.59	0.05 ± 0.01	0.06 ± 0.01	0.04 ± 0.01	1.2 ± 0.4	1.5 ± 0.4

Table 4.15: As in Table 4.2, for the A06 sample from 5 to 15 cm depth.

Isotope	$t_{1/2}$ (years)	FLUKA (Bq/g)	JEREMY (Bq/g)	Experiment (Bq/g)	FLU./Exp.	JER./Exp.
^{22}Na	2.6	0.002 ± 0.001	0.002 ± 0.001	< 0.003	/	/
^{60}Co	5.27	0.015 ± 0.004	0.020 ± 0.005	0.012 ± 0.003	1.2 ± 0.4	1.8 ± 0.5
^{133}Ba	10.5	4.0 ± 0.2	4.1 ± 0.3	3.5 ± 0.4	1.1 ± 0.2	1.1 ± 0.2
^{134}Cs	2.06	0.003 ± 0.001	0.002 ± 0.001	< 0.006	/	/
^{137}Cs	30.1	0.40 ± 0.05	0.006 ± 0.002	0.55 ± 0.08	0.7 ± 0.2	0.010 ± 0.005
^{152}Eu	13.5	0.65 ± 0.05	1.7 ± 0.2	0.60 ± 0.06	1.1 ± 0.2	2.9 ± 0.5
^{154}Eu	8.59	0.03 ± 0.01	0.05 ± 0.01	0.03 ± 0.01	1.0 ± 0.3	1.6 ± 0.5

Table 4.16: As in Table 4.2, for the A06 sample from 15 to 25 cm depth.

Isotope	$t_{1/2}$ (years)	FLUKA (Bq/g)	JEREMY (Bq/g)	Experiment (Bq/g)	FLU./Exp.	JER./Exp.
^{22}Na	2.6	0.002 ± 0.001	$0.0010 \pm 4\text{E-}4$	< 0.002	/	/
^{60}Co	5.27	0.006 ± 0.002	0.010 ± 0.002	0.006 ± 0.002	1.0 ± 0.4	1.8 ± 0.5
^{133}Ba	10.5	2.0 ± 0.2	2.0 ± 0.2	2.5 ± 0.3	0.8 ± 0.1	0.8 ± 0.1
^{134}Cs	2.06	0.002 ± 0.001	$5\text{E-}4 \pm 3\text{E-}4$	< 0.002	/	/
^{137}Cs	30.1	0.20 ± 0.05	0.004 ± 0.001	0.4 ± 0.1	0.5 ± 0.1	0.010 ± 0.005
^{152}Eu	13.5	0.33 ± 0.03	0.9 ± 0.1	0.7 ± 0.1	0.5 ± 0.1	$1.2 \pm .2$
^{154}Eu	8.59	0.03 ± 0.01	0.03 ± 0.01	0.04 ± 0.01	0.7 ± 0.3	0.7 ± 0.3

Table 4.17: As in Table 4.2, for the A06 sample from 25 to 30 cm depth.

Isotope	$t_{1/2}$ (years)	FLUKA (Bq/g)	JEREMY (Bq/g)	Experiment (Bq/g)	FLU./Exp.	JER./Exp.
^{22}Na	2.6	/	$0.0010 \pm 3\text{E-}4$	$< 0.005\text{a}$	/	/
^{60}Co	5.27	0.002 ± 0.002	0.005 ± 0.001	0.004 ± 0.003	0.5 ± 0.6	1.3 ± 0.9
^{133}Ba	10.5	1.2 ± 0.1	0.9 ± 0.1	1.8 ± 0.2	0.6 ± 0.1	0.5 ± 0.1
^{134}Cs	2.06	0.002 ± 0.001	$2\text{E-}4 \pm 1\text{E-}4$	$< 0.008\text{a}$	/	/
^{137}Cs	30.1	0.24 ± 0.04	0.004 ± 0.001	0.33 ± 0.05	0.8 ± 0.2	0.010 ± 0.005
^{152}Eu	13.5	0.15 ± 0.03	0.42 ± 0.05	0.6 ± 0.1	0.25 ± 0.05	0.7 ± 0.2
^{154}Eu	8.59	/	0.012 ± 0.004	0.02 ± 0.01	/	0.6 ± 0.2

Table 4.18: As in Table 4.2, for the A06 sample from 30 to 40 cm depth.

Isotope	$t_{1/2}$ (years)	FLUKA (Bq/g)	JEREMY (Bq/g)	Experiment (Bq/g)	FLU./Exp.	JER./Exp.
^{22}Na	2.6	$3\text{E-}4 \pm 2\text{E-}4$	$7\text{E-}4 \pm 3\text{E-}4$	$< 0.004\text{a}$	/	/
^{60}Co	5.27	0.001 ± 0.001	0.003 ± 0.001	0.003 ± 0.001	0.4 ± 0.4	1.0 ± 0.6
^{133}Ba	10.5	0.9 ± 0.1	0.5 ± 0.1	1.3 ± 0.2	0.7 ± 0.2	0.4 ± 0.1
^{134}Cs	2.06	0.001 ± 0.001	$1\text{E-}4 \pm 1\text{E-}4$	$< 0.006\text{a}$	/	/
^{137}Cs	30.1	0.15 ± 0.03	0.003 ± 0.001	0.27 ± 0.05	0.6 ± 0.2	0.010 ± 0.004
^{152}Eu	13.5	0.08 ± 0.02	0.22 ± 0.05	0.26 ± 0.03	0.3 ± 0.1	0.8 ± 0.2
^{154}Eu	8.59	/	0.006 ± 0.001	0.015 ± 0.005	/	0.4 ± 0.2

Table 4.19: As in Table 4.2, for the A06 sample from 40 to 50 cm depth.

Isotope	$t_{1/2}$ (years)	FLUKA (Bq/g)	JEREMY (Bq/g)	Experiment (Bq/g)	FLU./Exp.	JER./Exp.
^{22}Na	2.6	$3\text{E-}4 \pm 2\text{E-}4$	$5\text{E-}4 \pm 2\text{E-}4$	$< 0.005\text{a}$	/	/
^{60}Co	5.27	0.002 ± 0.001	$0.0010 \pm 4\text{E-}4$	$< 0.005\text{a}$	/	/
^{133}Ba	10.5	0.66 ± 0.05	0.27 ± 0.05	1.0 ± 0.1	0.7 ± 0.1	0.3 ± 0.1
^{134}Cs	2.06	0.001 ± 0.001	$1\text{E-}4 \pm 1\text{E-}4$	$< 0.006\text{a}$	/	/
^{137}Cs	30.1	0.09 ± 0.02	0.02 ± 0.01	0.22 ± 0.04	0.4 ± 0.1	0.009 ± 0.004
^{152}Eu	13.5	0.04 ± 0.01	0.11 ± 0.02	0.12 ± 0.02	0.4 ± 0.2	0.9 ± 0.3
^{154}Eu	8.59	0.005 ± 0.003	0.003 ± 0.001	$< 0.01\text{a}$	/	/

Chapter 5

Activation experiments

This chapter describes the activation experiments carried out at the CERF and H4IRRAD facilities at CERN. Natural iron and copper samples were activated in order to provide proton- and pion-induced spallation cross sections at 120 GeV/c for the production of 14 radioisotopes in ^{nat}Cu and 16 radioisotopes in ^{nat}Fe target. These spallation reactions are of direct relevance in activation studies, since copper and iron are commonly employed in high-energy particle accelerators and their surrounding structures. The accuracy of these measurements is strongly dependent on careful calibration of the beam monitor. For this reason the ionization chamber (IC) used as beam monitor was calibrated with the foil activation technique using the $^{27}\text{Al}(\text{p},3\text{pn})^{24}\text{Na}$ and the $^{nat}\text{Cu}(\text{p},\text{x})^{24}\text{Na}$ monitor reactions. The focus is on the specific conditions of mixed high energy beams, but the conclusions are obviously valid for a beam composed of a single particle type. First, the activation of hyperpure aluminium foils is discussed, focusing the attention on the different parameters on which the activation process critically depends. Then the alternative $^{nat}\text{Cu}(\text{p},\text{x})^{24}\text{Na}$ reaction is investigated, highlighting the features that makes it an ideal reaction for beam monitoring and its main advantages if compared to the $^{27}\text{Al}(\text{p},3\text{pn})^{24}\text{Na}$. The experimental results are also compared with FLUKA Monte Carlo simulations. The second part of the chapter is dedicated to the activation of the soil-shield samples at

the H4IRRAD facility. Two leaching procedures were used and compared to quantify the radioactivity leached from the activated soil into the groundwater. The results of the gamma spectrometry and liquid scintillation analyses are presented. The amount of tritium coming from the soil moisture and the soil bulk was also estimated. In order to validate the FLUKA capability in predicting the production of radioactivity in this specific context, the simulation results were benchmarked by the experimental results.

5.1 Irradiation at the CERF facility

The CERN-EU high-energy Reference Field (CERF) [44] facility is installed in one of the secondary beam lines (H6) from the Super Proton Synchrotron (SPS), in the North Experimental Area on the Preveessin (French) site of CERN (see Figure 5.1). A positive hadron beam (61% pions, 35% protons and 4% kaons) with momentum of 120 GeV/c is stopped in a copper target, 7 cm in diameter and 50 cm in length. The beam is delivered to the facility with a typical intensity in the range 10^6 to 10^8 particles per SPS spill. The beam extraction time is presently about 10 s over an SPS cycle of about 45 s. In the secondary beam areas (SBA) of CERN Super Proton Synchrotron (SPS) the beam monitoring is commonly carried out via ionization chambers (IC). The high energy beams are characterized by a current varying between a few fA and tens of pA. These currents are too low to allow using beam current transformers (BCT) and secondary electron emission monitors (SEEM), whereas scintillators are used only in the lower part of the intensity range to avoid saturation issues, and Faraday cups (FC) cannot be used for on-line monitoring. Therefore ICs remain one of the best solutions, coupled with a special electronics designed to deal with the very low currents produced during the beam spill. A specificity of the CERN SBAs is that the beams are usually mixed particles (e.g. protons, pions and kaons for positive polarity). The relative percentages depend on the beam energy [45].

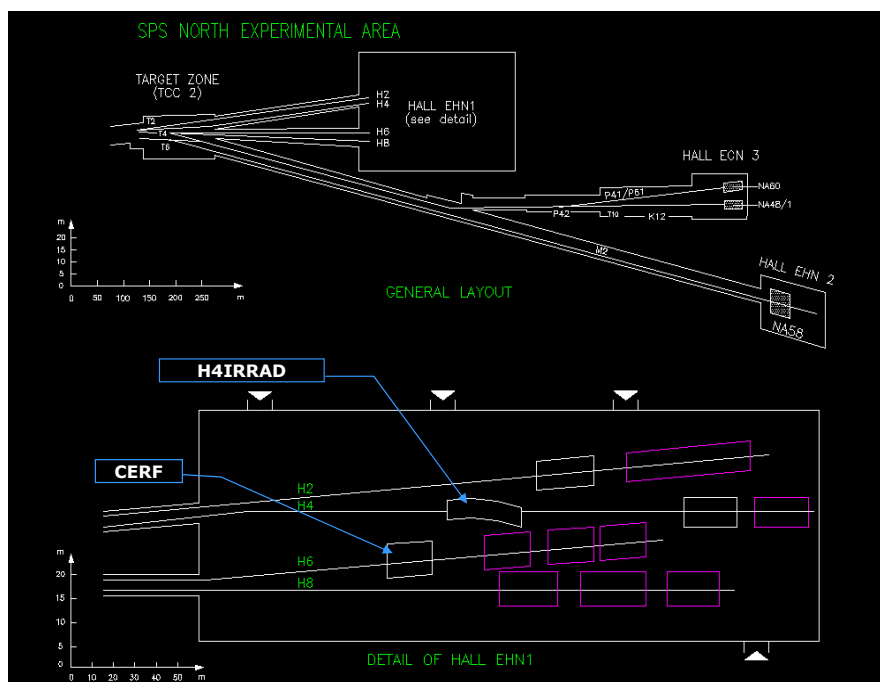
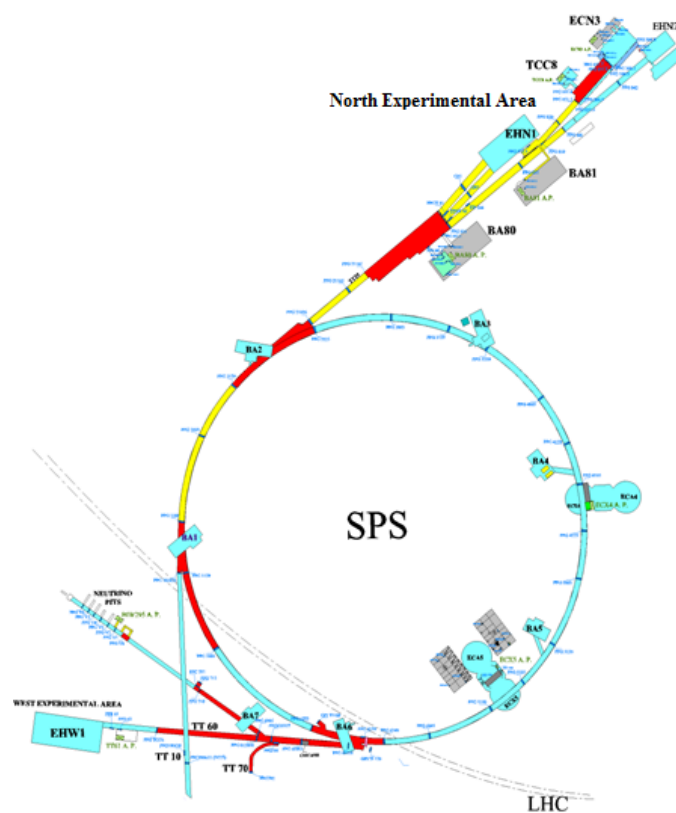


Figure 5.1: Schematic view of the SPS North Experimental Area with the CERF and the H4IRRAD facilities (adapted from [46]).

5.1.1 The Ionization Chamber (IC)

The ionization chamber (IC) used as beam monitor at CERF is a simple parallel-plate, transmission-type ionization chamber with a diameter of 185 mm [47]. The chamber has five parallel electrode plates made of Mylar, of 2.5 mg/cm² thickness and 17 mm inter-plate spacing. The central plate is the collector and the ones on either side are the polarity electrodes. A schematic view of the monitor is shown in Figure 5.2. The inter-plate spacing (17 mm) has been derived from an industrial computer tomography scan performed at CERN [48]. The voltage on the plates is supplied through a BNC cable by an external battery. The polarization voltage provided by this battery is about -270 V. The beam traverses 34 mm of air at atmospheric pressure in the sensitive part of the chamber. The IC is mounted on a standard pedestal normally used to support beam line components such as vacuum chambers. The output signal is fed into a charge digitizer and then to a National Instrument USB 6342 DAQ connected to a desktop computer. The data acquisition can be controlled via a LabVIEW program running on a PC. The data are saved on a log-file that records the differential and integrated IC readings (expressed in counts) every second.

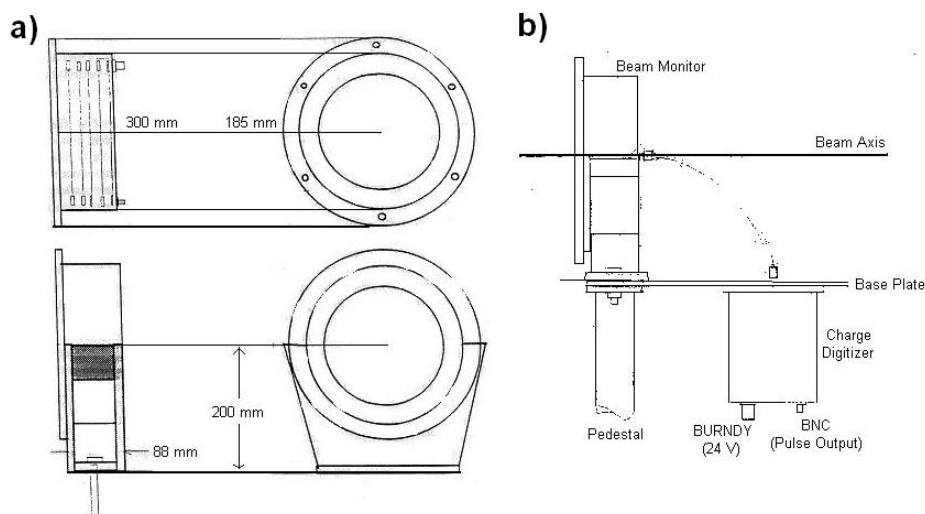


Figure 5.2: a) Schematic view of the IC and support; b) Sketch of the installation of the IC and charge digitizer.

5.1.2 Estimation of the calibration factor

The expected charge q collected on the plates of the IC per primary particle must be calculated to estimate the calibration factor:

$$q = E_{dep} \cdot \frac{e}{W_{air}} \quad (5.1)$$

where E_{dep} is the energy deposited by a primary particle in the sensitive volume of the IC, e is the electron charge ($1.609 \cdot 10^{-19}$ C) and W_{air} ($34.23 \pm 0.4\%$ eV) is the average energy released by the primary particles to produce a single ion pair in air [49].

Separated FLUKA simulations were run to assess the energy deposited by 120 GeV/c protons, positive pions and positive kaons in the air volume of the IC ($p = 0.963$ atm, $\rho = 1.12 \cdot 10^{-3}$ g/cm³). The geometry employed in the simulation is shown in Figure 5.3.

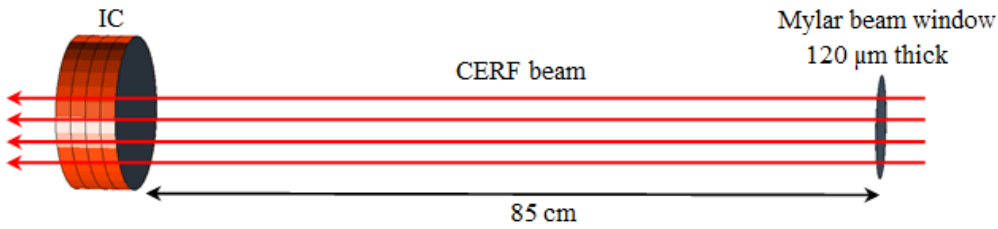


Figure 5.3: Scheme of the geometry employed in the FLUKA simulations.

In the FLUKA input file the DELTARAY card was activated to consider the delta rays production by muons and charged hadrons in the sensitive volume with an energy threshold of 50 keV. Electromagnetic transport cards (EMF and EMF-CUT) were activated setting the transport threshold energy for electrons and positrons to 50 keV and for photons to 10 keV. The energy deposition within the IC sensitive volume was scored by the USRBIN card. The results of the simulations give an energy deposition value of 7.92 keV for protons, 8.15 keV for positive pions and 7.94 keV for positive kaons. The results are affected by 1% statistical uncertainty. Taking the beam composition into account (61% pions, 35% protons, 4% kaons) [45] the weighted energy

deposition is 8.06 keV per primary particle. The expected charge deposited in the IC by a primary particle is then:

$$q = E_{dep} \cdot \frac{e}{W_{air}} = 8.06 \cdot 10^3 \text{ eV} \cdot \frac{1.609 \cdot 10^{-19} \text{ C}}{34.23 \text{ eV}} \quad (5.2)$$

By using the sensitivity factor of the charge digitizer ($k = 1.19 \text{ counts/pC}$) [47] the expected calibration factor is:

$$\begin{aligned} CF &= (q \cdot k)^{-1} = (3.79 \cdot 10^{-5} \text{ pC} \cdot 1.19 \text{ counts/pC})^{-1} \\ &= 22172 \text{ particles/count} \end{aligned} \quad (5.3)$$

This result is affected by the uncertainty on W_{air} (0.4%, systematic) and E_{dep} , whose uncertainty is the sum of two components, the one derived from the FLUKA simulations (1%, statistical) and the uncertainty on the knowledge of the active length of the IC (3%, i.e. 1 mm over 34 mm, statistical, which derives from the spatial resolution of the program employed to analyze the tomographic image). It should also be mentioned that there is also a systematic uncertainty on the FLUKA results, of the order of a few percent for the part due to ionization and of about 10% for the part due to nuclear interactions, which is not included in the uncertainties of the present result [50].

$$CF_{CERF} = 22172 \pm 789 \text{ particles/count} \quad (5.4)$$

Since the IC has also been used in the H4IRRAD facility for the soil-shield activation experiment, FLUKA simulations were run to estimate the expected calibration factor for the H4 beam (94% protons, 5% positive pions and 1% kaons, with a momentum of 400 GeV/c) [51]. The results give an energy deposition value of 8.32 keV for positive pions and 8.31 keV for protons, with 1% uncertainty. The kaon component has been neglected. By following the same procedure used above, one obtains an expected charge deposited per primary of $3.89 \cdot 10^{-17} \text{ C}$ and a IC calibration factor:

$$CF_{H4IRRAD} = 21628 \pm 758 \text{ particles/count} \quad (5.5)$$

5.2 The activation foil technique

Foil activation is a well-established technique for measuring the intensity of high energy proton beams. It is particularly convenient for the calibration of ICs used for on-line beam monitoring. One of its advantages is the accuracy that can be achieved if the cross section of the reaction of interest is known with a small uncertainty. When the protons traverse the foil they generate spallation reactions $A(p,x)B$, where A is the stable isotope of which the foil is constituted, B is the radioisotope produced in the foil by the spallation reaction, whose activity is determined via γ -spectrometry, x is the reaction product escaping the foil. An ideal monitor reaction should show the following properties [52]: cross section known with good accuracy; half-life of the radioisotope produced in the foil longer than the irradiation time, but not too long in order to obtain a detectable activity; γ -line(s) of the radioisotope produced in the foil easily detectable and distinguishable by γ -spectrometry; negligible contribution to the production of the radionuclide of interest by secondary particles formed by interaction of the proton beam in the target (neutrons and energetic secondary hadrons). Unfortunately none of the commonly used reactions satisfy all of these requirements and one has to find a compromise.

5.2.1 Theoretical basis

The production of a radionuclide of interest at a time t is expressed by the well-known formula (see §1.2 in Chapter 2):

$$n(t) = \frac{N\sigma\phi}{\lambda}(1 - e^{-\lambda t_{irr}}) \cdot e^{-\lambda t_{wait}} \quad (5.6)$$

where $n(t)$ is the number density of the atoms of the radionuclide of interest at time t (cm^{-3}), N is the number density of the target atoms (cm^{-3} , where $N = \rho \cdot N_{AV}/M$: ρ is the mass density in g cm^{-3} , N_{AV} is the Avogadro's number $6.022 \cdot 10^{23} \text{ mol}^{-1}$, M is the molar mass (expressed in g mol^{-1}), σ is

the production cross section of the selected radioisotope (cm^2), λ is its decay constant (s^{-1}), ϕ is the particle flux density ($\text{cm}^{-2} \text{s}^{-1}$), t_{irr} and t_{wait} (s) are the irradiation time and waiting time (i.e. the time elapsed from the end of the irradiation until the foil is counted). The specific activity induced in the target at time t is given by $a(t) = \lambda \cdot n(t)$, then:

$$a(t) = N\sigma\phi(1 - e^{-\lambda t_{irr}}) \cdot e^{-\lambda t_{wait}} \quad (5.7)$$

where $a(t)$ is expressed in Bq cm^{-3} . Being interested in the absolute activity $A(t)$ expressed in Bq, if L_1 , L_2 are the transverse dimensions of the target and Δx its thickness, $A(t) = a(t) \cdot L_1 L_2 \Delta x$, hence:

$$A(t) = N\Delta x \cdot \sigma \cdot \phi L_1 L_2 \cdot (1 - e^{-\lambda t_{irr}}) \cdot e^{-\lambda t_{wait}} \quad (5.8)$$

If $N_x = N \cdot \Delta x$ is the surface atomic density (cm^{-2}), the particle flux $\phi' = \phi \cdot L_1 \cdot L_2$ (number of particles per seconds traversing the foil) is given by:

$$\phi' = \frac{A(t)}{N_x \sigma (1 - e^{-\lambda t_{irr}}) \cdot e^{-\lambda t_{wait}}} \quad (5.9)$$

$A(t)$ is measured by γ -spectrometry, while t_{wait} and t_{irr} must be recorded. In the present experiment t_{wait} was recorded manually while t_{irr} was obtained from the log-file of the acquisition system.

5.2.2 The $^{27}\text{Al}(\text{p},3\text{pn})^{24}\text{Na}$ reaction

The $^{27}\text{Al}(\text{p},3\text{pn})^{24}\text{Na}$ reaction is one of the most extensively used beam monitor reactions. Its main advantages are:

- The short half-life of ^{24}Na (14.9590 h) results in a high specific activity so a relatively short irradiation time is adequate to obtain a reasonable activity to be determined by γ -spectrometry.
- ^{24}Na decays by β^- emission producing two γ -rays of energies 2.754 MeV and 1.369 MeV (branching ratios: 99.94% and 100%, respectively),

whose peaks can be easily identified by γ -spectrometry.

- The $^{27}\text{Al}(p,3pn)^{24}\text{Na}$ cross section is known with good accuracy in a wide energy range. Figure 5.4 plots the available cross section data for energies higher than 100 MeV [53].

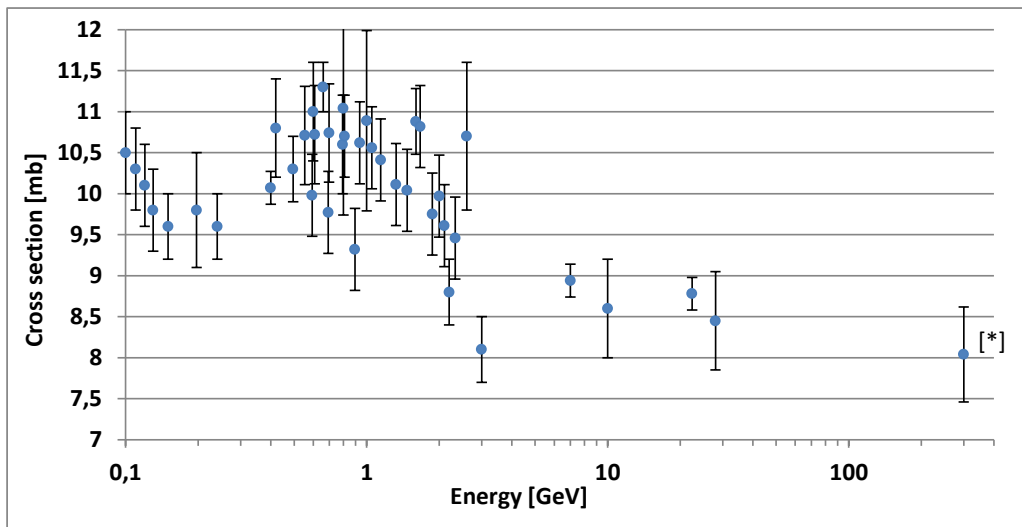


Figure 5.4: Summary of literature data for the cross section of the $^{27}\text{Al}(p,3pn)^{24}\text{Na}$ reaction [53]. [*] extrapolated value, obtained with an indirect method [54].

To obtain an accurate determination of the particle flux, as derived from expression (5.9), one must take into account several parameters on which the reaction critically depends:

- The cross section value at the energy of interest.
- The importance of the competing $^{27}\text{Al}(n,\alpha)^{24}\text{Na}$ reaction, as well as of the reactions induced by energetic secondary hadrons produced in the foils, in the determination of the total induced activity.
- The recoil of some of the nuclei produced in the spallation process that can leave the foil in the same direction of the primary beam.

Cross section

A first problem arises in the determination of the cross section to be employed in case of a mixed proton/pion beam. Whilst for the proton-induced spallation reaction the cross section data are available, for pion-induced reactions there are no published data. The value of the pion-induced cross section can be indirectly determined using the FLUKA code. Even if FLUKA cannot be used to derive the absolute value of the cross sections at very high energies with the required accuracy, it is much more reliable in the determination of the ratio of the cross sections of reactions induced by different particles at the same energy on the same target. One can therefore calculate the ratio between the cross section of pion- and proton-induced reactions and then derive the absolute value of the pion-induced one. The cross section ratio can be obtained by running the nuclear interaction models of FLUKA in interaction only mode, accounting for both absorption and quasi-elastic reactions [50]. The following parameters were set:

- mass and atomic number of the target nucleus: $M_{Al} = 27$, $Z_{Al} = 13$;
- beam particle: positive pions or protons;
- beam momentum: 120 GeV/c;
- number of events: 106.

The output file provides the cross section for each isotope produced in the interaction between the primaries and the target. By running one simulation for protons and one for pions, one obtains the ratio between the pion- and the proton-induced spallation cross section for the reaction of our interest: 0.764 ± 0.011 . Since the value of the proton-induced spallation cross section is known from the literature (8.3 ± 0.5 mb)¹, one can derive the value of

¹The reaction cross section for protons has been assumed to be 8.3 ± 0.5 mb. This value was derived from Cumming [52] for 28 GeV protons. No direct measurements are available for higher energies. Figure 5.4 plots the available cross section data for energies higher than 100 MeV [53]. The 300 GeV value comes from indirect measurements [54].

the pion-induced one: 6.3 ± 0.4 mb. By neglecting the kaon component, which has very limited importance, the effective cross section for the mixed proton-pion beam (63.5% pions and 36.5% protons, the kaon fraction has been re-distributed on the other two components according to their relative weight) is 7.1 ± 0.4 mb.

Competing reactions

Two competing mechanisms lead to the production of ^{24}Na : the reactions induced by energetic secondary hadrons and the $^{27}\text{Al}(n,\alpha)^{24}\text{Na}$. The latter has a threshold of 5.5 MeV and a cross section rising to 120 mb at 14 MeV [55]. Data in the literature are contradictory about the importance of this effect. Some authors showed it has little importance: Stehney et al. [56] measured a contribution of less than 1% per 200 mg/cm² foil thickness, while Cumming et al. [57] proposed a value of 0.25% per 100 mg/cm². Other authors estimated a bigger importance: Brandt et al. [58] reported that this effect has an influence in the order of $1.1 \pm 0.5\%$ per 100 mg/cm², while Grover [59] showed a strong dependence on foil thickness, about 3.3% per 100 mg/cm². All these estimates refer to protons; no data are available for different particles. The contribution of the competing reaction has here been determined by analysing the results obtained from the experiment carried out in 2011 and 2012 CERF runs [60–63]. It is worth noting that this contribution may also depend on the materials present upstream and downstream of the target as well as on the characteristics of the resulting neutron "halo". The experimental evaluation of this contribution can be done via the activation of foils of different thicknesses, because it is directly proportional to the mass thickness of the foil. One can express the calibration factor as the sum of two terms: the first is due to the activity induced by the primary particles, the second to the activity induced by the neutrons, which is proportional to the foil mass thickness and to a coefficient k (expressed in percent per 100 mg/cm²):

$$C_x = C_{prim} + k \cdot C_{prim} \cdot x \quad (5.10)$$

where C_x is the calibration factor obtained for a foil of mass thickness x and C_{prim} is the calibration factor extrapolated to zero thickness. The constant k here refers to the partial activity due to the primary particles, whereas in other papers the contribution refers to the total activity. This choice was done to make expression (5.10) more consistent (the numerical difference is nevertheless of little importance). One can derive the value of the constant k from the linear fit in Figure 5.9 (see §5.2.5): $C_{prim} = 22249$ particles/count, $k \cdot C_{prim} = 2581$ particles/count/mm. By normalizing the constant to the foil mass thickness ($1 \text{ mm} = 271 \text{ mg/cm}^2$, see Table 5.2) one then obtains $k = 0.116 \text{ mm}^{-1} = 4.3\% / 100 \text{ mg/cm}^2$, close to the data of Grover for protons [59]. It must be noted that the value obtained by Grover refers to the $^{27}\text{Al}(n,\alpha)^{24}\text{Na}$ reaction only, whereas here the two contributions cannot be evaluated separately.

Recoil nuclei effect

To take into account the effect due to recoiling nuclei, the foils were exposed in sandwiches and only the activity of the central one was employed in expression 5.9. Indeed, some of the nuclei produced in the spallation process can recoil in the same direction as the primary beam and leave the foil (due to the so-called Lorentz boost [64]). In this case they would not contribute to the foil activity (see Figure 5.5). In the central foil this effect is compensated by recoils received from the upstream one. To verify the importance of this effect, for some measurements several analyses were carried out (see Table 5.1 in §5.2.4). The induced activities in the three foils of the sandwich are all compatible within 2σ . This shows that the importance of this effect is very limited. This is confirmed by the FLUKA interaction models, which give a mean energy of the recoil ^{24}Na nuclei of about 2 MeV. This corresponds to a projected range of $2 \mu\text{m}$ in the Al target, i.e. only the nuclei produced in the last layer (a few microns) of the foil escape in the beam direction. This fraction corresponds to a maximum of about 0.4% on the overall activity for the 0.5 mm sandwich.

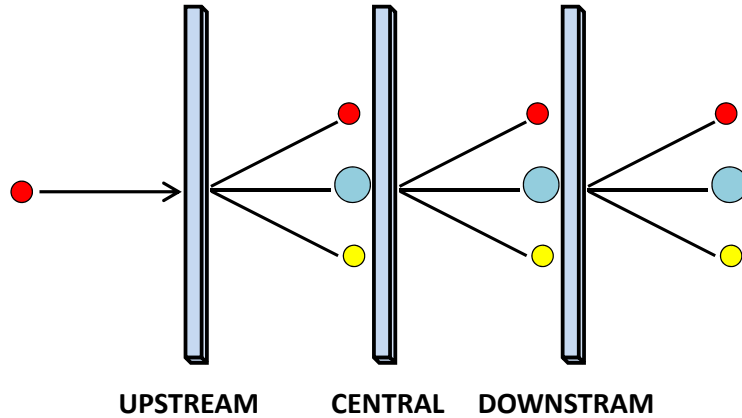


Figure 5.5: Recoil nuclei reaction scheme in the three-foil assembly set-up.

5.2.3 The $^{nat}\text{Cu}(p,x)^{24}\text{Na}$ reaction

The $^{nat}\text{Cu}(p,x)^{24}\text{Na}$ reaction is a promising alternative reaction for beam monitoring, as it shows two advantages when compared to $^{27}\text{Al}(p,3pn)^{24}\text{Na}$:

- The cross section, even if it is lower than that of $^{27}\text{Al}(p,3pn)^{24}\text{Na}$, is known with better accuracy at high energies. Figure 5.6 plots the available cross section data for energies higher than 500 MeV. At very high energies (30, 150, 400 and 800 GeV) Baker et al. [65] found an energy-independent cross section value of 3.59 ± 0.14 mb.
- ^{24}Na is produced only in deep spallation reactions induced by high-energy hadrons, while the secondary neutrons produce mostly isotopes close to the original target mass.

Cross section

For the $^{nat}\text{Cu}(p,x)^{24}\text{Na}$ reaction the proton-induced cross section at 120 GeV/c was assumed equal to the one calculated by Baker et al. [65] at 30, 150, 400 and 800 GeV, i.e. 3.59 ± 0.14 mb. To obtain the value of the pion-induced cross section the same method used for the Al activation was followed. The

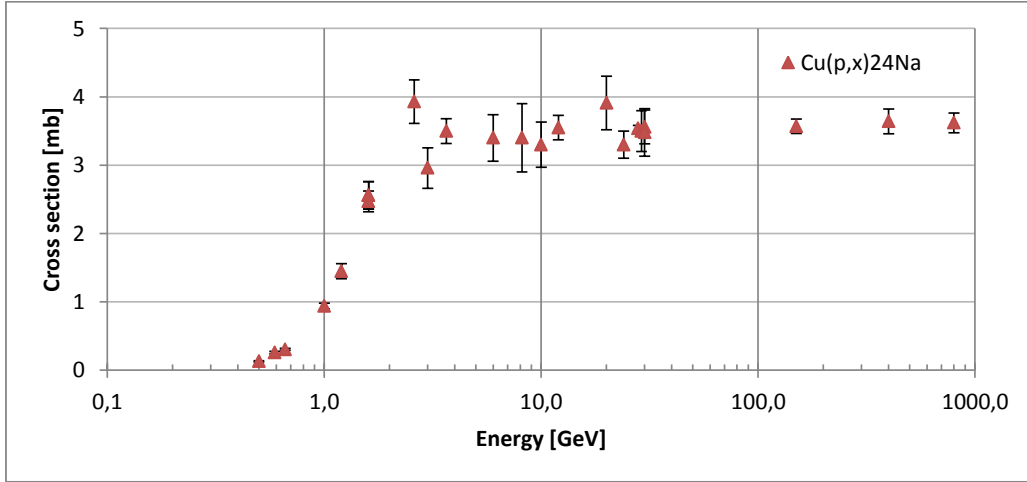


Figure 5.6: Summary of literature data for the cross section of the $^{nat}\text{Cu}(p,x)^{24}\text{Na}$ reaction [53].

ratio between the cross section of the pion-induced and the proton-induced reaction, as obtained via FLUKA, is equal to 0.726 ± 0.016 . The pion-induced reaction cross section is then 2.61 ± 0.12 mb. By neglecting the kaon component, the effective beam (63.5% pions, 36.5% protons) cross section is 2.93 ± 0.13 mb.

5.2.4 Experiments

Hyper-pure ^{27}Al and ^{nat}Cu foils from GoodFellow [66] were used: 99.999% ^{27}Al (impurities: Mg 1.2 ppm, Si 0.8 ppm, Cu 0.3 ppm, Fe 0.3 ppm) and 99.99% ^{nat}Cu (impurities: Ag 70 ppm, Fe 2 ppm, Ni 2 ppm, Pb 2 ppm, Si 2 ppm, Al 1 ppm, Bi 1 ppm, Ca 1 ppm, Mg 1 ppm, Sn 1 ppm, Mn <1 ppm, Na <1 ppm, Cr <1 ppm), with dimensions 50×50 mm². As verified via dedicated FLUKA simulations, the influence of these impurities on the total induced activity is negligible. The foils thicknesses were 2 mm, 1 mm and 0.5 mm for Al; 0.5 mm, 0.25 mm and 0.125 mm for Cu, with 1% estimated uncertainty. The corresponding mass thicknesses were, respectively, 540 mg/cm², 270 mg/cm² and 135 mg/cm² for Al; 446 mg/cm², 223 mg/cm² and 111.5 mg/cm² for Cu. The foils were fixed on a Plexiglas frame mounted

on both ends of a hollow aluminum tube of the same dimensions of the Cu target normally employed in the CERF facility, placed approximately one meter downstream of the IC (see Figures 5.7 and 5.8). The beam size was smaller than the foil dimensions so that all particles traversing the IC hit the foils. To evaluate the contribution of background radiation to the foil activation, in one of the experiments an additional foil was exposed out-of-beam. When possible the foils were exposed in sandwiches and only the activity of the central one was considered for analysis to take into account the recoil nuclei effect (see §5.2.2).

The results of the measurements are given in Table 5.1. Where available, the activity of the upstream and downstream foils is given. The value used in expression (5.9) was the activity of the central foil, except for measurement 1 where, due to the high uncertainties, an average of the central and downstream foil activities was employed. Due to problems in the peak identification during the γ -spectrometry of the ^{nat}Cu 0.250 mm foil, the data of this measurement could not be exploited. The foil exposed out of beam did not show any significant induced activity, confirming that the contribution of the scattered radiation (background) to the overall activity is negligible.

Table 5.1: Results of the Al foil activation experiment (n.a. = not available).

Al foils				
Measurement	1	2	3	4
Thickness [mm]	2.0	2.0	1.0	0.5
Irradiation time [s]	31200	31371	58223	31371
Integrated fluence [IC counts]	$2 \cdot 10^6$	$2.3 \cdot 10^6$	$3.8 \cdot 10^6$	$2.3 \cdot 10^6$
Upstream foil activity [Bq]	45.8 ± 2.2	n.a.	34.5 ± 1.9	n.a.
Central foil activity [Bq]	52.7 ± 5.4	56.8 ± 2.3	37.1 ± 1.9	12.3 ± 0.6
Downstream foil activity [Bq]	47.1 ± 1.6	n.a.	n.a.	n.a.
Cu foils				
Measurement	5	6	7	
Thickness [mm]	0.500	0.250	0.125	
Irradiation time [s]	54831	54831	54831	
Integrated fluence [IC counts]	$3.3 \cdot 10^6$	$3.3 \cdot 10^6$	$3.3 \cdot 10^6$	
Central foil activity [Bq]	8.4 ± 0.6	n.a.	2.3 ± 0.3	

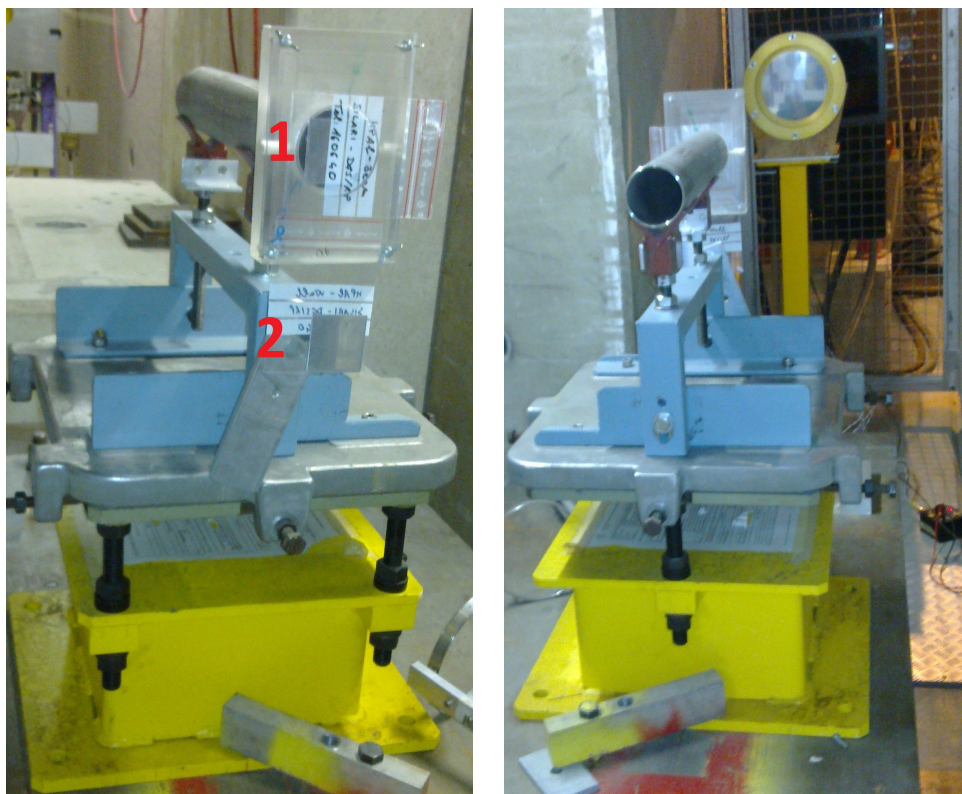


Figure 5.7: Left figure: experimental set-up for the foil activation: the sandwiched foils are mounted at the entrance of the hollow tube used as support (1), while one is fixed just below it, outside the beam, to measure background activation (2). Right figure: hollow tube with the foils mounted on its upstream face inside the irradiation cave. The IC is visible in the background.

5.2.5 IC calibration factor

To obtain the IC calibration factor one needs to know the parameters in expression (5.9). To improve the accuracy of the calculation, the irradiation time was subdivided in one-second irradiation periods and the total activity was obtained as the sum of the partial activities induced by each one-second irradiation, by taking into account the decay of ^{24}Na occurring from the end of each one-second irradiation until the arrival in the spectrometry laboratory. Therefore the beam-on/beam-off periods (i.e. spill time over the total SPS cycle) were exactly taken into account and fluctuations in the beam intensity

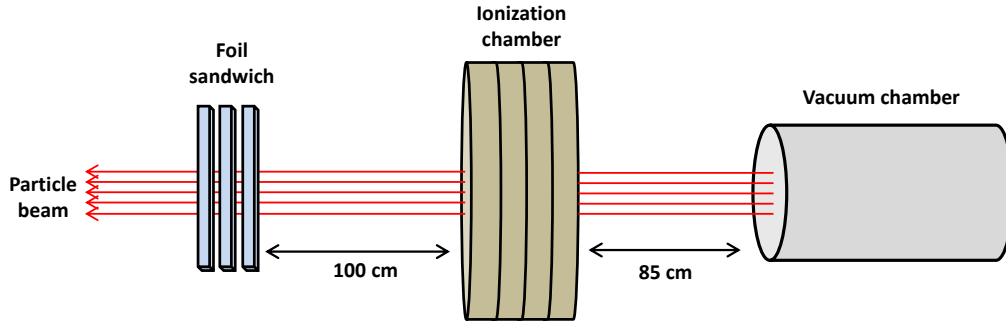


Figure 5.8: Foil activation experiment set-up (not to scale).

during the spill were also properly considered. The values of t_{irr} , t_{wait} and ϕ' were then derived from the IC acquisition log-files. The surface atomic densities N_x are given in Table 5.2 for each foil. The beam effective cross sections were calculated for Al and Cu foils as showed in §5.2.2 and §5.2.3, respectively.

Table 5.2: Foil surface atomic densities.

Al foils ($\rho_{Al} = 2.71 \text{ g/cm}^3$, $M_{Al} = 27 \text{ g/mol}$)			
Foil thickness X_{Al}	0.5 mm	1.0 mm	2.0 mm
$N_x [\text{cm}^2]$	$3.0222 \cdot 10^{21}$	$6.0445 \cdot 10^{21}$	$1.2089 \cdot 10^{22}$
Cu foils ($\rho_{Cu} = 8.92 \text{ g/cm}^3$, $M_{Cu} = 63.546 \text{ g/mol}$)			
Foil thickness X_{Cu}	0.125 mm	0.500 mm	
$N_x [\text{cm}^2]$	$1.0567 \cdot 10^{21}$	$4.2266 \cdot 10^{21}$	

Al foil activation

The raw calibration factors (before correction) for each experiment are listed in Table 5.3. The associated uncertainties derive from the uncertainties on the activity, the foil thickness (1%) and the cross section (5.6%). Only the experiments in which the sandwich configuration was employed are considered, since for all the others the results have lower reliability. The calibration factors from the aluminium activation need to be corrected for the contribution of the competing reactions to the overall activity. To ex-

Table 5.3: Raw calibration factors (before correction) as calculated from expression (5.9) for each Al foil.

Measurement	Foil thickness	Raw calibration factor [particles/count]
1	2.0 mm	27736 ± 1682
2	2.0 mm	27014 ± 1894
3	1.0 mm	25040 ± 1923
4	0.5 mm	23399 ± 17591

clude this contribution, which is proportional to the thickness of the foil, one has to extrapolate the calibration factor to zero thickness. Figure 5.9 plots the calibration factors calculated from the different measurements with the corresponding linear fit. The value extrapolated at zero thickness is

$$CF_{Al} = 22249 \pm 2100 \text{ particles/count} \quad (5.11)$$

where the uncertainty was calculated via the reduced chi-squared method.

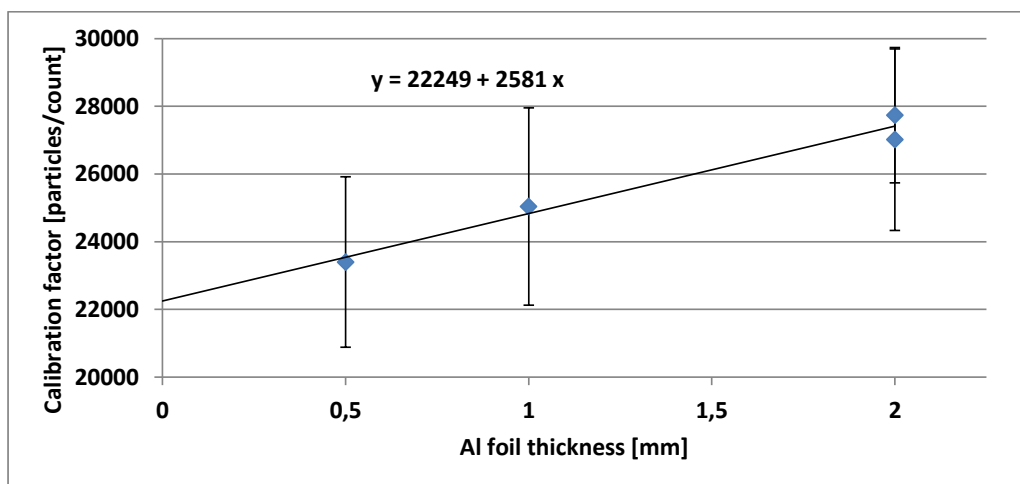


Figure 5.9: Plot of the calibration factors with the related uncertainties, as calculated via the activation of the Al foils. The line is the linear fit to the data.

Cu foil activation

The calibration factors have been derived from each Cu foil by following the same procedure used for the Al activation. Table 5.4 lists the obtained values, whose related uncertainties derive from the uncertainties on the activity, the foil thickness (1%) and the cross section (4.4%). An extrapolation of the data to zero thickness is not needed for the values obtained from the copper activation, showing the little importance of competing reactions induced by energetic secondary hadrons. In this case the best estimate of the calibration factor can be obtained by the "weighted average method". The calibration factor and its uncertainty are derived as follows:

$$\bar{x}_p = \frac{\sum_{i=1}^N w_i \bar{x}_i}{\sum_{i=1}^N w_i}, \quad \sigma_{x_p} = \frac{1}{\sqrt{\sum_{i=1}^N w_i}} \quad (5.12)$$

where the weighting factor w_i is related to the absolute uncertainty of each data:

$$w_i = \left(\frac{1}{\sigma_{x_i}} \right)^2 \quad (5.13)$$

The best estimation for the calibration factor is

$$CF_{Cu} = 22293 \pm 1462 \text{ particles/count} \quad (5.14)$$

Table 5.4: Raw calibration factors (before correction) as calculated from expression (5.9) for each Cu foil.

Measurement	Foil thickness	Raw calibration factor [particles/count]
5	0.500 mm	21707 ± 1762
6	0.250 mm	- -
7	0.125 mm	23587 ± 2620

5.2.6 Discussion

All the results given above lay on the assumptions that:

- The ^{27}Al and ^{nat}Cu atoms are homogeneously distributed in the exposed foils. This is guaranteed by the supplier.
- The effect of the impurities present in the foils on the induced activity is negligible. This has been verified via FLUKA simulations in which the impurities declared by the supplier have been included in the foils. The difference in the activity by adding the impurities was insignificant.
- The self-absorption of γ -rays in the activated foils is negligible. This has been verified by taking into account the most conservative case, i.e. the attenuation of the photons emitted by ^{24}Na in 2 mm of ^{27}Al and 0.5 mm of ^{nat}Cu . Since the mass attenuation coefficients are $3.54 \cdot 10^{-2} \text{ cm}^2/\text{g}$ and $3.59 \text{ cm}^2/\text{g}$ [67], respectively, the maximum attenuation that the γ -rays can undergo before being detected by the spectrometer is less than 2%. In any case, this small effect is taken into account by the spectrometry software.

The calibration factor estimated via the FLUKA simulations is in excellent agreement with the value determined experimentally (see Table 5.5). The present results are also in good agreement with past experimental results obtained with different calibration techniques: activation of ^{18}F (23000 ± 2300 particles/count [68]) and ^{12}C foils (23400 ± 1400 particles/count [69]), and coincidence of scintillators (22116 ± 92 particles/count [70]). More details on the monitor reactions for calibration of high-energy mixed hadron beams can be found in Ref. [47, 71] and in the second paper of the Appendix.

Table 5.5: IC calibration factor as obtained from the activation experiments and via FLUKA simulations.

Technique	IC calibration factor [particles/count]
Activation of ^{27}Al foils	22249 ± 2100
Activation of ^{nat}Cu foils	22293 ± 1493
FLUKA simulations	22172 ± 789

5.3 Activation of copper and iron samples

An accurate knowledge of the spallation product inventory (see §2.3 in chapter 2) within a target is important for many applications: disposal of material, operation, maintenance, safety, activation issues in high-energy particle accelerators [10] and benchmarking of Monte Carlo codes [72]. Since copper and iron are commonly employed in high-energy particle accelerators and their surrounding structures, the knowledge of their reaction cross section for a spallation product is therefore fundamental.

5.3.1 Theory

The cross section of the reaction $A(p,x)B$ or $A(\pi^+,x)B$, where A is ^{nat}Cu or ^{nat}Fe , B is the radioisotope produced in the foil by the spallation reaction and x is the reaction product escaping the foil, was measured via the foil activation technique (see §5.2). By using the expression (5.9), one obtains:

$$\sigma = \frac{A(t)}{N_x \phi' (1 - e^{-\lambda t_{irr}}) \cdot e^{-\lambda t_{wait}}} \quad (5.15)$$

where the particle flux ϕ' is obtained now from the calibrated IC, as showed in §5.1.1. The cross section σ is the beam effective cross section, i.e. averaged over the pion (63.5%) and proton (36.5%) components:

$$\sigma = 0.635 \sigma_\pi \pm 0.365 \sigma_p \quad (5.16)$$

where σ_p and σ_π are the proton- and pion-induced spallation cross sections. Their values can be derived if one knows the ratio σ_p/σ_π . This ratio was obtained from FLUKA simulations as showed in §5.2.2. The cross sections for protons and pions can then be easily derived:

$$\sigma_\pi = \frac{\sigma}{0.635 + 0.365 \frac{\sigma_p}{\sigma_\pi}} \quad \text{and} \quad \sigma_p = \frac{\sigma - 0.635 \sigma_\pi}{0.365} \quad (5.17)$$

5.3.2 Experimental set-up

The experiments were performed by exposing hyperpure ^{nat}Cu and ^{nat}Fe foils to the primary beam at the CERF facility. The foils with dimensions $50 \times 50 \text{ mm}^2$ have the following compositions, as declared by the GoodFellow [66]: 99.991% ^{nat}Cu , with impurities in ppm: Ag 70, Fe 2, Ni 2, Pb 2, Si 2, Al 1, Bi 1, Ca 1, Mg 1, Sn 1, Mn < 1, Na < 1, Cr < 1; 99.998% ^{nat}Fe , impurities in ppm: Ag 1, Al 2, Ca 3, Cr 1, Cu 2, Mg 2, Mn 1, Ni 1, Si 3. The effect of the impurities on the radioisotope production is negligible. This has been verified via several sets of FLUKA simulations, in which the foils were first simulated as 100% pure, and then with added impurities. The values of the surface atomic densities N_x are obtained from the foil density, the molar mass and the thickness (see Tables 5.2 and 5.6). The foil thick-

Table 5.6: Foil surface atomic densities.

Fe foils ($\rho_{Fe} = 7.874 \text{ g/cm}^3$, $M_{Fe} = 55.84 \text{ g/mol}$)	
Foil thickness X_{Fe}	2.0 mm
$N_x \text{ [cm}^2\text{]}$	$1.6983 \cdot 10^{22}$
Cu foils (see Table 5.2)	

nesses were 0.5 mm, 0.25 mm and 0.125 mm for ^{nat}Cu ; 2 mm for ^{nat}Fe , with 1% estimated uncertainty. The thicknesses were chosen as a compromise between the need of an induced activity high enough to reduce the statistical uncertainty of the γ -spectrometry measurements and the need of thin targets, i.e. targets in which the energy lost by the incident beam is small ($E_{loss}/E_{beam} \leq 5\%$ [64]). This reduces to a minimum the production of secondary particles inside the target, which generally undergo further collisions and could result in internuclear cascades. By assuming that the value of the interaction lengths for protons and pions at 120 GeV is similar to the one at 18 GeV (i.e. $140.2 \pm 3.2 \text{ g/cm}^2$ for protons, $163.8 \pm 9.0 \text{ g/cm}^2$ for pions [73]), the beam fraction that interacts in the target is always less than 1%. This guarantees that, even though the average fraction of energy of the incident beam lost in the target cannot be precisely estimated, the overall influence

of the target on the beam transmission is negligible.

The foils were fixed on a Plexiglas frame mounted on both ends of a hollow aluminium tube placed downstream the IC used as beam monitor (see Figure 5.8). The foils were irradiated in sandwiches of three to take into account the recoil nuclei effect (see §5.2.2). To evaluate the contribution of scattered radiation to the foil activation an additional foil was exposed out of beam.

5.3.3 Results

The foils were counted in the CERN γ -spectrometry laboratory with a Canberra low background coaxial high-purity germanium (HPGe) detector. For a more accurate analysis of the gamma lines, the activated foils were counted twice: a short (10 minutes) measurement immediately after the irradiation and a longer one (about 8 hours) later. The analysis was performed using the Canberra Genie 2000 and the PROcount 2000 software, which are comprehensive environments for data acquisition, display and analysis. They also take into account geometrical effects, self-absorption in the sample and decay of the isotope during the measurements, and provide a global uncertainty. Only the radioisotopes with an activity higher than 1 Bq were considered for the cross section calculations.

The beam effective cross section σ for each of the reactions of interest was derived from expression (5.15). The cross sections of the pion- and proton-induced reactions were calculated from expression (5.17). The foil exposed out of beam did not show any significant induced activity, confirming that the contribution of the scattered radiation (background) to the overall activity is negligible. Tables 5.7 and 5.8 list the cross sections of the spallation reactions that generated an activity in the foils higher than 1 Bq. The global uncertainty is the quadratic sum of the uncertainty on the γ -spectrometry, the one on the IC calibration factor (10%) and the uncertainty on the foil thickness, i.e. on the knowledge of N_x . The uncertainty on the beam composition is not taken into account since it is below 2% [45]. The produc-

tion of the radioisotopes listed in Tables 5.7 and 5.8 derives only from the proton- and pion-induced spallation reactions. For the reactions on ^{nat}Cu foils the cross section is the average of the values obtained from the three thicknesses. More details on the spallation cross sections for ^{nat}Fe and ^{nat}Cu targets for 120 GeV/c protons and pions can be found in the third paper of the Appendix. The paper also shows comparison between the cross section obtained at 120 GeV and the ones found in the literature at energies higher than 500 MeV for proton-induced spallation reactions (for the pion-induced reactions no data are available).

5.4 Activation of soil-shield samples

Accelerators and experiment facilities are typically sited either underground or at grade with thick concrete walls and substantial earth berms to provide cost-effective shielding. Radiation interacts with the shielding materials generating induced radioactivity in the concrete or earth. In general, the induced radioactivity remains confined in the shield material. However, some activation may occur outside the accelerator enclosure, primarily in adjacent groundwater and soil. If the production of radioactive nuclides in the accelerator structure and in the concrete walls of the accelerator room is a concern for the personnel, the radionuclides created in the groundwater or in the earth represent a collective danger, because they may be transported into the environment. Several authors investigated the radioisotope production in earth and water, either experimentally or via Monte Carlo simulations [74–92]. They describe and examine the most important isotopes of concern. Few researchers have addressed the problem of the radionuclide migration from the activated soil to the groundwater. This section focuses on the leaching of the radioactivity produced in CERN soil ("molasse"). The aim is to investigate the radionuclide production from secondary radiation in earth and water and to quantify the activity concentration of the radionuclides leaching into the groundwater. The study mainly focuses on ^3H and

Table 5.7: Cross sections of the spallation reactions on ^{nat}Cu derived from the activation experiment.

Proton reaction	σ_p [mb]	Pion reaction	σ_π [mb]
$^{nat}\text{Cu}(p,x)^{41}\text{Ar}$	0.62 ± 0.11	$^{nat}\text{Cu}(\pi^+,x)^{41}\text{Ar}$	0.43 ± 0.08
$^{nat}\text{Cu}(p,x)^{42}\text{K}$	2.23 ± 0.40	$^{nat}\text{Cu}(\pi^+,x)^{42}\text{K}$	1.69 ± 0.30
$^{nat}\text{Cu}(p,x)^{43}\text{K}$	0.93 ± 0.19	$^{nat}\text{Cu}(\pi^+,x)^{43}\text{K}$	0.66 ± 0.14
$^{nat}\text{Cu}(p,x)^{43}\text{Sc}$	2.73 ± 0.26	$^{nat}\text{Cu}(\pi^+,x)^{43}\text{Sc}$	2.62 ± 0.25
$^{nat}\text{Cu}(p,x)^{44}\text{Sc}$	3.80 ± 0.17	$^{nat}\text{Cu}(\pi^+,x)^{44}\text{Sc}$	3.46 ± 0.15
$^{nat}\text{Cu}(p,x)^{47}\text{Sc}$	1.85 ± 0.22	$^{nat}\text{Cu}(\pi^+,x)^{47}\text{Sc}$	1.42 ± 0.17
$^{nat}\text{Cu}(p,x)^{48}\text{Cr}$	0.21 ± 0.06	$^{nat}\text{Cu}(\pi^+,x)^{48}\text{Cr}$	0.21 ± 0.06
$^{nat}\text{Cu}(p,x)^{48}\text{Sc}$	1.16 ± 0.21	$^{nat}\text{Cu}(\pi^+,x)^{48}\text{Sc}$	0.83 ± 0.15
$^{nat}\text{Cu}(p,x)^{52}\text{Mn}$	3.83 ± 0.52	$^{nat}\text{Cu}(\pi^+,x)^{52}\text{Mn}$	3.87 ± 0.52
$^{nat}\text{Cu}(p,x)^{55}\text{Co}$	0.51 ± 0.10	$^{nat}\text{Cu}(\pi^+,x)^{55}\text{Co}$	0.56 ± 0.11
$^{nat}\text{Cu}(p,x)^{56}\text{Mn}$	2.68 ± 0.14	$^{nat}\text{Cu}(\pi^+,x)^{56}\text{Mn}$	2.01 ± 0.10
$^{nat}\text{Cu}(p,x)^{57}\text{Ni}$	0.77 ± 0.14	$^{nat}\text{Cu}(\pi^+,x)^{57}\text{Ni}$	0.77 ± 0.14
$^{nat}\text{Cu}(p,x)^{58}\text{Co}$	18.82 ± 6.01	$^{nat}\text{Cu}(\pi^+,x)^{58}\text{Co}$	18.07 ± 5.77
$^{nat}\text{Cu}(p,x)^{61}\text{Cu}$	11.12 ± 0.51	$^{nat}\text{Cu}(\pi^+,x)^{61}\text{Cu}$	11.46 ± 0.52

Table 5.8: Cross sections of the spallation reactions on ^{nat}Fe derived from the activation experiment.

Proton reaction	σ_p [mb]	Pion reaction	σ_π [mb]
$^{nat}\text{Fe}(p,x)^{24}\text{Na}$	4.02 ± 0.45	$^{nat}\text{Fe}(\pi^+,x)^{24}\text{Na}$	2.96 ± 0.33
$^{nat}\text{Fe}(p,x)^{41}\text{Ar}$	0.84 ± 0.16	$^{nat}\text{Fe}(\pi^+,x)^{41}\text{Ar}$	0.53 ± 0.10
$^{nat}\text{Fe}(p,x)^{42}\text{K}$	4.28 ± 0.57	$^{nat}\text{Fe}(\pi^+,x)^{42}\text{K}$	3.18 ± 0.43
$^{nat}\text{Fe}(p,x)^{43}\text{K}$	1.42 ± 0.19	$^{nat}\text{Fe}(\pi^+,x)^{43}\text{K}$	0.92 ± 0.12
$^{nat}\text{Fe}(p,x)^{43}\text{Sc}$	3.72 ± 0.63	$^{nat}\text{Fe}(\pi^+,x)^{43}\text{Sc}$	3.73 ± 0.63
$^{nat}\text{Fe}(p,x)^{44}\text{Sc}$	8.32 ± 0.93	$^{nat}\text{Fe}(\pi^+,x)^{44}\text{Sc}$	7.87 ± 0.88
$^{nat}\text{Fe}(p,x)^{46}\text{Sc}$	6.07 ± 2.36	$^{nat}\text{Fe}(\pi^+,x)^{46}\text{Sc}$	4.87 ± 1.89
$^{nat}\text{Fe}(p,x)^{47}\text{Sc}$	3.96 ± 0.54	$^{nat}\text{Fe}(\pi^+,x)^{47}\text{Sc}$	2.93 ± 0.40
$^{nat}\text{Fe}(p,x)^{48}\text{Cr}$	0.59 ± 0.08	$^{nat}\text{Fe}(\pi^+,x)^{48}\text{Cr}$	0.64 ± 0.08
$^{nat}\text{Fe}(p,x)^{48}\text{Sc}$	0.61 ± 0.13	$^{nat}\text{Fe}(\pi^+,x)^{48}\text{Sc}$	0.37 ± 0.08
$^{nat}\text{Fe}(p,x)^{48}\text{V}$	16.55 ± 2.09	$^{nat}\text{Fe}(\pi^+,x)^{48}\text{V}$	16.25 ± 2.05
$^{nat}\text{Fe}(p,x)^{51}\text{Cr}$	29.47 ± 11.61	$^{nat}\text{Fe}(\pi^+,x)^{51}\text{Cr}$	28.19 ± 11.11
$^{nat}\text{Fe}(p,x)^{52}\text{Fe}$	0.49 ± 0.07	$^{nat}\text{Fe}(\pi^+,x)^{52}\text{Fe}$	0.54 ± 0.08
$^{nat}\text{Fe}(p,x)^{52}\text{Mn}$	10.31 ± 1.16	$^{nat}\text{Fe}(\pi^+,x)^{52}\text{Mn}$	10.48 ± 1.18
$^{nat}\text{Fe}(p,x)^{54}\text{Mn}$	44.82 ± 8.83	$^{nat}\text{Fe}(\pi^+,x)^{54}\text{Mn}$	43.21 ± 8.51
$^{nat}\text{Fe}(p,x)^{55}\text{Co}$	0.62 ± 0.08	$^{nat}\text{Fe}(\pi^+,x)^{55}\text{Co}$	0.51 ± 0.07

^{22}Na , which are the longest-lived radionuclides and the most problematic from a radiation protection point of view.

5.4.1 Soil samples

The soil samples used for the irradiation were collected on the Preveessin site, at a location where a new beam dump was installed 24 m depth downstream of the ECN3 experimental area (see Figure 5.1). CERN is located in the Geneva basin, which is filled by sedimentary deposits called molasse. The chemical analysis of the molasse rock was carried out by the EMPA laboratory in Dubendorf via X-ray fluorescence spectrometry (WD-XRF). Soil samples were dried before the XRF measurements. The XRF analysis is not reliable in quantifying the 1st and 2nd period elements (from H to Ne) in inorganic solid matrices [93]. For this reason, the oxygen and carbon contents were extrapolated using typical values of molasse soil [90]. The results of this chemical assay are shown in Table 5.9. The knowledge of the natural water content of the soil (moisture) is essential to discriminate the fraction of radioactivity leaching into groundwater from the soil from the fraction coming from the moisture. The moisture was measured in the CERN HSE Environmental laboratory by drying a known amount of earth. The soil moisture content may be expressed by weight as the ratio of the mass of water present to the dry weight of the soil sample. To determine this ratio, the samples and container were weighed in the laboratory both before and after drying, the difference being the mass of water originally in the sample. The water content measured in the soil specimen was 5% by weight. Three cylindrical plastic containers of 5 cm in height and 4.5 cm in diameter were filled with 100 g of soil. A sample of tap water was collected in a 50 ml plastic container 10 cm long and 2.5 cm in diameter (Figure 5.10). Additional information on the samples, their natural radioactivity and the chemical analysis can be found in Refs. [94] and [95].

Table 5.9: Chemical composition of dried soil sample (density: $\sim 1.4 \text{ g/cm}^3$).

Element	O	Si	Ca	Al	C	Fe	Mg	K	Na	Ti
(g/100 g)	38.8*	24	16	6.8	5*	4	2	1.9	0.7	0.42
Element	Mn	Ba	P	Sr	Zn	Cr	Zr	Eu	Ni	S
(g/100 g)	0.11	0.06	0.06	0.05	0.03	0.02	0.02	0.01	0.01	0.01

*Extrapolated value, not quantifiable by XRF analysis.

**Figure 5.10:** Soil and water samples used in the activation experiment.

5.4.2 H4IRRAD facility and irradiation set-up

The activation experiment was carried out at the H4IRRAD facility [51], which is installed in the H4 beam line in the North Experimental Area of the SPS (see Figure 5.1). The facility is being operated with the SPS attenuated primary beam with momentum of $400 \text{ GeV}/c$ and average intensity of $3 \cdot 10^9$ protons per pulse over a supercycle of about 45 seconds and an extraction length of ~ 5 seconds. The beam intensity in H4IRRAD is usually monitored by an argon ionization chamber (XION). This chamber was calibrated via a comparison with scintillators placed in the H4 beam line and with the calibrated Ionization Chamber (IC) normally used as beam monitor at CERF in H6 (see §5.1.1). One XION-count corresponds to (6900 ± 690) particles

impinging on the target [96]. Figure 5.11 shows the beam intensity profile and the accumulated number of protons as a function of the irradiation time as recorded during the experiment. The soil and water containers were installed under the copper target on which the SPS proton beam is stopped (Figure 5.12).

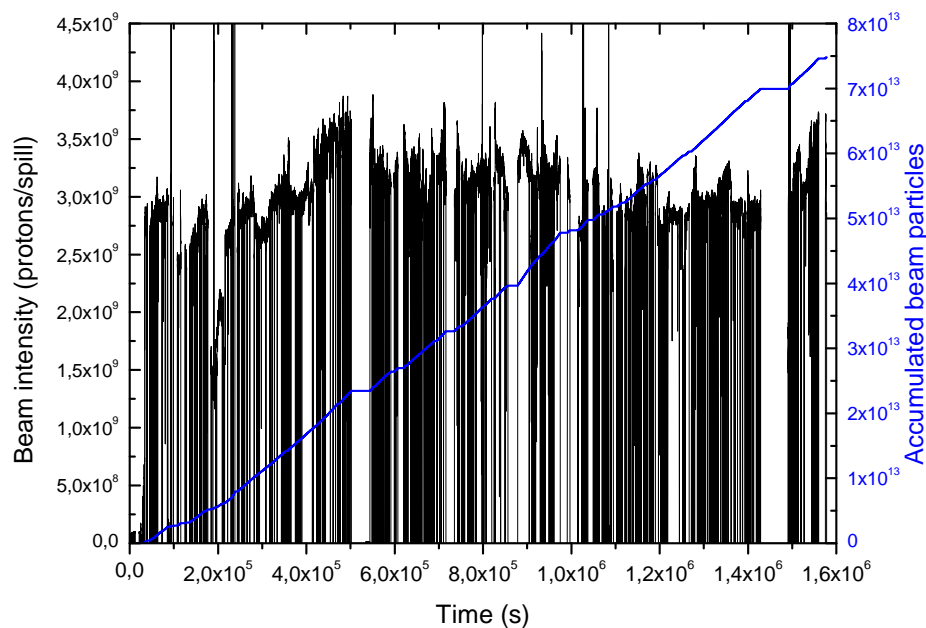


Figure 5.11: Irradiation profile of the samples. The number of protons in each spill (left scale) is shown together with the accumulated total number of protons (right scale).

5.4.3 FLUKA simulations and experimental results

The specific activities of the radionuclides in the samples were predicted by Monte Carlo simulations with the FLUKA code. The simulations were performed using a detailed geometrical model of the experimental facility implemented by the H4IRRAD team [51]. Figure 5.13 shows the target station as implemented in the FLUKA simulations. The irradiated samples



Figure 5.12: H4IRRAD target area. The samples were installed on the aluminum table just below the copper target.

were depicted in details with the actual size, the Plexiglas container and their position near the target, as they are showed in Figure 5.10. The elemental compositions of the samples were those obtained from the chemical analysis, to which 5% of water (moisture) was added.

The full hadronic cascade was simulated in the irradiation area, including particles back-scattered from the tunnel walls. For an accurate description of all nuclear processes relevant for isotope production, the evaporation of heavy fragments and the coalescence mechanism were explicitly turned on via two separated PHYSICS cards. The card DEFAULTS was used to set defaults for precision simulations. The particle transport threshold was set at 100 keV, except neutrons transported down to thermal energies. The low energy neutron transport (below 20 MeV) was performed using the multi-group approach with the 260 group library. The cascades initiated by $3 \cdot 10^3$ primary protons were simulated in a total of 100 FLUKA runs, for a total of $3 \cdot 10^5$ primaries. The total irradiation time was $1.73 \cdot 10^6$ seconds with an average beam intensity of $4.33 \cdot 10^7$ p/s, i.e. about $7.5 \cdot 10^{13}$ accumulated

number of protons (see Figure 5.11). Significant use of region-importance biasing was made in order to enhance the statistical accuracy of the results.

The production of residual nuclei and their radioactive decay were simulated in the same run. The RESNUCLEi card scored the residual nuclei produced in inelastic interactions, while the radioactive decay was calculated using the RADDECAY, DCYSCORE, DCYTIMES and IRRPROFILE cards, taking into account the decay chains, build-up of isotopes and the irradiation profile. The USRTRACK card scored the particle spectral fluences in the sample region. Figure 5.14 shows the differential distributions of the energy fluence of neutrons, protons and charged pions. The results of the FLUKA simulations are showed in Table 5.10.

Immediately after the irradiation period, the induced radioactivity of the samples was very high. Most of this radioactivity was due to very short half-life radioisotopes. Since the radioisotopes of interest to this study have medium and long half-life, the samples were let decaying for 10 days before counting. The earth and water samples were measured at the CERN Analytical Laboratory with a high sensitivity, low-background high-purity germanium (HPGe) detector by Canberra. The data acquisition and analysis was carried out using Canberra's Genie-2000 spectrometry software and the PROcount-2000 counting procedure software (see §5.3.3). Three gamma spectrometry analyses were performed for each sample, at cooling times of one week, one month and two months.

The tritium activity of the water was determined using a liquid scintillation counter (Packard TRI-CARB 3180TR/SL), measuring a mixture of 8 ml of activated water and 12 ml of so-called liquid scintillation cocktail (Packard Ultima Gold LLF). In case of high precision measurements, distillation is usually recommended requiring well controlled conditions where other radionuclides present in the sample (e.g. ^{22}Na) may significantly increase the result for tritium. This was not needed in the present case, as the potential interference of other radionuclides in the tritium pulse-height window was negligible.

Table 5.10 shows the results of the gamma spectrometry and tritium measurements for the soil and water samples after 10 days of cooling time. Only radionuclides with the smallest experimental uncertainty, lowest ratio between measured activity and MDA (Minimum Detectable Amount) and comparable cooling time and half-life are reported. Quoted errors include statistical uncertainties of the FLUKA simulations and statistical and systematic uncertainties of the gamma spectrometry analysis. Experimental values and FLUKA predictions are in very good agreement for the soil as well as the water.

Table 5.10: Results of experiment and calculations for the specific activity in the soil and water samples after 10 days of cooling time.

SOIL				
Nuclide	$t_{1/2}$	Experiment	FLUKA [Bq/g]	Exp/FLUKA
^3H	12.32 y	–	14.1 ± 0.3	–
^7Be	53.1 d	425 ± 32	257 ± 4	1.65
^{22}Na	2.6 y	12.5 ± 0.8	10.2 ± 0.2	1.23
^{46}Sc	83.8 d	3.02 ± 0.19	2.99 ± 0.35	1.01
^{48}V	16 d	9.33 ± 0.50	12.3 ± 1.1	0.76
^{51}Cr	27.7 d	25.0 ± 2.3	27.2 ± 1.4	0.92
^{52}Mn	5.59 d	6.01 ± 0.43	6.95 ± 0.49	0.87
^{54}Mn	312 d	6.02 ± 0.42	5.74 ± 0.23	1.05
^{56}Co	77.3 d	0.40 ± 0.04	0.86 ± 0.09	0.46
^{58}Co	70.9 d	0.22 ± 0.04	0.35 ± 0.05	0.62
WATER				
Nuclide	$t_{1/2}$	Experiment	FLUKA [Bq/g]	Exp/FLUKA
^3H	12.32 y	28.9 ± 2.6	27.6 ± 0.5	1.05
^7Be	53.1 d	523 ± 48	480 ± 12	1.09

5.4.4 Leaching procedure

Radionuclides affecting the groundwater come from leaching. Two leaching possibilities were investigated: 1) water stagnation with irradiated soil (mixing system); 2) water percolation through the irradiated soil (flowing system). In this work, we used the usual (standard) leaching procedure for the measurements of the leaching factor, consisting of 10 parts by weight



Figure 5.13: Detail of the irradiation set-up used in the FLUKA geometry. The aluminium target holder is shown in green, the copper target in blue and the irradiated soil sample in brown. The drawing is obtained using SimpleGeo [35].

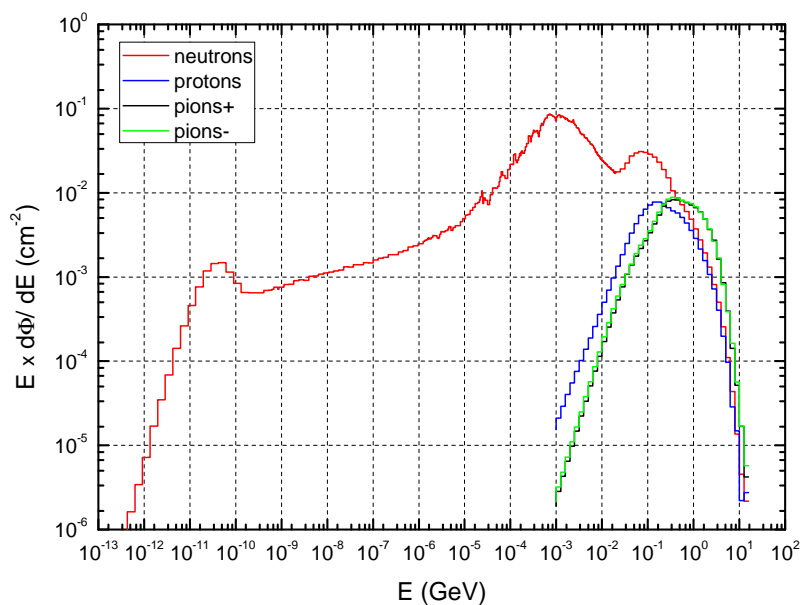


Figure 5.14: Fluence spectra of protons, neutrons and charged pions at the location of the soil and water samples.

of water and one part of irradiated soil [81–85]. To measure the amount of radioactivity passed from the irradiated soil to the water in both systems, leached water samples were systematically measured by gamma spectrometry as well as by scintillation analysis.

Soil-water mixing system

In the mixing system, 100 g of the irradiated soil were placed in a graduated flask together with 1 litre of distilled (tritium free) water (Figure 5.15). After vigorous shaking to disperse the soil in the water, the mixture was stirred for 8 hours. To measure the radioactivity leached out, 100 ml sample of the hazy water was filtered through a Millipore filter (0.45 μm). The gamma activity in the water was measured with a Germanium detector while β emitters were measured with a liquid scintillation spectrometer after evaporation. The analyses on the water were repeated 4 times after 11, 43, 72 and 134 days after the soil irradiation.



Figure 5.15: Soil-water mixing system.

Soil-water flowing system

In the flowing system (Figure 5.16) a sample of 100 g of irradiated soil was placed in a funnel with a Millipore filter ($0.45\ \mu\text{m}$) connected to a graduated container. A glass separatory funnel was placed over the funnel and filled with 1 litre of distilled (tritium free) water. The glass stopcock allowed controlling the rate of addition of the water to 125 ml/h (8 hours for 1 litre of water). The leached water was measured by gamma spectrometry and liquid scintillation counting.



Figure 5.16: Soil-water flowing system.

5.4.5 Data analysis

The experimental results were analysed and corrected for the decay time and for the radionuclide concentration. In order to quantify the right amount of radioactivity transferred from the soil into the water, the activity of each radioisotope was reported to 10 days after the irradiation as time reference

using the following equation:

$$A(t_{10d}) = A(t) \exp \left[-\frac{\ln(2)}{t_{1/2}}(t_{10d} - t) \right] \quad (5.18)$$

where $A(t_{10d})$ is the activity after 10 days of decay time, $A(t)$ is the activity at a generic time t and $t_{1/2}$ is the radionuclide half-life.

A further correction was needed for the soil-water mixing system. Since for every measurement the liquid scintillation analysis was performed using 0.1 litre of water, a correction for the measured activity $A(m_i)$ was applied:

$$A_c(m_i) = A(m_i) + A(m_{i-1})/10 \quad (5.19)$$

where m_i is the measurement $i = 1, 2, 3, 4$; $A_c(m_i)$ is the activity corrected for the measurement m_i ; $A(m_i)$ is the activity found in the measurement m_i and $A(m_{i-1})$ is the activity found in the previous measurement m_{i-1} .

The specific activities measured in the water as a function of the mixing time for the soil-water mixing system are given in Figure 5.17 and in Table 5.11. The ^3H concentration in the water quickly increases to 95.6% (518 Bq/l) of the total activity after 8 hours of mixing time. It takes one month to rise to 99.8% (541 Bq/l) and 2 months to reach 542 Bq/l, the maximum value measured in the water. A similar behaviour was found for ^{22}Na . The highest concentration was measured after 123 days with 144 Bq/l. Eight hours are enough to reach 67% (96.7 Bq/l) of the total ^{22}Na activity measured in the leached water. Half of the total ^{48}V activity was measured after 8 hours and the maximum activity is measured after 61 days with 16.1 Bq/l.

The results of the water analysis for the soil-water flowing system are given in Figure 5.18 and in Table 5.12. The specific activity of ^3H decreases from 384 Bq/l to 3.23 Bq/l after the first washing. The same behaviour is observed for ^{22}Na that passes from 126 Bq/l to 12.7 Bq/l in one wash. The concentrations of ^{48}V and ^{51}Cr vary little even after three washes. ^{48}V slowly decreases from 4.51 Bq/l to 1.95 Bq/l whereas ^{51}Cr decreases from 13.0 Bq/l to 8.33 Bq/l.

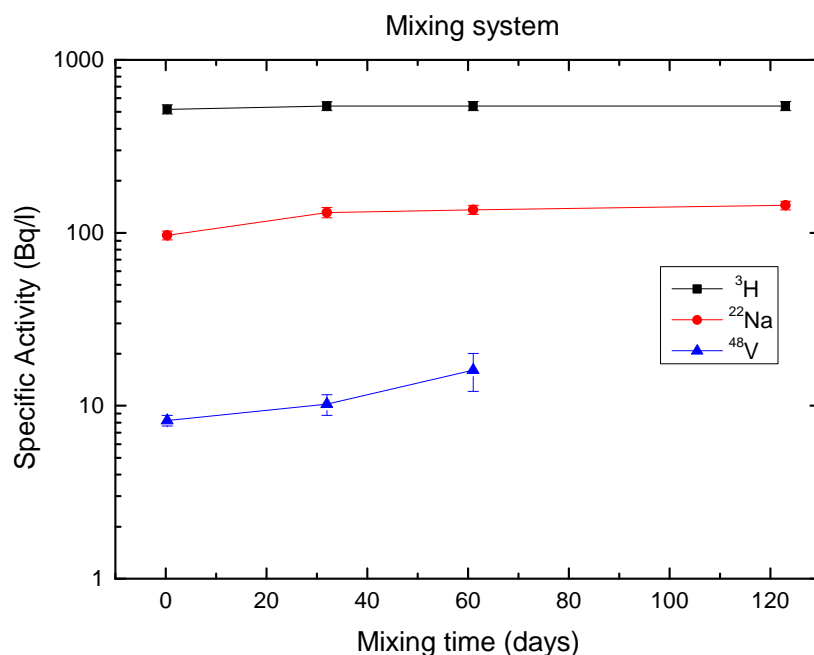


Figure 5.17: Specific activity of the leached water as a function of the mixing time for the soil-water mixing system, after correction for the decay and the concentration.

5.4.6 Fraction of radioactivity leached into the water

The activity concentration of the leached water for both systems was compared with the radioactivity measured in the activated soil in order to estimate the fraction leached out. Tables 5.14 and 5.15 show the ratio $A_i(\text{leachedwater})/A_i(\text{soil})$ for the mixing and flowing systems, respectively, where A_i is the activity of the radionuclide i . Since the liquid scintillation analysis cannot be performed on the soil, the tritium activity measured in the leached water was compared with the tritium estimated in the soil by the FLUKA simulations. Figure 5.19 shows the leached fraction of ^3H and ^{22}Na , the two radionuclides of major interest in this study. Most of the radioactivity leached into the water just after 8 hours of mixing time (mixing system) or after the first washing (flowing system). In the first case, the longer the soil is mixed with the water, the more radioactivity is leached out. After two

Table 5.11: Radioactivity measured in the leached water after correction for the decay and the concentration for the soil-water mixing system.

Mixing time	Specific Activity (Bq/l)			
	³ H ($t_{1/2}=12.32$ y)	⁷ Be ($t_{1/2}=53.1$ d)	²² Na ($t_{1/2}=2.6$ y)	⁴⁸ V ($t_{1/2}=16$ d)
8 h	518 ± 31	5.84 ± 3.03	96.7 ± 5.8	8.21 ± 0.49
32 d	541 ± 32	–	131 ± 8	10.2 ± 1.3
61 d	542 ± 32	–	136 ± 8	16.1 ± 2.1
123 d	542 ± 33	–	144 ± 9	–

Table 5.12: Radioactivity measured in the leached water including the decay correction for the soil-water flowing system.

Flowing time	Specific Activity (Bq/l)				
	³ H ($t_{1/2}=12.32$ y)	⁷ Be ($t_{1/2}=53.1$ d)	²² Na ($t_{1/2}=2.6$ y)	⁴⁸ V ($t_{1/2}=16$ d)	⁵¹ Cr ($t_{1/2}=27.7$ d)
8 h	384 ± 23	8.48 ± 2.40	126 ± 6	4.51 ± 0.28	13.0 ± 3.2
8 h	3.23 ± 0.93	–	12.7 ± 0.9	2.55 ± 1.4	9.16 ± 4.57
8 h	1.67 ± 0.90	–	3.15 ± 0.22	1.95 ± 1.23	8.33 ± 3.67
8 h	2.05 ± 1.09	–	4.71 ± 0.54	–	–

months of mixing, 39% of the ³H and 11% of the ²²Na are leached into the water. For the flowing system, the fraction leached in one wash is 27% for ³H and 10% for ²²Na. As from the second filtration step, the fraction leached falls down to a few per cent for both radioisotopes. It is clear that the mixing system is a much more efficient way to extract radioactivity from the activated soil. It is also interesting to compare the tritium leached into the water with its activity in the bulk and in the moisture of the activated soil. The tritium activity in the soil moisture $A_{trit}(\text{moisture})$ can be estimated from the tritium activity measured in the activated water sample (Table 5.10). Since the measured soil moisture is 5% by weight (see §5.4.1), i.e. 5 g for 100 g of soil, it can be assumed that:

$$A_{trit}(\text{moisture}) = A_{trit}(\text{water}) \times 5 \text{ g} = (145 \pm 9) \text{ Bq} \quad (5.20)$$

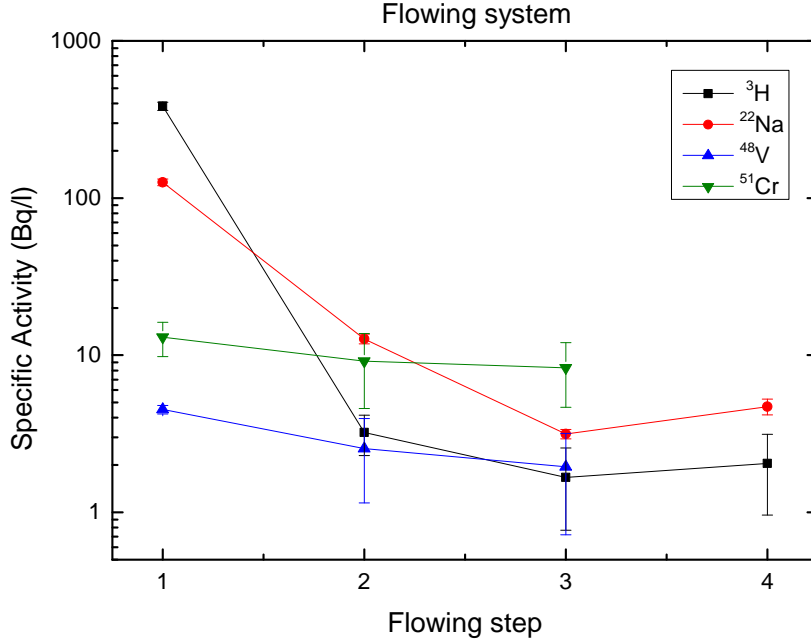


Figure 5.18: Specific activity of the leached water as a function of the filtration steps including decay time correction for the water-soil flowing system.

where $A_{trit}(water)$ is the specific activity of ^3H in the activated water, i.e. (28.9 ± 2.9) Bq/g. The total activity of ^3H in the soil $A_{trit}^{tot}(soil)$, is given by:

$$A_{trit}^{tot}(soil) = A_{trit}(soil) \times 100 \text{ g} = (1410 \pm 30) \text{ Bq} \quad (5.21)$$

where $A_{trit}(soil)$ is the specific activity of ^3H estimated by FLUKA in the soil (Table 5.10), i.e. (14.1 ± 0.3) Bq/g. The tritium activity in the bulk of the activated soil $A_{trit}(bulk)$ can thus be estimated as follow:

$$A_{trit}(bulk) = A_{trit}^{tot}(soil) - A_{trit}(moisture) = (1265 \pm 105) \text{ Bq} \quad (5.22)$$

where $A_{trit}(moisture)$ and $A_{trit}^{tot}(soil)$ and are given by expressions (5.20) and (5.21). Table 5.15 summarizes the results and shows the moisture fraction leached $A_{trit}(leached\ water)/A_{trit}(moisture)$ and the bulk fraction leached

$A_{trit}(leached\ water)/A_{trit}(bulk)$ for the mixing and flowing system. Both systems leached out 100% of tritium produced in the moisture. The mixing system extracted 32% of tritium produced in the bulk, whereas the flowing system only 20%.

The complete gamma spectrometry and liquid scintillation results and more details on the calculations I performed to estimate the radionuclides leached into the groundwater can be found in Refs. [94, 95].

Table 5.13: Fraction of radioactivity leached into the water in the mixing system. *Compared with the tritium activity estimated by FLUKA simulations (Table 5.10).

Nuclide	$t_{1/2}$	Fraction Leached (%)			
		8 h	32 d	61 d	123 d
$^3\text{H}^*$	12.32 y	36.7	38.4	38.5	38.5
^7Be	53.1 d	0.01	–	–	–
^{22}Na	2.6 y	7.74	10.5	10.9	11.5
^{48}V	16 d	0.88	1.09	1.73	–

Table 5.14: Fraction of radioactivity leached into the water in the flowing system. *Compared with the tritium activity estimated by FLUKA simulations (Table 5.10).

Nuclide	$t_{1/2}$	Fraction Leached (%)			
		8 h	32 d	61 d	123 d
$^3\text{H}^*$	12.32 y	27.2	0.23	0.12	0.15
^7Be	53.1 d	0.02	–	–	–
^{22}Na	2.6 y	10.1	1.02	0.25	0.38
^{48}V	16 d	0.48	0.27	0.21	–
^{51}Cr	27.7 d	0.52	0.37	0.33	–

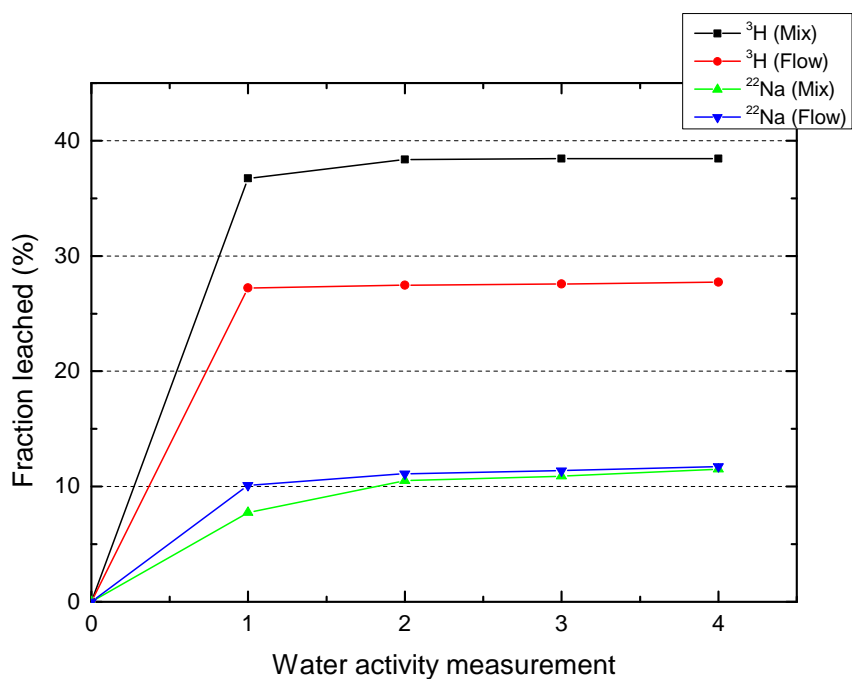


Figure 5.19: Fraction of ^3H and ^{22}Na activities leached into the water for both systems.

Table 5.15: Fraction of tritium activity leached out from soil bulk and moisture for both systems.

	Activity (Bq)	
	^3H (mixing)	^3H (flowing)
Soil bulk (FLUKA)	1265 ± 105	1265 ± 105
Soil moisture (5 g)	145 ± 9	145 ± 9
Leached water	542 ± 33	384 ± 23
Fraction of moisture activity leached out	100%	100%
Fraction of bulk activity leached out	31.4%	18.9%

Chapter 6

Prediction of the induced radioactivity for the future CERN Linac4 accelerator

This chapter discusses the FLUKA Monte Carlo simulations performed to predict the residual radioactivity in the new 160 MeV proton linear accelerator (Linac4) that is being installed at CERN to replace the present 50 MeV Linac2 as injector of the Proton Synchrotron Booster (PSB). This study is based on the assumption that Linac4 will be operated at the design beam parameters for LHC high-luminosity operation during a period of 30 years, with a schedule of about 7000 hours per year. In this work, I estimated the induced radioactivity in the main linac accelerator components and the residual dose rate in the tunnel for various beam energies and several decay times. The component activation was also compared with the exemption limits according to the current Swiss legislation and to the CERN design values.

6.1 The Linac4 injector

A programme for the progressive replacement and upgrade of the LHC injectors has been defined at CERN for two main reasons: firstly, to increase the LHC luminosity beyond the nominal value by the improving the beam brightness from the injector complex, which is now the main limiting factor towards higher luminosity. A second motivation is the replacement of the present cascade of injectors, which has been built between 1959 and 1978 and in the past few years has raised concerns for its long-term reliability, with a more modern, reliable and easier to maintain system, where transfer energies and beam parameters are optimized for the LHC needs [97]. Moreover, new low energy accelerators can be made compatible with operation at higher beam power that could be required by future physics needs. One of the main elements in this project of renovation of the LHC injection chain is the Linac4 accelerator.

Linac4 is a 160 MeV, 40 mA H^- accelerator which in a few years will be the source of protons for all accelerators at CERN [98, 99]. It is an 86-m long normal-conducting linac made of an H^- source, a Low Energy Beam Transport (LEBT), a Radio Frequency Quadrupole (RFQ), a chopping line and a sequence of three accelerating structures (Table 6.1):

- Drift-Tube Linac (DTL) consisting of three tanks with output energy of 50 MeV;
- Cell-Coupled DTL (CCDTL) consisting of 7 modules of three coupled 3-cell DTL-type cavities with output energy of 100 MeV;
- Pi-Mode Structure (PIMS) consisting of 12 tanks of 7-cell pi-mode structures with output energy of 160 MeV.

Linac4 will operate at 2 Hz, with a peak current of 40 mA and a pulse length of 0.4 ms as PSB injector. These parameters correspond to 0.08% beam duty cycle and 0.032 mA average current or $2 \cdot 10^{14}$ protons/s, equivalent to a beam power of 5.1 kW at the top energy of 160 MeV. Linac4 has been designed

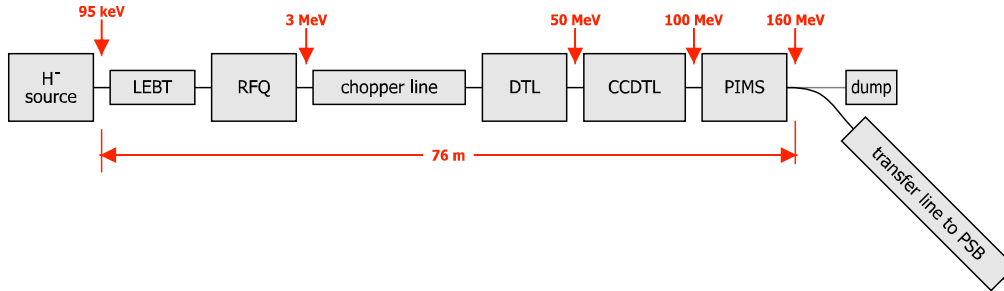


Figure 6.1: Schematic view of the Linac4.

to replace the present 50 MeV Linac2 as injector of the Proton Synchrotron Booster (PSB). The higher injection energy will allow the production by the PSB of beams with increased brightness as required by the High-Luminosity LHC. The overall architecture of the Linac4 is schematically shown in Fig. 6.1

Table 6.1: Linac4 main accelerating structures and their output energies.

	DTL	CCDTL	PIMS
Number of cavities	3	7×3	12
Length [m]	19	26	23
Output Energy [MeV]	50	100	160

6.2 Prediction of induced radioactivity in machine components

The estimation of the induced radioactivity in the components of the accelerator is particularly important for maintenance interventions and the final disposal of radioactive waste. Safety is the main reason to perform a radiation protection study already during the design and construction phase. It must be demonstrated that the ALARA (As Low As Reasonably Achievable) principle has been taken into account in the design of the new facility. Components that can become activated must be designed in such a way as to facilitate dismantling, handling and storage of the activated parts in order to minimize the radiation dose to workers.

In order to assess the residual activation for various beam energies and several decay times a series of FLUKA Monte Carlo simulations were performed, using a detailed geometrical model of the accelerator based on the existing geometry implemented in the code a few years ago [100].

6.2.1 FLUKA calculations

Apart for components directly hit by the beam (e.g. collimators or aperture restrictions), most of the induced activity in proton accelerators in the 100 MeV range is due to the stray neutron field. Monte Carlo models used to estimate induced radioactivity in accelerator components must be able to reliably predict nuclide production in arbitrary target elements and at energies ranging from thermal neutrons to neutrons with energy close to the maximum accelerator energy. In this study we used the Monte Carlo code FLUKA (version 2011.2.17), which is an appropriate code for estimating induced radioactivity in a wide range of accelerator facilities (see chapter 3).

Geometry

The FLUKA simulations were performed using a detailed geometrical model of the main accelerating structures based on the existing geometry implemented a few years ago for a previous study [100]. This geometry was modified in the material composition of the DTL tanks, where the ST-52 steel was replaced by ST-304L steel, and in the CCDTL section, where two-thirds of the electro-magnetic quadrupoles (EMQ) were replaced by permanent magnetic quadrupoles (PMQ). In the new CCDTL geometry the EMQs are used between modules and the PMQs between tanks [101].

Beam loss assumptions and irradiation profile

In a linear accelerator the equipment activation is produced by scattered particles escaping from the fields generated for controlling the focusing and the acceleration and hitting the vacuum chamber. It is hard to predict and

identify the beam loss locations because they will not be equally distributed along the machine. Losses typically occur in the aperture restrictions of quadrupoles, due to possible mismatch between linac sections. According to the estimated particle loss distribution, it was assumed that constant losses of 0.1 W occur every 10 m at selected points along the machine. This value comes from the analysis of the beam losses [102] for a 6% duty cycle scenario, indicating a maximum loss of 1 W in some "hot spots". During the LINAC4 operation as PSB injector at 0.033% duty cycle, losses would be theoretically reduced by a factor of 180 although it is expected that the sensitivity of the beam loss monitors would not allow reaching such a low loss level. A conservative value of 0.1 W per loss location was therefore assumed, 18 times higher than the minimum achievable loss level [103]. Table 6.2 shows the seven beam losses for the three main accelerating structures with a total length of 70 m. It is evident that with increasing energy the number of lost particles decreases for constant lost beam power (0.1 W every 10 m). The calculation of the induced radioactivity was performed in three positions (noted in bold in Table 6.2), representative of typical aperture restrictions in the various sections of Linac4: the first drift tube of the third DTL tank at 31 MeV, the quadrupole at 80 MeV within the CCDTL section and the last quadrupole at 155 MeV within the PIMS section. For each position the calculations also took into account the activation due to the two loss points upstream and downstream. It should be underlined that this approach is rather innovative in this type of study. The induced radioactivity depends

Table 6.2: Beam loss assumptions along the main accelerating structures. The three activation study points are shown in bold.

	DTL		CCDTL		PIMS		
Distance [m]	4	12	23	35	45	55	66
Energy [MeV]	11	31	57	80	100	128	155
Beam loss [p/s]	5.67E+10	2.01E+10	1.09E+10	7.80E+09	6.24E+09	4.88E+09	4.03E+09

on the irradiation profile, which includes periods of operation at various beam intensities alternating with shutdown (maintenance) periods. Although the Linac4 irradiation profile during its 30 years of planned operation is clearly

impossible to predict exactly, a simplified but quite realistic irradiation profile was derived from the present Linac2 yearly schedule, which consists of an average operating time of 5000 hours per year. To include a safety margin, an average of 7000 hours per year was used in the present calculations (corresponding to the yearly schedule of Linac2 without the year-long shut-down every 4 years). The time profile of the irradiation included 29 cycles of 9.7 months of operation and 2.3 months of shutdown period, followed by a final operating period of 9.7 months. The total irradiation time was $2.1 \cdot 10^5$ hours and the accumulated number of protons was $1.52 \cdot 10^{19}$ for the DTL at 31 MeV, $5.90 \cdot 10^{18}$ for the CCDTL at 80 MeV and $3.04 \cdot 10^{18}$ for the PIMS at 155 MeV. Figures 6.2 - 6.4 show the profiles of the beam losses in these positions and the accumulated number of lost protons as a function of the irradiation time.

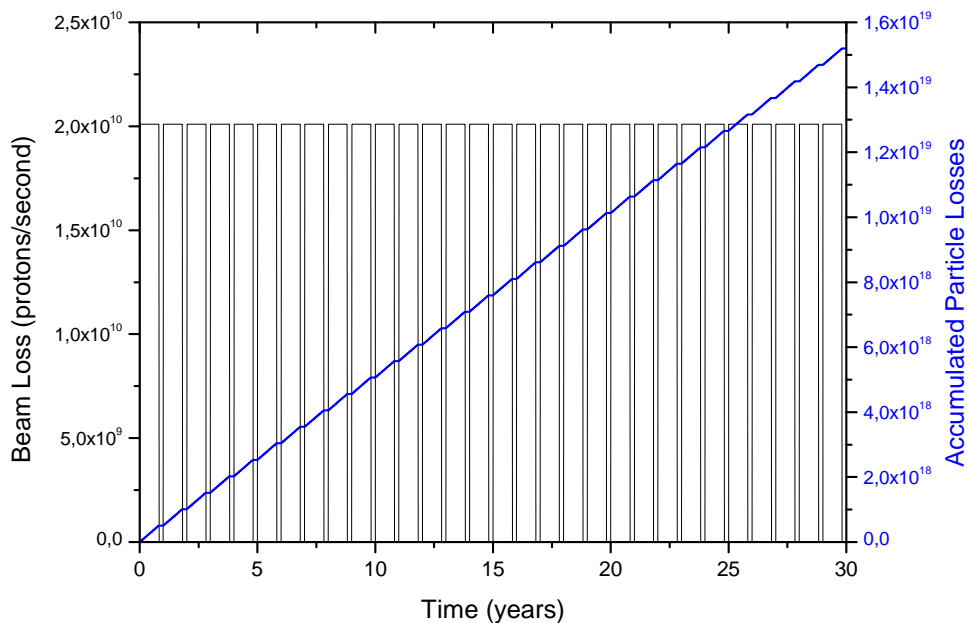


Figure 6.2: Beam loss profile and accumulated number of lost protons as a function of irradiation time in the DTL section (31 MeV).

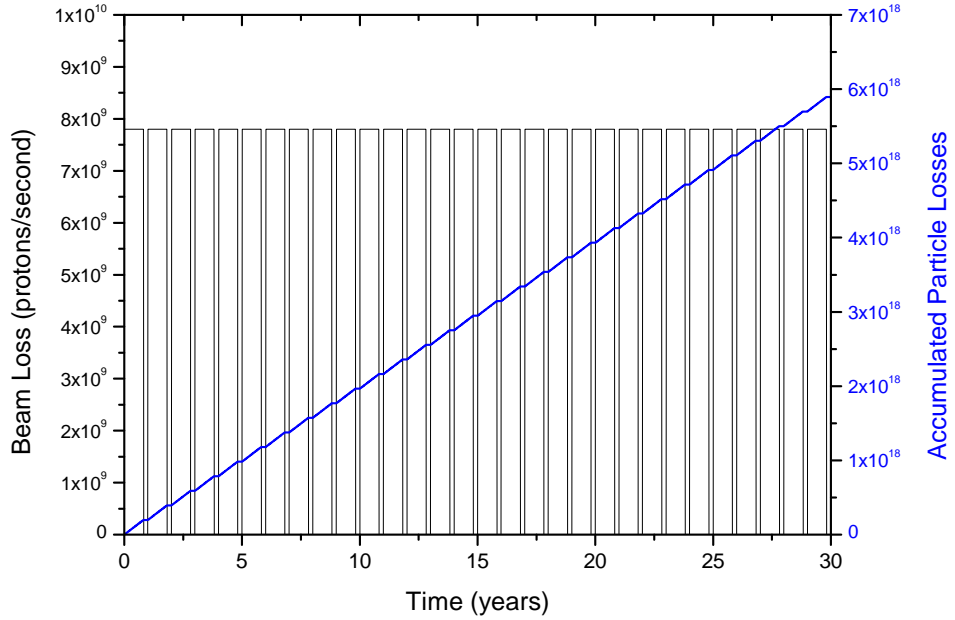


Figure 6.3: Beam loss profile and accumulated number of lost protons as a function of irradiation time in the CCDTL section (80 MeV).

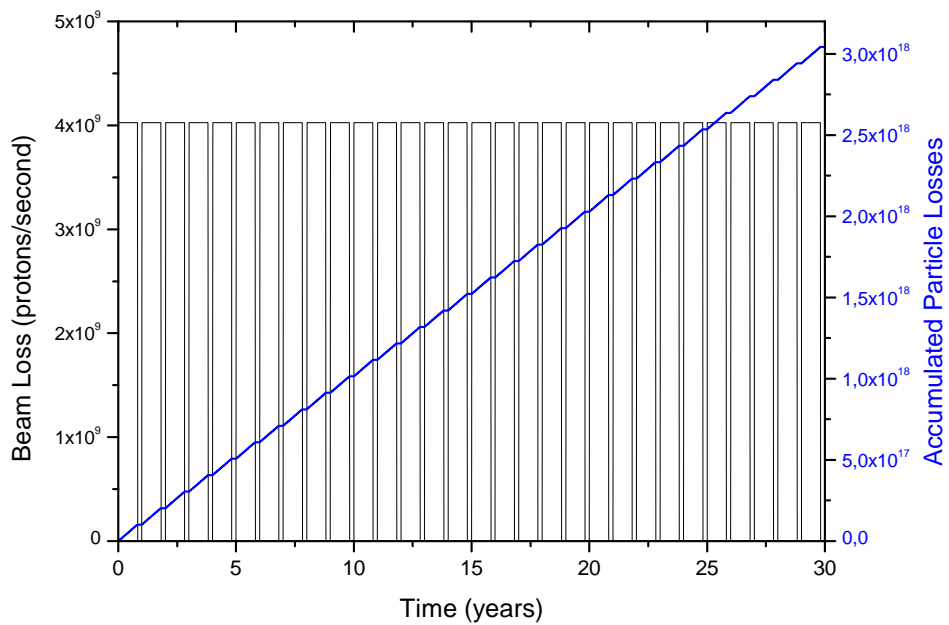


Figure 6.4: Beam loss profile and accumulated number of lost protons as a function of irradiation time in the PIMS section (155 MeV).

Physics

The full electromagnetic and hadronic cascades were simulated in the main accelerator components including particles back-scattered from the beam tunnel walls. The cascades initiated by $1 \cdot 10^7$ primary protons were simulated in a total of 100 FLUKA runs (for a total of $1 \cdot 10^9$ primaries) for every beam loss (7 loss points). For an accurate description of all the nuclear processes relevant for isotope production, the evaporation of heavy fragments and the coalescence mechanism were explicitly turned on via two separated PHYSICS cards. The card DEFAULTS was used, setting defaults for precision simulations. The particle transport threshold was set at 100 keV, except for neutrons that were transported down to thermal energies. The low energy neutron transport (below 20 MeV) was performed using the multi-group approach, updated to the new 260 group library. The RADDECAY card with the "Decays option" activated was used to simulate radioactive decays and to set the corresponding transport conditions. This allows the time evolution of induced radioactivity to be calculated analytically for fixed cooling times considering daughter nuclei as well as associated radiation at these fixed times.

Scoring

The production of residual nuclei and their radioactive decay were performed by FLUKA in the same run. The RESNUCLEi card scored the residual nuclei produced in inelastic interactions, while the radioactive decay was calculated using the RADDECAY, DCYSCORE, DCYTIMES and IRRPROFILE cards, taking into account the decay chains, build-up of isotopes and the irradiation profile. The USRBIN card scored the dose equivalent (DOSE-EQ card) along the accelerator tunnel and the total activity (ACTIVITY card) in selected regions. The USRTRACK card scored the particle spectra in the three beam impact areas under study. The data files produced were then post-processed with an offline code distributed together with FLUKA (usr-suvev.f) to merge results in binary form and to compute standard deviations

over several runs.

Particle fluence spectra

Each Monte Carlo simulation included the scoring of energy spectra of neutrons, protons and photons at the three beam impact points under study. Apart for components directly hit by the beam (e.g. collimators or aperture restrictions), most of the induced radioactivity in proton accelerators in the 100 MeV range is due to the stray neutron field. Figure 6.5 compares the neutron energy spectra at the location of the three loss points under study for all sections. Figure 6.6 compares the neutron fluence spectra in the drift tube and in the tank surrounding the beam impact point in the DTL (shown in Figure 6.7).

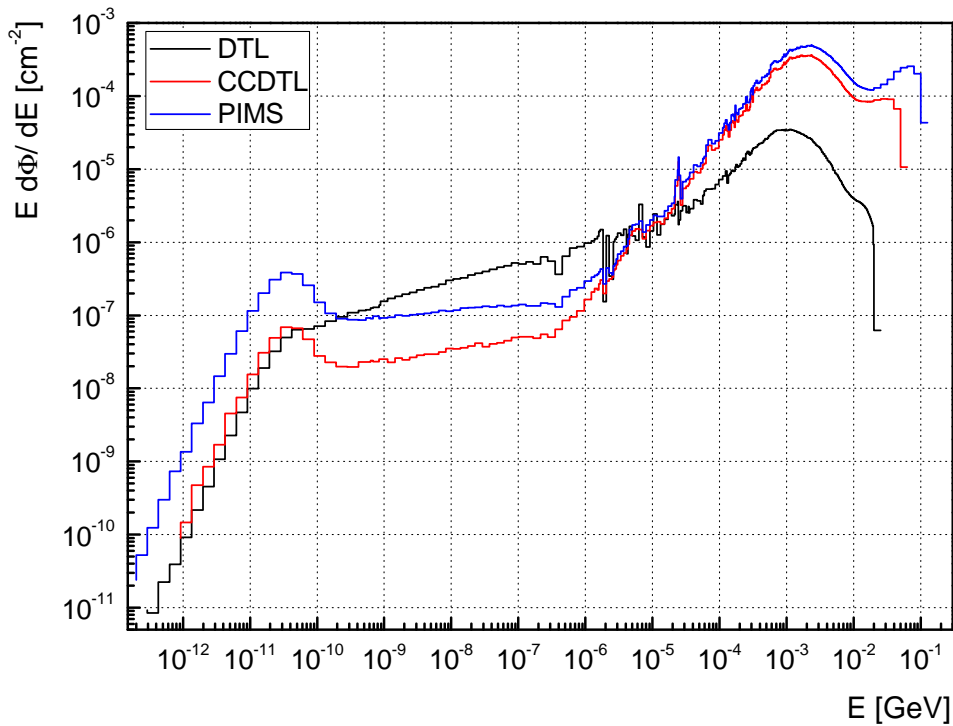


Figure 6.5: Comparison of the neutron fluence spectra at the three beam impact points: 31 MeV (DTL), 80 MeV (CCDTL), 155 MeV (PIMS).

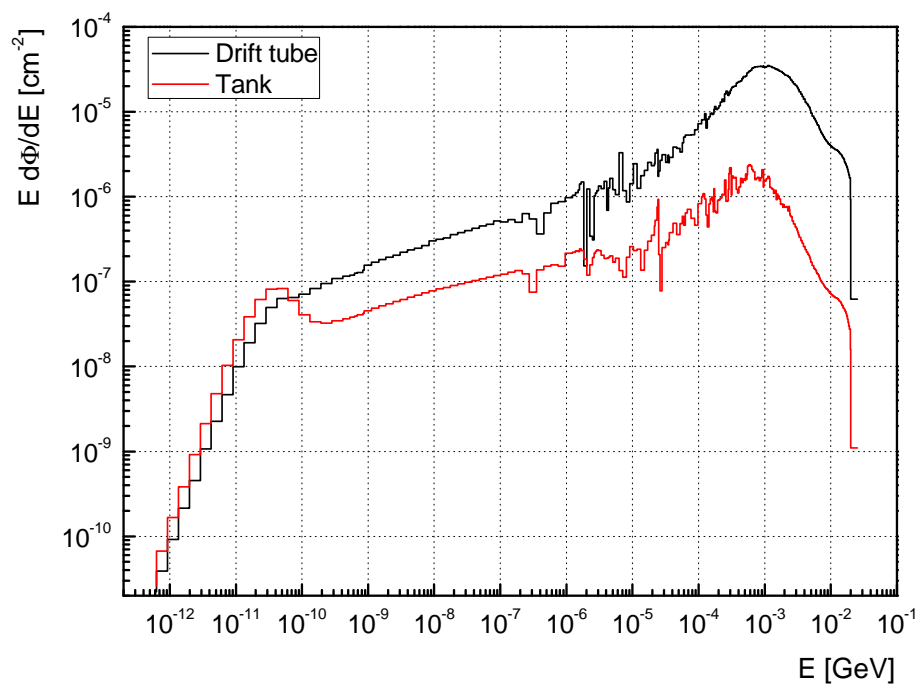


Figure 6.6: Comparison of the neutron fluence spectra in the first drift tube and in the third tank of the DTL section.

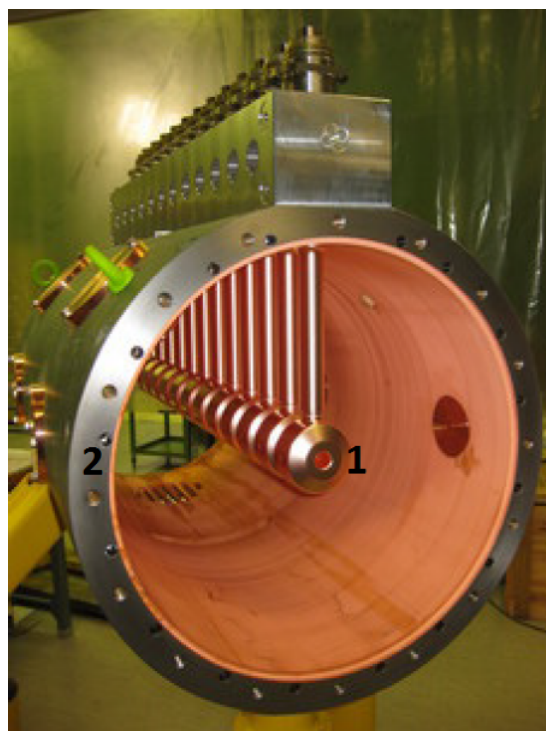


Figure 6.7: Half section of a full-scale DTL prototype in assembly stage [Courtesy of Linac4 team]. The numbers indicate the first drift tube (1) and the tank (2) where the neutron spectra of Figure 6.6 were simulated.

6.2.2 Induced Radioactivity

Residual radioactivity was scored for the most important components of the accelerator for several decay times, from just after the final shutdown up to 500 years. For each component we estimated not only the activation produced by the direct impact of the beam at the given loss point, but also the induced radioactivity due to the secondary particles coming from the two adjacent loss points, downstream and upstream. The complete radionuclide inventory for each component and all sections can be found in Ref. [104].

For every radionuclide the specific activity for several cooling times was compared with the exemption limits given in the current Swiss legislation (Swiss ORaP 2013) [105] and with the CERN exemption values used in design studies [106] for future accelerators (Table 6.3). The latter represent, for each nuclide, the minimum of the exemption limits that will be adopted by future European Directives and national legislations and are thus considered as conservative values. They are much more restrictive than those provided in the present Swiss legislation

Drift Tube Linac (DTL)

In the DTL section the proton beam impinges with a small angle (1 mrad) on the first drift tube of the third tank. The specific activity has been estimated in the following components of the third tank: the drift tubes; the permanent magnetic quadrupoles (PMQ); the stems; the girders; the tank; the vacuum chamber and the electromagnetic quadrupole (EMQ) upstream of the loss point; the waveguide and the support closest to the loss point.

Figure 6.8 shows the specific radioactivity as a function of cooling time for the DTL. It is interesting to notice that the PMQs are the most active components, as expected due to their high cobalt content. After 50 years of decay time the residual activation of the drift tubes exceeds that of the PMQs because of the high production yield of ^{63}Ni , which is the longest-lived radionuclide ($t_{1/2} = 96 \text{ y}$) found in the radionuclide inventories.

Figures 6.9 and 6.10 show the ratio between the specific activity and the

Table 6.3: Main radionuclides found in the Linac4 components and current (Swiss) and future (design) exemption limits.

Nuclide	$T_{1/2}$	LE [Bq/kg]	
		Swiss [105]	Design [106]
^3H	12.3 y	2.00E+005	1.00E+005
^{22}Na	2.6 y	3.00E+003	1.00E+002
$^{44}\text{Ti}/\text{Sc}$	47.3 y	2.00E+003	2.00E+003
^{45}Ca	163 d	1.00E+004	1.00E+004
^{46}Sc	83.83 d	7.00E+003	1.00E+002
^{48}V	16.24 d	5.00E+003	1.00E+003
^{49}V	330 d	6.00E+005	6.00E+005
^{51}Cr	27.7 d	3.00E+005	1.00E+005
^{52}Mn	5.6 d	6.00E+003	1.00E+003
^{54}Mn	312.5 d	1.00E+004	1.00E+002
^{55}Fe	2.7 y	3.00E+004	3.00E+004
^{56}Co	78.76 d	4.00E+003	1.00E+002
^{57}Co	270.9 d	5.00E+004	1.00E+003
^{58}Co	70.8 d	1.00E+004	1.00E+003
^{59}Fe	44.5 d	6.00E+003	1.00E+003
^{60}Co	5.27 y	1.00E+003	1.00E+002
^{63}Ni	96 y	7.00E+004	7.00E+004
^{65}Zn	243.9 d	3.00E+003	1.00E+002
^{88}Y	106.6 d	8.00E+003	8.00E+003
^{88}Zr	83.4 d	3.00E+004	3.00E+004
^{145}Sm	340 d	5.00E+004	5.00E+004
^{149}Eu	93.1 d	1.00E+005	1.00E+005
^{152}Eu	13.33 y	7.00E+003	1.00E+002
^{154}Eu	8.8 y	5.00E+003	1.00E+002
^{155}Eu	4.96 y	3.00E+004	1.00E+003

Swiss exemption limits (Figure 6.9) or the CERN design values (Figure 6.10) as a function of cooling time, integrated over all radioisotopes for the main components of the accelerator. In the DTL structure most of the components are below the limits of specific activity soon after the shutdown. Only the vacuum chamber, the drift tube and the PMQs need more than 2, 10 and 50 years of cooling time, respectively (Figure 6.10). The PMQs show the highest fraction of the exemption limit and the longest decay time to decrease below the limit because of their high cobalt content: after 2 years of decay time the highest contribution (56.5%) to the quantity is given by ^{60}Co .

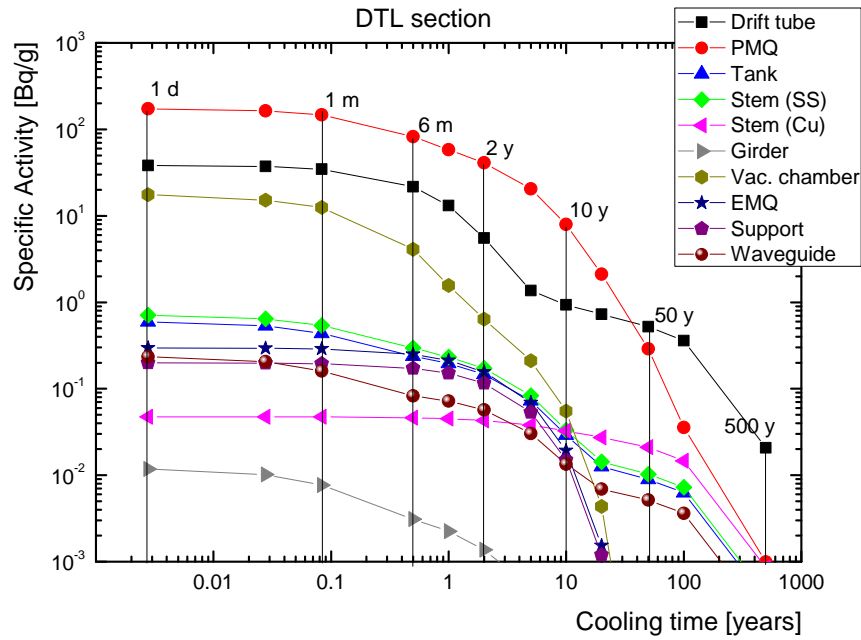


Figure 6.8: Specific radioactivity as a function of cooling time in the main DTL components.

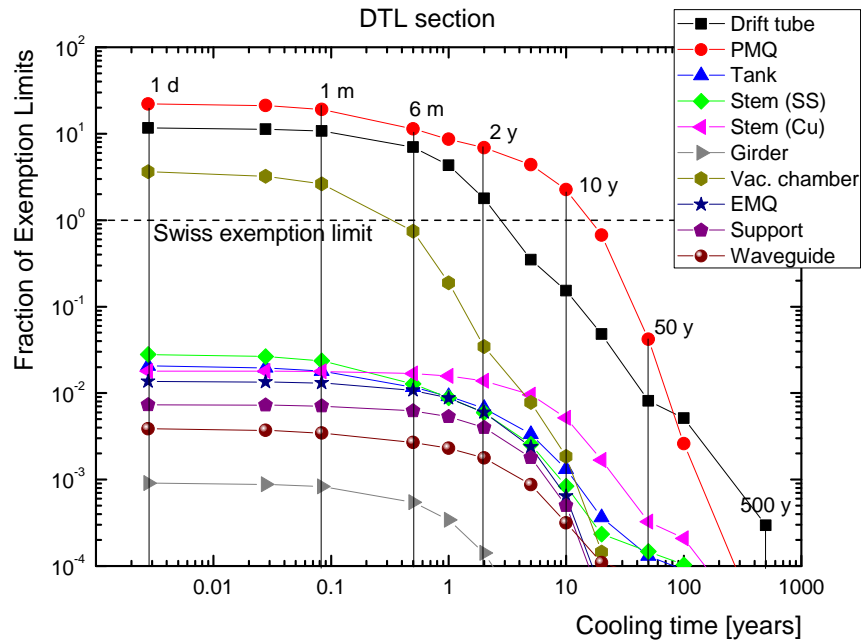


Figure 6.9: Fraction of Swiss exemption limits (specific activity) as a function of cooling time for the DTL components.

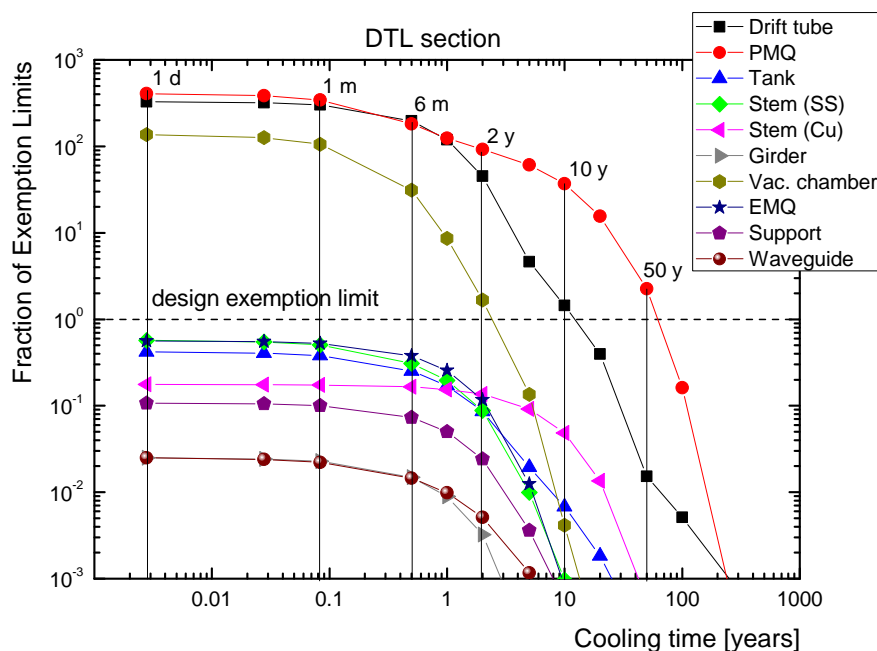


Figure 6.10: Fraction of CERN design exemption limits (specific activity) as a function of cooling time for the DTL components.

Cell Coupled Drift Tube Linac (CCDTL)

In the CCDTL section the proton beam impinges with a small angle (1 mrad) on the vacuum chamber between the first and the second tank of the 5th module. The specific activity has been estimated in the following components in the 5th module: the vacuum chamber and the PMQ between the first and the second cavity; the EMQ closest to the loss point; the tank wall downstream of the loss point; the copper plating downstream of the loss point; the first nose-cone downstream of the loss point; the first drift tube downstream of the loss point; the copper and stainless steel stem downstream of the loss point; the waveguide and the support closest to the loss point.

The most active component in the CCDTL is the vacuum chamber because it is directly hit by the beam (Figure 6.11). After 2 years of cooling, the main contributors to the total activity are ^{54}Mn and ^{55}Fe , whilst $^{44}\text{Ti}/\text{Sc}$

and ^{63}Ni are responsible for the residual radioactivity at very long decay times. If the specific activities of the support and the waveguide are below the Swiss exemption limits already at the shutdown (Figure 6.12), at least two years are required in case of the design exemption limits (Figure 6.13). After 50 years all CCDTL components are below the design limits except for the vacuum chamber and the PMQs.

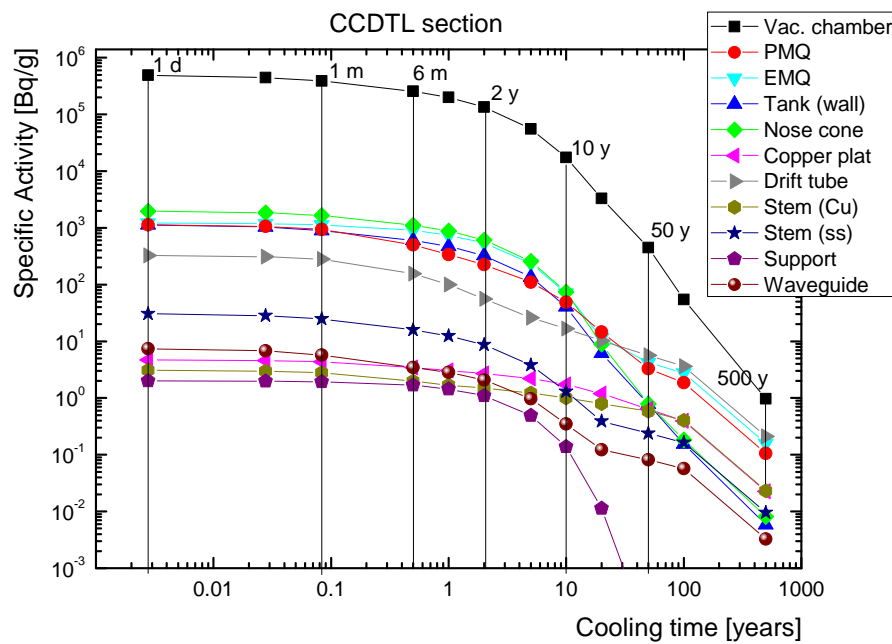


Figure 6.11: Specific radioactivity as a function of cooling time in the main CCDTL components.

Pi-Mode accelerating structure (PIMS)

In the PIMS section the proton beam impinges with a small angle (1 mrad) on the vacuum chamber between the 11th and the 12th tank. The residual radioactivity has been estimated in the following components: the vacuum chamber between the 11th and the 12th tank; the EMQ adjacent to the vacuum chamber; the left and the external wall of the 12th tank downstream of

the loss point; the external wall of the 11th tank upstream of the loss point; the nose-cone and the copper cylinder of the 12th tank located downstream of the loss point; the support and the waveguide closest to the loss point. As evident from Figure 6.14, the most active components are the vacuum chamber and the EMQ, with specific activity higher than 1×10^4 Bq/g after one year of cooling. The major contribution to the total fraction of the design exemption limits after two years of cooling comes from ^{54}Mn for both the vacuum chamber and the EMQ. In spite of the higher beam energy than in the other sections of the accelerator, the support is below the Swiss limits from the beginning (Figure 6.15), but for the design limits most of the PIMS components are still rather radioactive after five years (Figure 6.16).

Total radioactivity

A region-independent scoring (Cartesian binning) of the distribution of the total radioactivity over the three beam loss points in each section of the linac was carried out for five cooling times. Figure 6.17 shows the activation profile in the third DTL tank. The activity was estimated in 182 bins, 83.5 cm high (x-axis), 105 cm wide (y-axis) and 4 cm long (z-axis), for a total length of 7.28 m. The beam loss points at 12 m distance and 31 MeV energy is clearly visible. Starting from 1 month of decay time, a wavy profile is visible due to the substantially higher residual activation of the PMQs with respect to the rest of the machine. Beyond 19 m the activity increases again because of the next beam loss point. Figure 6.18 shows the activation profile of the fifth CCDTL module, which consists of three tanks. The activity was estimated in 179 bins, 105 cm high (x-axis), 76 cm wide (y-axis) and 2 cm long (z-axis), for a total length of 3.58 m. The beam loss points at 35 m distance and 80 MeV energy is clearly visible. Figure 6.19 shows the activation profile of the 12th and 13th PIMS tank. The activity was estimated in 190 bins, 80 cm high (x-axis), 55 cm wide (y-axis) and 2 cm long (z-axis), for a total length of 3.8 m. The beam loss points at 66 m distance and 155 MeV energy is clearly visible.

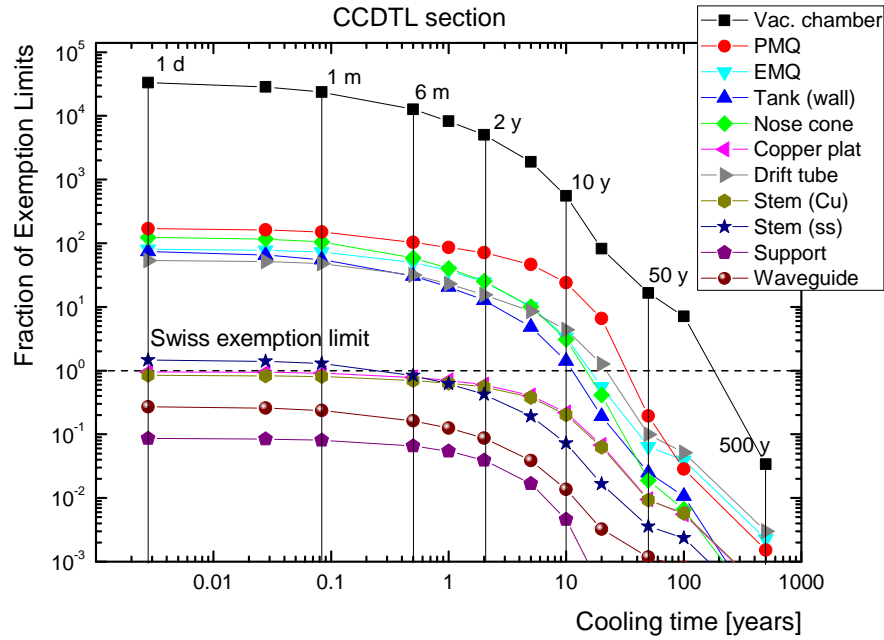


Figure 6.12: Fraction of Swiss exemption limits (specific activity) as a function of cooling time for the CCDTL components

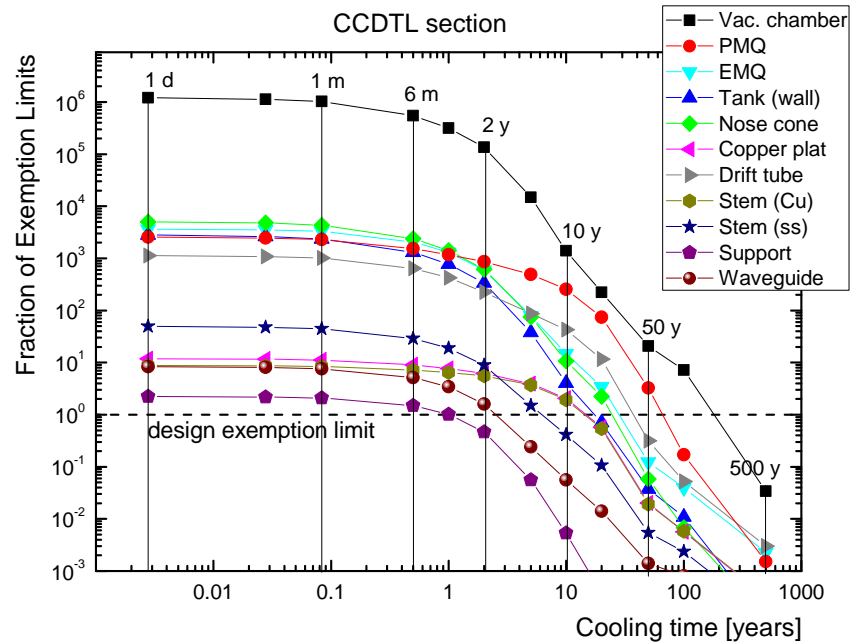


Figure 6.13: Fraction of CERN design exemption limits (specific activity) as a function of cooling time for the CCDTL components.

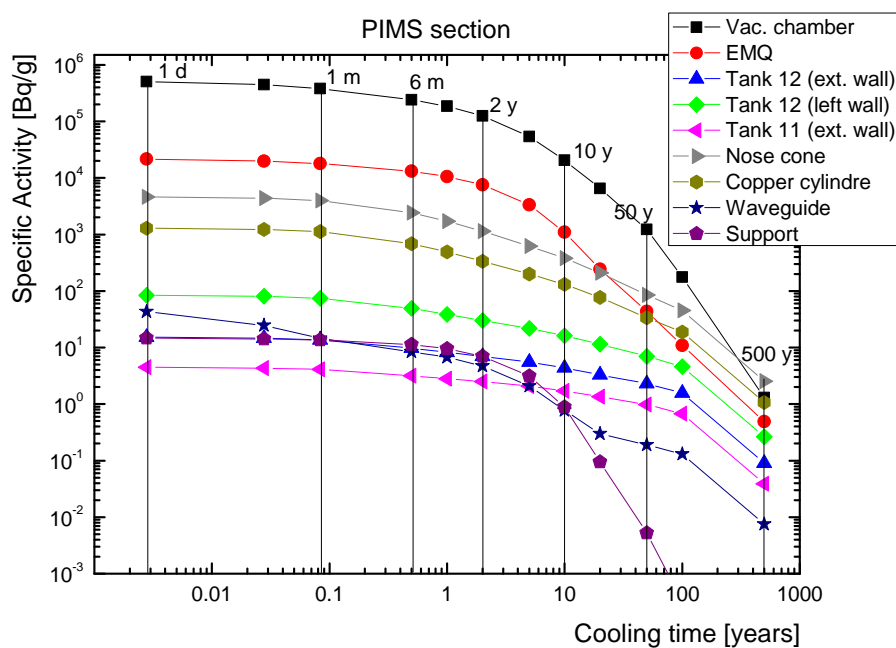


Figure 6.14: Specific radioactivity as a function of cooling time in the main PIMS components.

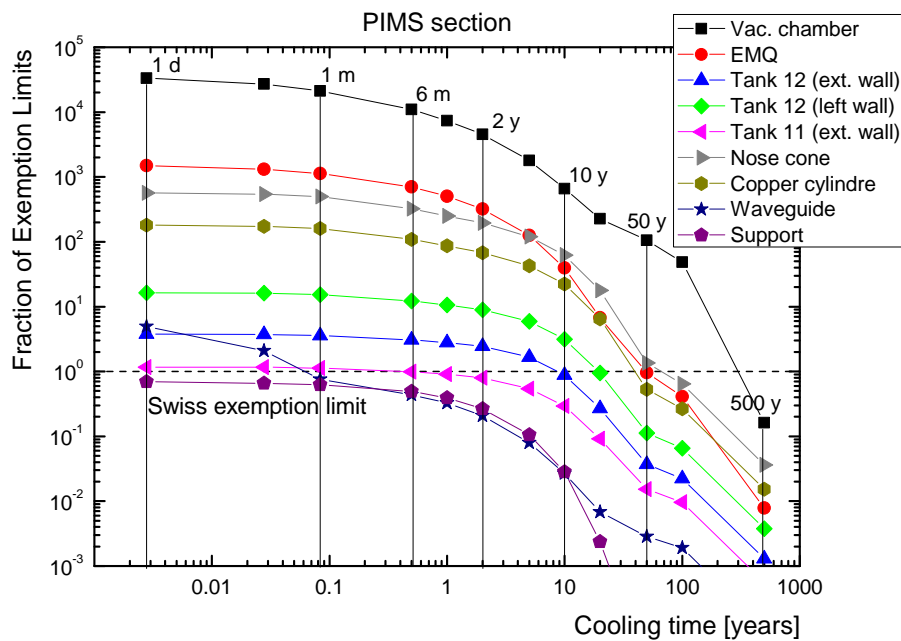


Figure 6.15: Fraction of Swiss exemption limits (specific activity) as a function of cooling time for the PIMS components.

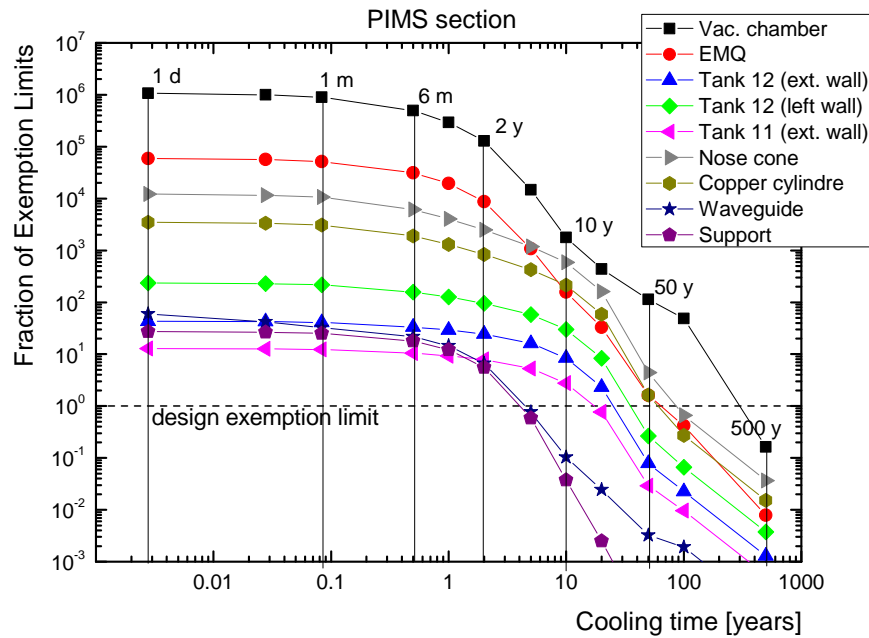


Figure 6.16: Fraction of CERN design exemption limits (specific activity) as a function of cooling time for the PIMS components.

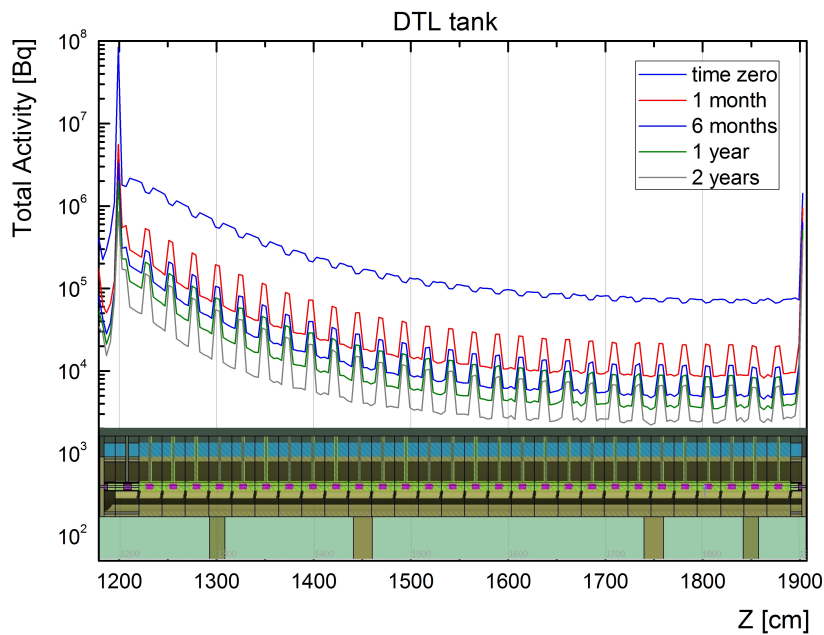


Figure 6.17: Profile of the total radioactivity in the third DTL tank along the beam axis (z) for five decay times.

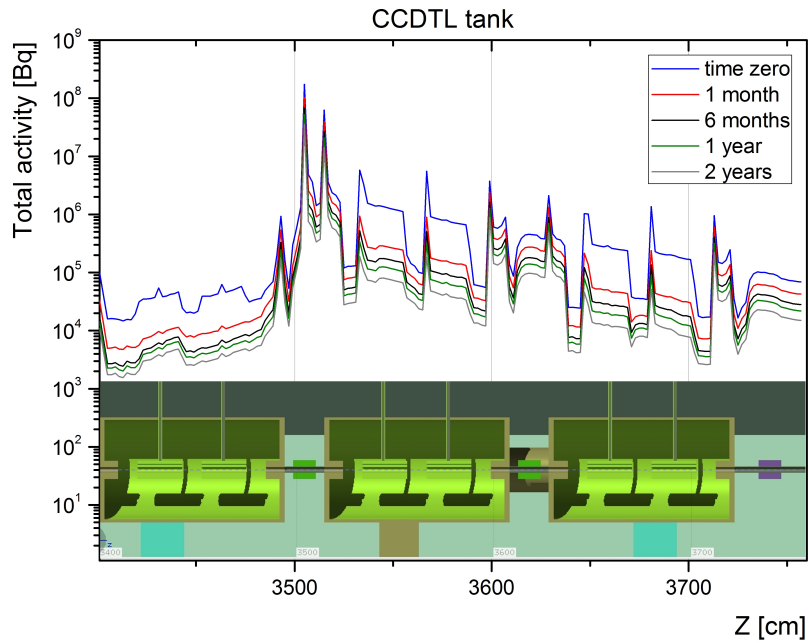


Figure 6.18: Profile of the total radioactivity in the fifth CCDTL module along the beam axis (z) for five decay times.

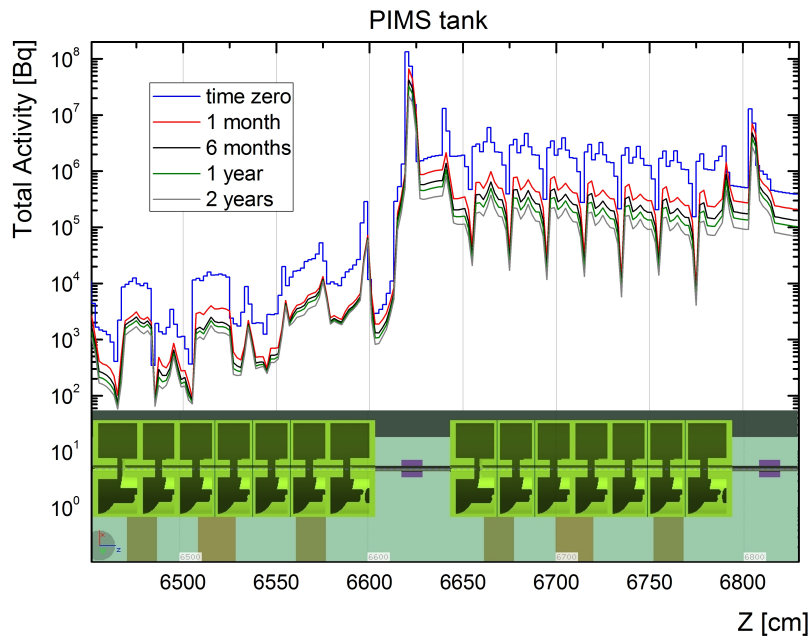


Figure 6.19: Profile of the total radioactivity in the 12th and 13th PIMS tank along the beam axis (z) for five decay times.

6.3 Estimation of residual dose rates

The ambient dose equivalent rate due to residual radioactivity was calculated along the beam axis both inside and at 10 cm distance from the tanks for 5 decay times: immediately after the end of the operation and after one month, six months, one year and two years. Each plot takes into account the dose rate due to the beam loss point under study and the two adjacent loss points, downstream and upstream. The dose rate plots for every cooling time and all machine sections can be found in Ref. [104].

6.3.1 Drift Tube Linac (DTL)

In the DTL section the dose rates are rather low due to the comparatively low beam energy. Figure 6.20 shows the dose rate inside the tank for 5 decay times. Dose rate peaks of about 100 $\mu\text{Sv/h}$ and 500 $\mu\text{Sv/h}$ can be observed at the beam impact points at 11 MeV and 31 MeV, respectively. The last peak is due to the dose rate from the downstream loss point at 57 MeV energy. Figure 6.21 shows the DTL dose rate at 10 cm from the tank. After one month of decay time the dose rate decreases below 1 $\mu\text{Sv/h}$ and never exceeds 10 $\mu\text{Sv/h}$ even immediately after shutdown. Figure 6.22 shows the dose rate plot calculated along the z-axis of the DTL section (top view, y-axis) after 6 months of cooling time.

6.3.2 Cell Coupled Drift Tube Linac (CCDTL)

Whereas the DTL quadrupoles are shielded by the drift tube and by the tank, the quadrupoles in the other sections of the accelerator are directly accessible. The ambient dose equivalent rate inside the CCDTL tank is showed in Figure 6.23. A dose rate of 10 mSv/h can be reached at the 80 MeV beam loss point, which is a critical location because of the permanent magnetic quadrupole (PMQ) near the vacuum chamber. Figure 6.24 shows that a few localized "hot spots" in correspondence of the quadrupoles can push the dose rate up to 100 $\mu\text{Sv/h}$ at 10 cm from the tank. On the other

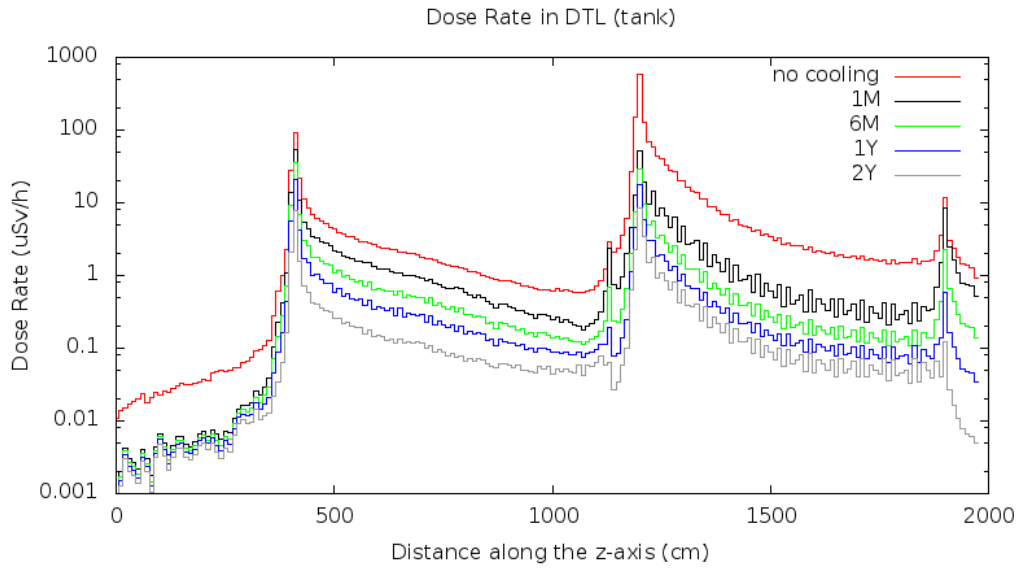


Figure 6.20: Ambient dose equivalent rate inside the DTL tank along the beam axis (z) for five decay times.

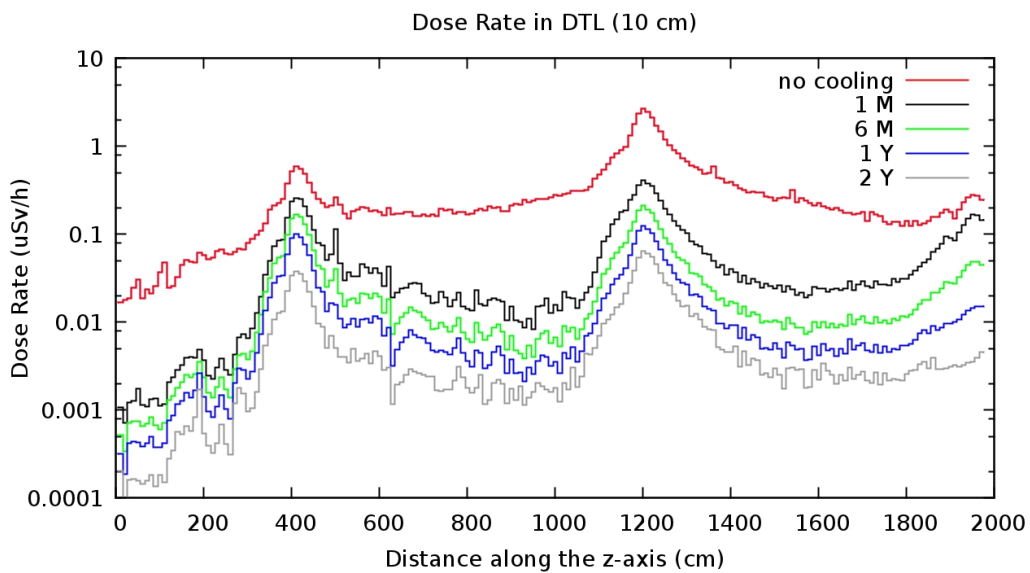


Figure 6.21: Ambient dose equivalent rate at 10 cm from the DTL tank along the beam axis (z) for five decay times.

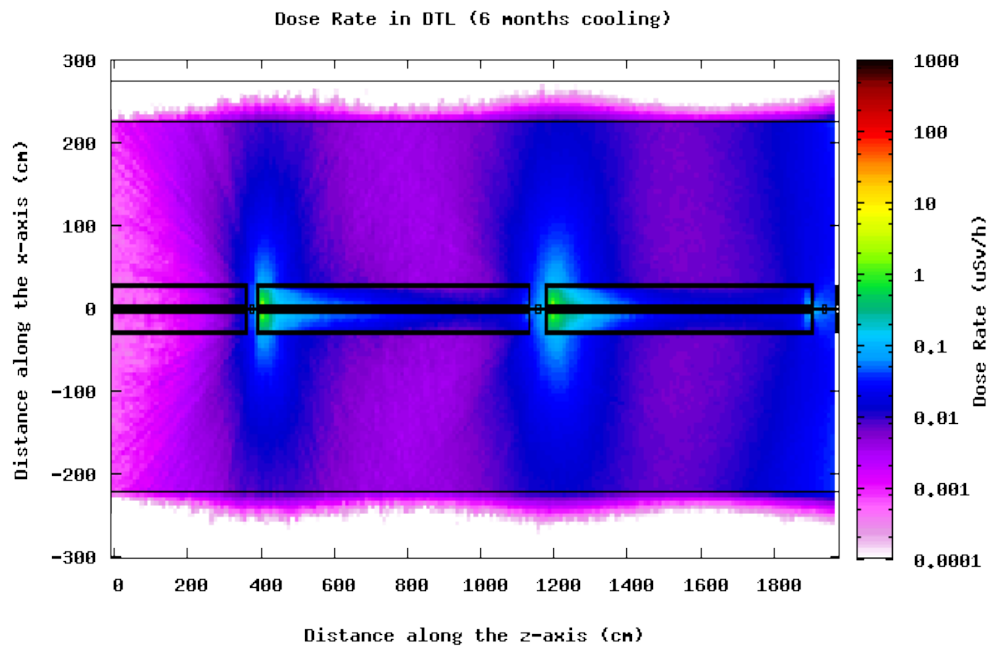


Figure 6.22: Ambient dose equivalent rate in the DTL section after 6 months of cooling time.

hand, the dose rate decreases quickly far from the beam loss points reaching $0.1 \mu\text{Sv/h}$ in just one month of cooling time. The difference in the dose rate between the first (EMQ) and the second (PMQ) activation point is rather due to the different material composition than to the difference in energy. Starting from 6 months of cooling time the dose rate peaks caused by the PMQ magnets along the CCDTL section are clearly visible. Figure 6.25 shows the dose rate plot calculated along the z-axis of the CCDTL section (top view, y-axis) after 6 months of cooling time.

6.3.3 Pi-Mode accelerating structure (PIMS)

In the PIMS structure the dose rate distribution is more uniform (Figure 6.26). Although the beam losses can occur at the maximum energy, the

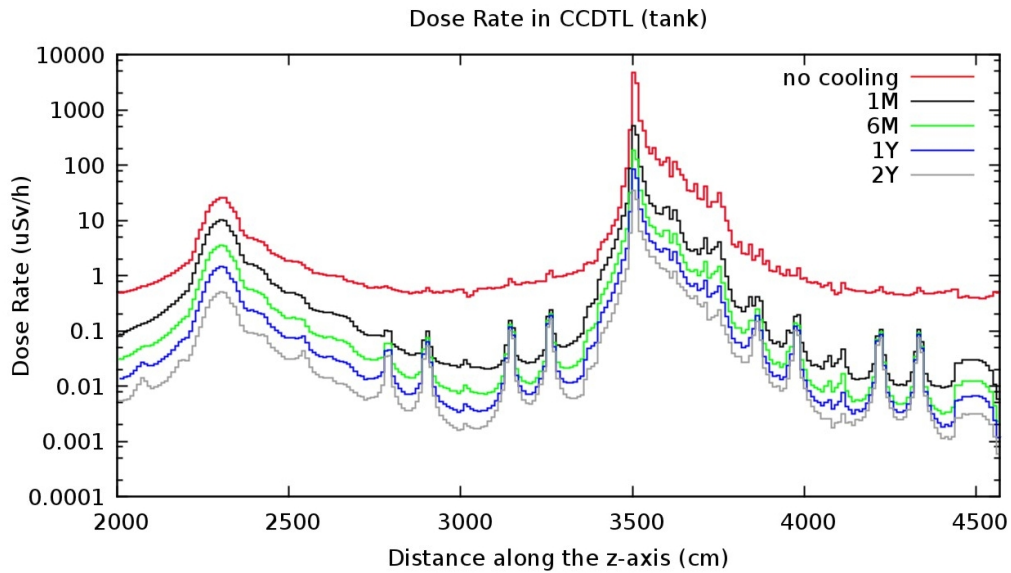


Figure 6.23: Ambient dose equivalent rate inside the CCDTL tank along the beam axis (z) for five decay times.

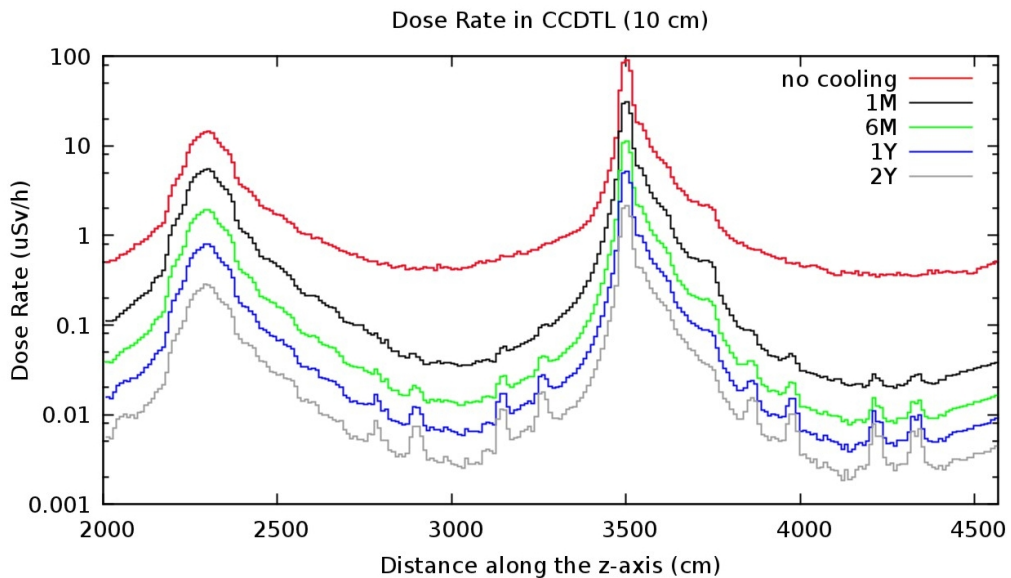


Figure 6.24: Ambient dose equivalent rate at 10 cm from the CCDTL tank along the beam axis (z) for five decay times.

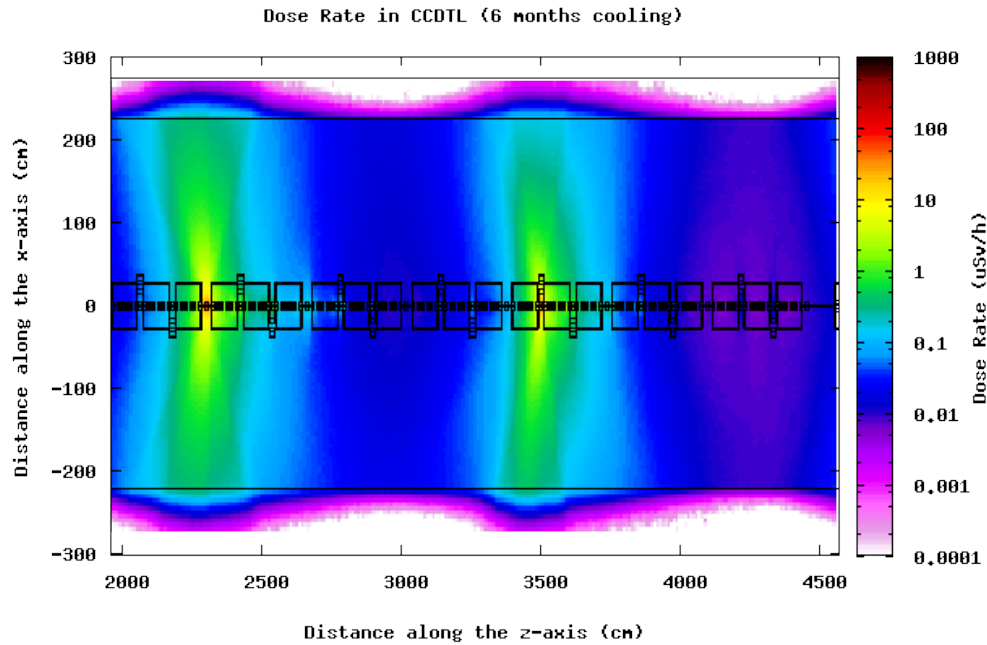


Figure 6.25: Ambient dose equivalent rate in the CCDTL section after 6 months of cooling time.

highest dose rate does not exceed $100 \mu\text{Sv/h}$ at 10 cm from the tank (Figure 6.27). Along the accelerating structure the dose rate varies in the range $0.01 - 1 \mu\text{Sv/h}$ after 2 years of decay time. Figure 6.28 shows the dose rate plot calculated along the z-axis of the PIMS section (top view, y-axis) after 6 months of cooling time.

6.4 Discussion

FLUKA simulations using a detailed geometrical model of the accelerator were carried out to predict the induced radioactivity in Linac4 after 30 years of operation and for various decay times. The following estimations were performed: residual radioactivity in the main accelerator components; comparison with current (Swiss) and future (CERN design) exemption limits;

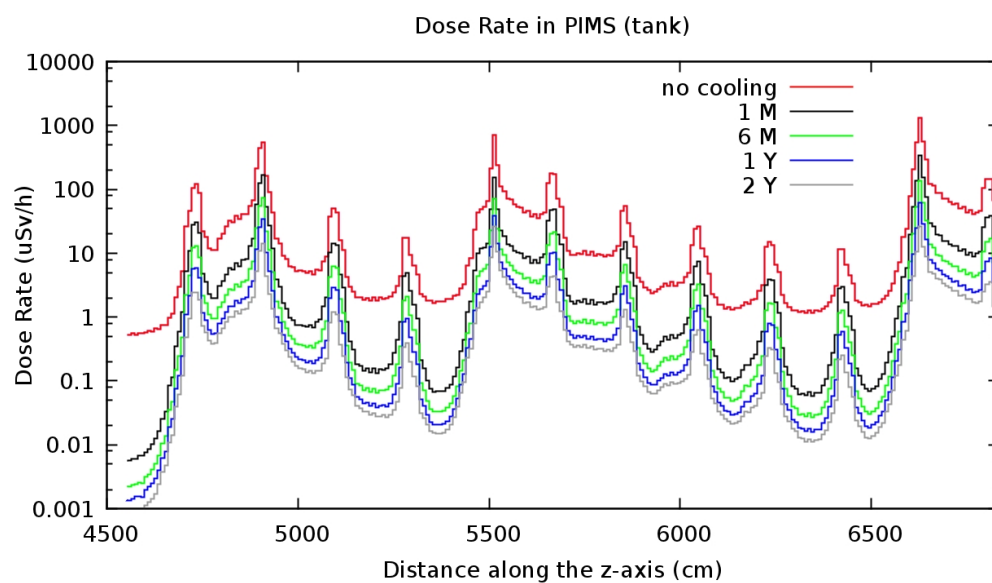


Figure 6.26: Ambient dose equivalent rate inside the PIMS tank along the beam axis (z) for five decay times.

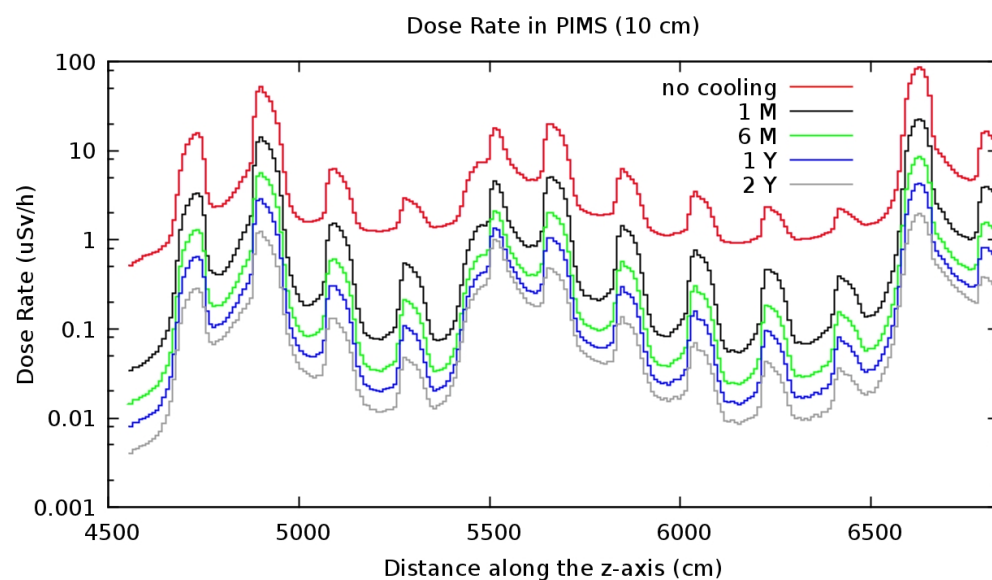


Figure 6.27: Ambient dose equivalent rate at 10 cm from the PIMS tank along the beam axis (z) for five decay times.

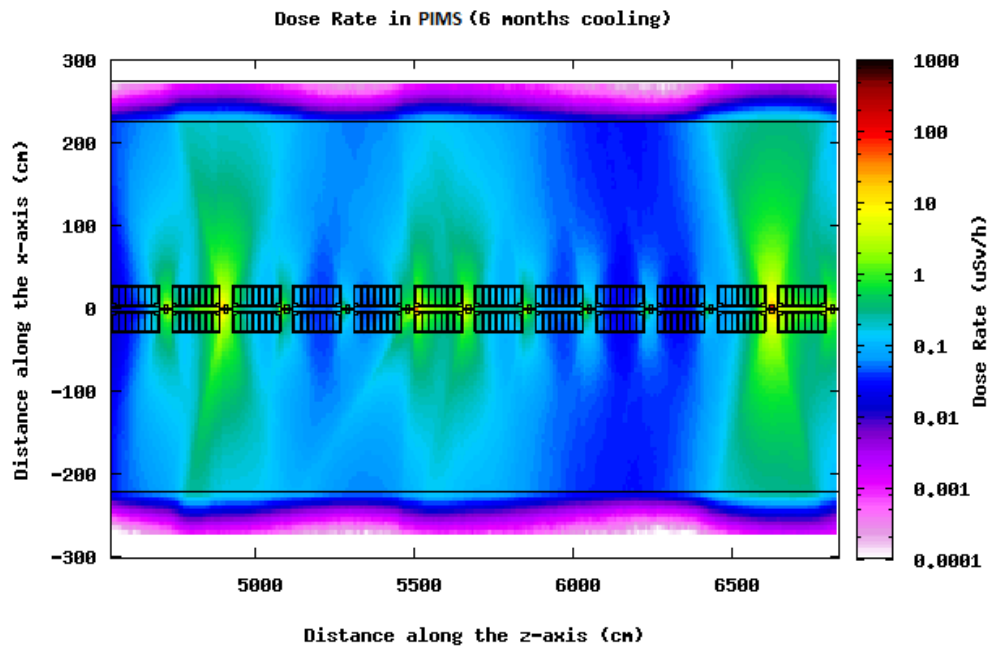


Figure 6.28: Ambient dose equivalent rate in the PIMS section after 6 months of cooling time.

profile of the total activity for the three beam loss points under study; dose rate in the whole accelerator structure for five cooling times (time zero, one month, six months, one year, two years); particle energy spectra (neutrons, protons and photons) at the beam impact points.

It is predicted that most of the components in the DTL can be dismantled soon after the final shutdown. The mean storage time required is two years for the vacuum chamber, 10 years for the drift tubes and 50 years for the PMQs. In the CCDTL the dismantling is recommended after two years of cooling. After 10 years about half of the accelerator components are below the exemption limits. The longest decay time foreseen is 100 years for the vacuum chamber. In the PIMS the dismantling should start after five years of cooling. Half of the PIMS components are expected to be below the limits after 20 years. The longest estimated decay time is 100 years for the vacuum

chamber. Dose rates at 10 cm from the tank vary in the range of 0.1 to 1 $\mu\text{Sv/h}$ for the DTL and between 1 $\mu\text{Sv/h}$ and 100 $\mu\text{Sv/h}$ for the CCDTL. Although the beam losses can occur at the maximum energy in the PIMS, the highest dose rate does not exceed 100 $\mu\text{Sv/h}$ at 10 cm from the tank.

It is important to point out that the values of the induced radioactivity predicted in this study were estimated for the most probable scenario available at the present time, i.e. 0.1 W of beam losses every 10 m for 30 year operation. In case of a different loss pattern, irradiation profile or machine operating parameters, one can expect a corresponding increase/decrease in beam losses and, therefore, in machine activation depending on the new scenario. It is most likely that the activation will not be uniformly distributed along the machine. The components indicated as activated in this study could in reality be only partially radioactive, depending on the distance from the beam loss points. It may be feasible that, at the time of dismantling, a given component is cut in pieces and that each piece is either disposed of as conventional waste or stored as radioactive. This is of course hard to predict at this stage and only operational radiation protection measurements on each machine components after the final shutdown will provide the real activation scenario and allow deciding e.g. on the required cooling time.

More details on the Linac4 study can be found in Refs. [104, 107, 108] and in the forth paper of the Appendix.

Conclusions

This thesis presents the study of induced radioactivity I carried out in different proton accelerator facilities. During my PhD work I studied in detail three selected cases using both computational (Monte Carlo and analytical) techniques and experimental measurements.

The first case was the analysis of the radiological status of the old CERN 600 MeV synchro-cyclotron 20 years after shutdown. Gamma spectrometry measurements were performed on concrete cores taken from various parts of the building walls. I calculated the activation products and the residual radioactivity in the barite walls using the FLUKA and JEREMY codes. The calculation was rather challenging due to the uncertainties in the FLUKA input values: irradiation conditions over 33 years of operation (from 1957 to 1990), size and elemental composition of the concrete samples, estimate of the beam losses and of their location with respect to the shielding walls, etc. The results of the simulations were compared with the gamma spectrometry measurements. In most cases the difference between measured and calculated value is within a factor of 2 for both codes, a rather remarkable agreement. These results demonstrate that both FLUKA and JEREMY can be successfully used to simulate the isotope production and the residual radioactivity with only a very approximate knowledge of the irradiation profile and after a very long (20 years) cooling time.

The second case under study was the activation of metallic and soil-shield samples. The main focus was set on the calculation of the cross sections of proton- and pion-induced spallation reactions on ^{nat}Cu and ^{nat}Fe

targets at 120 GeV. Since copper and iron are used in all accelerator facilities, these spallation reactions are of utmost importance in activation studies. The cross sections for the production of 14 radioisotopes in copper and 16 radioisotopes in iron were measured. The cross sections obtained in this thesis are totally "brand-new": data on proton-induced spallation reactions are only available at lower energies (below 30 GeV) and no data have been published for pion-induced reactions. To obtain accurate cross section measurements, the calibration factor of our primary beam monitor (an ionization chamber) was carefully verified via different techniques. The well-known $^{27}\text{Al}(p,3pn)^{24}\text{Na}$ monitor reaction was employed along with, for the first time, the $^{nat}\text{Cu}(p,x)^{24}\text{Na}$ as a promising reaction for beam monitoring. Their theoretical bases were explained in detail and the various factors to be taken into account for a proper calibration were discussed. The calibration factor estimated via FLUKA simulations is in excellent agreement, within the uncertainties, with those obtained with the activation experiments performed in this thesis work. These values are also in good agreement with the results obtained in the past with different techniques.

The activation of the soil-shield samples was performed at the H4IRRAD test facility at CERN. Gamma spectrometry and beta scintillation analysis were carried out to determine the radioactivity induced in the samples. I used FLUKA to benchmark the experimental results and to estimate the concentration of the ^3H in the soil. Two leaching procedures were employed and compared to quantify the amount of radioactivity leached out of the soil into the water. The mixing system was able to remove up to 39% of ^3H and 12% of ^{22}Na from the irradiated soil. The flowing system extracted 28% of ^3H and 11% of ^{22}Na . I was also able to distinguish the amount of tritium coming from the soil moisture and the one coming from the soil bulk. This was the first time that such a result could be obtained. For both systems the amount of tritium leached out was 100% of the tritium produced in the soil moisture, but only 31% (mixing) and 20% (flowing) of the tritium produced in the soil bulk.

Finally, I performed a detailed study to predict the induced radioactivity in the new CERN injector linac, Linac4, after 30 years of foreseen operation and for various decay times by FLUKA simulations. The induced radioactivity was estimated for the most probable scenario, i.e. 0.1 W of beam losses every 10 m for 30 year operation. Seven beam losses for the three main accelerating structures were simulated. For each position, my calculations also took into account the activation due to the two loss points upstream and downstream, a rather innovative approach in this type of study.

The results of this thesis provide with new insight into nuclear physics. They contribute to a better understanding of the nuclear processes leading to induced radioactivity in proton accelerator facilities. This study confirmed the prediction capabilities of the nuclear interaction models employed by FLUKA at the energies of interest. The new experimental cross sections obtained in this work at 120 GeV are comparable with the values available in the literature at the highest energies, i.e. around 20-30 GeV, confirming that the cross section is energy independent above a certain energy. This behaviour is coherent with the fact that above about a few hundred MeV, the total elastic and non-elastic cross sections for hadron-nucleus collisions are approximately constant as it is foreseen by many physical models.

Appendix

The publications related to this thesis are reprinted in this appendix. I am the corresponding and main author of papers 1 and 4.

1. P. Carbonez, F.P. La Torre, R. Michaud and M. Silari, *Residual radioactivity at the CERN 600 MeV synchro-cyclotron*, Nuclear Instruments and Methods in Physics Research A 694 (2012) 234-245.
2. A. Ferrari, F.P. La Torre, G.P. Manessi, F. Pozzi and M. Silari, *Monitoring reactions for the calibration of high-energy mixed hadron beams*, submitted to: Physical Review Special Topics - Accelerators and Beams, Ref. ZN10088 (2014).
3. A. Ferrari, F.P. La Torre, G.P. Manessi, F. Pozzi and M. Silari, *Spallation cross sections for ^{nat}Fe and ^{nat}Cu targets for 120 GeV/c protons and pions*, submitted to: Physical Review C, Ref. CN10349 (2014).
4. J. Blaha, F.P. La Torre, M. Silari and J. Vollaure, *Long-term residual radioactivity in an intermediate-energy proton linac*, submitted to: Nuclear Instruments and Methods in Physics Research A, Ref. NIMA-D-13-01100 (2013).



Contents lists available at SciVerse ScienceDirect

Nuclear Instruments and Methods in Physics Research A

journal homepage: www.elsevier.com/locate/nima

Residual radioactivity at the CERN 600 MeV synchro-cyclotron

P. Carbonez^a, F.P. La Torre^{a,b,*}, R. Michaud^a, M. Silari^a^a CERN, 1211 Geneva 23, Switzerland^b University of Bern, LHEP, Sidlerstrasse 5, 3012 Bern, Switzerland

ARTICLE INFO

Article history:

Received 28 March 2012

Received in revised form

19 July 2012

Accepted 1 August 2012

Available online 14 August 2012

Keywords:

Induced radioactivity

Residual radioactivity

Activation

FLUKA

Jeremy code

Gamma spectrometry

ABSTRACT

The 600 MeV synchro-cyclotron (SC) was the first accelerator that came into operation at CERN in 1957. It provided beams for CERN's first particle and nuclear physics experiments and operated for 33 years until it was shut down in 1990. In view of a planned partial decommissioning of the facility, a range of measurements were carried out to evaluate the levels of residual radioactivity in the accelerator and its surrounding after about 20 years of cooling time. Gamma spectrometry measurements were performed on 113 samples collected inside the three floors of the accelerator vault, on the cyclotron itself and on concrete samples taken from various parts of the building walls, up to a depth of 50 cm in the shield. About 40% of all samples contain traces of neutron-induced radionuclides, mainly ⁶⁰Co (in metals), ¹³³Ba, ¹³⁷Cs, ¹⁵²Eu and ¹⁵⁴Eu (in concrete). Values of specific activities range from 5 mBq/g to 781 Bq/g. The maximum activity induced in concrete was observed at the depth of 40 cm in the wall near the cyclotron extraction channel. The laboratory measurements were supplemented by in-situ gamma spectrometry performed with the ISOCS system. A complete dose rate survey was also performed yielding isodose maps of the three levels of the building. The isotope production and the residual radioactivity in the barite walls of the SC bunker were simulated with the FLUKA and JEREMY codes in use at CERN for predicting residual radioactivity in activated accelerator components, and the results compared with the gamma spectrometry data. A detailed comparison of calculated and measured specific activities shows generally good agreement, to within a factor 2 in most cases. These results serve as indirect validation of the capabilities of these codes to correctly predict residual radioactivity with only a very approximate knowledge of the irradiation profile and after a very long (20 years) cooling time. Overall the results provided in this paper may be of use for estimating residual radioactivity in proton accelerators of comparable energy and for benchmarking computer codes.

© 2012 Elsevier B.V. All rights reserved.

1. Introduction

The 600-MeV synchro-cyclotron (SC) was the very first accelerator designed and built at CERN. The accelerator energy was suggested by Enrico Fermi himself. The machine started operation in 1957, soon after CERN was founded, before the proton synchrotron (PS) was commissioned. Apart from an interruption to undergo a major upgrade in the early 1970s (which included the installation of a new axial ion source, radiofrequency system, magnet coils and vacuum chamber), the accelerator had been in operation for 33 years until it was shut down in 1990, providing experiments with proton, neutron, muon and pion beams. The first CERN ISOLDE facility was also served by the SC beam from 1967 until 1990, when it was moved to its present location at the PS Booster. During its 33 years of operation the accelerator has

produced a wealth of physics results, which are concisely summarised in the Proceedings of the SC 33 Symposium held at CERN in April 1991 [1]. Only to mention a few, the π -e ν decay experiment, the π^+ - π^0 decay experiment and the muon capture experiment. The two experimental rooms were decommissioned within a few years after shutdown, whereas the shielded vault housing the accelerator has remained untouched to allow for radioactive decay of its components. The building also served as a storage area for discarded equipment coming from the dismantled experimental areas.

In view of a partial decommissioning of the accelerator and related equipment, a thorough measurement campaign was conducted to evaluate the levels of residual radioactivity after about 20 years of cooling time. Induced radioactivity at particle accelerators is an important radiation safety issue for sorting out radioactive and conventional waste and for potential free-releasing metallic scrap. The main problem 20 years after shutdown is due to the presence of long-lived radionuclides, their activity concentration (specific activity) and, to a lesser extent, the related dose rate.

* Corresponding author at: CERN, Route De Meyrin, CH-1211, Genève 23, Switzerland.
Tel.: +41 227677752.

E-mail address: francesco.paolo.la.torre@cern.ch (F.P. La Torre).

This work is the first step of a larger project, the purpose of which is to finally convert the SC building into an exhibition hall open to the general public [2]. In order to achieve this goal, a complete radiological characterization of the accelerator vault, including laboratory and in-situ gamma spectrometry measurements with the ISOCs detector (In Situ Object Counting System), was performed. Radiation levels were surveyed and dose rate maps of the activated areas were drawn. One hundred and thirteen samples collected from the scrap material, the walls and the machine in the building were analyzed by gamma spectrometry. This measurement campaign provided information on the proper measures that will have to be taken at the time of decommissioning, on the amount of scrap material that can be expected to be radioactive and on the radionuclide inventory in the material to be removed, information which is needed for its elimination towards a final repository. The residual nuclei produced in the shielding walls and their activities were calculated with the Monte Carlo code FLUKA [3,4] and the analytical code JEREMY [5]. The calculations were performed at the approximate locations where core samples were taken from the shielding walls (see Section 3), in order to allow a direct comparison of experimental data and predictions. The results of the calculations and of the gamma spectrometry are compared and discussed.

The experimental and computational results provided in this paper are intended to be of use for estimating residual radioactivity in proton accelerators of comparable energy, for providing guidelines for similar dismantling project and for benchmarking predictive tools, be Monte Carlo or analytical codes.

2. The radiological situation

2.1. Twenty years ago

When the SC was closed at the end of 1990 after 33 years of service, there were comparatively high levels of induced radioactivity around the accelerator, with the presence of isotopes with half-lives of several years. The accelerator was not constructed to be readily dismantlable, the vacuum chamber being welded to the magnet pole pieces. There were radioactive parts which needed special consideration. In case of decommissioning, the need to physically separate the vacuum chamber from the magnet assembly was in contrast with the comparatively high induced radioactivity and the contamination of parts of the installation. A subsidiary problem was that all the large steel blocks forming the magnet yoke were tack welded together as well as being bolted.

In November 1991, eleven months after the end of operation, a radiological survey was carried out, when all machine components were still in place [6]. Fig. 1 shows a map of the residual dose rate inside the SC hall measured at that time. Dose rates varied between 0.5 mSv/h at 40 cm from the entrance of the vacuum chamber and 1 mSv/h all around the vacuum chamber. Higher values were present inside the chamber. The dose rate inside the SC hall varied from a minimum of 10 μ Sv/h far from the machine up to a maximum of 150 μ Sv/h near the proton and neutron beam lines.

The long-term problem of induced radioactivity in accelerators is of course created by the presence of long lived radionuclides, the majority of which have half-lives of several years. Using decay-corrected dose rates measured after different decay periods, it was estimated that one would have had to wait until the year 2079 before the specific activity of ^{60}Co inside the SC vacuum chamber would have fallen below 2 Bq/g [7,8], the reference value for free release at that time. Pros and cons of various options were considered in 1991 and it was finally decided to wait for a sufficient number of years to allow for radioactive decay.

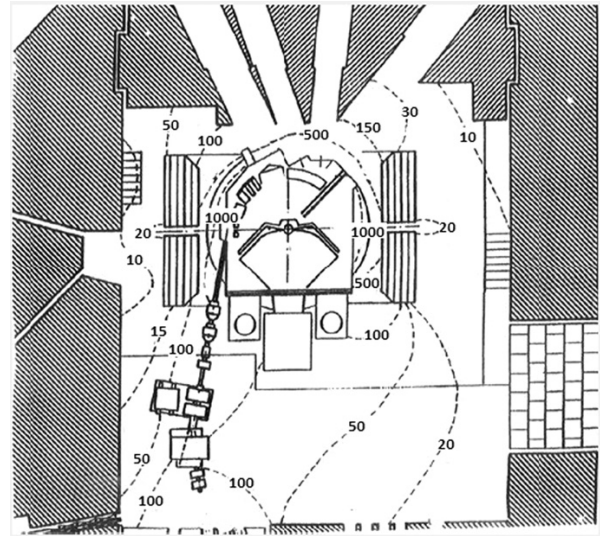


Fig. 1. Dose rate (μ Sv/h) eleven months after the machine shutdown [6].

2.2. The present situation

From a radiation protection point-of-view, after a decay period of 20 years there is no justification to wait further for decommissioning the facility. All short- and medium-lived radionuclides have either disappeared or decayed below undetectable levels, whilst the long-lived ones will not decay substantially over the next 10 or 20 years. As mentioned above, since the SC was shut down in December 1990, the shielded vault housing the accelerator has remained locked. In the mid-90's the two experimental rooms were decommissioned, and the buildings surrounding the accelerator vault refurbished and converted into office space.

The major piece of equipment present in the accelerator vault is the cyclotron itself. The heaviest component is the magnet, which consists of approximately 2500 t of iron. A complete decommissioning of the facility that implies the removal of the accelerator will be much more expensive than a partial decommissioning that foresees the elimination of all material present in the hall except for the accelerator (magnet, coils, RF system, ion source and vacuum system), followed by a clean-up (both radiological and conventional) of all equipment that is left in place. As the SC is an important piece of CERN history, it has been decided that the building, the accelerator and other historical equipment, properly cleaned, will be converted into a public exhibition hall.

The synchro-cyclotron building consists of three levels: the ground floor at street level, which corresponds to the accelerator mid-plane with the extraction beam lines; the underground level-1 that accommodates the bottom part of the machine; the underground level-2 housing the axial support of the ion source and the hydraulic bearing of two mobile shielded walls.

The rest of the paper describes the measurements undertaken to characterize the present radiological status of the SC hall and to benchmark computer codes used for estimating residual radioactivity.

3. Radiation levels: Isodose maps

The dose rates inside the three floors and on the walls of the accelerator vault were surveyed with an Automess 6150 AD6 GM survey meter. In order to reach uncomfortable locations, a telescoping

probe extendible to a length of approximately 4 m (Teletector 6150 ADT) was used, measuring both photon and beta radiation.

The ambient dose equivalent rate inside the whole building was measured so as to draw a map of the activated areas. Fig. 2 shows the isodose curves measured on the ground floor of the SC hall where the cyclotron mid-plane and the extraction channels are located. On this floor the dose rate varies between a minimum of $0.5 \mu\text{Sv/h}$, near the access staircase, and a maximum of $200 \mu\text{Sv/h}$ inside the cyclotron vacuum chamber. The highest dose rates are expected from elements having been exposed to the proton beam and to stray neutrons inside the chamber, like the acceleration electrode (the so-called “dee”), the internal target supports and platform, the probe and diagnostic targets, the coil, the ion source and the extraction channel. It is known from measurements that the level of the gamma radiation field is highest between the pole pieces, and that the proton beam that is scattered in all directions when it passes through the target, is absorbed by the dee and the pole faces of the cyclotron. Thus it is natural to assume that the iron of the magnet poles and the copper of the dee are the most radioactive parts of the machine [9].

Concerning the walls of the SC vault, the highest values of dose rate were found close to the north ($\sim 20 \mu\text{Sv/h}$) and south walls ($\sim 10 \mu\text{Sv/h}$). There are basically two reasons for this: first, these walls were traversed by the SC extracted beams, the neutron and proton beams in the north and south wall, respectively, with beam losses occurring during particle transport. Second, these walls are made of heavy barite concrete in which long-lived radionuclides (e.g., ^{133}Ba) have accumulated (see Section 5).

All around the machine, the mean radiation level is only $1 \mu\text{Sv/h}$ to $2 \mu\text{Sv/h}$, except for some “hot spots” near radioactive scrap material with a dose rate peak of $160 \mu\text{Sv/h}$ or close to a locker containing radioactive equipment. No dose rate measurements could be made just in front of the machine close to the large vacuum pumps, because of material interposed there and obstructing the access.

The level-1 contains the present entrance to the SC vault (on the east side of Fig. 3). Here the mean dose rate is $\sim 0.5 \mu\text{Sv/h}$. This location is heavily shielded by the magnet yoke and there is no radioactive scrap material present. Slightly higher radiation levels,

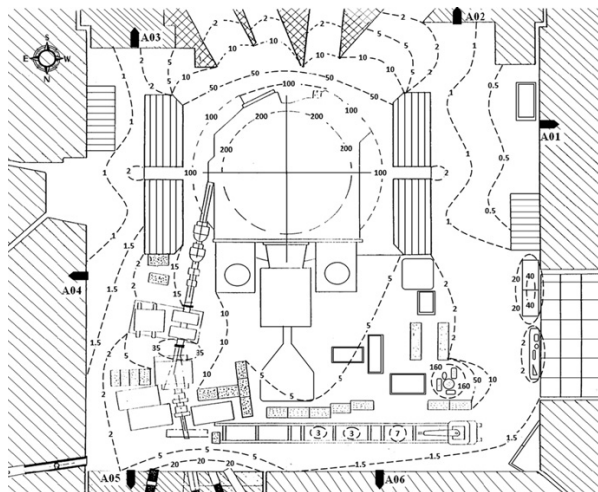


Fig. 2. Isodose curves ($\mu\text{Sv/h}$) on the SC level 0 (ground floor), measured in December 2010. The locations where concrete samples were taken are also shown (A01 to A06). Note that the North points to the bottom of the figure. This drawing reproduces the geometry of the SC hall at the end of 1990. The sketches in the following Fig. 3 (level-1) and 4 (level-2) were obtained from this figure.

of the order of $1\text{--}2 \mu\text{Sv/h}$ are found near the vacuum pumps and the highest, about $5 \mu\text{Sv/h}$, in contact with them. Only one “hot spot” of $\sim 1.6 \mu\text{Sv/h}$ is found far from the machine on a workdesk near the west wall (Fig. 3), hosting radioactive equipment.

The lowest level-2 has an ambient dose rate very low, about $0.1 \mu\text{Sv/h}$, approximately equal to the natural background ($\sim 0.08 \mu\text{Sv/h}$). Inside the small room located underneath the accelerator and housing the axial ion source, the radiation levels are even lower, about $0.05 \mu\text{Sv/h}$. The dose rate values increase inside a room located on the south side of the vault (top of Fig. 4, not shown in the figure) housing the hydraulic bearing of the two movable neutron-shielding walls. Here two cupboards containing old radioactive equipments show a dose rate of up to $15 \mu\text{Sv/h}$. At the opposite side of this level, on the north side, there is a small room also not showed in Fig. 4 housing the proton transfer line from the SC to the old ISOLDE facility. Here, a dose rate of up to $5 \mu\text{Sv/h}$ was measured near the transfer line components.

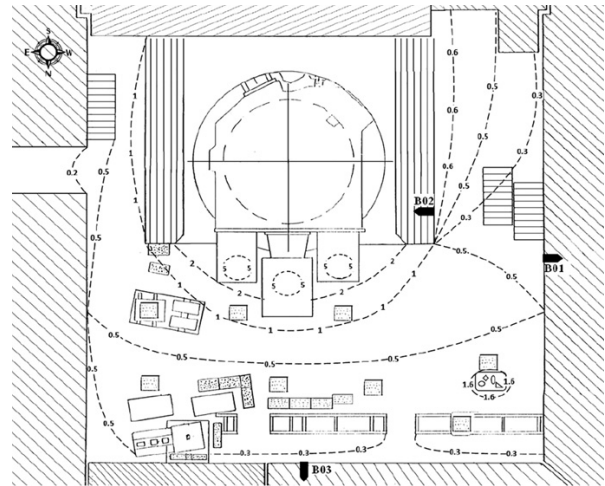


Fig. 3. Isodose curves ($\mu\text{Sv/h}$) on the SC underground level-1 measured in December 2010. The locations where concrete samples were taken are also shown (B01 to B03).

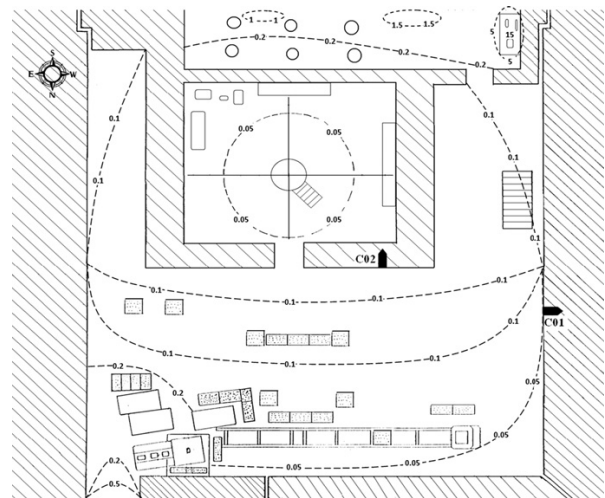


Fig. 4. Isodose curves ($\mu\text{Sv/h}$) of the SC underground level-2 measured in December 2010. The locations where concrete samples were taken are also shown (C01 and C02).

4. Specific activity in material samples

Between July and December 2010, 113 samples were collected from the three levels of the SC building and analyzed by γ -spectrometry. Among these samples, 69 were represented by metallic parts, plates and blocks, pipe clumps, knobs, plugs and connectors, screw bolts, washers and nuts, cable hooks and one sample of oil used in the accelerator, picked up from scrap material or taken from the machine (approximately 20 samples per floor). The remaining 44 were concrete samples extracted from the SC walls. Gamma spectrometry measurements were performed using an extended range coaxial Ge detector (XtRa Canberra, 2 keV FWHM at 1.33 MeV, relative efficiency $\geq 40\%$) and a coaxial Ge detector (Canberra, 1.8 keV FWHM at 1.33 MeV, relative efficiency $\geq 40\%$) of the ISOCs station. The counting time ranged between a few minutes and several hours depending on the residual radioactivity of the sample.

Table 1 lists the radionuclides identified along with their half-life, the number of samples containing each given radionuclide and the sample material. For each radionuclide the table gives the minimum and maximum specific activity detected in the samples. The main radionuclide detected in almost every sample is ^{60}Co . The activity of this radionuclide accounts for most of the residual radioactivity in the machine and in the surrounding material due to the large neutron capture cross-section of the $^{59}\text{Co}(n,\gamma)^{60}\text{Co}$ reaction.

The most recurrent radionuclide observed after ^{60}Co is ^{44}Ti . This radionuclide is very common in an accelerator environment. Steel, although mainly consisting of iron, exists in many different compositions including elements heavier than ^{44}Ti . Stainless steel also contains various fractions of natural chromium. Furthermore, in accelerator materials one can find titanium, vanadium and chromium in the form of impurities. Therefore, ^{44}Ti can easily be produced from isotopes of these elements in spallation and fragmentation reactions. ^{44}Ti has a half-life of about 60 years and decay by electron capture, which in itself is very difficult to detect, but it decays to the excited state of ^{44}Sc , which has a much shorter half-life, with its own gamma and positron emissions. Since a longer half-life means a lower production rate and thus a lower specific activity, one usually sees the pair $^{44}\text{Ti}/^{44}\text{Sc}$ in radioactive materials that have been cooling down for several years, when the shorter-lived radionuclides have been reduced significantly.

The relatively short half-life of ^{22}Na ($t_{1/2}=2.6$ yr) compared to the cooling period (~ 20 yr) is responsible for the detection of a small amount of this radionuclides in two cases only. ^{22}Na is typically produced via the $^{23}\text{Na}(n,2n)^{22}\text{Na}$ reaction induced by fast neutrons.

Traces of ^{26}Al were found in one sample. This is a block fully made of aluminium, found in the vault but probably coming from inside the accelerator. This could explain the presence of ^{26}Al , which

is produced via the $^{27}\text{Al}(p,pn)^{26}\text{Al}$ and $^{26}\text{Mg}(p,n)^{26}\text{Al}$ reactions by high-energy protons. Indeed, most aluminium alloys use magnesium as an alloying element in order to improve the material strength. Another possible production reaction is $^{27}\text{Al}(n,2n)^{26}\text{Al}$.

^{42}Ar was detected in one sample, which is the most active sample collected with its 781 Bq/g of ^{60}Co and 89.3 Bq/g of $^{44}\text{Ti}/^{44}\text{Sc}$ (Table 1). Because of the long half-life of the argon radionuclide ($t_{1/2}=32.3$ yr), one usually sees $^{42}\text{Ar}/^{42}\text{K}$. This sample is a block fully made of copper certainly coming from inside the cyclotron (due to its high dose rate of ~ 30 $\mu\text{Sv/h}$), since a way to produce ^{42}Ar from copper is through spallation reactions induced by high-energy protons [10]. This kind of reactions was employed at the synchro-cyclotron, where targets of different materials (including copper) were bombarded by 600 MeV protons in order to estimate rare gas production cross-sections [11].

^{152}Eu and ^{154}Eu were only detected in one sample, an electronic component with ceramic cover. The europium isotopes evidently come from neutron capture on trace amounts of ^{151}Eu and ^{153}Eu .

Far less expected was the presence of the long-lived mercury radioisotope ^{194}Hg with a half-life of 444 years, which is most probably due to past experiments employing this radioisotope at the former ISOLDE facility [12]. In 1980 the 600 MeV proton beam was used to bombard a molten Pb target via spallation reactions and produce, among others isotopes, ^{194}Hg which is volatile. Due to the long half-life the radionuclide detected was ^{194}Au ($t_{1/2}=38$ h), daughter nuclide of ^{194}Hg .

In summary, of the 69 samples collected, only 19 contain at least one radionuclide with a specific activity higher than 1 Bq/g (the exemption limit given in the Swiss legislation [13] for most radionuclides found in particle accelerator structures) and among these, only 6 were fixed to the building or to the machine and thus certainly belonging to the SC vault.

5. ISOCs measurements

The ISOCs (In-Situ Object Counting System) γ -spectrometer, a portable coaxial Ge detector (Canberra, 1.8 keV FWHM at 1.33 MeV, relative efficiency $\geq 40\%$) was used to obtain a qualitative estimation of the radionuclides present in the synchro-cyclotron vault. The ISOCs measurements were performed at level-1 of the SC building, "looking" at the machine components as well as at the walls. This level was chosen because of the presence of too much radioactive scrap material on the ground floor (level 0) and of the very low radiation levels on the underground level-2. Fig. 5 illustrates where the measurements were performed and the approximate ISOCs field-of-view.

Seven measurements were performed with the 30 degrees shield collimator to minimize the interfering radiation. The results are given in Table 2, confirming the γ -spectrometry

Table 1

List of the radionuclides measured in the 113 samples collected inside the SC vault. For ^{60}Co and $^{44}\text{Ti}/^{44}\text{Sc}$ the maximum value found in one single sample coming from inside the accelerator is given in brackets.

Radionuclide	$t_{1/2}$ (years)	Number of samples	Range of specific activity (Bq/g)		Material
			Minimum	Maximum	
Co-60	5.27	55	0.05 \pm 0.01	40 \pm 4 (781 \pm 47)	Iron/steel
Ti-44/Sc-44	60.0	4	0.020 \pm 0.005	0.15 \pm 0.04 (90 \pm 9)	Iron/steel
Ar-42/K-42	32.3	1	12.6 \pm 3.6*	12.6 \pm 3.6*	Copper
Na-22	2.60	2	0.010 \pm 0.005	1.52 \pm 0.02	Aluminium
Hg-194/Au-194	444	2	0.020 \pm 0.005	0.9 \pm 0.1	Stainless steel
Eu-152	13.5	1	0.30 \pm 0.03	0.30 \pm 0.03	Ceramic/electronic
Eu-154	8.59	1	0.030 \pm 0.004	0.030 \pm 0.004	Ceramic/electronic
Al-26	7.4E+5	1	0.002 \pm 0.001	0.002 \pm 0.001	Aluminium

measurements of material samples discussed in Section 4. About the same radionuclides found in the samples were identified by ISOCS at the same places where the samples were collected.

Only for the ISC-01, ISC-02 and ISC-07 measurements it was possible to define a geometry template for ISOCS, in order to obtain a quantitative analysis. It should be pointed out that the parameters used in the geometry template (such as wall density and depth) were approximate values and thus the specific activity obtained is only an estimate of the exact values that were found with the laboratory γ -spectrometry.

6. Specific activity in concrete

During operation of an accelerator, the shielding walls are activated by secondary particles, mainly neutrons, produced by nuclear reactions on targets and at beam loss points during acceleration, extraction and transport of the particle beam. Although the specific activity of the radioisotopes induced in materials surrounding the accelerator is generally low, the amount of activated material could be rather large. The residual

radioactivity in the concrete shields of the SC was also determined by γ -spectrometry.

A total of 11 concrete cores were taken, 9 of which from the walls and 2 from the SC basement. The cores were distributed as follows: 6 at ground level (Fig. 2), 3 at underground level-1 (Fig. 3) and 2 at underground level-2 (Fig. 4). The concrete cores were 50 cm deep and 5 cm in diameter. Each core was cut in slices of about 10 cm thickness. In all, 44 concrete samples were analyzed.

The main radioisotopes found in concrete are ^{133}Ba , ^{152}Eu , ^{154}Eu , ^{137}Cs and ^{60}Co (Tables 3 and 4). The east, north and south walls at the SC ground floor are made of barite concrete, which has improved shielding properties as compared to ordinary concrete but worst features concerning activation. All samples taken from the barite concrete walls show some residual radioactivity. ^{133}Ba and ^{137}Cs were only detected in barite concrete.

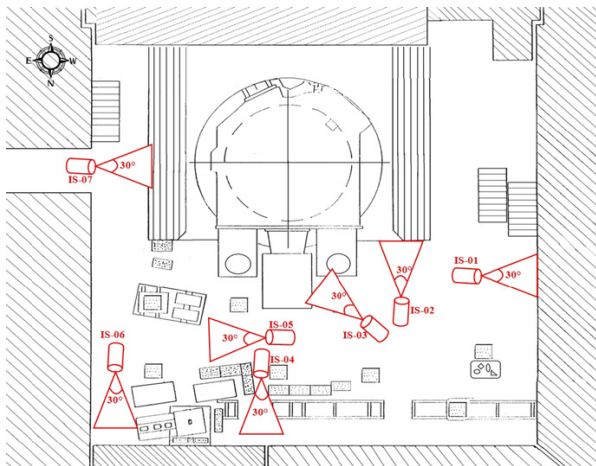


Fig. 5. ISOCS measurements on the SC underground level-1.

Table 2

Radionuclides identified with the ISOCS system on SC level-1.

Position	Description	Material composition	Radionuclide	$t_{1/2}$ (years)	Activity (Bq/g)
ISC-01	West wall	Concrete	Co-60	5.27	1.5 ± 0.2
			Eu-152	13.5	0.8 ± 0.1
			Ti/Sc-44	63.0	0.07 ± 0.02
			Na-22	2.6	0.04 ± 0.01
ISC-02	Accelerator (North side)	Iron/concrete	Co-60	5.27	9 ± 1
			Eu-152	13.5	1.2 ± 0.2
			Na-22	2.6	0.004 ± 0.003
ISC-03	Vacuum pumps	Iron/steel	Co-60	5.27	Qualitative
ISC-04	Generators	Iron/concrete	Eu-152	13.5	Qualitative
			Eu-152	13.5	Qualitative
			Na-22	2.6	Qualitative
ISC-05	Passageway	Iron/concrete	Co-60	5.27	Qualitative
			Eu-152	13.5	Qualitative
			Na-22	2.6	Qualitative
ISC-06	Corner	Iron/concrete	Co-60	5.27	Qualitative
			Eu-152	13.5	Qualitative
			Hg/Au-194	444	Qualitative
			Na-22	2.4	Qualitative
			Co-60	5.27	0.010 ± 0.001
ISC-07	Accelerator (East side)	Iron/steel	Co-60	5.27	

Table 3

List of radionuclides detected in the barite concrete samples (level 0).

Radionuclide	$t_{1/2}$ (years)	Number of samples	Range of specific activity (Bq/g)	
			Minimum	Maximum
Ba-133	10.5	29	0.33 ± 0.04	116 ± 12
Eu-152	13.5	29	0.05 ± 0.01	20 ± 2
Cs-137	30.1	29	0.05 ± 0.01	18 ± 3
Eu-154	8.59	20	0.010 ± 0.002	1.0 ± 0.1
Co-60	5.27	25	0.010 ± 0.005	0.22 ± 0.02
Na-22	2.6	9	0.005 ± 0.003	0.06 ± 0.02
Cs-134	2.06	8	0.005 ± 0.002	0.04 ± 0.01

Table 4

List of radionuclides measured in ordinary concrete (levels 0, -1 and -2).

Radionuclide	$t_{1/2}$ (years)	Number of samples	Range of specific activity (Bq/g)	
			Minimum	Maximum
Eu-152	13.5	9	0.010 ± 0.002	0.18 ± 0.02
Co-60	5.27	9	0.005 ± 0.001	0.010 ± 0.002
Eu-154	8.59	1	0.010 ± 0.003	0.010 ± 0.003
Na-22	2.6	2	0.005 ± 0.003	0.005 ± 0.003

The activation of trace elements (e.g., europium) and of metals in sand yields long-lived radionuclides. These are mainly created by neutron capture with high cross-sections and by threshold reactions with lower yield. Because of the high cross-section of ^{151}Eu for thermal neutrons and the long half-life of ^{152}Eu , this radionuclide is present in large quantities in activated concrete. ^{152}Eu was observed in all concrete samples, without exception, while only 21 samples contain ^{154}Eu . The most probable production reactions are $^{151}\text{Eu}(n,\gamma)^{152}\text{Eu}$ and $^{153}\text{Eu}(n,\gamma)^{154}\text{Eu}$. The several-year half-lives ($t_{1/2} (^{152}\text{Eu})=13.5$ yr and $t_{1/2} (^{154}\text{Eu})=8.6$ yr) and very large capture cross-sections for thermal neutrons greatly enhance the sensitivity with which even minute concentrations of Eu in the concrete is revealed after many years of exposure to neutrons.

The presence of the caesium isotopes ^{137}Cs and ^{134}Cs was also detected in barite concrete. The first radionuclide comes from neutron capture on trace amounts of ^{136}Ba and ^{137}Ba via the $^{136}\text{Ba}(n,\gamma)^{137\text{m}}\text{Ba}$ and $^{137}\text{Ba}(n,p)^{137}\text{Cs}$ reactions (one should remember that the 662 keV gamma of ^{137}Cs actually comes from $^{137\text{m}}\text{Ba}$), respectively, whereas ^{134}Cs is produced via the $^{134}\text{Ba}(n,p)^{134}\text{Cs}$ reaction and the $^{133}\text{Cs}(n,\gamma)^{134}\text{Cs}$ reaction on trace amounts of ^{134}Ba and ^{133}Cs , respectively. ^{137}Cs was detected in a larger number of samples (29 samples) compared to ^{134}Cs (8 samples). This gap can be explained by the large difference in their half-lives: $t_{1/2} (^{137}\text{Cs})=30.1$ yr compared to $t_{1/2} (^{134}\text{Cs})=2.06$ yr.

It should be noted that although concrete is typically composed of 1.7% sodium, only a small amount of ^{22}Na was detected, because of its comparatively short half-life ($t_{1/2}=2.6$ yr). It is possible that this radionuclide is produced in $^{23}\text{Na}(n,2n)^{22}\text{Na}$ reactions, but it may also come from the $^{27}\text{Al}(n,2p4n)^{22}\text{Na}$ spallation reaction, a reaction frequently used in activation detectors.

Figs. 6–8 show the activity depth profiles of the main radionuclides observed in barite concrete collected from the east, south and north walls, respectively. The most activated core was the A-05 sample, extracted from the north wall, near the proton transfer line (Fig. 2). The results of the gamma spectrometry for this sample indicates that the specific activity of long-lived radionuclides such as ^{133}Ba , ^{137}Cs and ^{60}Co peaks at a depth of about 35 cm and decrease to a lower level over a depth of 45 cm. The maximum activity is 116 Bq/g for ^{133}Ba . This means that fast neutrons from the beam loss point are slowed down inside the concrete and the thermal neutron component increases up to a depth of about 35 cm. The europium radioisotopes show a more

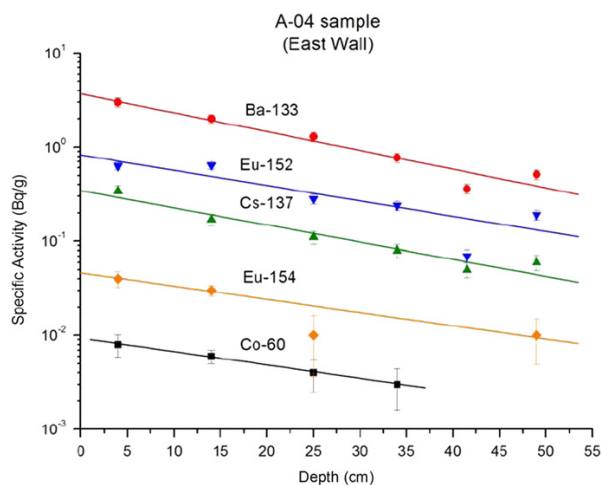


Fig. 6. Depth profile of the residual radioactivity in the east wall made of barite concrete (see Fig. 2).

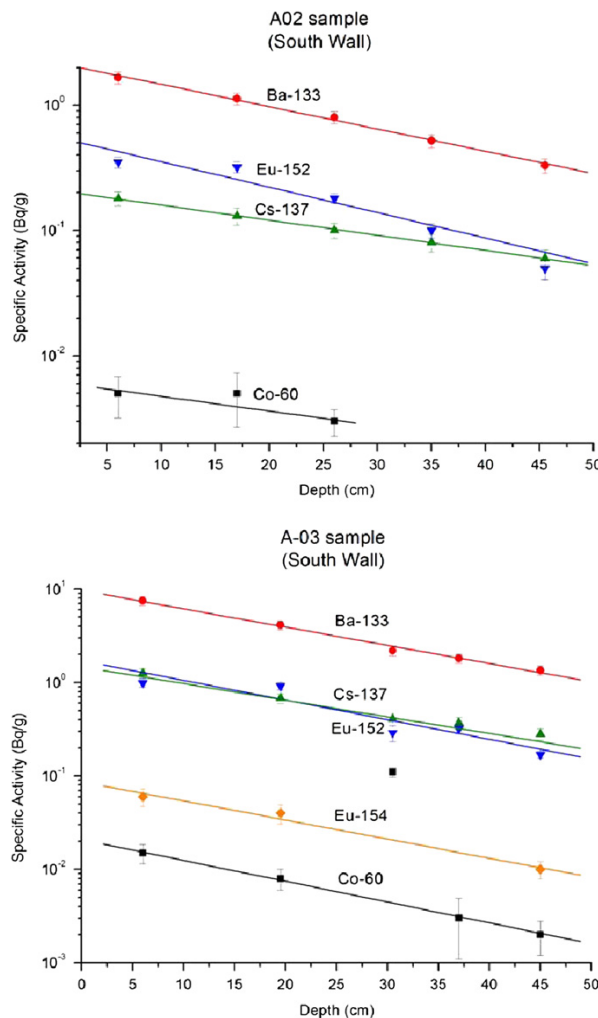


Fig. 7. Depth profile of the residual radioactivity in the south wall made of barite concrete (see Fig. 2).

complicated depth profile: a peak at a depth of 10 cm to 20 cm followed by a decrease, then the activity seems to increase again to a maximum value at 45 cm. This behaviour is not easy to explain. Sample A-05 was the only core where ^{134}Cs and ^{22}Na were detected at each depth in the wall. ^{134}Cs has a maximum value at the surface and then it seems to stay constant. However, the uncertainty is very large, because of its MDA (minimum detectable activity). The radioactivity of ^{22}Na induced by fast neutrons is the highest at the concrete surface and slowly decreases deep into the wall.

In the remaining barite concrete samples only radionuclides induced by thermal neutron capture reactions, which decrease exponentially with depth, were detected. The attenuation curves of ^{152}Eu and ^{137}Cs are similar.

Sample A-03 in Fig. 7 shows a clear peak of ^{60}Co at 30 cm depth, which is due to a steel bar in the concrete. In fact, because concrete is reinforced with steel bars, some pieces of steel were extracted during the concrete core drilling. In one of the samples $^{44}\text{Ti}/^{44}\text{Sc}$, which is normally found in metallic samples, was detected.

Summarizing, of the 44 concrete samples analyzed, only 24 have at least one radionuclide with a specific activity higher than 1 Bq/g and all of these are made of barite concrete.

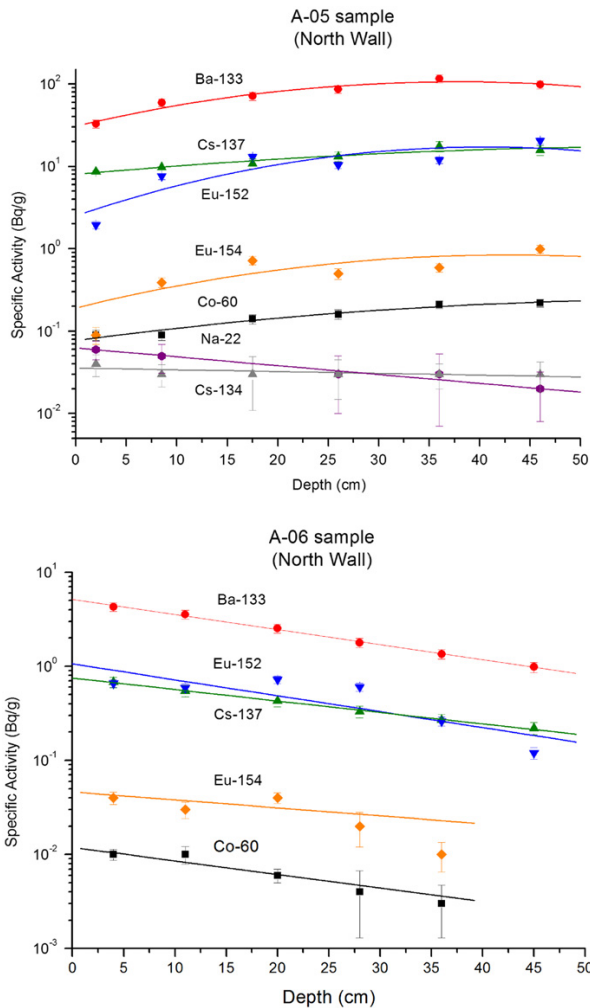


Fig. 8. Depth profile of the residual radioactivity in the north wall made of barite concrete (see Fig. 2).

7. FLUKA and JEREMY calculations

The residual nuclei produced in the shielding walls and their activities were calculated with the Monte Carlo code FLUKA [3,4] and the analytical code JEREMY [5]. FLUKA is a multiparticle transport and interaction Monte Carlo code, covering an extended range of energies (from thermal to cosmic ray energies), particles (hadrons, heavy ions and leptons) and materials. FLUKA is one of the best validated Monte Carlo codes and it is extensively employed for a wide range of applications, among which the prediction of induced radioactivity in accelerator environments [14–17].

JEREMY is an analytical code which computes the radionuclide inventory of objects exposed to the radiation fields in particle accelerators. The approach chosen for the computation of the induced radioactivity is based on two steps. First, the particle spectra of the radiation environment must be known, either experimentally or calculated (by FLUKA in the present case, as explained below). Given the fluence spectra as input, the radioactivity build-up and decay are calculated by JEREMY for each isotope of interest. The fluence spectra of the particles in the hadronic cascades are folded offline with isotope production

cross-sections. The code is written in the Python language and automatically provides a scripting interface that facilitates in-depth data analysis, since all computed quantities are accessible to the user. It is a hands-on code, providing a very fast approach and it is much more user-friendly and faster to use than a Monte Carlo simulation tool. For these reasons in this work JEREMY was used in addition to FLUKA, even if it could be expected that the results had less agreement with the experimental data than FLUKA as it will be shown below.

The calculations were performed at the approximate locations where core samples were taken from the shielding walls, in order to allow a direct comparison of experimental data and predictions. The concentration of the various radionuclides in the core samples was calculated on the basis of a simplified description of the experimental hall. In fact, even if a detailed description of the cyclotron bunker and equipment as it was over the 33 years of operation is not feasible, we will demonstrate that the geometry adopted is good enough to predict with sufficient accuracy the long-lived isotopes in the SC walls (on the proton extraction side). The whole SC hall ($16 \times 17 \times 7 \text{ m}^3$) was modelled together with the 5.5 m thick North, South and East walls made of barite concrete and the 4 m thick West wall made of ordinary concrete. Most of the induced radioactivity in the SC walls was due to the stray neutron radiation generated by the beam losses in the SC extraction system. The low extraction efficiency (see below) depended mainly on beam scattering on the iron septum of the extraction channel, on the losses at the external target, at the exit of the bending magnets and at the entrance of the proton channel wall [18–20]. In order to simulate the overall beam losses that occurred in the extraction system, a 600 MeV proton beam impinging on a $60 \times 100 \times 100 \text{ cm}^3$ steel target was used for the FLUKA simulations. The origin of the coordinate frame of the FLUKA geometry was chosen to be in the centre of the SC hall, the z-axis coinciding with the beam axis and the y-axis pointing up, whereas the steel target was placed around the proton extraction

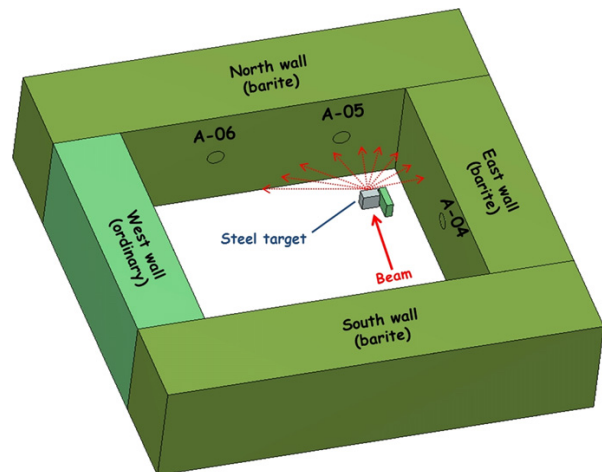


Fig. 9. Three-dimensional view of the SC geometry used in the FLUKA simulations. The picture was obtained using SimpleGeo [31].

Table 5

Typical composition of the barite concrete (density 3.2 g/cm^3) used for the FLUKA calculations, in mass fractions (adapted from Ref. [21,22]).

Composition	Ba	O	Ca	Fe	S	Si	H	Al	Na	Mg	Cs	Co	Eu
(wt%)	45	40	5	5	2.5	1	0.7	0.5	0.3	0.2	$5\text{E-}4$	$1\text{E-}4$	$5\text{E-}5$

channel, at 5 m distance from the North wall and 3 m from the East wall. Furthermore, a $150 \times 40 \times 100 \text{ cm}^3$ wall made of ordinary concrete was placed between the target and the East wall to simulate the brick wall shielding the East side. Fig. 9 shows the FLUKA geometry used in the simulations.

The elemental composition of the barite concrete used in the simulations is given in Table 5. Since it was not possible to perform a chemical analysis of the actual concrete of the SC walls, the composition of a typical barite concrete was used for the FLUKA simulations [21,22]. The full hadronic cascade was simulated in the target and in the concrete, including particles back-scattered from the walls. The electromagnetic component of the radiation field was disregarded, as its contribution to induced radioactivity is minor as compared to that caused by the hadronic component. Neutrons were transported down to thermal energies; for all other hadrons a threshold of 1 keV was used. Residual nuclei production was treated using the new evaporation model of FLUKA and taking into account heavy fragment evaporation and coalescence mechanism.

Historical beam profile measurements showed that the full width at half-maximum of the approximately Gaussian beam shape was $\sim 1 \text{ cm}$ after the Improvement Programme [18,23]. This shape, together with the energy spread in the extracted proton beam ($\sim 1 \text{ MeV}$), was taken into account in the calculations.

The induced radioactivity depends on the irradiation profile, which includes periods of operation at various beam intensities alternating with shutdown periods. Although the actual SC irradiation profile during its 33 years of operation is clearly impossible to obtain, a careful historical investigation of the SC operation allowed a simplified but realistic irradiation profile to be derived. From the CERN Annual Reports [24] it was possible to reliably reconstruct the total beam working time. During the first operational period (1957–1973) the SC (called SC1) was operated for a total of $8.7\text{E}+4 \text{ h}$ ($\sim 10 \text{ yr}$). This period was followed (from June 1973 to the end of 1974) by an 18 month shut-down due to the Improvement Programme. In the second part of its life (1974–1990) the upgraded SC (SC2) was operated for a total of $7\text{E}+4 \text{ h}$ ($\sim 8 \text{ yr}$).

The SC performance data were retrieved from the many status reports [25–30]. Above all, Allardyce et al. [28] declared a very low extraction efficiency ranging between 5–7% for the SC1 and one order of magnitude higher (50–70%) for the SC2 after the Improvement Programme. Since the SC1 internal beam current was about $1 \mu\text{A}$ ($\sim 6.24\text{E}+12$ protons per second) and $1.5 \mu\text{A}$ ($\sim 9.36\text{E}+12$ protons per second) for the SC2 (this is an average value versus a nominal value of $10 \mu\text{A}$), we calculated a beam loss of $5.8\text{E}+12$ protons per second for the SC1 operational period and $3.12\text{E}+12$ protons per second for the SC2. As from 1978 the SC was used to accelerate heavy ion as well. Since the ion intensity was lower than that of protons by up to a factor of 5 [30] and ions were accelerated just for a few years, only the proton beam irradiation profile was considered in the FLUKA simulations.

For each concrete region two types of scoring were used. In one case, the production of residual nuclei and their radioactive decay were performed by FLUKA in the same run. The RESNUCLEi card scored the residual nuclei produced in inelastic interactions, while the radioactive decay was calculated using the RADDECAY, DCYSCORE, DCYTIMES and IRRPROFILE cards, taking into account the decay chains and build-up of isotopes, and the irradiation profile. The output data files were then post-processed to obtain the specific activity, since the mass of the scored region had to be obtained from its volume and the density of the barite concrete. The USRSUW routine of the FLUKA package was used to read results in binary form and to compute standard deviations over several runs.

In the second case, FLUKA calculated only the particle spectral fluences that were used as input data into JEREMY. The differential distributions of the energy fluence of protons, pions, neutrons and low-energy ($E < 20 \text{ MeV}$) neutrons were scored separately for all concrete samples and the results were written into output files (JEREMY input files). The USTSUW routine was used to read the USRTRACK results in binary form from several runs and to compute statistical uncertainties. Both codes include in the calculations the radioactive decay of all radionuclides during the activation period.

8. Results and discussion

This calculated and measured specific activities were compared for each concrete core. The experimental results, the simulation results and their ratios are summarized in Table 6 (for sample A-04), Table 7 (sample A-05), Table 8 (sample A-06) and in Figs. 10 and 11. The quoted errors include statistical and systematic uncertainties of the gamma spectrometry measurements as well as statistical uncertainties in the FLUKA and JEREMY simulations. It can be observed that, even if the uncertainties in the FLUKA input values (irradiation conditions, geometry, concrete elemental composition, etc.) are quite large, the agreement between calculated and measured activities is rather good, in most cases within a factor of 2.

A rather remarkable agreement is found between the measured and calculated values of residual radioactivity for the A-04 and A-06 samples throughout their thickness (50 cm). At their location in the vault, the particle spectrum is dominated by a thermal neutron component and the residual activity decreases exponentially with depth in the shield.

A different picture is observed for the activity depth profile in the A-05 concrete core. The residual radioactivity in the core surface is particularly well reproduced by the codes, but a striking difference is noted as from a depth of 25 cm in the wall (Fig. 12 for Ba-133). Here a fast neutron component coming from beam losses not only in the cyclotron extraction channel but also in the bending magnet and in the beam pipes traversing the wall in the A-05 sample area, are slowed down inside the concrete,

Table 6

Comparison of calculated and measured specific activity in the A-04 sample from 0 cm to 10 cm depth.

Isotope	$t_{1/2}$ (years)	FLUKA (Bq/g)	JEREMY (Bq/g)	Experiment (Bq/g)	FLUKA/Exp.	JEREMY/Exp.
Na-22	2.6	$0.0010 \pm 3\text{E}-4$	0.003 ± 0.001	$< 0.004^a$	–	–
Co-60	5.27	0.017 ± 0.004	0.030 ± 0.004	0.009 ± 0.002	1.9 ± 0.6	3.5 ± 1.0
Ba-133	10.5	5.5 ± 0.2	5.8 ± 0.4	3.0 ± 0.4	1.8 ± 0.3	1.9 ± 0.3
Cs-134	2.06	0.004 ± 0.001	0.002 ± 0.001	$< 0.006^a$	–	–
Cs-137	30.1	0.46 ± 0.05	0.010 ± 0.002	0.34 ± 0.05	1.4 ± 0.3	0.03 ± 0.01
Eu-152	13.5	0.90 ± 0.05	2.3 ± 0.2	0.63 ± 0.06	1.4 ± 0.2	3.6 ± 0.5
Eu-154	8.59	0.04 ± 0.01	0.08 ± 0.01	0.04 ± 0.01	1.0 ± 0.3	1.9 ± 0.4

^a Minimum detectable activity (MDA).

Table 7

As in Table 6, for the A-05 sample from 0 cm to 5 cm depth.

Isotope	$t_{1/2}$ (years)	FLUKA (Bq/g)	JEREMY (Bq/g)	Experiment (Bq/g)	FLUKA/Exp.	JEREMY/Exp.
Na-22	2.6	0.03 ± 0.01	0.04 ± 0.01	0.06 ± 0.02	0.5 ± 0.2	0.7 ± 0.3
Co-60	5.27	0.09 ± 0.01	0.11 ± 0.01	0.09 ± 0.01	1.0 ± 0.2	1.2 ± 0.2
Ba-133	10.5	37 ± 2	30 ± 2	33 ± 4	1.1 ± 0.1	0.9 ± 0.1
Cs-134	2.06	0.04 ± 0.01	0.010 ± 0.005	0.04 ± 0.01	1.0 ± 0.3	0.3 ± 0.2
Cs-137	30.1	6.4 ± 0.5	0.07 ± 0.02	8.6 ± 1.2	0.7 ± 0.1	0.010 ± 0.005
Eu-152	13.5	3.0 ± 0.2	7.7 ± 0.6	1.9 ± 0.2	1.5 ± 0.2	3.8 ± 0.6
Eu-154	8.59	0.19 ± 0.03	0.30 ± 0.03	0.10 ± 0.02	1.9 ± 0.6	3.0 ± 0.9

Table 8

As in Table 6, for the A-06 sample from 0 cm to 5 cm depth.

Isotope	$t_{1/2}$ (years)	FLUKA (Bq/g)	JEREMY (Bq/g)	Experiment (Bq/g)	FLUKA/Exp.	JEREMY/Exp.
Na-22	2.6	0.002 ± 0.001	0.002 ± 0.001	0.003 ± 0.002	0.7 ± 0.5	0.7 ± 0.5
Co-60	5.27	0.009 ± 0.004	0.020 ± 0.005	0.012 ± 0.002	0.8 ± 0.3	1.8 ± 0.4
Ba-133	10.5	4.7 ± 0.2	4.5 ± 0.3	4.3 ± 0.5	1.1 ± 0.1	1.0 ± 0.1
Cs-134	2.06	0.003 ± 0.001	0.002 ± 0.001	< 0.003 ^a	–	–
Cs-137	30.1	0.5 ± 0.1	0.010 ± 0.002	0.7 ± 0.1	0.7 ± 0.2	0.010 ± 0.005
Eu-152	13.5	0.7 ± 0.1	1.6 ± 0.2	0.7 ± 0.1	1.0 ± 0.2	2.3 ± 0.4
Eu-154	8.59	0.05 ± 0.01	0.06 ± 0.01	0.04 ± 0.01	1.2 ± 0.4	1.5 ± 0.4

^a Minimum detectable activity (MDA).

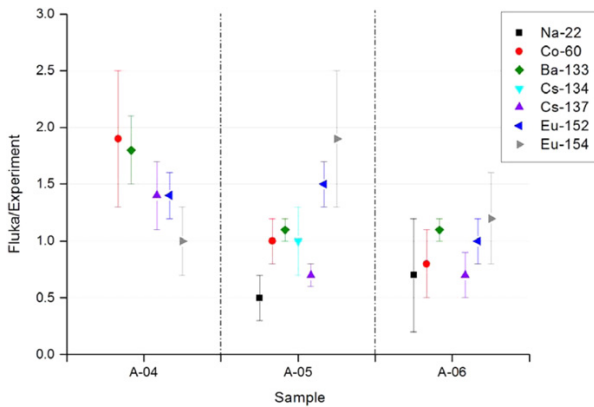


Fig. 10. Ratios of FLUKA over measured specific activities in concrete samples at a wall depth of 5–10 cm.

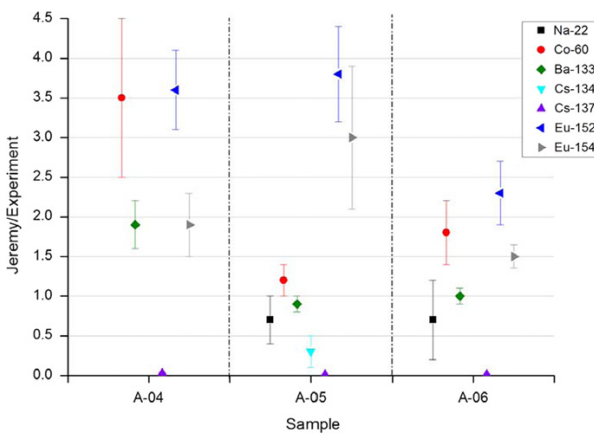


Fig. 11. Ratios of JEREMY over measured specific activities in concrete samples at a wall depth of 5–10 cm.

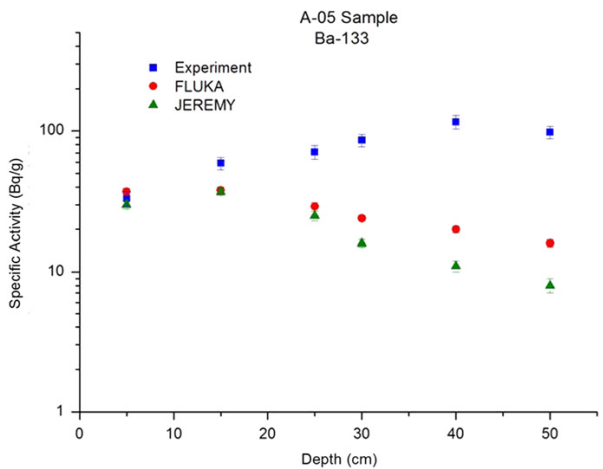
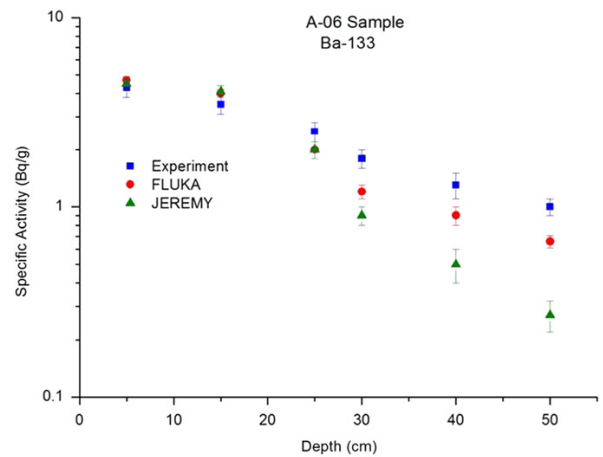


Fig. 12. Depth profile of the measured and calculated activity of Ba-133 in the North wall: A-05 sample (top) and A-06 sample (bottom).

increasing the thermal neutron component up to a depth of about 35 cm. These particular beam loss conditions were not taken into account in detail in the FLUKA calculations, which can explain the

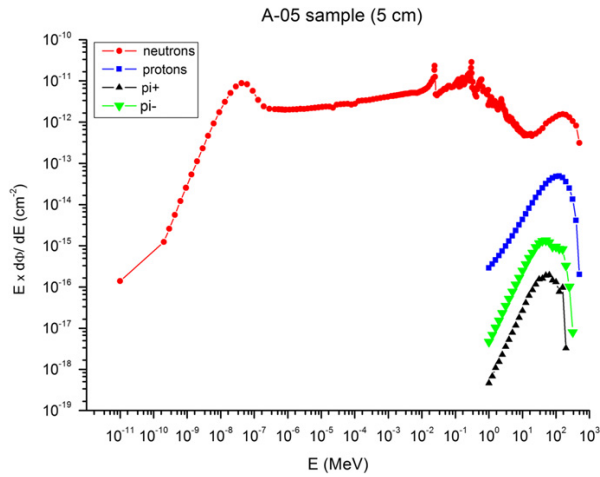


Fig. 13. Energy spectra of neutron, protons and charged pions in the A-05 sample at 5 cm depth in the shield.

discrepancies observed between measured and calculated values in the A-05 sample as from a depth of 25 cm.

To better understand the above, Figs. 13–15 show some representative particle spectral fluences simulated by FLUKA. Fig. 13 shows, for the A-05 sample at a depth of 5 cm, that the neutron component largely dominates over the other particles. The same is valid for all other locations and depths in the shield, confirming that the induced radioactivity is essentially due to neutrons. The neutron spectra at a depth of 5 cm and 50 cm in the A05 sample are shown in Fig. 14. One notices that the importance of the thermal component over the fast neutron component in the simulated spectrum remarkably increases with increasing depth. The same behaviour is observed for the A06 sample, also located in the forward direction but at an emission angle of approximately 60 degrees. As for the A04 sample, located in the transverse direction, Fig. 15 shows that the shape of the neutron spectral fluence does not change substantially from the sample surface to 50 cm depth.

The residual radioactivity of Ba-133 is well described by the codes as shown in Fig. 12 and Fig. 16. This radionuclide was measured with high accuracy since it was the most active one and except for the A-05 sample, measured and calculated values are within a factor of 2 for both codes. The caesium radionuclides are generally well reproduced by FLUKA, whereas JEREMY underestimates ^{134}Cs and shows very little reliability in the calculation of the residual activity of ^{137}Cs , underestimating it by up to a factor of 100. This could be due to problems with the processing

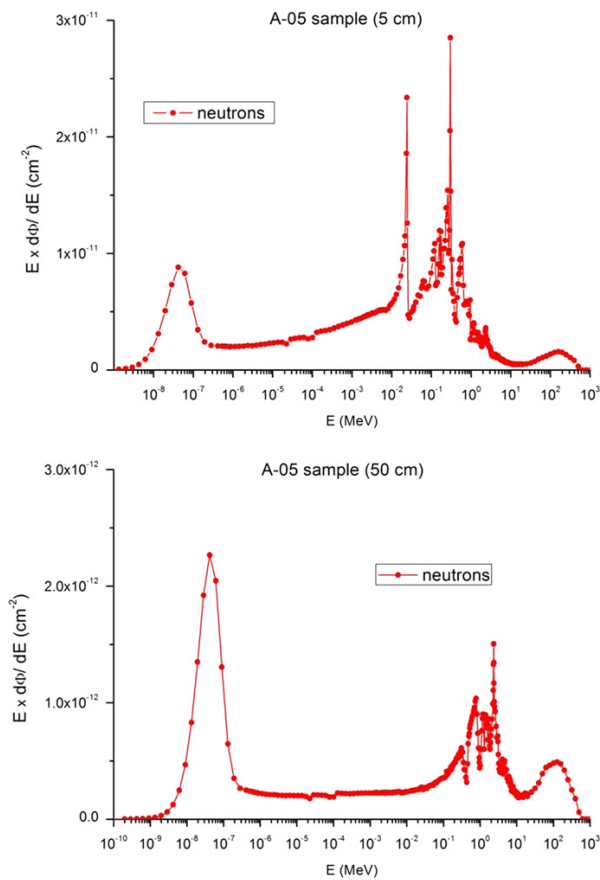


Fig. 14. Comparison of neutron energy spectra at 5 cm (top) and 50 cm (bottom) depth in the shield for the A-05 sample.

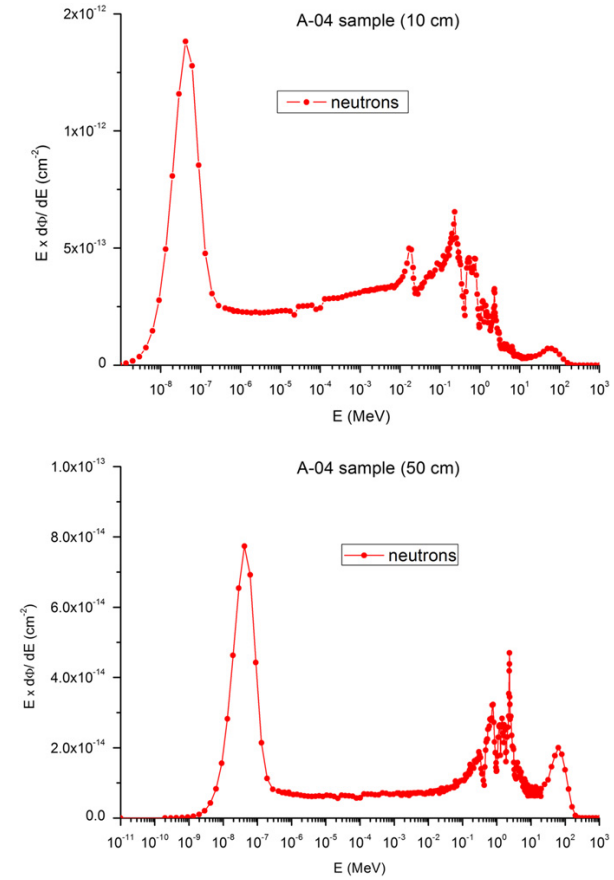


Fig. 15. Comparison of neutron energy spectra at 10 cm (top) and 50 cm (bottom) depth in the shield for the A-04 sample.

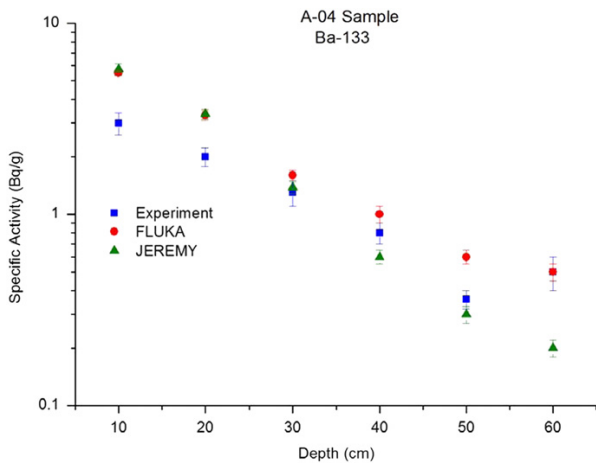


Fig. 16. Depth profile of the measured and calculated activity of Ba-133 in the East wall (A-04 core sample).

of the JEREMY cross-section database [32,33], which is currently under revision. The predicted values of ^{152}Eu and ^{154}Eu match the measured ones within a factor of 2 for FLUKA and within a factor of 4 for JEREMY. Larger discrepancies can be observed for deeper samples (from a depth of 30 cm). A possible reason is the variable thickness of the samples measured by gamma spectrometry, as for practical reasons the 50-cm long concrete cores could not be sliced in pieces of equal thickness. The FLUKA calculations were performed assuming that all samples had the same dimensions (10 cm thick), whereas the actual samples have an average thickness varying from 5 cm to 15 cm. The larger discrepancies between experimental and Monte Carlo data observed for the deeper samples is just because the actual samples deviate more and more from the corresponding "MC samples" with increasing depth. The remaining isotopes, ^{60}Co and ^{22}Na , are well described by the calculations, in spite of the very low residual radioactivity left after 20 years of cooling. Uncertainties in the elemental composition are expected to be the main reason for the discrepancies.

9. Conclusions

In order to establish the present radiological status of the old CERN synchro-cyclotron 20 years after shutdown, gamma spectrometry measurements were performed on 113 samples collected inside the three levels of the accelerator vault, on the cyclotron itself and on concrete cores taken from various parts of the building walls, up to a depth of 50 cm in the shield. About 40% of all samples contain traces of neutron-induced radionuclides, mainly ^{60}Co (in metals), ^{133}Ba , ^{137}Cs , ^{152}Eu and ^{154}Eu (in concrete). Values of specific activities vary in the range 5 mBq/g to 781 Bq/g. The maximum activity induced in concrete by spallation reactions was observed at a depth of 40 cm in the wall near the cyclotron extraction channels. The measurements were supplemented by in-situ gamma spectrometry measurements with the ISOCS detector. A complete dose rate survey was also performed yielding isodose maps of the three levels of the building.

The activation products and the residual radioactivity in the barite walls of the SC vault were calculated with the FLUKA and JEREMY codes. The results of the simulations were compared with the gamma spectrometry measurements. In most cases the difference between measured and calculated value is within a factor of 2 for both codes, a rather remarkable agreement. This study demonstrates that both FLUKA and JEREMY can be successfully

used to simulate the isotope production and the residual radioactivity with only a very approximate knowledge of the irradiation profile and after a very long cooling time.

The complete set of experimental and computational data complementing the results discussed in this paper is provided in Refs. [34–36].

Acknowledgements

The authors would like to thank Jacques Wolf for helping in retrieving various SC status reports from the archives. We are grateful to Matteo Magistris and Robert Froeschl for useful discussions and for providing their results of previous studies.

References

- [1] G. Fidecaro, Thirty-three years of physics at the CERN synchro-cyclotron, in: Proceeding of the SC 33 Symposium at CERN, 22 April 1991, Physics Report 225 (1993).
- [2] M. Silari, A Proposal to Convert the CERN 600 MeV Synchrocyclotron Building into Public Exhibition Hall, CERN Internal Report, CERN-SC-2010-015-RP-TN (2010).
- [3] A. Ferrari, P.R. Sala, A. Fassò and J. Ranft, FLUKA: A Multi-particle Transport Code, CERN-2005-10, INFN/TC_05/11, SLAC-R-773 (2005).
- [4] G. Battistoni, S. Muraro, P.R. Sala, F. Cerutti, A. Ferrari, S. Roesler, A. Fassò and J. Ranft, The FLUKA code: description and benchmarking, in: Proceedings of the Hadronic Shower Simulation Workshop 2006, Fermilab 6–8 September 2006, M. Albrow, R. Raja Eds., AIP Conference Proceeding 896, 31–49 (2007).
- [5] R. Froeschl, JEREMY—a code for radiological characterization of accelerator components including detailed uncertainty estimation, in: Second International Workshop on Accelerator Radiation Induced Activation ARIA2011, Israel (2011).
- [6] C. Lambert and J. Wolf, Interventions dans la cadre des travaux de démantèlement du Synchrocyclotron, CERN Technical Report (unnumbered) (2005).
- [7] B.W. Allardyce, G.F. Spinney and J.W.N. Tuyn, The Decommissioning of the CERN Synchrocyclotron: A Preliminary Report, CERN Technical Memorandum PS-90-57(SC) (1990).
- [8] G.F. Spinney, Decommissioning the CERN Synchro-cyclotron, CERN Technical Report, CERN-MT-92-02-ESM (1992).
- [9] M. Barbier, Radioactivity Induced in Materials by High-energy Particles, CERN Technical Report, CERN-64-09 (1964).
- [10] S. Regnier, Physical Review C: Nuclear Physics 20 (1979) 1517.
- [11] K. Goebel, K. Schultes and J. Zähringer, Production Cross-sections of Tritium and Rare Gases in Various Target Elements, CERN Technical Report, CERN-64-12 (1964).
- [12] P. Hornshøj, H.L. Nielsen, N. Rud and H.L. Ravn, The Half-life of ^{194}Hg Determined by Means of Quantitative On-line Mass Separation, CERN Technical Report, CERN-EP-80-178 (1980).
- [13] Ordonnance du 22 juin 1994 sur la radioprotection (ORaP), Number 814.501. Conseil fédéral suisse, Juin 1994 (Etat le 1er janvier 2011).
- [14] M. Brugger, Y. Donjoux, A. Mitaroff and S. Roesler, Measurement and simulation of induced activity at the CERN-EU high energy reference field facility, in: Proceedings of the Sixth International Meeting on Nuclear Applications of Accelerator Technology, San Diego, CA, 1–5 June 2003, pp. 391–398 (2003).
- [15] M. Brugger, H. Khater, S. Mayer, A. Prinz, S. Roesler, L. Ulrici, H. Vincke, Radiation Protection Dosimetry 116 (1–4) (2005) 6.
- [16] L. Ulrici, M. Brugger, T. Otto, S. Roesler, Nuclear Instruments and Methods in Physics Research A562 (2006) 596.
- [17] M. Brugger, A. Ferrari, S. Roesler, L. Ulrici, Nuclear Instruments and Methods in Physics Research A562 (2006) 814.
- [18] S. Lindbäck, Study of the Present Extraction System for the CERN Synchro-cyclotron, CERN-73-08 (1973).
- [19] M. Mörpurgo, Improvements to the CERN Synchro-cyclotron Extraction System, Conference on High Energy Cyclotron Improvement, Williamsburg 1964, Proceedings, CERN Report, MSC/26/68 (1964).
- [20] L. Dick, L. di Lella, L. Feuvrais and M. Spighel, Preliminary Investigation of Factors Affecting External Beams from the CERN Synchrocyclotron, Conference on High Energy Cyclotron Improvement, Williamsburg 1964, CERN Report, MSC-24-30/80 (1964).
- [21] A. Brandl, C. Hranitzky, S. Rollet, Radiation Protection Dosimetry 115 (1–4) (2005) 195.
- [22] J.H. Hubbell, S.M. Seltzer, Tables of X-ray Mass Attenuation Coefficients and Mass Energy-Absorption Coefficients, NIST X-ray Attenuation Database Table 2, National Institute of Standards and Technology, USA, 1996.
- [23] Synchro-cyclotron de 600 MeV. Number 3 in Cahier Technique. Geneve, first ed., CERN/PIO 74-1 (1974).
- [24] CERN Annual Report (1958–1990), <http://library.web.cern.ch/library/Library/AnnualReport.html>.

- [25] G. Brianti and E.G. Michaelis, Summary of the Seminar on SC Improvements Programme, CERN Technical Report, MSC/M-la/13 M53 (1966).
- [26] H. Beger, F. Blythe, G. Le Dallic, H. Lustig, E.G. Michaelis and N. Vogt-Nilsen, Report on the CERN SC improvement programme, in: Proc. Seventh International Conference on Cyclotrons and their Applications, Zurich (1975).
- [27] R. Deltenre and J.W.N. Tuyn, Flux Density Measurements inside and behind the B-pipe with a Proton Beam Hitting The Wall of the Sc Proton Room, CERN Technical Memorandum, CERN HS-RP/TM/76-11 (1976).
- [28] B.W. Allardyce, H. Beger, R. Galiana, R. Giannini, E.G. Michaelis and S. Talas, Performance & prospects of the reconstructed CERN 600 MeV synchro-cyclotron, in: Seventh IEEE Particle Accelerator Conference, Chicago, USA, IEEE Trans. Nucl. Sci. NS24 (1977).
- [29] B.W. Allardyce, A. Fiebig, G. Le Dallic, J.H.B. Madsen, P.H. Stanley, IEEE Transactions on Nuclear Science 26 (1979).
- [30] B.W. Allardyce, The CERN synchrocyclotron today, CERN/PS-COP/81-30, in: Ninth International Conference on Cyclotrons and their Applications, GANIL, Caen (1981).
- [31] C. Theis, K.H. Buchegger, M. Brugger, D. Forkel-Wirth, S. Roesler, H. Vincke, Nuclear Instruments and Methods A562 (2006) 827.
- [32] JEREMY Isotope Production Cross-sections: Low Energy Neutrons from JEFF 3.1.1 Library (Including Isomere Branching Ratios); High Energy Particles from FLUKA Models.
- [33] A. Santamarina et al., The JEFF-3.1.1 Nuclear Data Library, Technical Report JEFF Report 22, Nuclear Energy Agency, Paris (2009).
- [34] F.P. La Torre and M. Silari, Analytical and Monte Carlo Calculations of the Residual Radioactivity in the Walls of the 600 MeV Synchrocyclotron Vault, CERN Technical Note, CERN-DGS-2012-012-RP-TN (2012).
- [35] P. Carbonez, F.P. La Torre, R. Michaud and M. Silari, Residual Radioactivity at the CERN 600 MeV Synchro-cyclotron, CERN Technical Note, CERN-SC-2011-026-RP-TN (2011).
- [36] F.P. La Torre, Residual Radioactivity at the CERN 600 MeV Synchro-cyclotron, Master Thesis, IUSS Pavia—Institute for Advanced Study, Academic year 2009–2010.

Monitoring reactions for the calibration of high-energy mixed hadron beams

A. Ferrari¹, F.P. La Torre^{1,2}, G.P. Manessi^{1,3}, F. Pozzi^{1,4}, M. Silari¹

¹CERN, 1211 Geneva 23, Switzerland

²University of Bern, AEC-LHEP, Sidlerstrasse 5, 3102 Bern, Switzerland

³University of Liverpool, Department of Physics, L69 7ZE Liverpool, UK

⁴Technische Universität München, Lehrstuhl für Nukleartechnik, Boltzmannstrasse 15, 85748 Garching, Germany

Abstract

The well-known foil activation technique was used to calibrate an ionization chamber employed for the on-line beam monitoring of a 120 GeV/c mixed proton/pion beam at CERN. Two monitoring reactions were employed: the standard $^{27}\text{Al}(p,3pn)^{24}\text{Na}$ and the alternative $^{\text{nat}}\text{Cu}(p,x)^{24}\text{Na}$. The parameters on which the technique critically depends and the adopted solutions are thoroughly analysed: the cross section, the contribution of the competing reactions to the induced activity and the recoil nuclei effect. The experimental results are compared with FLUKA Monte Carlo simulations and with past results obtained with various calibration techniques. The comparison confirms that both reactions can be effectively employed. The $^{\text{nat}}\text{Cu}(p,x)^{24}\text{Na}$ reaction shows advantages because its cross section is known at very high energies with a low uncertainty and the production of ^{24}Na is not affected by competing neutron-induced reactions. The contribution of the competing reactions in the case of the $^{27}\text{Al}(p,3pn)^{24}\text{Na}$ reaction has been estimated to be 4.3% / 100 mg/cm², whereas the effect of recoil nuclei is negligible.

I. INTRODUCTION

The intensity of high energy proton beams is monitored via measurements of the beam current, which has to be determined in an absolute manner [1]. Different devices can be employed: beam current transformers (BCTs) [2], Faraday cups (FCs) [3] or particle detectors such as scintillators [4], ionization chambers (ICs) [5] and secondary electron emission monitors (SEEMs) [6]. BCTs measure the magnetic field induced by the passage of the particles, FCs measure the beam electrical charge, while particle detectors measure the energy lost by particles in matter. Each technique shows some limitations: BCTs works at high beam currents; FCs are destructive and can be used only for low currents; scintillators are not radiation hard and show saturation effects above a certain threshold; ICs usually produce very low outputs; SEEMs can only be used for high intensities and show some drawbacks, such as the surface effect [7].

In the secondary beam areas (SBAs) of CERN Super Proton Synchrotron (SPS) the beam monitoring is commonly carried out via ICs. The high energy beams are characterized by a current varying between a few fA and tens of pA. These currents are too low to allow using BCTs and SEEMs, whereas scintillators are used only in the lower part of the intensity range to avoid saturation issues, and FCs cannot be used for on-line monitoring. Therefore ICs remain one of the best solutions, coupled with a special electronics designed to deal with the very low currents produced during the beam spill. A specificity of the CERN SBAs is that the beams are usually mixed particles (e.g. protons, pions and kaons for positive polarity). The relative percentages depend on the beam energy [8].

This paper discusses the foil activation technique for the calibration of ICs employed for monitoring high energy hadron beams. The focus is on the specific conditions of mixed high energy beams, but the conclusions are obviously valid for a beam composed of a single particle type. First, the activation of hyperpure aluminium foils via the well-known $^{27}\text{Al}(p,3pn)^{24}\text{Na}$ reaction is discussed, focusing the attention on the different parameters on which the activation process critically depends. Then the alternative $^{\text{nat}}\text{Cu}(p,x)^{24}\text{Na}$ reaction is investigated, highlighting the features that makes it an ideal reaction for beam monitoring and its main advantages if compared to the $^{27}\text{Al}(p,3pn)^{24}\text{Na}$. Finally the experimental results are compared with FLUKA [9,10] Monte Carlo simulations and with past results obtained via other calibration techniques.

II. THE ACTIVATION FOIL TECHNIQUE

Foil activation is a well-established technique for measuring the intensity of high energy proton beams. It is particularly convenient for the calibration of ICs used for on-line beam monitoring. One of its advantages is the accuracy that can be achieved if the cross section of the reaction of interest is known with a small uncertainty. When the protons traverse the foil they generate spallation reactions $A(p,x)B$, where A is the stable isotope of which the foil is constituted, B is the radioisotope produced in the foil by the spallation reaction, whose activity is determined via γ -spectrometry, x is the reaction product escaping the foil. An ideal monitor reaction should show the following properties:

- Cross section known with good accuracy.
- Half-life of the radioisotope produced in the foil longer than the irradiation time, but not too long in order to obtain a detectable activity.
- γ -line(s) of the radioisotope produced in the foil easily detectable and distinguishable by γ -spectrometry.
- Negligible contribution to the production of the radionuclide of interest by secondary particles formed by interaction of the proton beam in the target (neutrons and energetic secondary hadrons).

Unfortunately none of the commonly used reactions satisfy all of these requirements and one has to find a compromise. The bases of the activation theory are given in paragraph II.A and the two monitor reactions employed in this study are discussed in paragraphs II.B and II.C. The discussion will refer for simplicity to a proton beam, but the evaluations are valid for a generic hadron beam.

A. Theory

If $A(t)$ (Bq) is the activity induced in the foil, t_{IRR} and t_{WAIT} (s) are the irradiation time and waiting time (i.e. the time elapsed from the end of the irradiation until the foil is counted), N_x is the foil surface atomic density

(cm^{-2}), σ is the production cross section of the selected radioisotope (cm^2), the particle flux ϕ' (number of particles per second traversing the foil) can be obtained as (see Appendix):

$$\phi' = \frac{A(t)}{N_x \cdot \sigma \cdot (1 - e^{-\lambda \cdot t_{\text{IRR}}}) \cdot e^{-\lambda \cdot t_{\text{WAIT}}}} \quad (1)$$

$A(t)$ is measured by γ -spectrometry, while t_{WAIT} and t_{IRR} must be recorded. In the present experiment t_{WAIT} was recorded manually while t_{IRR} was obtained from the log-file of the acquisition system.

B. The $^{27}\text{Al}(p,3pn)^{24}\text{Na}$ reaction

The $^{27}\text{Al}(p,3pn)^{24}\text{Na}$ reaction is one of the most extensively used beam monitor reactions. Its main advantages are:

- The short half-life of ^{24}Na (14.9590 h) results in a high specific activity so a relatively short irradiation time is adequate to obtain a reasonable activity to be determined by γ -spectrometry.
- ^{24}Na decays by β^- emission producing two γ -rays of energies 2.754 MeV and 1.369 MeV (branching ratios: 99.94% and 100%, respectively), whose peaks can be easily identified by γ -spectrometry.
- The $^{27}\text{Al}(p,3pn)^{24}\text{Na}$ cross section is known with good accuracy in a wide energy range. Fig. 1 plots the available cross section data for energies higher than 0.5 GeV. The 300 GeV value comes from indirect measurements [11].
- Hyperpure ^{27}Al foils are readily available.

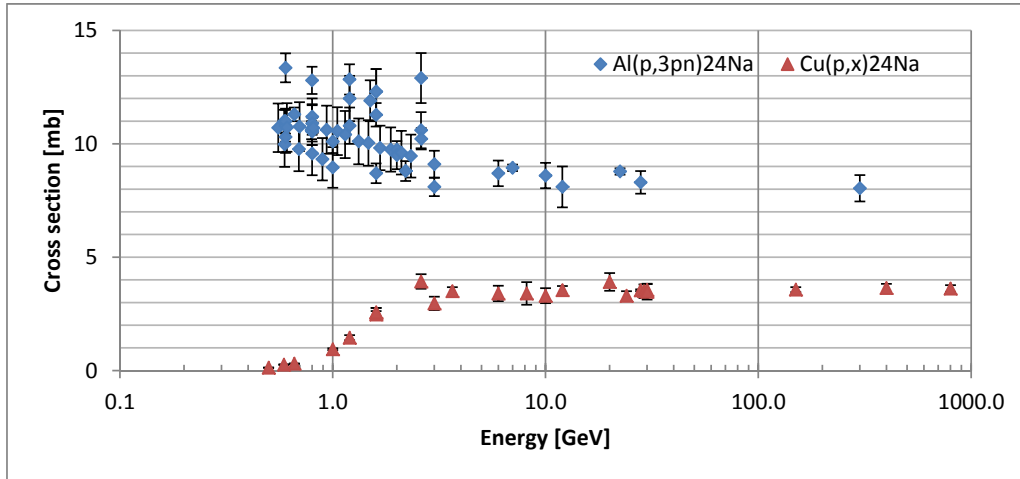


FIG. 1. Cross section data available in the literature for the $^{27}\text{Al}(p,3pn)^{24}\text{Na}$ and the $^{\text{nat}}\text{Cu}(p,x)^{24}\text{Na}$ reactions for energies higher than 0.5 GeV [12].

To obtain an accurate determination of the particle flux, as derived from expression (1), one must take into account several parameters on which the reaction critically depends:

- The cross section value at the energy of interest.
- The importance of the competing $^{27}\text{Al}(n,\alpha)^{24}\text{Na}$ reaction, as well as of the reactions induced by energetic secondary hadrons produced in the foils, in the determination of the total induced activity.
- The recoil of some of the nuclei produced in the spallation process that can leave the foil in the same direction of the primary beam (see Fig. 2).

A first problem arises in the determination of the cross section to be employed in case of a mixed proton/pion beam. Whilst for the proton-induced spallation reaction the cross section data are available, for pion-induced reactions there are no published data. The value of the pion-induced cross section can be indirectly determined using the FLUKA code. Even if FLUKA cannot be used to derive the absolute value of the cross sections at very high energies with the required accuracy, it is much more reliable in the determination of the ratio of the cross sections of reactions induced by different particles at the same energy on the same target. One can therefore calculate the ratio between the cross section of pion- and proton-induced reactions and then derive

the absolute value of the pion-induced one. The cross section ratio can be obtained by running the nuclear interaction models of FLUKA in interaction only mode, accounting for both absorption and quasi-elastic reactions. The output file provides the cross section for each isotope produced in the interaction between the primaries and the target. By running two simulations (for protons and for pions) one obtains the ratio between the pion- and the proton-induced cross sections for the reaction of interest. Since the value of the proton-induced spallation cross section of interest is known from the literature, one can derive the pion-induced cross section and thus obtain the effective cross section for the mixed beam.

The importance of the reactions induced by neutrons and energetic secondary hadrons in the production of ^{24}Na is discussed in Sec. IV.A.1. This effect has been evaluated *a posteriori* by analysing the induced activities of all the exposed foils.

The foils were irradiated in sandwiches of three to take into account the recoil of some of the nuclei produced in the spallation process that can leave the foil in the same direction of the primary beam (due to the so-called Lorentz boost [13]). In order to maintain the equilibrium between the loss of recoil nuclei knocked out of the foil and the gain of nuclei knocked into the foil from upstream material, only the central one must be considered for data analysis, whereas the upstream and the downstream ones act as catchers. These catchers, having the same thickness of the central foil, are thick enough to capture all the knocked on or knocked back products. The importance of this effect is quantified in Sec. IV.A.2.

C. The $^{nat}\text{Cu}(p,x)^{24}\text{Na}$ reaction

The $^{nat}\text{Cu}(p,x)^{24}\text{Na}$ reaction is a promising alternative reaction for beam monitoring, as it shows two advantages when compared to $^{27}\text{Al}(p,3pn)^{24}\text{Na}$:

- The cross section, even if it is lower than that of $^{27}\text{Al}(p,3pn)^{24}\text{Na}$, is known with better accuracy at high energies. Fig. 1 plots the available cross section data for energies higher than 0.5 GeV. At very high energies (30, 150, 400 and 800 GeV) Baker et al. [14] found an energy-independent cross section value of 3.59 ± 0.14 mb.
- ^{24}Na is produced only in deep spallation reactions induced by high energy hadrons, while the secondary neutrons produce mostly isotopes close to the original target mass.

The following two parameters play an important role in the determination of the particle flux:

- The value of the reaction cross section at the energy of interest.
- The recoiling nuclei as discussed above.

In case of mixed proton/pion beams the same procedure described in Sec. 2.B. can be followed to obtain the effective beam cross section. Values of proton-induced reaction cross sections are widely available in the literature. As for the ^{27}Al foils, the ^{nat}Cu foils were exposed in sandwiches to compensate for the recoil effect.

III. EXPERIMENT

A. Experimental set-up

The foil activation technique was employed to calibrate the IC used for beam monitoring at the CERN-EU high-energy Reference Field (CERF) facility [15] at CERN. The CERF facility is installed in one of the secondary beam lines (H6) from the SPS in the North Experimental Area. A positive hadron beam (61% pions, 35% protons and 4% kaons [8]) with momentum of 120 GeV/c is stopped in a copper target. The beam is delivered to the facility with a typical intensity in the range 10^6 to 10^8 particles per SPS spill. The beam extraction time is presently about 10 s over an SPS cycle of about 45 s (in the past it was 2.5 s over a 15 s cycle).

The beam monitoring is provided by an air-filled, parallel-plate, transmission type IC placed in the beam a few meters upstream of the target. The IC has a diameter of 185 mm and consists of five parallel electrode plates made of Mylar with 17 mm inter-plate spacing. The central plate is the collector and the ones on either side are the polarity electrodes. The polarization voltage on these plates is supplied by an external battery. The beam traverses 34 mm of air at atmospheric pressure in the sensitive part of the chamber. The output signal is fed into

a charge digitizer and then to a National Instrument USB 6342 DAQ connected to a desktop computer (PC). The data are saved on a log-file that records the differential and integrated IC readings (expressed in counts) every second.

Hyper-pure ^{27}Al and $^{\text{nat}}\text{Cu}$ foils from Goodfellow [16] were used: 99.999% ^{27}Al (impurities: Mg 1.2 ppm, Si 0.8 ppm, Cu 0.3 ppm, Fe 0.3 ppm) and 99.99% $^{\text{nat}}\text{Cu}$ (impurities: Ag 70 ppm, Fe 2 ppm, Ni 2 ppm, Pb 2 ppm, Si 2 ppm, Al 1 ppm, Bi 1 ppm, Ca 1 ppm, Mg 1 ppm, Sn 1 ppm, Mn <1 ppm, Na <1 ppm, Cr <1 ppm), with dimensions $50 \times 50 \text{ mm}^2$. The foils thicknesses were 2 mm (540 mg/cm^2), 1 mm (270 mg/cm^2) and 0.5 mm (135 mg/cm^2) for Al; 0.5 mm (446 mg/cm^2), 0.25 mm (223 mg/cm^2) and 0.125 mm (111.5 mg/cm^2) for Cu, with 1% estimated uncertainty. The foils were fixed on a Plexiglas frame mounted on both ends of a hollow aluminium tube of the same dimensions of the target normally employed at CERF (Fig. 2), placed downstream of the IC. The beam size was smaller than the foil dimensions so that all particles traversing the IC hit the foils. To evaluate the contribution of scattered radiation to the foil activation, in one of the experiments an additional foil was exposed out of beam.

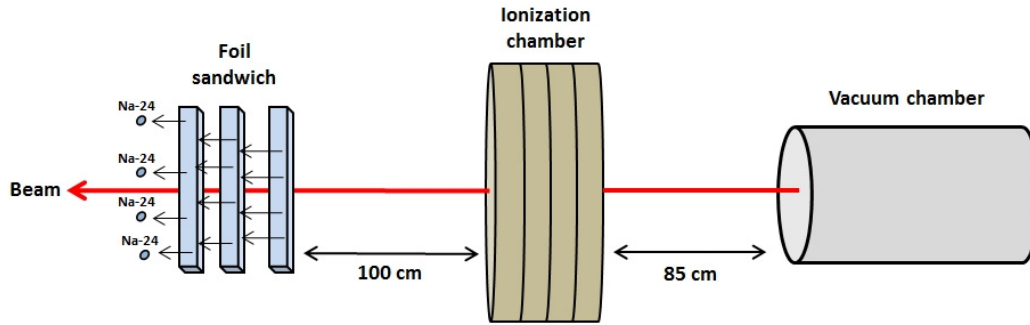


FIG. 2. Foil activation experiment set-up (not to scale).

B. Results

The results of the measurements are given in Table I. Where available, the activity of the upstream and downstream foils is given. The value used in expression (1) was the activity of the central foil, except for measurement 1 where, due to the high uncertainties, an average of the central and downstream foil activities was employed. Due to problems in the peak identification during the γ -spectrometry of the $^{\text{nat}}\text{Cu}$ 0.250 mm foil, the data of this measurement could not be exploited. The foil exposed out of beam did not show any significant induced activity, confirming that the contribution of the scattered radiation (background) to the overall activity is negligible.

Table I. Results of the foil activation experiment (uncertainties quoted at 1σ).

Al foils				
Measurement	1	2	3	4
Thickness [mm]	2.0	2.0	1.0	0.5
Irradiation time [s]	31200	31371	58223	31371
Integrated fluence [IC counts]	$2 \cdot 10^6$	$2.3 \cdot 10^6$	$3.8 \cdot 10^6$	$2.3 \cdot 10^6$
Upstream foil activity [Bq]	45.8 ± 2.2	n.a.	34.5 ± 1.9	n.a.
Central foil activity [Bq]	52.7 ± 5.4	56.8 ± 2.3	37.1 ± 1.9	12.3 ± 0.6
Downstream foil activity [Bq]	47.1 ± 1.6	n.a.	n.a.	n.a.
Cu foils				
Measurement	5	6	7	
Thickness [mm]	0.500	0.250	0.125	
Irradiation time [s]	54831	54831	54831	
Integrated fluence [IC counts]	$3.3 \cdot 10^6$	$3.3 \cdot 10^6$	$3.3 \cdot 10^6$	
Central foil activity [Bq]	8.4 ± 0.6	n.a.	2.3 ± 0.3	

n.a. = not available

To obtain the IC calibration factor one needs to know the parameters in expression (1). To improve the accuracy of the calculation, the irradiation time was subdivided in one-second irradiation periods and the total activity was obtained as the sum of the partial activities induced by each one-second irradiation, by taking into account the decay of ^{24}Na occurring from the end of each one-second irradiation until the arrival in the spectrometry laboratory. Therefore the beam-on/beam-off periods (i.e. spill time over the total SPS cycle) were exactly taken into account and fluctuations in the beam intensity during the spill were also properly considered. The values of t_{IRR} , t_{WAIT} and ϕ' were then derived from the IC acquisition log-files. The surface atomic densities N_x are given in Table II for each foil. The beam effective cross section was calculated as follows. For the $^{27}\text{Al}(p,3pn)^{24}\text{Na}$ reaction the proton-induced cross section at 120 GeV/c was assumed equal to the one calculated by Cumming [17] at 28 GeV/c, i.e. 8.3 ± 0.5 mb. The pion/proton cross section ratio was obtained by the FLUKA interaction models as described in Sec. 2.B, which gave 0.764 ± 0.011 . The pion-induced cross section is then 6.3 ± 0.4 mb. By neglecting the kaon component, which has very limited importance, the beam effective cross section (63.5% pions and 36.5% protons, the kaon fraction was re-distributed on the other two components according to their respective weight) is 7.1 ± 0.4 mb. For the $^{\text{nat}}\text{Cu}(p,x)^{24}\text{Na}$ reaction the proton-induced cross section at 120 GeV/c was assumed equal to the one calculated by Baker et al. [14] at 30, 150, 400 and 800 GeV, i.e. 3.59 ± 0.14 mb. The pion/proton cross section was found to be equal to 0.726 ± 0.016 . The pion-induced cross section is then 2.61 ± 0.12 mb and the beam effective cross section is 2.93 ± 0.13 mb.

Table II. Foil surface atomic densities.

Al foils ($\rho_{\text{Al}} = 2.71 \text{ g/cm}^3$, $M_{\text{Al}} = 27 \text{ g/mol}$)			
Foil thickness X_{Al}	0.5 mm	1.0 mm	2.0 mm
N_x	$3.0222 \cdot 10^{21} \text{ cm}^2$	$6.0445 \cdot 10^{21} \text{ cm}^2$	$1.2089 \cdot 10^{22} \text{ cm}^2$
Cu foils ($\rho_{\text{Cu}} = 8.92 \text{ g/cm}^3$, $M_{\text{Cu}} = 63.546 \text{ g/mol}$)			
Foil thickness X_{Cu}	0.125 mm	0.500 mm	
N_x	$1.0567 \cdot 10^{21} \text{ cm}^2$	$4.2266 \cdot 10^{21} \text{ cm}^2$	

From expression (1) one can derive the value of the raw calibration factors (before correction) for each experiment (see Table III), where the uncertainties derive from the uncertainties on the activity, on the foil thickness (1%) and on the cross section (5.6% and 4.4% for $^{27}\text{Al}(p,3pn)^{24}\text{Na}$ and $^{\text{nat}}\text{Cu}(p,x)^{24}\text{Na}$, respectively). The uncertainty on the beam composition is not taken into account since it is reported as below 2% [8].

Table III. Raw calibration factors (before correction) as calculated from expression (1).

Measurement	Foil thickness	Raw calibration factor (before correction) [particles/count]
1	2.0 mm (Al)	27736 ± 1682
2	2.0 mm (Al)	27014 ± 1894
3	1.0 mm (Al)	25040 ± 1923
4	0.5 mm (Al)	23399 ± 1759
5	0.500 mm (Cu)	21707 ± 1762
6	0.250 mm (Cu)	—
7	0.125 mm (Cu)	23587 ± 2620

The calibration factors from the aluminium activation need to be corrected for the contribution of the competing reactions to the overall activity. To exclude this contribution, which is proportional to the thickness of the foil, one has to extrapolate the calibration factor to zero thickness. Fig. 3 plots the calibration factors calculated from the different measurements with the corresponding linear fit. The extrapolated value is 22249 ± 2100 particles/count, where the uncertainty is calculated via the reduced chi-square method. This correction is not needed for the values obtained from the copper activation, showing the little importance of competing reactions induced by energetic secondary hadrons. In this case the best estimate of the calibration factor can be obtained by the “weighted average method”. The calibration factor and its uncertainty are derived as follows:

$$\bar{x}_p = \frac{\sum_{i=1}^N w_i \bar{x}_i}{\sum_{i=1}^N w_i}, \quad \sigma_{x_p} = \frac{1}{\sqrt{\sum_{i=1}^N w_i}}, \quad (2)$$

where the weighting factor w_i is related to the absolute uncertainty of each data:

$$w_i = \left(\frac{1}{\sigma_{x_i}} \right)^2 . \quad (3)$$

The best estimation for the calibration factor is 22293 ± 1462 particles/count.

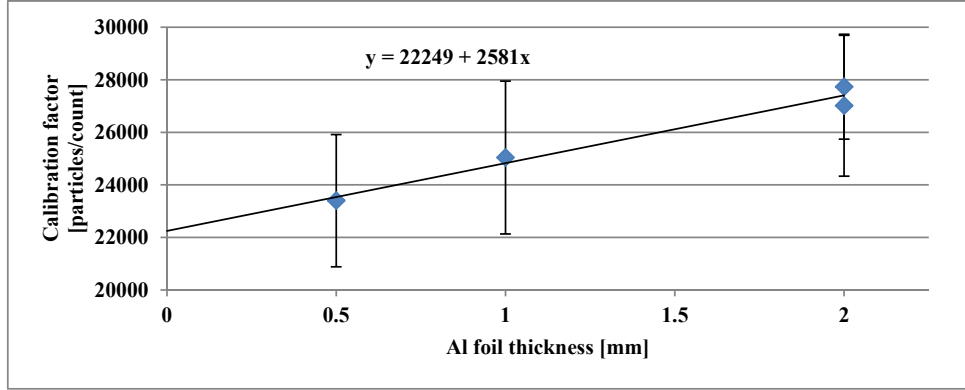


FIG. 3. Calibration factors calculated via the activation of the aluminium foils and linear fit to the data.

All the results given above lay on the assumptions that:

- The ^{27}Al and $^{\text{nat}}\text{Cu}$ atoms are homogeneously distributed in the exposed foils. This is guaranteed by the supplier.
- The effect of the impurities present in the foils on the induced activity is negligible. This has been verified via FLUKA simulations in which the impurities declared by the supplier have been included in the foils. The difference in the activity by adding the impurities was insignificant.
- The self-absorption of γ -rays in the activated foils is negligible. This has been verified by taking into account the most conservative case, i.e. the attenuation of the photons emitted by ^{24}Na in 2 mm of ^{27}Al and 0.5 mm of $^{\text{nat}}\text{Cu}$. Since the mass attenuation coefficients are $3.54 \cdot 10^{-2} \text{ cm}^2/\text{g}$ and $3.59 \text{ cm}^2/\text{g}$ [18], respectively, the maximum attenuation that the γ -rays can undergo before being detected by the spectrometer is less than 2%. In any case, this small effect is taken into account by the spectrometry software.

IV. DISCUSSION

The values of the calibration factor as derived via the activation of the aluminium and the copper foils are coherent within their range of uncertainties. These results can be compared with the calibration factor obtained via direct FLUKA simulations of the IC. The calibration factor can be derived via the knowledge of the expected charge q collected on the plates of the IC per primary particle:

$$q = E_{\text{dep}} \cdot \frac{e}{W_{\text{AIR}}} , \quad (4)$$

where E_{dep} is the energy deposited by a primary particle in the sensitive volume of the IC, e is the electron charge ($1.609 \cdot 10^{-19} \text{ C}$) and W_{AIR} ($34.23 \pm 0.4\% \text{ eV}$ [19]) is the average energy released by the primaries to produce a single ion pair in air. The energy deposited by 120 GeV/c protons, pions and kaons in the air volume of the IC ($p = 0.963 \text{ atm}$, $\rho = 1.12 \cdot 10^{-3} \text{ g/cm}^3$) was assessed by FLUKA simulations. The computed deposited energy accounts for the energy transported away by the delta rays that escape from the volume, and for the energy lost in the sensitive volume by the particle through nuclear reactions. The geometry employed in the simulation is shown in Fig. 2.

The results give an energy deposition value of 7.92 keV for protons, 8.15 keV for pions and 7.94 keV for kaons (with 1% uncertainty). Taking into account the beam composition (61% pions, 35% protons, 4% kaons) the weighted energy deposition is 8.06 keV per primary. The expected charge deposited in the IC per primary particle is then:

$$q = E_{dep} \cdot \frac{e}{W_{AIR}} = 8.06 \cdot 10^3 \text{ eV} \cdot \frac{1.609 \cdot 10^{-19} \text{ C}}{34.23 \text{ eV}} = 3.79 \cdot 10^{-17} \text{ C}. \quad (5)$$

From the sensitivity factor of the IC charge digitizer ($c = 8.403 \cdot 10^{-13} \text{ C/count}$, determined experimentally) one obtains the value of the calibration factor, i.e. the number of primaries needed to obtain one pulse from the charge digitizer: $c/q = 22172 \pm 789 \text{ particles/count}$. The uncertainty is given by the uncertainty on W_{AIR} (0.4% systematic) and on E_{dep} , whose uncertainty is the sum of two components, the one derived from FLUKA simulations (1% statistical) and the one derived from the knowledge of the active length of the IC (3%, i.e. 1 mm over 34 mm, statistical). It should also be mentioned that there is also a systematic uncertainty on the FLUKA results, of the order of a few percent for the part due to ionization and of about 10% for the part due to nuclear interactions, which is not included in the uncertainties of the present result.

The calibration factor estimated via the FLUKA simulations is in excellent agreement with the value determined experimentally (see Table IV). The present results are also in good agreement with past experimental results obtained with different calibration techniques: activation of ^{18}F ($23000 \pm 2300 \text{ particles/count}$ [20]) and ^{12}C foils ($23400 \pm 1400 \text{ particles/count}$ [21]), and coincidence of scintillators ($22116 \pm 92 \text{ particles/count}$ [22]).

Table IV. IC calibration factor as obtained from the activation experiments and via FLUKA simulations.

Technique	IC calibration factor [particles/count]
Activation of ^{27}Al foils	22249 ± 2100
Activation of $^{\text{nat}}\text{Cu}$ foils	22293 ± 1493
FLUKA simulations	22172 ± 789

A. $^{27}\text{Al}(p,3px)^{24}\text{Na}$ reaction

The activation of aluminium foils proved to be a reliable technique for the determination of the intensity of high energy hadron beams and the calibration of an IC. However, attention must be paid to the factors that could severely affect the experimental results. The cross section value has been discussed in Sec. 2.B. This section describes *a posteriori* the effects of the competing reactions and of the recoil nuclei escaping the foil, based on the present experimental results.

1. Competing reactions

Two competing mechanisms lead to the production of ^{24}Na : the $^{27}\text{Al}(n,\alpha)^{24}\text{Na}$ and the reactions induced by energetic secondary hadrons. The $^{27}\text{Al}(n,\alpha)^{24}\text{Na}$ reaction has a threshold of 5.5 MeV and a cross section rising to 120 mb at 14 MeV [23]. Data in the literature are contradictory about the importance of this effect. Some authors showed it has little importance: Stehney [24] measured a contribution of less than 1% per 200 mg/cm² foil thickness, while Cumming et al. [25] proposed a value of 0.25% per 100 mg/cm². Other authors estimated a bigger importance: Brandt et al. [26] reported that this effect has an influence in the order of $1.1 \pm 0.5\%$ per 100 mg/cm², while Grover [27] showed a strong dependence on foil thickness, about 3.3% per 100 mg/cm². All these estimates refer to protons; no data are available for different particles. The contribution of the competing reactions has here been determined by analysing the results obtained from the present experiment. It is worth noting that this contribution may also depend on the materials present upstream and downstream of the target as well as on the characteristics of the resulting neutron “halo”.

One can express the calibration factor as the sum of two terms: the first is due to the activity induced by the primary particles, the second to the activity induced by the secondary particles (neutrons and high energy hadrons), which is proportional to the foil mass thickness and to a coefficient k (expressed in percent per 100 mg/cm²):

$$C_x = C_{\text{prim}} + k \cdot C_{\text{prim}} \cdot x, \quad (6)$$

where C_x is the calibration factor obtained for a foil of mass thickness x and C_{prim} is the calibration factor extrapolated to zero thickness. The constant k here refers to the partial activity due to the primary particles, whereas in other papers the contribution refers to the total activity. This choice was done to make expression (6) more consistent (the numerical difference is nevertheless of little importance). One can derive the value of the

constant k from the linear fit in Fig. 3: $C_{\text{prim}} = 22249$ particles/count, $k \cdot C_{\text{prim}} = 2581$ particles/count/mm. By normalizing the constant to the foil mass thickness ($1 \text{ mm} = 271 \text{ mg/cm}^2$, see Table II) one then obtains $k = 0.116 \text{ mm}^{-1} = 4.3\% / 100 \text{ mg/cm}^2$, close to the data of Grover for protons [27]. It must be noted that the value obtained by Grover refers to the $^{27}\text{Al}(n,\alpha)^{24}\text{Na}$ reaction only, whereas here the two contributions cannot be evaluated separately.

2. Recoil nuclei effect

To take into account the recoil nuclei effect only the activity of the central foil of the sandwich was employed in expression (1) (except for measurement 1). The loss of nuclei knocked out of the foil is in fact not compensated in the case of the upstream one. To verify the importance of the effect, for some measurements several analyses were carried out (see Table I). However all the activity values are compatible within 2σ . This shows that the importance of this effect is very limited. This is confirmed by the FLUKA interaction models, which give a mean energy of the recoil ^{24}Na nuclei of about 2 MeV. This corresponds to a projected range of $2 \mu\text{m}$ in the Al target, i.e. only the nuclei produced in the last layer (a few microns) of the foil escape in the beam direction. This fraction corresponds to a maximum of about 0.4% on the overall activity for the 0.5 mm sandwich.

B. $^{\text{nat}}\text{Cu}(p,x)^{24}\text{Na}$

The IC calibration performed via the activation of copper foils showed results consistent with those obtained by the better known activation of aluminium foils. Moreover, due to the higher accuracy with which the cross section of the $^{\text{nat}}\text{Cu}(p,x)^{24}\text{Na}$ reaction is known, the final uncertainty is lower. The validity of this alternative reaction is also confirmed by the agreement with the results obtained from the FLUKA simulations. The $^{\text{nat}}\text{Cu}(p,x)^{24}\text{Na}$ reaction has the advantage that there are no competing neutron-induced reactions producing ^{24}Na and that the contribution from energetic secondary hadrons is negligible.

V. CONCLUSIONS

Both monitoring reactions employed in the present activation experiment showed to be reliable. This is confirmed by the excellent agreement between the value of the IC calibration factor derived from the measurements with the two materials with the value obtained from the FLUKA simulations and from past calibrations carried out with different techniques. The $^{\text{nat}}\text{Cu}(p,x)^{24}\text{Na}$ reaction shows several advantages if compared to $^{27}\text{Al}(p,3px)^{24}\text{Na}$: competing reactions play a little role and the final uncertainty on the result is lower because of the higher accuracy with which the absolute cross section is known at very high energies. However, since the cross section is lower than that of the $^{27}\text{Al}(p,3px)^{24}\text{Na}$ reaction, a longer irradiation time is necessary in order to decrease the statistical uncertainty of the γ -spectrometry measurements. The effect of the competing reactions on the overall activity in the case of the activation of aluminium foils has been derived for the mixed proton/pion beam at CERF, i.e. $4.3\% / 100 \text{ mg/cm}^2$. Similarly the effect of loss of recoil nuclei knocked out of the foil showed to be of very little importance.

Acknowledgements

The authors wish to thank Matteo Magistris for providing access to the γ -spectrometry laboratory, Yann Donjoux and Francesco Cerutti for useful discussions, Nicolas Sabbi, Nicolas Riggaz and Biagio Zaffora for performing the γ -spectrometry measurements and Clizia Severino for assisting with some of the measurements.

APPENDIX

The production of a radionuclide of interest at a time t is expressed by the well-known formula:

$$n(t) = \frac{N\sigma\phi}{\lambda} (1 - e^{-\lambda t_{IRR}}) \cdot e^{-\lambda t_{WAIT}}, \quad (A1)$$

where $n(t)$ is the number density of the atoms of the radionuclide of interest at time t (cm^{-3}), N is the number density of the target atoms (cm^{-3} , where $N = \rho \cdot N_{AV}/M$: ρ is the mass density in $\text{g}\cdot\text{cm}^{-3}$, N_{AV} is the Avogadro's number $6.022 \cdot 10^{23} \text{ mol}^{-1}$, M is the molar mass expressed in $\text{g}\cdot\text{mol}^{-1}$), σ is the production cross section of the selected radioisotope (cm^2), λ is its decay constant (s^{-1}), ϕ is the particle flux density ($\text{cm}^{-2}\cdot\text{s}^{-1}$), t_{IRR} and t_{WAIT} (s) are the irradiation time and waiting time. The specific activity induced in the target at time t is given by $a(t) = \lambda \cdot n(t)$:

$$a(t) = N\sigma\phi(1 - e^{-\lambda t_{IRR}}) \cdot e^{-\lambda t_{WAIT}}, \quad (A2)$$

where $a(t)$ is expressed in $\text{Bq}\cdot\text{cm}^{-3}$. If L_1, L_2 are the transverse dimensions of the target and Δx its thickness the absolute activity $A(t) = a(t) \cdot L_1 \cdot L_2 \cdot \Delta x$ in Bq is equal to:

$$A(t) = N\Delta x \cdot \sigma \cdot \phi L_1 L_2 \cdot (1 - e^{-\lambda t_{IRR}}) \cdot e^{-\lambda t_{WAIT}}. \quad (A3)$$

If $N_x = N \cdot \Delta x$ is the surface atomic density (cm^{-2}), the particle flux $\phi' = \phi \cdot L_1 \cdot L_2$ (number of particles per second traversing the foil) is given by (expression 1 in section II.A):

$$\phi' = \frac{A(t)}{N_x \cdot \sigma \cdot (1 - e^{-\lambda t_{IRR}}) \cdot e^{-\lambda t_{WAIT}}}. \quad (A4)$$

References

- [1] P. Forck, Beam current measurements, lecture given at the Joint Universities Accelerator School (JUAS), Archamps, France, 2013, available at: http://www-bd.gsi.de/conf/juas/current_trans.pdf.
- [2] J. Belleman, D. Belohrad, L. Jensen, M. Krupa, and A. Topaloudis, in Proceedings of the 2nd International Beam Instrumentation Conference (IBIC), Oxford, 2013.
- [3] J. Harasimowicz and C.P. Welsch, in Proceedings of the 2010 Beam Instrumentation Workshop (BIW), Santa Fe, New Mexico, USA, 2010.
- [4] J.H. So, H.J. Kim, H. Kang, H. Park, S. Ryu, and S. W. Jung, *J. Korean Phys. Soc.* 50 (2007) 1506-1509.
- [5] H.S. Kim, S.H. Park, Y.K. Kim, J.H. Ha, S.M. Kang, and C.E. Chung, *J. Korean Phys. Soc.* 48 (2006) 213-217.
- [6] K. Bernier, G. de Rijk, G. Ferioli, E. Hatziangeli, A. Marchionni, V. Palladino, G.R. Stevenson, T. Tabarelli de Fatis, and E. Tsesmelis, CERN Yellow Report 97-07, 1997.
- [7] L. Badano, O. Ferrando, M. Caccia, C. Cappellini, V. Chmill, M. Jastrzab, K. Abbas, U. Holzwarth, P.N. Gibson, in Proceedings of the 2007 European Workshop on Beam Diagnostics and Instrumentation for Particle Accelerators (DIPAC), Venice, Italy, 2007.
- [8] H.W. Atherton, C. Bovet, N. Doble, G. Von Holtey, L. Piemontese, A. Placci, M. Placidi, D.E. Plane, M. Reinharz, and E. Rossa, CERN Yellow Report 80-07, 1980.
- [9] G. Battistoni, S. Muraro, P.R. Sala, F. Cerutti, A. Ferrari, S. Roesler, A. Fassò, J. Ranft, in Proceedings of the 2006 Hadronic Shower Simulation Workshop, Fermilab, US, 2006, M. Albrow, R. Raja eds., AIP Conference Proceeding 896, 31-49, 2007.
- [10] A. Fassò, A. Ferrari, J. Ranft, and P.R. Sala, CERN-2005-10, INFN/TC_05/11, SLAC-R-773, 2005.
- [11] S.B. Kaufman, M.W. Weisfield, E.P. Steinberg, B.D. Wilkins, and D.J. Henderson, *Phys. Rev. C* 19 (1979) 962-964 .
- [12] Nuclear reaction database (EXFOR): <http://cdf.e.sinp.msu.ru/>, 2013.
- [13] D. Filges, F. Goldenbaum, Handbook of spallation research, Wiley-VCH, Weinheim, 2009.
- [14] S.I. Baker, R.A. Allen, and P. Yurista, *Phys. Rev. C* 43 (1991) 2862-2865.
- [15] A. Mitaroff and M. Silari, *Radiat. Prot. Dosim.* 102 (2002) 7-22.
- [16] GoodFellow, See online catalogue at <http://www.goodfellow.com>, 2013.
- [17] J.B. Cumming, *Annu. Rev. Nucl. Sci.* 13 (1963) 261-286.
- [18] Korea Atomic Energy Research Institute (KAERI), Photon cross sections and attenuation coefficients, <http://atom.kaeri.re.kr>, 2013.
- [19] IAEA, Technical Report Series 398, 2000.
- [20] M.C. Hopper, C. Raffinsoe, and G.R. Stevenson, CERN/TIS/RP/TM/93-21, 1993.
- [21] G.R. Stevenson, J.C. Liu, K. O'Brien, and J. Williams, CERN/TIS/RP/TM/94-15, 1994.
- [22] H. Vincke, S. Mayer, I. Efthymiopoulos, A. Fabich, D. Forkel-Wirth, M.J. Muller, and C. Theis, CERN/SC/RP/TN/2004-090, 2004.
- [23] J.P. Butler and D.C. Santry, *Can. J. Phys.* 41 (1963) 372.
- [24] A.F. Stehney, *Nucl. Instrum. Methods* 59 (1968) 102-108.
- [25] J.B. Cumming, J. Hudis, A.M. Poskanzer, and S. Kaufman, *Phys. Rev.* 128 (1962) 2392.
- [26] R. Brandt, C. Gfeller, and W. Stotzel-Riezler, *Nucl. Instrum. Methods* 62 (1968) 109-112.
- [27] J.R. Grover, *Phys. Rev.* 126 (1962) 1540.

Spallation cross sections for ^{nat}Fe and ^{nat}Cu targets for 120 GeV/c protons and pions

A. Ferrari¹, F.P. La Torre^{1,2}, G.P. Manessi^{1,3}, F. Pozzi^{1,4}, M. Silari¹

¹CERN, 1211 Geneva 23, Switzerland

²University of Bern, AEC-LHEP, Sidlerstrasse 5, 3102 Bern, Switzerland

³University of Liverpool, Department of Physics, L69 7ZE Liverpool, UK

⁴Technische Universität München, Lehrstuhl für Nukleartechnik, Boltzmannstrasse 15, 85748 Garching, Germany

Abstract

Spallation cross sections from thin natural copper and iron targets bombarded by a mixed 120 GeV/c proton/pion beam were measured in an activation experiment at CERN. The beam intensity was monitored by a calibrated ionisation chamber and the activity of several spallation products was measured (14 for copper and 16 for iron) by γ -spectrometry, allowing the absolute cross section of the mixed hadron beam to be derived. Monte Carlo simulations with the FLUKA code provided the ratio between the proton- and pion-induced reaction cross sections for a given spallation product, allowing to extrapolate the individual cross sections for the proton- and the pion-induced reactions. Where possible the values were compared with literature data and showed to be generally in agreement with the highest energy data available.

I. INTRODUCTION

Spallation refers to nuclear inelastic reactions that occur when subatomic particles with incident energy higher than 100-150 MeV interact with a target nucleus. At these energies the de Broglie wavelength is short enough to allow the particle to interact with the individual nucleons inside the nucleus. The incident particle first undergoes a series of reactions with the nucleons, where high-energy secondary particles (such as protons, neutrons and pions) from a few MeV up to the energy of the incident particle are created inside the nucleus (intranuclear cascade). Some of these high-energy hadrons, together with low-energy particles in the MeV range, leave the nucleus and may induce other spallation reactions in a different nucleus (internuclear cascade). This process mainly occurs in thick targets. The nucleus, which is in an excited state, relaxes by emitting low energy particles, mostly neutrons. After evaporation the final nucleus (spallation product) may be radioactive and decay by γ -emission [1]. An accurate knowledge of the spallation product inventory within a target is important for many applications: disposal of material, operation, maintenance, safety and decay heat analysis for neutron spallation sources [2], activation issues in high-energy particle accelerators [3] and benchmarking of Monte Carlo codes [4]. The knowledge of the reaction cross section for a spallation product is therefore fundamental. Spallation cross section data are widely available for energies up a few GeV [5], but for higher energies (especially above 28 GeV) very limited data have been published. This is particularly true for pion-induced reactions for which, to the best of our knowledge, no data are available. The aim of this paper is to provide proton- and pion-induced spallation cross sections at 120 GeV/c for the production of 14 radioisotopes in ^{nat}Cu and 16 radioisotopes in ^{nat}Fe targets. These have been derived from activation experiments carried out with a 120 GeV/c mixed proton/pion beam at the CERN-EU high-energy Reference Field (CERF) facility [6] at CERN. These spallation reactions are of direct relevance in activation studies, since ^{nat}Cu and ^{nat}Fe are commonly employed in high-energy particle accelerators and their surrounding structures.

II. MATERIALS AND METHODS

A. Experimental set-up

The experiments were performed by exposing hyperpure ^{nat}Cu and ^{nat}Fe foils to the primary beam at the CERF facility, which is installed in one of the secondary beam lines (H6) from the Super Proton Synchrotron (SPS) in the North Experimental Area on the Prévessin site of CERN. The incoming hadron beam is composed by 61% positive pions, 35% protons and 4% positive kaons [7] with momentum of 120 GeV/c. For simplicity we assume that the particle energy is 120 GeV, even if the actual value is slightly lower. For the calculations the kaon fraction has been re-distributed on the other two components according to their relative weight, i.e. the beam composition has been assumed to be 63.5% positive pions and 36.5% protons. This re-distribution has a negligible effect because of the limited importance of the kaon component, whose relative weight is well below the final relative uncertainty on the cross section values derived from the experiment, and because the kaon-induced spallation cross section lies in between the proton- and the pion-induced one as verified via FLUKA [8,9] Monte Carlo simulations. The beam is delivered to CERF with a typical intensity in the range 10^6 to 10^8 particles per SPS spill, with a beam extraction time of about 10 s over an SPS cycle of about 45 s.

The ^{nat}Cu and ^{nat}Fe foils with dimensions $50 \times 50 \text{ mm}^2$ were fixed on a Plexiglas frame mounted on both ends of a hollow aluminium tube placed downstream of an ionisation chamber (IC) used as beam monitor (see Fig. 1). The foils were irradiated in sandwiches of three to take into account the recoil of some of the nuclei produced in the spallation process that can leave the foil in the same direction of the primary beam (due to the so-called Lorentz boost [1]). To maintain the equilibrium between the loss of recoil nuclei knocked out of the foil and the gain of nuclei knocked into the foil from upstream material, only the central one must be considered for data analysis, whereas the upstream and the downstream ones act as catchers. These catchers, having the same thickness of the central foil, are thick enough to capture all the knocked on or knocked back products. The beam size was smaller than the foil dimensions so that all particles traversing the IC hit the foils. To evaluate the contribution of scattered radiation to the foil activation an additional foil was exposed out of beam.

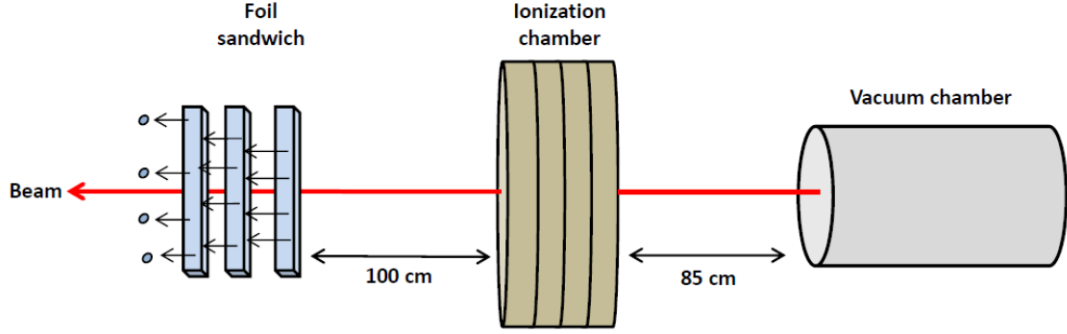


FIG. 1. Experimental set-up (not to scale).

The foil thicknesses were 0.5 mm, 0.25 mm and 0.125 mm for $^{\text{nat}}\text{Cu}$; 2 mm for $^{\text{nat}}\text{Fe}$, with 1% estimated uncertainty. The thicknesses were chosen as a compromise between the need of an induced activity high enough to reduce the statistical uncertainty of the γ -spectrometry measurements and the need of thin targets, i.e. targets in which the energy lost by the incident beam is small ($E_{\text{loss}} / E_{\text{beam}} \leq 5\%$ [1]). This reduces to a minimum the production of secondary particles inside the target, which generally undergo further collisions and could result in internuclear cascades. By assuming that the value of the interaction lengths for protons and pions at 120 GeV is similar to the one at 18 GeV (i.e. $140.2 \pm 3.2 \text{ g/cm}^2$ for protons, $163.8 \pm 9.0 \text{ g/cm}^2$ for pions [10]), the beam fraction that interacts in the target is always less than 1%. This guarantees that, even though the average fraction of energy of the incident beam lost in the target cannot be precisely estimated, the overall influence of the target on the beam transmission is negligible.

B. Theory

The cross section of the reaction $A(p,x)B$ or $A(\pi^+,x)B$, where A is $^{\text{nat}}\text{Cu}$ or $^{\text{nat}}\text{Fe}$, B is the radioisotope produced in the foil by the spallation reaction and x is the reaction product escaping the foil, was measured via the well-established foil activation technique (see e.g. [11] and references therein quoted). If $A(t)$ (Bq) is the activity of the radioisotope B, λ is its decay constant (s^{-1}), t_{IRR} and t_{WAIT} (s) are the irradiation time and waiting time (i.e. the time elapsed from the end of the irradiation until the foil is counted), N_x is the foil surface atomic density (cm^{-2}), ϕ' is the particle flux (number of particles per second traversing the foil), the production cross section σ of the radioisotope B can be obtained as [11]:

$$\sigma = \frac{A(t)}{N_x \cdot \phi' \cdot (1 - e^{-\lambda t_{\text{IRR}}}) \cdot e^{-\lambda t_{\text{WAIT}}}} \quad (1)$$

$A(t)$ is measured by γ -spectrometry, while t_{WAIT} and t_{IRR} must be recorded. In the present experiment t_{WAIT} was recorded manually while t_{IRR} was obtained from the log-file of the acquisition system. The cross section σ is the beam effective cross section, i.e. averaged over the pion and proton components: $\sigma = 0.635 \cdot \sigma_{\pi} + 0.365 \cdot \sigma_p$, where σ_p and σ_{π} are the proton- and pion-induced spallation cross sections. Their values can be derived if one knows the ratio σ_p / σ_{π} . This ratio can be obtained from FLUKA simulations. Although FLUKA cannot compute the absolute cross section value at very high energies with the required accuracy, it is reliable in determining the cross section ratio of a reaction induced by different particles at the same energy. The ratio can be obtained by running the nuclear interaction models of FLUKA in interaction only mode, accounting for both absorption and quasi-elastic reactions [11]. The output file provides the cross section for each isotope produced in the interaction between the primary and the target. By running two simulations (for protons and for pions) one obtains the ratio σ_p / σ_{π} for the reaction of interest. The cross sections for protons and pions can then be easily derived:

$$\sigma_{\pi} = \frac{\sigma}{0.635 + 0.365 \frac{\sigma_p}{\sigma_{\pi}}} \quad \text{and} \quad (2)$$

$$\sigma_p = \frac{\sigma - 0.635 \cdot \sigma_{\pi}}{0.365} \quad (3)$$

C. Parameters

The hyperpure ^{nat}Cu and ^{nat}Fe foils have the following compositions, as declared by the manufacturer [12]: 99.991% ^{nat}Cu , with impurities in ppm: Ag 70, Fe 2, Ni 2, Pb 2, Si 2, Al 1, Bi 1, Ca 1, Mg 1, Sn 1, Mn < 1, Na < 1, Cr < 1; 99.998% ^{nat}Fe , impurities in ppm: Ag 1, Al 2, Ca 3, Cr 1, Cu 2, Mg 2, Mn 1, Ni 1, Si 3. The effect of the impurities on the radioisotope production is negligible. This has been verified via several sets of FLUKA simulations, in which the foils were first simulated as 100% pure, and then with added impurities. The values of the surface atomic densities N_x to be used in expression (1) are obtained from the foil density, the molar mass and the thickness (see Table I).

Table I. Foil atomic surface densities.

Fe foils ($\rho_{\text{Fe}} = 7.874 \text{ g/cm}^3$, $M_{\text{Fe}} = 55.840 \text{ g/mol}$)			
Foil thickness X_{Fe}	2.0 mm		
N_x	$1.6983 \cdot 10^{22} \text{ cm}^{-2}$		
Cu foils ($\rho_{\text{Cu}} = 8.920 \text{ g/cm}^3$, $M_{\text{Cu}} = 63.546 \text{ g/mol}$)			
Foil thickness X_{Cu}	0.125 mm	0.250 mm	0.500 mm
N_x	$1.0567 \cdot 10^{21} \text{ cm}^{-2}$	$2.1133 \cdot 10^{21} \text{ cm}^{-2}$	$4.2266 \cdot 10^{21} \text{ cm}^{-2}$

The beam monitoring was provided by an air-filled, parallel-plate, transmission type IC, calibrated with the foil activation technique using the $^{27}\text{Al}(p,3p)^{24}\text{Na}$ and $^{nat}\text{Cu}(p,x)^{24}\text{Na}$ monitor reactions [11]. The beam intensity recorded by the IC was written every second in a log-file, from which the value of ϕ' to be used in expression (1) was obtained. Since the beam intensity was recorded every second, the irradiation time was subdivided in one second irradiation slots ($t_{\text{IRR}} = 1 \text{ s}$). For each of these slots a corresponding waiting time t_{WAIT} was considered. Thanks to this method any fluctuation in the beam intensity during the irradiation was properly taken into account.

The foils were counted in the CERN γ -spectrometry laboratory with a Canberra low background coaxial high-purity germanium (HPGe) detector. For a more accurate analysis of the gamma lines, the activated foils were counted twice: a short (10 minutes) measurement immediately after the irradiation and a longer one (about 8 hours) later. The analysis was performed using the Canberra Genie 2000 and the PROcount 2000 software, which are comprehensive environments for data acquisition, display and analysis. They include a set of spectrum analysis algorithms, which provide nuclide identification, interference correction, weighted mean activity, background subtraction and efficiency correction. They also take into account geometrical effects, self-absorption in the sample and decay of the isotope during the measurements, and provide a global uncertainty. Only the radioisotopes with an activity higher than 1 Bq were considered for the cross section calculations.

III. RESULTS

The beam effective cross section σ for each of the reactions of interest was derived from expression (1) by employing the values of N_x , ϕ' , $A(t)$, t_{WAIT} and t_{IRR} , obtained as explained in Section II. The cross sections of the proton- and pion-induced reactions were calculated from expressions (2) and (3). The foil exposed out of beam did not show any significant induced activity, confirming that the contribution of the scattered radiation (background) to the overall activity is negligible. Tables II and III list the cross sections of the spallation reactions that generated an activity in the foils higher than 1 Bq. The global uncertainty is the quadratic sum of the uncertainty on the γ -spectrometry, the one on the IC calibration factor (10%) and the uncertainty on the foil thickness, i.e. on the knowledge of N_x . The uncertainty on the beam composition is not taken into account since it is below 2% [7]. The production of the radioisotopes listed in Tables II and III derives only from the proton- and pion-induced spallation reactions. For the reactions on ^{nat}Cu foils the cross section is the average of the values obtained from the three thicknesses.

Table II. Cross sections of the spallation reactions on ^{nat}Cu derived from the activation experiment.

$^{nat}\text{Cu}(p,x)^{41}\text{Ar}$	$0.62 \pm 0.11 \text{ mb}$	$^{nat}\text{Cu}(\pi^+,x)^{41}\text{Ar}$	$0.43 \pm 0.08 \text{ mb}$
$^{nat}\text{Cu}(p,x)^{42}\text{K}$	$2.23 \pm 0.40 \text{ mb}$	$^{nat}\text{Cu}(\pi^+,x)^{42}\text{K}$	$1.69 \pm 0.30 \text{ mb}$
$^{nat}\text{Cu}(p,x)^{43}\text{K}$	$0.93 \pm 0.19 \text{ mb}$	$^{nat}\text{Cu}(\pi^+,x)^{43}\text{K}$	$0.66 \pm 0.14 \text{ mb}$

${}^{\text{nat}}\text{Cu}(p,x){}^{43}\text{Sc}$	2.73 ± 0.26 mb	${}^{\text{nat}}\text{Cu}(\pi^+,x){}^{43}\text{Sc}$	2.62 ± 0.25 mb
${}^{\text{nat}}\text{Cu}(p,x){}^{44}\text{Sc}$	3.80 ± 0.17 mb	${}^{\text{nat}}\text{Cu}(\pi^+,x){}^{44}\text{Sc}$	3.46 ± 0.15 mb
${}^{\text{nat}}\text{Cu}(p,x){}^{47}\text{Sc}$	1.85 ± 0.22 mb	${}^{\text{nat}}\text{Cu}(\pi^+,x){}^{47}\text{Sc}$	1.42 ± 0.17 mb
${}^{\text{nat}}\text{Cu}(p,x){}^{48}\text{Cr}$	0.21 ± 0.06 mb	${}^{\text{nat}}\text{Cu}(\pi^+,x){}^{48}\text{Cr}$	0.21 ± 0.06 mb
${}^{\text{nat}}\text{Cu}(p,x){}^{48}\text{Sc}$	1.16 ± 0.21 mb	${}^{\text{nat}}\text{Cu}(\pi^+,x){}^{48}\text{Sc}$	0.83 ± 0.15 mb
${}^{\text{nat}}\text{Cu}(p,x){}^{52}\text{Mn}$	3.83 ± 0.52 mb	${}^{\text{nat}}\text{Cu}(\pi^+,x){}^{52}\text{Mn}$	3.87 ± 0.52 mb
${}^{\text{nat}}\text{Cu}(p,x){}^{55}\text{Co}$	0.51 ± 0.10 mb	${}^{\text{nat}}\text{Cu}(\pi^+,x){}^{55}\text{Co}$	0.56 ± 0.11 mb
${}^{\text{nat}}\text{Cu}(p,x){}^{56}\text{Mn}$	2.68 ± 0.14 mb	${}^{\text{nat}}\text{Cu}(\pi^+,x){}^{56}\text{Mn}$	2.01 ± 0.10 mb
${}^{\text{nat}}\text{Cu}(p,x){}^{57}\text{Ni}$	0.77 ± 0.14 mb	${}^{\text{nat}}\text{Cu}(\pi^+,x){}^{57}\text{Ni}$	0.77 ± 0.14 mb
${}^{\text{nat}}\text{Cu}(p,x){}^{58}\text{Co}$	18.82 ± 6.01 mb	${}^{\text{nat}}\text{Cu}(\pi^+,x){}^{58}\text{Co}$	18.07 ± 5.77 mb
${}^{\text{nat}}\text{Cu}(p,x){}^{61}\text{Cu}$	11.12 ± 0.51 mb	${}^{\text{nat}}\text{Cu}(\pi^+,x){}^{61}\text{Cu}$	11.46 ± 0.52 mb

Table III. Cross sections of the spallation reactions on ${}^{\text{nat}}\text{Fe}$ derived from the activation experiment.

${}^{\text{nat}}\text{Fe}(p,x){}^{24}\text{Na}$	4.02 ± 0.45 mb	${}^{\text{nat}}\text{Fe}(\pi^+,x){}^{24}\text{Na}$	2.96 ± 0.33 mb
${}^{\text{nat}}\text{Fe}(p,x){}^{41}\text{Ar}$	0.84 ± 0.16 mb	${}^{\text{nat}}\text{Fe}(\pi^+,x){}^{41}\text{Ar}$	0.53 ± 0.10 mb
${}^{\text{nat}}\text{Fe}(p,x){}^{42}\text{K}$	4.28 ± 0.57 mb	${}^{\text{nat}}\text{Fe}(\pi^+,x){}^{42}\text{K}$	3.18 ± 0.43 mb
${}^{\text{nat}}\text{Fe}(p,x){}^{43}\text{K}$	1.42 ± 0.19 mb	${}^{\text{nat}}\text{Fe}(\pi^+,x){}^{43}\text{K}$	0.92 ± 0.12 mb
${}^{\text{nat}}\text{Fe}(p,x){}^{43}\text{Sc}$	3.72 ± 0.63 mb	${}^{\text{nat}}\text{Fe}(\pi^+,x){}^{43}\text{Sc}$	3.73 ± 0.63 mb
${}^{\text{nat}}\text{Fe}(p,x){}^{44}\text{Sc}$	8.32 ± 0.93 mb	${}^{\text{nat}}\text{Fe}(\pi^+,x){}^{44}\text{Sc}$	7.87 ± 0.88 mb
${}^{\text{nat}}\text{Fe}(p,x){}^{46}\text{Sc}$	6.07 ± 2.36 mb	${}^{\text{nat}}\text{Fe}(\pi^+,x){}^{46}\text{Sc}$	4.87 ± 1.89 mb
${}^{\text{nat}}\text{Fe}(p,x){}^{47}\text{Sc}$	3.96 ± 0.54 mb	${}^{\text{nat}}\text{Fe}(\pi^+,x){}^{47}\text{Sc}$	2.93 ± 0.40 mb
${}^{\text{nat}}\text{Fe}(p,x){}^{48}\text{Cr}$	0.59 ± 0.08 mb	${}^{\text{nat}}\text{Fe}(\pi^+,x){}^{48}\text{Cr}$	0.64 ± 0.08 mb
${}^{\text{nat}}\text{Fe}(p,x){}^{48}\text{Sc}$	0.61 ± 0.13 mb	${}^{\text{nat}}\text{Fe}(\pi^+,x){}^{48}\text{Sc}$	0.37 ± 0.08 mb
${}^{\text{nat}}\text{Fe}(p,x){}^{48}\text{V}$	16.55 ± 2.09 mb	${}^{\text{nat}}\text{Fe}(\pi^+,x){}^{48}\text{V}$	16.25 ± 2.05 mb
${}^{\text{nat}}\text{Fe}(p,x){}^{51}\text{Cr}$	29.47 ± 11.61 mb	${}^{\text{nat}}\text{Fe}(\pi^+,x){}^{51}\text{Cr}$	28.19 ± 11.11 mb
${}^{\text{nat}}\text{Fe}(p,x){}^{52}\text{Fe}$	0.49 ± 0.07 mb	${}^{\text{nat}}\text{Fe}(\pi^+,x){}^{52}\text{Fe}$	0.54 ± 0.08 mb
${}^{\text{nat}}\text{Fe}(p,x){}^{52}\text{Mn}$	10.31 ± 1.16 mb	${}^{\text{nat}}\text{Fe}(\pi^+,x){}^{52}\text{Mn}$	10.48 ± 1.18 mb
${}^{\text{nat}}\text{Fe}(p,x){}^{54}\text{Mn}$	44.82 ± 8.83 mb	${}^{\text{nat}}\text{Fe}(\pi^+,x){}^{54}\text{Mn}$	43.21 ± 8.51 mb
${}^{\text{nat}}\text{Fe}(p,x){}^{55}\text{Co}$	0.62 ± 0.08 mb	${}^{\text{nat}}\text{Fe}(\pi^+,x){}^{55}\text{Co}$	0.51 ± 0.07 mb

A comparison between the cross section obtained at 120 GeV and the ones found in the literature at lower energies is given in the Appendix, which shows the data available for proton-induced spallation reactions (for the pion-induced reactions no data are available) at energies higher than 500 MeV.

IV. CONCLUSIONS

A comparison with literature data of the cross sections of proton- and pion-induced spallation reactions on ${}^{\text{nat}}\text{Cu}$ and ${}^{\text{nat}}\text{Fe}$ targets obtained in this experiment showed that in most cases the cross section at 120 GeV is comparable with the values available at the highest energies, i.e. around 20-30 GeV, confirming that the cross section is energy independent above a certain energy. This behaviour is coherent with the fact that above about a few hundred MeV, the total elastic and non-elastic cross sections for hadron-nucleus collisions are approximately constant [1]. This is foreseen by many physical models: the Sihver model [13], valid for $Z_{\text{target}} \leq 26$, which assumes that in a proton-nucleus interaction the cross section is energy-independent for energies above 200 MeV; the limiting fragmentation model [14], which assumes the energy-independence of the

cross section for sufficiently high energies of the bombarding particle; the Letaw model [15], valid for $Z_{\text{target}} > 5$, which assumes that in a proton-nucleus interaction the cross section is energy independent above 2 GeV, with a possible small increase at very high energies (≥ 100 GeV); the Glauber model [16], which allows to compute reliably the hadron-nucleus cross section on the basis of the hadron-proton one and of the nuclear density distribution, which predicts cross sections almost constant at energies above a few GeV with a slow increase at the highest energies. Further activation experiments are foreseen in the next future to validate the results presented in this paper.

ACKNOWLEDGEMENTS

The authors wish to thank Matteo Magistris for providing access to the γ -spectrometry laboratory, Nicolas Riggaz and Biagio Zaffora for performing the γ -spectrometry measurements and Clizia Severino for helping in some of the measurements.

APPENDIX

Figures A1 and A2 plot the cross section values available in the literature [5] as a function of energy for proton-induced spallation reactions on ^{nat}Cu and ^{nat}Fe , respectively, at energies higher than 500 MeV, together with the values derived in this paper at 120 GeV. The cross section distributions for reactions where very few data are available in the literature ($^{nat}\text{Cu}(p,x)^{41}\text{Ar}$, $^{nat}\text{Fe}(p,x)^{41}\text{Ar}$, $^{nat}\text{Fe}(p,x)^{43}\text{Sc}$, $^{nat}\text{Fe}(p,x)^{44}\text{Sc}$) are not shown.

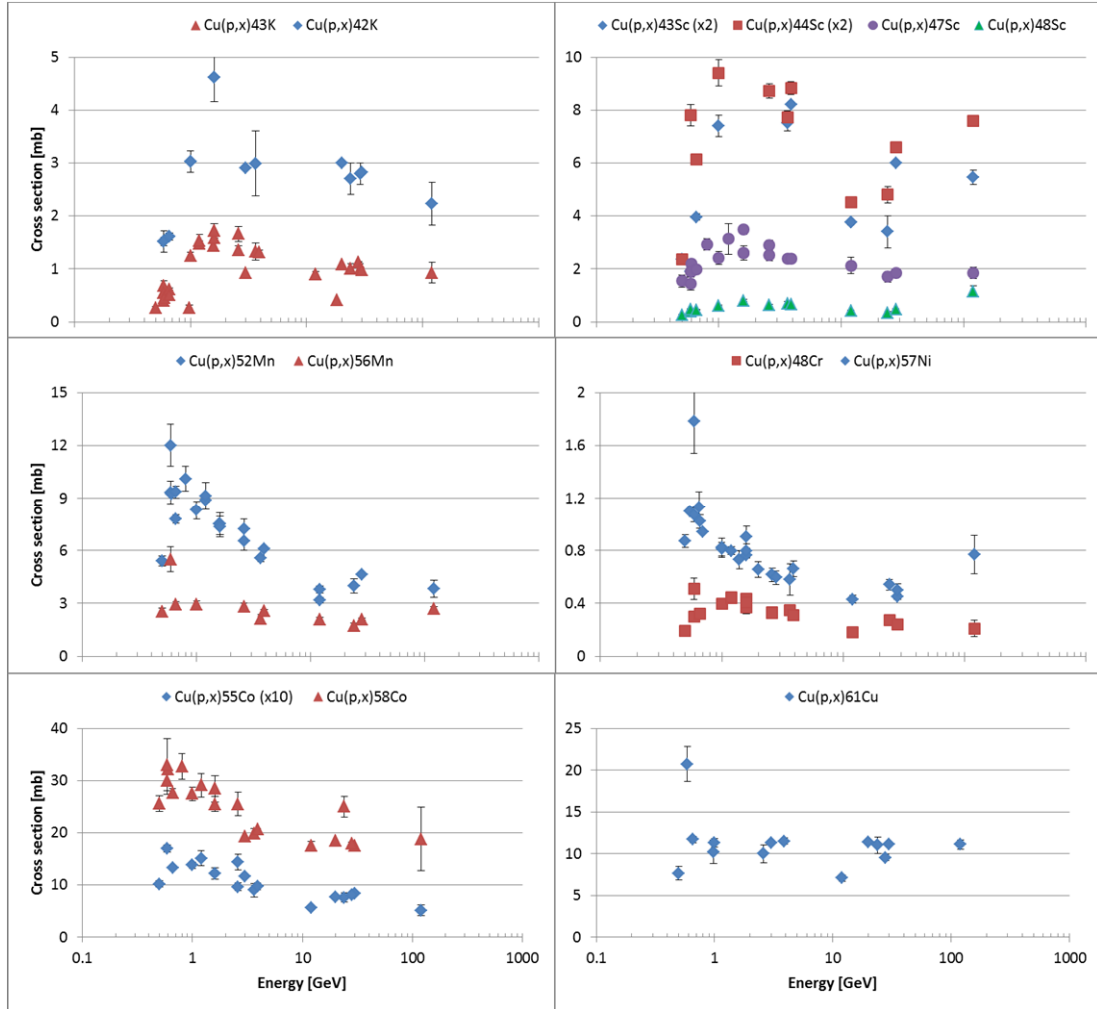


Figure A1. Cross sections of the spallation reactions on ^{nat}Cu .

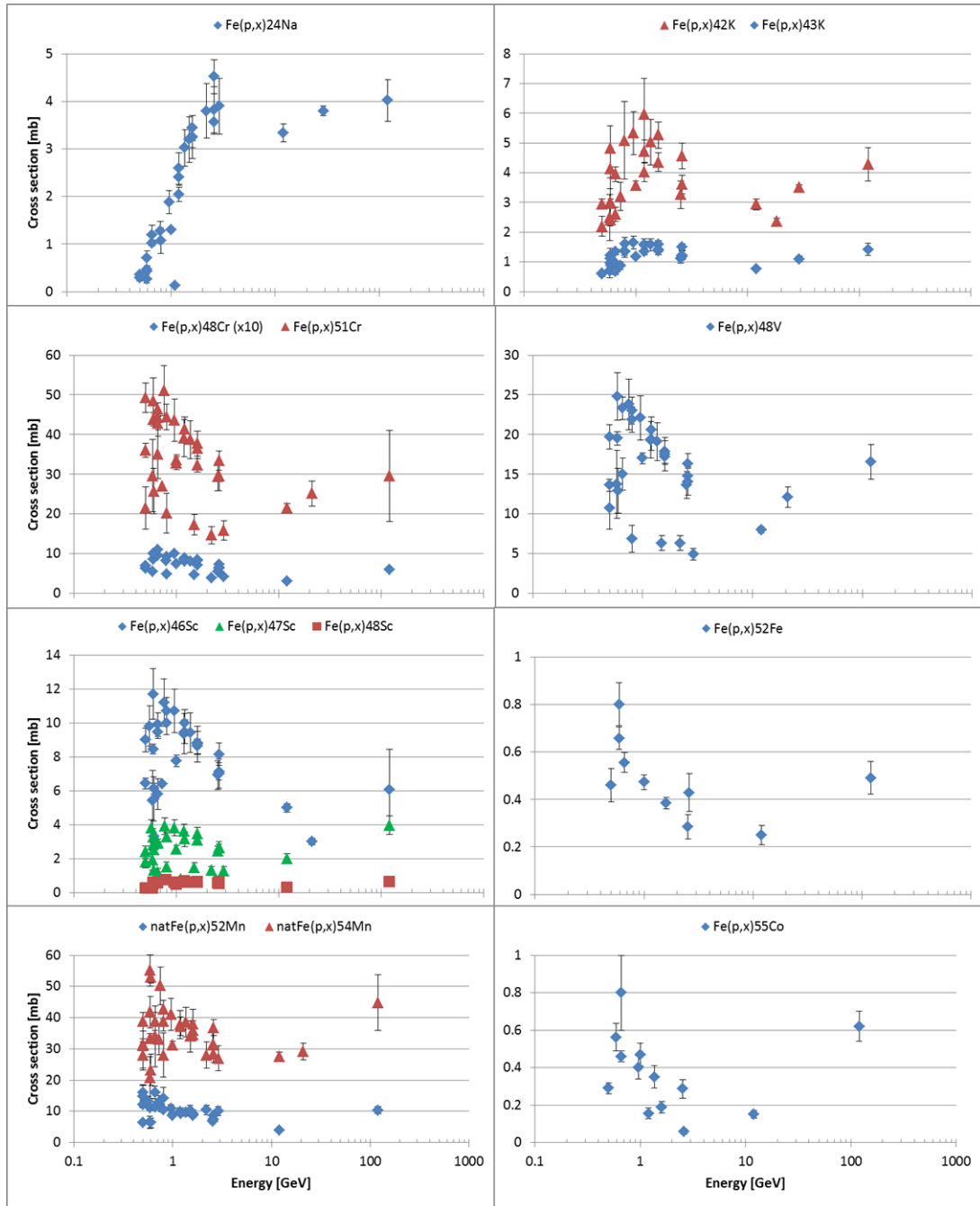


Figure A2. Cross sections of the spallation reactions on ^{nat}Fe .

References

- [1] D. Filges, F. Goldenbaum, Handbook of spallation research, Wiley-VCH, Weinheim, 2009.
- [2] W.S. Charlton, T.A. Parish, A.P. Belian, and C.A. Beard, Nucl. Instrum. Meth. B 142 (1998) 9-16.
- [3] National Council on Radiation Protection and measurements (NCRP), Report No. 144, 2005.
- [4] L. Sihver, D. Mancusi, K. Niita, T. Sato, L. Townsend, C. Farmer, L. Pinsky, A. Ferrari, F. Cerutti, I. Gomes, Acta Astronaut. 63 (2008) 865-877.
- [5] Nuclear reaction database (EXFOR): <http://cdfe.sinp.msu.ru/>, 2013.
- [6] A. Mitaroff and M. Silari, Radiat. Prot. Dosim. 102 (2002) 7-22.
- [7] H.W. Atherton, C. Bovet, N. Doble, G. Von Holtey, L. Piemontese, A. Placci, M. Placidi, D.E. Plane, M. Reinharz, and E. Rossa, CERN Yellow Report 80-07, 1980.
- [8] G. Battistoni, S. Muraro, P.R. Sala, F. Cerutti, A. Ferrari, S. Roesler, A. Fassò, J. Ranft, in Proceedings of the 2006 Hadronic Shower Simulation Workshop, Fermilab, US, 2006, M.Albrow, R. Raja eds., AIP Conference Proceeding 896, 31-49, 2007.
- [9] A. Fassò, A. Ferrari, J. Ranft, and P.R. Sala, CERN-2005-10/INFN/TC_05/11, SLAC-R-773, 2005.
- [10] H. Crannell, C.J. Crannell, H. Whiteside, J.F. Ormes, M.J. Ryan, Phys. Rev. D (1973) 730-740.
- [11] A. Ferrari, F.P. La Torre, G.P. Manessi, F. Pozzi, and M. Silari, submitted to: Phys. Rev. Spec. Top. – Acc. Bea. (PRST-AB)
- [12] GoodFellow, See online catalogue at <http://www.goodfellow.com>, 2013.
- [13] L. Sihver, C.H. Tsao, R. Silberberg, T. Kanai, and A.F. Barghouty, Phys. Rev. C 47 (1993) 1225-1236.
- [14] J. Benecke, T.T. Chou, C.N. Yang, and E. Yen, Phys. Rev. 188 (1969) 2159-2169.
- [15] J.R. Letaw, R. Siberberg, and C.H. Tsao, Astrophys. J. Suppl. Ser. 51 (1983) 271-276.
- [16] R.J. Glauber and G. Matthiae, Nucl. Phys. B21 (1970) 135-157.

Long-term residual radioactivity in an intermediate-energy proton linac

J. Blaha^a, F.P. La Torre^{a,b,*}, M. Silari^a, J. Vollaire^a

^aCERN, 1211 Geneva 23, Switzerland

^bUniversity of Bern, AEC-LHEP, Sidlerstrasse 5, 3012 Bern, Switzerland

Abstract

A new 160 MeV H⁻ linear accelerator (LINAC4) is being installed at CERN to replace the present 50 MeV LINAC2 as proton injector of the PS Booster (PSB). During operation, the accelerator components will be activated by the beam itself and by the secondary radiation field. Detailed Monte Carlo simulations, for various beam energies and several decay times, were performed to predict the residual radioactivity in the main accelerator components and to estimate the residual dose rate inside the tunnel. The results of this study will facilitate future dismantling, handling and storage of the activated parts and consequently minimize the radiation dose to involved workers. The component activation was also compared with the exemption limits given in the current Swiss legislation and to the CERN design values, in order to make predictions for the future storage and disposal of radioactive waste. The airborne radioactivity induced by particles escaping the beam dump and the activation of the beam dump cooling water circuit were also quantified. The aim of this paper is to provide data of sufficiently general interest to be used for similar studies at other intermediate-energy proton accelerator facilities.

Keywords: Radiation Protection, Induced radioactivity, Residual Dose, Activation, Monte-Carlo, FLUKA, Hadron Accelerator, Dump

Contents

1 Introduction	2	5 Airborne radioactivity and water activation	8
2 FLUKA calculations	2	5.1 Residual and released air activity	9
2.1 Beam loss assumptions and irradiation profile	2	5.2 Estimation of committed effective doses	9
2.2 Geometry and material choice	3	5.3 Activation of cooling water	10
2.3 Physics settings	3	6 Individual and collective doses for the dump exchange	10
2.4 Neutron fluence spectra	3	7 Results and conclusions	11
3 Dose rates	4		
3.1 Dose rates profiles and maps	5		
4 Induced radioactivity	6		
4.1 Specific activity in linac components	7		
4.2 Specific activity in dump components	7		
4.3 Total radioactivity distribution in linac components	8		

*Corresponding author at: CERN, Route de Meyrin, CH-1211, Geneva 23, Switzerland.

Tel.: +41 227677752

Email address: francesco.paolo.la.torre@cern.ch (F.P. La Torre)

1. Introduction

The estimation of the induced radioactivity in an accelerator facility is particularly important for maintenance interventions and the final disposal of radioactive waste. Safety is the main reason to perform a radiation protection study already during the design and construction phase. It must be demonstrated that the ALARA (As Low As Reasonable Achievable) principle has been taken into account in the design of the new facility. Components that could be activated must be designed in such a way as to facilitate their dismantling, handling and storage in order to minimize the radiation dose to workers.

LINAC4 is a new 160 MeV H^- accelerator which in a few years will be the source of protons for all accelerators at CERN. It is an 80-m long normal-conducting linac made of an H^- source, a Radio Frequency Quadrupole (RFQ), a chopping line and a sequence of three accelerating structures: a Drift-Tube Linac (DTL), a Cell-Coupled DTL (CCDTL) and a Pi-Mode Structure (PIMS) [1, 2]. LINAC4 will operate at 1.1 Hz, with a peak current of 40 mA and a pulse length of 0.4 ms as Proton Synchrotron Booster (PSB) injector. These parameters correspond to 0.08% beam duty cycle and 0.032 mA average current or 2×10^{14} protons/s, equivalent to a beam power of 5.1 kW at the top energy of 160 MeV. LINAC4 has been designed to replace the present 50 MeV LINAC2 as injector of the PSB. The higher injection energy will allow the production by the PSB of beams with increased brightness as required by the High-Luminosity LHC (Large Hadron Collider). LINAC4 accelerating structures have also been designed to be the front-end of a future high-power Superconducting Proton Linac (SPL) [3].

LINAC4 is terminated by a dump collecting the beam which is not intended for further utilization. When the beam interacts with the dump, hadronic interactions produce mixed radiation fields with large numbers of neutrons and other highly penetrating particles. Moreover, the material of the dump becomes highly activated. In addition, the LINAC4 accelerator complex is built in a way (e. g. depth and orientation of the tunnels) that it allows a future possible connection to the SPL. Consequently, the dump will not be integrated inside the wall as it is a common solution in similar facilities, but it will be placed at the junction between the accelerator and the transfer tunnel (Figure 1). Therefore an effective shielding surrounding the dump is needed in order to limit activation of the adjacent structures and to protect the personnel accessing the machine.

Activation of the accelerator components at energy

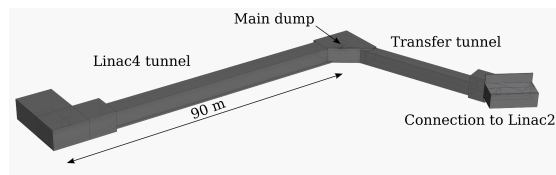


Figure 1: Layout of the LINAC4 underground tunnel complex.

between 3 and 160 MeV generates a large volume of (mostly weakly) radioactive stainless steel and copper, which also include permanent magnetic quadrupoles made of a samarium-cobalt alloy. These components will be subjected to very different levels of activation, depending on the beam loss patterns, on the type of material and on the geometry.

This work provides information on beam loss assumptions, accelerator structure and material composition, in order to make the results of sufficiently general interest and provide guidelines for similar studies for intermediate-energy proton accelerators.

2. FLUKA calculations

Monte Carlo models used to estimate induced radioactivity in accelerator components must be able to reliably predict nuclide production in arbitrary target elements and for neutron energies ranging from thermal to a value close to the maximum accelerator energy. In this study the Monte Carlo code FLUKA [4, 5], which is an appropriate code for estimating induced radioactivity in a wide range of accelerator facilities [6], was used.

2.1. Beam loss assumptions and irradiation profile

In a linear accelerator the equipment activation is produced by scattered particles escaping from the fields generated for controlling beam focusing and acceleration and hitting the vacuum chamber. It is hard to predict and identify the beam loss locations because they will not be equally distributed along the machine. Losses typically occur in the aperture restrictions of quadrupoles, due to possible mismatch between linac sections. According to the estimated particle loss distribution, it was assumed that constant losses of 0.1 W occur every 10 m at selected points along the machine. This value comes from the analysis of the beam losses [7] for a 6% duty cycle scenario, indicating a maximum loss of 1 W in some "hot spots". During the LINAC4 operation as PSB injector at 0.033% duty cycle, losses would be theoretically reduced by a factor of 180 although it is expected that the sensitivity of the beam loss monitors would not allow reaching such

a low loss level. A conservative value of 0.1 W per loss location was therefore assumed, 18 times higher than the minimum achievable loss level [8]. Table 1 shows the seven beam losses for the three main accelerating structures with a total length of 70 m. It is evident that with increasing energy the number of lost particles decreases for constant lost beam power. The calculation of the induced radioactivity was performed in three positions (noted in bold in Table 1), representative of typical aperture restrictions in the various sections of LINAC4: the first drift tube of the third DTL tank at 31 MeV, the quadrupole at 80 MeV within the CCDTL section and the last quadrupole at 155 MeV within the PIMS section. For each position the calculations took into account the activation due to the two loss points upstream and downstream of the one under study, a rather innovative approach in this type of study.

The induced radioactivity depends on the irradiation profile, which includes periods of operation at various beam intensities alternating with shutdown (maintenance) periods. Although the LINAC4 irradiation profile during its 30 years of planned operation is clearly impossible to predict exactly, a simplified but quite realistic irradiation profile was derived from the present LINAC2 yearly schedule, which consists of an average operating time of 5000 hours per year. To include a safety margin, an average of 7000 hours per year was used in the present calculations (corresponding to the yearly schedule of LINAC2 without the year-long shutdown every 4 years).

Concerning the beam dump activation, three operation periods of LINAC4 were taken into account: the one month commissioning phase with a nominal beam power of 2.84 kW, the nine months reliability run with 1/4 of the nominal power to assess the operational availability of the machine before connection to the PSB, and the normal operation during the LINAC4 life time when the dump will be exposed to the beam only occasionally. More details for each operation phase are listed in Table 2.

2.2. Geometry and material choice

The simulations were performed with FLUKA (version 2011.2.17) using a detailed geometrical model of the main accelerating structures based on the existing geometry implemented a few years ago for a previous study [10, 11]. The geometry includes three DTL tanks with permanent magnetic quadrupoles (PMQ) housed in the drift tubes; seven CCDTL modules of three tanks, with PMQs between tanks and electro magnetic quadrupoles (EMQ) between modules [12]; 12 tanks for

the PIMS made of 7-cell pi-mode structures with external EMQs.

The beam dump consists of a core and its shielding. A cylindrical graphite core, with an effective thickness of 60 cm, is surrounded by a stainless steel jacket with incorporated water cooling system [13]. The shielding, which was designed to fulfill both radiation protection requirements and structural constraints, consists of steel blocks surrounding the core and borated concrete blocks used as the outermost layer. The borated concrete was chosen to enhance its shielding properties against neutrons as well as to lower the induced activity in the concrete shielding. Overall dimensions of the shielding are $240 \times 200 \times 224$ cm³ (length \times width \times height) with a total weight of 36.3 tons. The detailed geometry is shown in Figure 2.

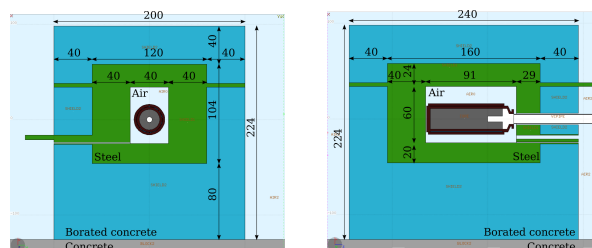


Figure 2: Front (left) and side (right) view of the beam dump and its shielding as implemented in FLUKA. Dimensions are in cm.

2.3. Physics settings

The full electromagnetic and hadronic cascades were simulated in the main accelerator components including particles back-scattered from the beam tunnel walls. For an accurate description of all the nuclear processes relevant for isotope production, the evaporation of heavy fragments and the coalescence mechanism were explicitly turned on. Defaults setting for precision simulations were used. The particle transport threshold was set at 100 keV, except for neutrons that were transported down to thermal energies. The low energy neutron transport (below 20 MeV) was performed using the multi-group approach, updated to the new 260 group library. The Decays option was used to simulate radioactive decays and to set the corresponding transport conditions. This allows the time evolution of induced radioactivity to be calculated analytically for fixed cooling times, considering daughter nuclei as well as the associated radiation.

2.4. Neutron fluence spectra

Apart for components directly hit by the beam (e.g. collimators or aperture restrictions), most of the induced

Table 1: Beam loss assumptions along the main accelerating structures. The three activation study points are shown in bold.

	DTL		CCDTL		PIMS		
Distance [m]	4	12	23	35	45	55	66
Energy [MeV]	11	31	57	80	100	128	155
Beam loss [p/s]	5.67E+10	2.01E+10	1.09E+10	7.80E+09	6.24E+09	4.88E+09	4.03E+09

Table 2: LINAC4 operation scenarios [9] and corresponding parameters (irradiation time and average intensity) of the irradiation profiles as implemented in FLUKA. One month pause between the commissioning and reliability run, and six months pause between reliability run and normal operation was considered.

	Mean power [W]	Duration	Irradiation time [s]	Average intensity [p/s]	Total number of protons
Commissioning run	2841.6	1 month (12 hours/day)	2.63E+06	5.54E+13	1.48E+20
Reliability run	710.4	9 months (24 hours/day)	2.37E+07	2.77E+13	6.56E+20
Normal operation	2841.6	30 years (2 hours/week)	9.47E+08	1.33E+12	1.26E+21

radioactivity in proton accelerators in the 100 MeV range is due to the stray neutron field. Figure 3 compares the neutron fluence spectra in the drift tube and in the tank surrounding the beam impact point in the DTL. Figure 4 compares the neutron energy spectra at the location of the three loss points under study for all sections.

The neutron fluence spectra computed for the beam dump are plotted in Figure 5 and show that the combination of the iron and borated concrete reduce considerably the secondary neutrons by two orders of magnitude over the whole energy range. The iron layer has significant impact on the high energy neutron component whilst the concrete is more effective from the fast down to the thermal energies.

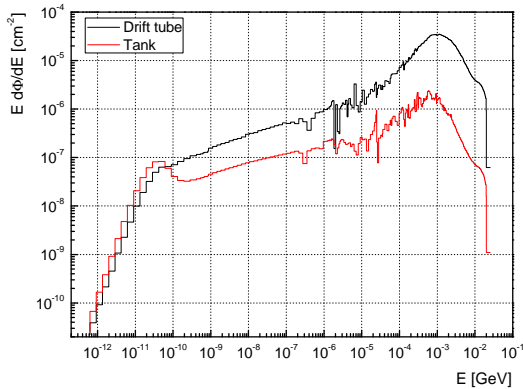


Figure 3: Comparison of the neutron fluence spectra in the first drift tube and in the third tank of the DTL section.

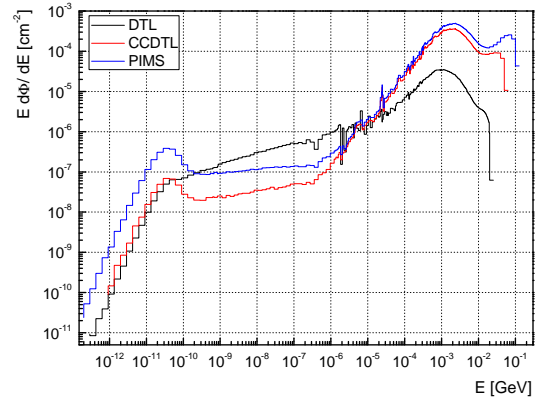


Figure 4: Comparison of the neutron fluence spectra at the three beam impact points: 31 MeV (DTL), 80 MeV (CCDTL), 155 MeV (PIMS).

3. Dose rates

The personnel accessing the accelerator tunnel after the beam stop, e.g for performing the maintenance of the accelerator elements, will be exposed to remnant radiation originating from the activated part of the machine. In order to estimate the time after which access can be granted, the residual dose rate profiles and maps were calculated for several cooling times. Each plot shown below takes into account the dose rate due to the beam loss point under study and the two loss points downstream and upstream. The ambient dose equivalent rate around the dump was also calculated.

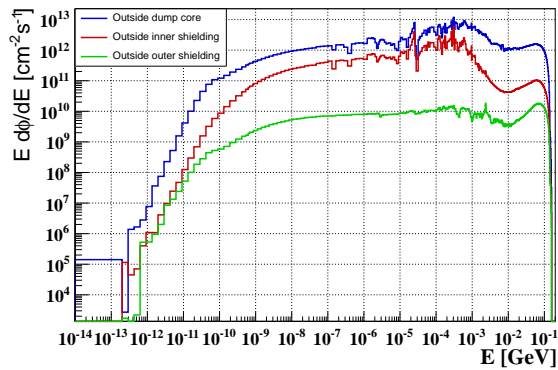


Figure 5: Neutron fluence spectra at the boundary between dump (air volume around the dump) and inner shielding (steel), between inner and outer shielding (borated concrete), and outside the shielding.

3.1. Dose rates profiles and maps

In the DTL section the dose rates are rather low due to the comparatively low beam energy. Figure 6 shows the dose rate inside the DTL tank for 5 decay times. Dose rate peaks of about $100 \mu\text{Sv/h}$ and $500 \mu\text{Sv/h}$ can be observed at the beam impact points at 11 MeV and 31 MeV, respectively. The last peak is due to the dose rate from the downstream loss point at 57 MeV energy.

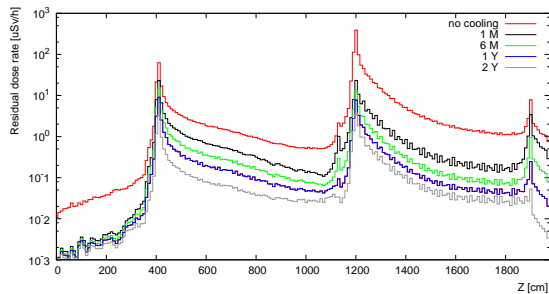


Figure 6: Ambient dose equivalent rate inside the DTL tank along the beam axis (z) for five decay times.

Whereas the DTL quadrupoles are shielded by the drift tube and by the tank, the quadrupoles in the other sections of the accelerator are directly accessible. The ambient dose equivalent rate inside the CCDTL tank is shown in Figure 7. A dose rate of almost 10 mSv/h can be reached at the 80 MeV beam loss point, which is a critical location because of the permanent magnetic quadrupole (PMQ) near the vacuum chamber. A few localized hot spots in correspondence of the quadrupoles can push the dose rate up to $100 \mu\text{Sv/h}$ at 10 cm from the tank. On the other hand, the dose rate decreases quickly far from the beam loss points reaching $0.1 \mu\text{Sv/h}$ in just one month of cooling time. The difference in the dose

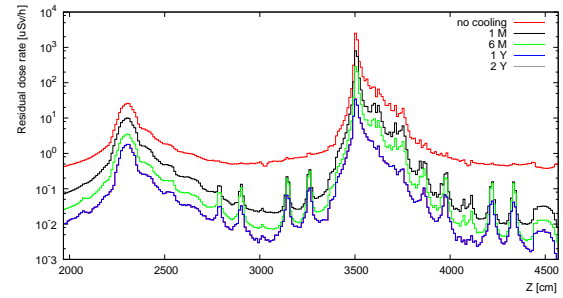


Figure 7: Ambient dose equivalent rate inside the CCDTL tank along the beam axis (z) for five decay times.

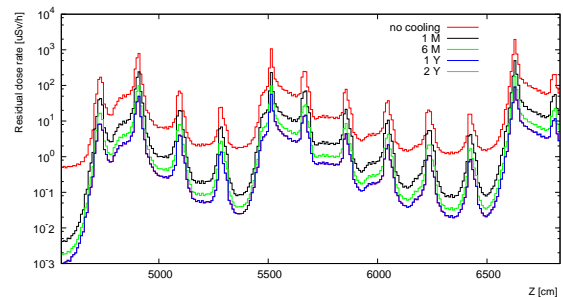


Figure 8: Ambient dose equivalent rate inside the PIMS tank along the beam axis (z) for five decay times.

rate between the first (EMQ) and the second (PMQ) activation point is rather due to the different material composition than to the difference in energy. Starting from 6 months of cooling time the dose rate peaks caused by the PMQ magnets along the CCDTL section are clearly visible. In the PIMS structure the dose rate distribution is more uniform (Figure 8). Although the beam losses can occur at the maximum energy, the highest dose rate does not exceed 2 mSv/h .

The dose rate profiles in the dump proximity are shown in Figure 9: the ambient dose equivalent rate falls down steadily due to fast decaying nuclei in activated parts of the shielding. In concrete it is mainly because of the relatively short half life ($T_{1/2}=15 \text{ h}$) of ^{24}Na . The dose rate reaches a level of a few $\mu\text{Sv/h}$ at 1 m distance after 1 day of cooling. After about one week the residual dose rate remains almost stable and decreases slowly as the long lived ^{22}Na ($T_{1/2}=2.6 \text{ y}$) in concrete decays. The highest values of the residual dose rate outside the dump shielding are in upstream locations (for $Z > -9400 \text{ cm}$ in Figure 9 right) because of the activated beam pipe and due to the residual radiation coming from openings in the shielding around the pipe and holes for dump services.

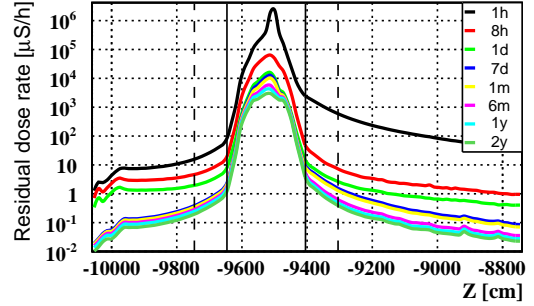
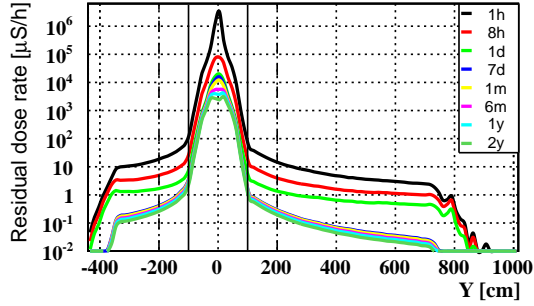


Figure 9: Ambient dose equivalent rates after several cooling times on an imaginary plane at the center of the dump perpendicular (left) and along the beam direction (right) after 30 years of LINAC4 operation. Full vertical lines indicate the shielding boundary and dashed lines mark a 1 m distance from the shielding.

The dose rate maps in Figure 10 and in Figure 11 were calculated along the z-axis of the accelerator (top view, y-axis). Figure 10 shows the dose rate plots in the PIMS section for three beam losses (100 MeV, 128 MeV and 155 MeV) and several cooling times (1 month, 6 months, 1 year and 2 years). In Figure 11 the maps providing the spatial distribution of ambient dose equivalent rates around the dump are shown for different cooling times ranging from 1 hour to 2 years.

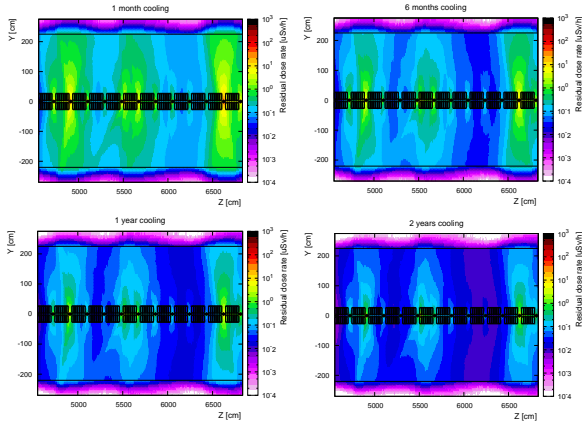


Figure 10: Ambient dose equivalent rates calculated in the PIMS section for several cooling times after 30 years of LINAC4 operation.

4. Induced radioactivity

The residual radioactivity for the most important accelerator components was calculated for several decay times. Not only the activation produced by the direct impact of the beam at the given loss point was estimated, but also the induced radioactivity due to the secondary particles coming from the two loss points down-

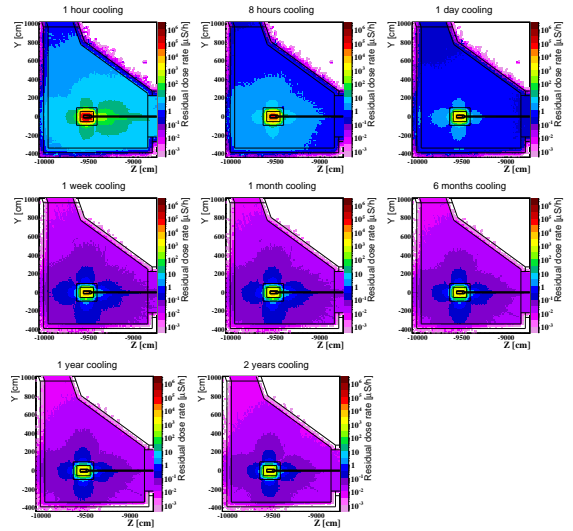


Figure 11: Ambient dose equivalent rates calculated in the dump section for several cooling times after 30 years of LINAC4 operation.

stream and upstream. The induced specific activity A_i for each radionuclide i and for several cooling times was compared with the CERN exemption values LE_i used in design studies for future accelerators [14]. These values represent, for each nuclide, the minimum of the exemption limits that are likely to be adopted by future European Directives and national legislations and are thus considered as conservative values. They are much more restrictive than those provided e.g. in the present Swiss legislation [15] as shown in Table 3. Thus, for a mixture of n radionuclides a ratio R is defined using the summation rule:

$$R = \sum_{i=1}^n \frac{A_i}{LE_i} \quad (1)$$

where both A_i and LE_i are expressed in Bq/kg .

Table 3: Main radionuclides found in the LINAC4 components and current (Swiss) and future (design) exemption limits.

Nuclide	$T_{1/2}$	LE [Bq/kg]	
		Swiss [15]	Design [14]
^3H	12.3 y	2.00E+005	1.00E+005
^{22}Na	2.6 y	3.00E+003	1.00E+002
$^{44}\text{Ti}/\text{Sc}$	47.3 y	2.00E+003	2.00E+003
^{45}Ca	163 d	1.00E+004	1.00E+004
^{46}Sc	83.83 d	7.00E+003	1.00E+002
^{48}V	16.24 d	5.00E+003	1.00E+003
^{49}V	330 d	6.00E+005	6.00E+005
^{51}Cr	27.7 d	3.00E+005	1.00E+005
^{52}Mn	5.6 d	6.00E+003	1.00E+003
^{54}Mn	312.5 d	1.00E+004	1.00E+002
^{55}Fe	2.7 y	3.00E+004	3.00E+004
^{56}Co	78.76 d	4.00E+003	1.00E+002
^{57}Co	270.9 d	5.00E+004	1.00E+003
^{58}Co	70.8 d	1.00E+004	1.00E+003
^{59}Fe	44.5 d	6.00E+003	1.00E+003
^{60}Co	5.27 y	1.00E+003	1.00E+002
^{63}Ni	96 y	7.00E+004	7.00E+004
^{65}Zn	243.9 d	3.00E+003	1.00E+002
^{88}Y	106.6 d	8.00E+003	8.00E+003
^{88}Zr	83.4 d	3.00E+004	3.00E+004
^{145}Sm	340 d	5.00E+004	5.00E+004
^{149}Eu	93.1 d	1.00E+005	1.00E+005
^{152}Eu	13.33 y	7.00E+003	1.00E+002
^{154}Eu	8.8 y	5.00E+003	1.00E+002
^{155}Eu	4.96 y	3.00E+004	1.00E+003

4.1. Specific activity in linac components

In the DTL section, the proton beam impinges on the first drift tube of the third tank. The specific activity was estimated in the following components of the third tank: the drift tubes; the permanent magnetic quadrupoles (PMQ); the stems; the girders; the tank; the vacuum chamber and the electromagnetic quadrupole (EMQ) upstream of the loss point; the waveguide and the support closest to the loss point. Figure 12 shows the specific radioactivity as a function of cooling time for the DTL. It is interesting to notice that the PMQs are the most active components, as expected due to their high cobalt content. After 2 years of decay time, the main contributors to R in the PMQs are ^{60}Co (57%) and ^{152}Eu (26%), whereas ^{55}Fe (which has a much higher LE) mostly contributes to the total activity (69%). For the drift tubes almost all activity (and R) is due to ^{65}Zn and ^{60}Co , but the long decay time is due to ^{63}Ni , which is the longest-lived radionuclide ($T_{1/2}=96$ y) found in the radionuclide inventory. In the CCDTL section the

proton beam impinges on the vacuum chamber between the first and the second tank of the 5th module. The specific activity was estimated in the following components: the vacuum chamber and the PMQ between the first and the second cavity; the EMQ closest to the loss point; the tank wall, the copper plating, the first nose-cone, the first drift tube, the copper and stainless steel stem downstream of the loss point; the waveguide and the support closest to the loss point. The most active component in the CCDTL is the vacuum chamber because it is directly hit by the beam (Figure 13). After 2 years of cooling, the major contribution to the activity comes from ^{55}Fe (76%) and ^{54}Mn (9%), but the ratio R is dominated by ^{54}Mn (90%) and ^{57}Co (4%). $^{44}\text{Ti}/^{44}\text{Sc}$ and ^{63}Ni are responsible for the residual radioactivity at very long decay times. In the PIMS section the proton beam impinges on the vacuum chamber between the 11th and the 12th tank. The residual radioactivity was estimated in the following components: the vacuum chamber between the 11th and the 12th tank; the EMQ adjacent to the vacuum chamber; the left wall and the external wall of the 12th tank downstream of the loss point; the external wall of the 11th tank upstream of the loss point; the nose-cone and the copper cylinder of the 12th tank located downstream of the loss point; the support and the waveguide closest to the loss point. As evident from Figure 14, the most active components are the vacuum chamber and the EMQ, with specific activity higher than 1×10^7 Bq/kg after 1 year of cooling. For the vacuum chamber, the major contribution to R after 2 years of cooling comes from ^{54}Mn (90%) and ^{57}Co (4%), whereas the major contribution to the activity comes from ^{55}Fe (65%) and ^{49}V (10%). The EMQs activity is dominated by ^{55}Fe (79%) and ^{54}Mn (11%), but the main contribution to R is due to ^{54}Mn (92%) and ^{60}Co (3%). Table 4 shows the fraction R of CERN design exemption limits for some selected components after 2 years of cooling time.

4.2. Specific activity in dump components

Assuming 2 years of cooling time after 30 years of accelerator operation, mainly long lived radionuclides remain in the dump materials. In case of the dump core, which consists of pure carbon, almost all total activity and R are due to ^3H . For other parts of the core made of stainless steel, the main contributors are ^{55}Fe (76%) and ^{54}Mn (11%), contrary to R where the main contributors are ^{54}Mn (88%) and ^{60}Co (7%). A different situation is found for the steel shielding where ^{55}Fe (49%) and ^{60}Co (38%) account for most of the activity. The low LE_i value associated with ^{60}Co leads to its 86% contribution to R . The second most important contributor to

Table 4: Fraction of CERN design exemption limits $R = \sum_i A_i/LE_i$ for the main accelerator components after 2 years of cooling time.

Component	Material	DTL	CCDTL	PIMS
Vacuum Chamber	Stainless steel (316L)	1.67E+00	1.35E+05	1.28E+05
Drift tube	Copper	4.53E+01	2.24E+02	/
PMQ	Samarium-cobalt alloy	9.23E+01	8.62E+02	/
EMQ	Low carbon magnetic steel	1.17E-01	5.95E+02	8.73E+03
Stem	Copper	1.36E-01	5.55E+00	/
Stem	Stainless steel (316L)	8.79E-02	8.87E+00	/
Tank	Stainless steel (304L)/Copper (PIMS)	8.59E-02	1.91E+01	9.58E+01
Girder	Aluminium (AW6082)	3.24E-03	/	/
Nose-cone	Stainless steel (304L)/ Copper (PIMS)	/	6.17E+02	2.47E+03
Cylinder	Copper	/	/	8.30E+02
Plating	Copper	/	6.20E+00	/
Waveguide	Stainless steel (304L)	5.13E-03	1.60E+00	6.62E+00
Support	Steel (ST-37)	2.42E-02	4.68E-01	5.53E+00

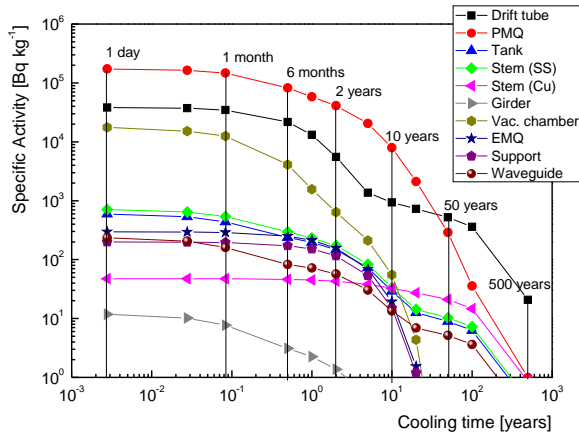


Figure 12: Specific radioactivity as a function of cooling time in the main DTL components.

R is ^{54}Mn (11%). The difference in the values for the steel of the dump core and of the shielding is due to their different material compositions. In case of the borated concrete shielding, the principal contributions to the activity come from ^3H (75%) and ^{55}Fe (11%). As expected, the contribution to R is dominated by ^{22}Na (87%); the second significant contribution is from ^{54}Mn (11%). Finally, the specific activity and fraction of the exemption limits for each component during the dump decommissioning are summarized in Table 5.

4.3. Total radioactivity distribution in linac components

In order to evaluate the activity distribution inside the Linac a region-independent scoring (Cartesian binning) of the total radioactivity over the three beam loss points in each section of the linac was carried out for 5 cooling

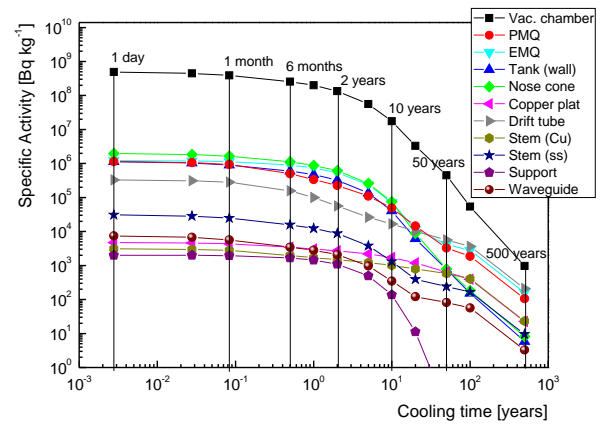


Figure 13: Specific radioactivity as a function of cooling time in the main CCDTL components.

times: immediately after the end of the operation and after 1 month, 6 months, 1 year and 2 years. Figure 15 shows the activation profile of the fifth CCDTL module, which consists of three tanks. The beam loss points at 35 m distance and 80 MeV energy is clearly visible.

5. Airborne radioactivity and water activation

Personnel accessing the LINAC4 tunnel shortly after the beam is stopped can be exposed not only to residual radiation from the activated structures, but also to radiation from the activated air through external exposure and inhalation. Moreover, certain amount of airborne radioactivity will be released off-site the building. It is therefore necessary to estimate the air activation and its radiological impact. Since the main contribution to the airborne radioactivity and water activation will come

Table 5: Specific activity and fraction of CERN design exemption limits for the dump after 30 years of operation and 2 years of cooling time.

Component	Material	Mass [tons]	Activity [Bq/kg]	$\sum_i A_i/LE_i$
Dump core	Graphite/steel	0.34	3.60E+08	4.58E+04
Inner shielding	Steel	15.89	8.72E+05	3.89E+03
Outer shielding	Borated concrete	20.07	2.31E+03	2.17E+00

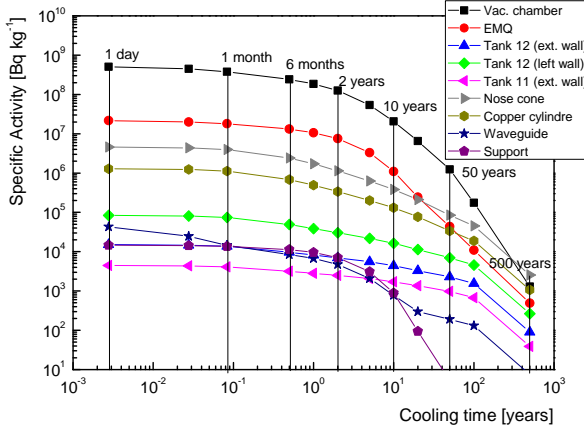


Figure 14: Specific radioactivity as a function of cooling time in the main PIMS components.

from the dump only this component was considered for this study.

5.1. Residual and released air activity

The time evolution of the activity was calculated for all radionuclides produced in the air by folding the track-length spectra computed by FLUKA for different hadrons (n , p , π^+ , π^-) with the energy dependent production cross section of the target nuclide in the air compound. This two-step technique [16] allows obtaining the production yields with sufficient statistical precision also for low-density media in comparison of computing the same quantity in FLUKA directly. The total yield for each radionuclide is given in Table 6.

Assuming a simple laminar flow model with a partial air exchange of $Q = 2000 \text{ m}^3/\text{h}$ out of a total air volume $V = 1330 \text{ m}^3$ of the tunnel, one can calculate the activity of a radionuclide at the end of the irradiation time t_{irr} for a given beam intensity I by [17]:

$$A_{res} = \frac{Y\lambda I}{\lambda'} \left(1 - e^{-\lambda' t_{irr}}\right), \quad \text{where } \lambda' = \lambda + \frac{Q}{V}.$$

Y and λ denote the radionuclide production yield per primary proton and the decay probability per unit time. λ' is the effective decay constant taking into account the air exchange during the irradiation (the ratio Q/V

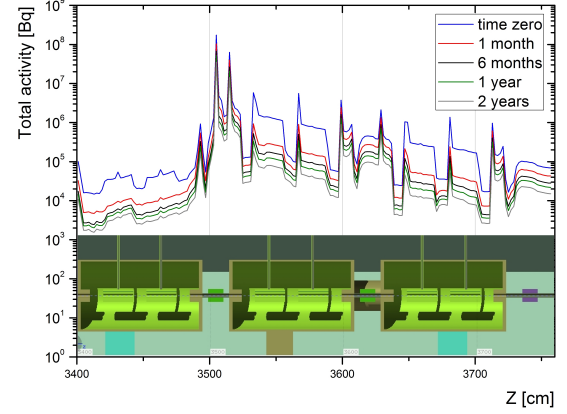


Figure 15: Profile of the total radioactivity in the 5th CCDTL module along the beam axis (z) for five decay times.

represents the fraction of the total air renewed per unit time). The saturation activity, i.e. the activity at the equilibrium between radionuclide production and decay including the air renewal, is reached after about 90 minutes. The total residual activity just after the beam stop has been estimated to be about 33 MBq. The contribution of each radionuclide to the total activity is listed in Table 6.

The activity released into the atmosphere during the irradiation can be obtained for each radionuclide by [17]:

$$A_{atm} = \frac{Y\lambda I}{\lambda'} \frac{Q}{V} \left(t_{irr} - \frac{1 - e^{-\lambda' t_{irr}}}{\lambda'} \right) e^{-\lambda t_{rel}},$$

where t_{rel} is the time needed for the activated air to reach the release point. Its value was estimated, based on the length of the air path and the velocity of the air in the tunnel and in ventilation ducts, to be around 5 minutes. The annual activity released in the environment during the LINAC4 normal operation phase is about 3 GBq.

5.2. Estimation of committed effective doses

The activity concentrations were calculated with the assumption that the activity in air is distributed homogeneously throughout the LINAC4 tunnel and the dump

area, which leads to a value of 25 kBq/m³. The radiological importance of a radionuclide can be obtained from a comparison of the computed activity concentration for each radionuclide with the guideline values CA [Bq/m³]¹ for airborne activity concentration according to the Swiss legislation [15]. As shown in Table 6 the most important radionuclides are ¹¹C (T_{1/2} = 20.4 min), ¹³N (T_{1/2} = 9.97 min), ¹⁵O (T_{1/2} = 122 s), and ⁴¹Ar (T_{1/2} = 109.34 min). Those positron emitters account for almost 99% or 97.8% of the total CA or specific activity fractions, respectively.

A worker performing an intervention just after the machine shutdown will be exposed to the external (via immersion in activated air) as well as to internal (via intake of radioactive air through breathing) radioactivity. The effective dose rates due to the external exposure was estimated for a given radionuclide from the fraction of its CA value. The effective dose rates for internal exposure were calculated supposing a standard breathing rate of 1.2 m³/h and using the dose coefficients for inhalation e_{inh} [Sv/Bq] as given by the Swiss legislation [15]. The effective dose rates for external exposure were calculated by using the CA values. The total effective dose rate for external exposure and inhalation was estimated to be 3.6 μSv/h. This value is mostly due to external exposure, mainly by the above mentioned positron emitters.

5.3. Activation of cooling water

The main dump will be connected to a closed demineralised water circuit which is used to cool the main dump, the dumps in the measurement lines and other equipment installed inside the transfer tunnel. The water flowing through the dump cooling system will be activated via hadronic interactions of the secondary particles produced in the dump. In order to estimate the activity of the water flowing inside the dump, the production yields of the radionuclides in the water circuit were calculated. The values obtained for a total irradiated volume of 2.5 l inside the dump are given in Table 7. Then the activity in the cooling water at the end of the irradiation period t_{irr} for a given production rate $P = Y \times I$, where Y is the yield and I is the beam intensity, is calculated by:

$$A_1 = P_1 (1 - e^{-\lambda t_{irr1}}),$$

$$A_2 = P_2 (1 - e^{-\lambda t_{irr2}}) + A_1 e^{-\lambda(t_{offA} + t_{irr2})},$$

¹The CA is a guidance value for chronic occupational exposure to airborne activity. Exposure to an airborne activity concentration CA for 40 hours per week and 50 weeks per year yields a committed effective dose of 20 mSv[15].

$$A_3 = P_3 (1 - e^{-\lambda t_{irr3}}) + A_2 e^{-\lambda(t_{offB} + t_{irr3})},$$

where t_{offA} and t_{offB} stand for the first and second pause (1 and 6 months) between accelerator operation; index 1, 2, and 3 corresponds to the commissioning, reliability run and normal operation, respectively. Considering that the cooling loop is closed, one can obtain the activity concentration in Bq/m³ by dividing the activity by the total volume of cooling water that is estimated to be approximately 1.5 m³. The results obtained are summarized in Table 7. From a radiological point of view, the most important radionuclides are the long lived ³H and ⁷Be having a total activity at the end of the LINAC4 life time equal to about 7.8 and 1.8 MBq, respectively. It should be noted that ³H will be distributed homogeneously along the whole cooling loop with an activity concentration increasing proportionally with the irradiation time up to about 5.2 Bq/cm³ at the end of the accelerator life time. On the other hand, ⁷Be will be captured by a special filter (e. g. in demineraliser) and thus it will increase the activity in those parts of the loop.

Table 7 compares the total and specific activity with the exemption limits as given by the Swiss legislation [15]. This legislation is applicable (i.e. the water is considered as radioactive) if the specific activity exceeds one per cent of the exemption limit LE as a weekly mean and/or the total activity release per month is larger than 100 times the LE. It should be stressed that the LINAC4 water cooling circuit is a closed loop and no release of the activated water into the environment is foreseen during its life time.

6. Individual and collective doses for the dump exchange

During LINAC4 operation the dump components as well as its shielding will be highly activated and the residual dose rates will reach levels at which any maintenance or intervention must be planned in advance. The worst case is the loss of the dump functionality that will result in its complete replacement. In order to protect personnel who will perform such an intervention, the procedure must be optimized based on the ALARA (As Low As Reasonably Achievable) principle. For this reason the dump shielding was designed in a way that it permits an easy access to the core and its removal.

Individual and collective doses received by workers who will be involved in the dump exchange were calculated for each intervention step knowing the detail work procedure including the number of workers, their precise locations and duration of each work action. The

Table 6: Total radionuclide production yields in the air for a proton interaction in the dump and corresponding residual activity and activity released into the atmosphere, airborne activity concentration values (CA) according to the Swiss legislation [15], and dose rates for internal and external exposure of personnel accessing the LINAC4 tunnel.

Nuclide	Half life [s]	Yield per primary	Residual activity [Bq]	Activity released into atmosphere [Bq]	CA [Bq/m ³]	Activity concentration/CA	Dose rate for internal and external exposure [μ Sv/h]
C-11	1.22E+03	5.94E-08	3.72E+06	1.52E+10	7.00E+04	4.00E-02	1.07E-02
N-13	5.98E+02	2.26E-07	1.81E+07	6.17E+10	7.00E+04	1.94E-01	1.94E+00
O-15	1.22E+02	9.66E-08	9.79E+06	8.64E+09	7.00E+04	1.05E-01	1.05E+00
P-32	1.23E+06	3.86E-10	5.35E+01	2.72E+05	2.00E+03	2.02E-05	1.40E-04
Cl-38	2.23E+03	3.14E-09	1.45E+05	6.41E+08	4.00E+04	2.72E-03	9.55E-03
Cl-39	3.34E+03	5.19E-09	1.85E+05	8.52E+08	2.00E+05	6.98E-04	1.27E-02
Ar-41	6.58E+03	3.89E-08	8.32E+05	3.99E+09	5.00E+04	1.25E-02	1.25E-01
Total	–	–	3.31E+07	9.13E+10	–	3.56E-01	3.15E+00

Table 7: Total radionuclide production yields in the water cooling circuit for an irradiated volume of 2.5 l for a proton interaction in the dump and corresponding total and specific activity. The latter is calculated assuming a total volume of 1.5 m³ of water inside the cooling loop. Total activity A_i and activity concentration a_i in water cooling circuit compared to an exemption limit LE_i for a given radionuclide and its relative contribution.

Nuclide	Half life	Yield per primary	Total activity [Bq]	Activity concentration [Bq/cm ³]	LE _i [Bq/kg ³ or Bq]	a _i /(LE _i /100)	A _i /(100LE _i)
H-3	12.33 y	6.01E-06	7.80E+06	5.20E+00	6.00E+05	8.66E-01	8.66E-05
Be-7	53.22 d	1.32E-06	1.76E+06	1.17E+00	4.00E+05	2.93E-01	2.93E-05
Total	–	–	9.56E+06	6.37E+00	–	1.16E+00	1.16E-04

residual dose rates at a given location and estimated individual and collective doses for different cooling times are summarized in Table. 8. The individual and collective doses are less than 0.2 mSv if 8 hours of cooling time are considered. Those values are well under the CERN design criteria and therefore the established intervention scenario can be considered as optimized.

Table 8: Expected maximum individual and collective doses for the dump exchange intervention, and maximum dose equivalent rate during the intervention.

Cooling time	1h	8h	1d	1w	1m
Individual dose [μ Sv]	1585	126	23	15	12
Collective dose [μ Sv]	2055	167	32	20	16
Dose rate [μ Sv/h]	698	57	10	7	6

7. Results and conclusions

A set of FLUKA simulations using a detailed geometrical model of the accelerator was carried out to predict the induced radioactivity in LINAC4 after several years of operation and for various decay times. The following estimations were performed: residual radioactivity in the main components; comparison with the future (design) exemption limits; profile of the total activity for

the three beam loss points under study; dose rate in the whole accelerator structure for relevant cooling times.

It is predicted that most of the components in the DTL can be dismantled soon after the final shutdown. The mean storage time required is: 2 years for the vacuum chamber and 10 years for the drift tubes. The PMQs will exceed the limits for at least 50 years after final shutdown. In the CCDTL the dismantling is recommended after 2 years of cooling. After 10 years about half of the accelerator components are below the limits. The longest decay time foreseen is 100 years for the vacuum chamber. In the PIMS the dismantling should start after 5 years of cooling. Half of the PIMS components are expected to be below the limits after 20 years. The longest estimated decay time is 100 years for the vacuum chamber.

Dose rates at 10 cm from the tank vary in the range of 0.1-1 μ Sv/h for the DTL and between 1 μ Sv/h and 100 μ Sv/h for the CCDTL. Although the beam losses can occur at the maximum energy in the PIMS, the highest dose rate does not exceed 100 μ Sv/h at 10 cm from the tank.

The residual dose rates show that the dump area will be accessible after a short cooling time. The activity released into the atmosphere was estimated and the effective dose due to airborne radioactivity was found to be under the limits for workers accessing the tunnel. Ra-

dionuclide production in water was quantified for the dump cooling system. The individual and collective doses for the dump exchange were calculated. The intervention for the dump replacement is possible within 24 hours after a dump failure. The radionuclide inventory for all dump materials was established and give an important input for radioactive waste management during the decommission of the LINAC4.

It is important to point out that the values of the induced radioactivity predicted in this study were estimated for the most probable scenario at the present time, i.e. 0.1 W of beam losses every 10 m for 30 years of irradiation. In case of different losses, irradiation profile or machine operating parameters, an increase/decrease in beam losses can be expected and, therefore, in machine activation depending on the new scenario. It is most likely that the activation will not be uniformly distributed along the machine. The components indicated as activated in this study could in reality be only partially radioactive, depending on the distance from the beam loss points. It may be feasible that a given component is cut in pieces, and each piece is either disposed as conventional waste or stored as radioactive. This is of course hard to predict at this stage and only operational radiation protection measurements on each machine components after the final shutdown will provide the real activation scenario and allow deciding e.g. on the required cooling time.

Acknowledgements

The authors are grateful to Maurizio Vretenar for providing the technical specifications needed for the present study and for many useful discussions.

References

- [1] M. Vretenar, et al., Linac4 Technical Design Report, Tech. Rep. CERN-AB-2006-084. CARE-Note-2006-022-HIPPI, CERN, Geneva (Dec 2006).
- [2] M. Vretenar, et al., The LINAC4 Project at CERN (CERN-ATS-2011-041) (2011) 4 p.
- [3] M. Vretenar, et al., Conceptual design of the SPL II: A high-power superconducting H^- linac at CERN, CERN, Geneva, 2006.
- [4] G. Battistoni, S. Muraro, P. R. Sala, F. Cerutti, A. Ferrari, et al., The FLUKA code: Description and benchmarking, AIP Conf.Proc. 896 (2007) 31–49. doi:10.1063/1.2720455.
- [5] A. Ferrari, P. R. Sala, A. Fass, J. Ranft, FLUKA: A multi-particle transport code (program version 2005), CERN, Geneva, 2005.
- [6] M. Brugger, A. Ferrari, S. Roesler, L. Ulrici, Validation of the FLUKA Monte Carlo code for predicting induced radioactivity at high-energy accelerators, Nucl. Instrum. Methods Phys. Res., A 562 (2006) 814–818.
- [7] S. Maury, Y. Body, O. Brunner, D. Chapuis, J.-P. Corso, C. De Almeida, N. Lopez, S. Prodon, J. Pierlot, LINAC4 Safety File, Tech. Rep. L4-S-SR-0002, EDMS 905423, CERN, Geneva (Jun 2008).
- [8] M. Vretenar, Private communication, CERN, Geneva (2013).
- [9] A. Lombardi, G. Bellodi, V. Dimov, J.-B. Lallement, User Specifications for LINAC4 Dumps - Engineering Parameters (Ref. WP 2.3), Tech. Rep. CERN-L4-T-EP-0006 rev.1.0, EDMS 1184637, CERN, Geneva (Jun 2012).
- [10] E. Mauro, M. Silari, Radiation protection studies for a high-power 160 MeV proton linac, Nucl. Instrum. Methods Phys. Res., A 605 (3) (2009) 249–265.
- [11] E. Mauro, M. Silari, Residual dose rates and induced radioactivity in the linac4 tunnel, Tech. Rep. CERN Technical Note, CERN-SC-2008-069-RP-TN, CERN, Geneva (2008).
- [12] P. A. Thonet, Linac4 inter-tank permanent magnet quadrupoles, Tech. Rep. Linac4 Project Document L4-MQM-ES-0002 rev.1.0, CERN, Geneva (2012).
- [13] I. V. Leitaov, C. Maglioni, Design specifications for the Linac4 main dump, Lbe and Lbs dumps, Tech. Rep. CERN-L4-T-ES-0007, EDMS 1256894, CERN, Geneva (Dec 2012).
- [14] S. Roesler, C. Theis, Exemption and clearance of material at cern, Tech. Rep. EDMS 942170 v.5, CERN, Geneva (Jan 2012).
- [15] Ordonnance sur la radioprotection (ORaP), Tech. Rep. 814.501 (Jan 2013).
- [16] M. Huhtinen, Determination of cross-sections for assessments of air activation at lhc, Tech. Rep. CERN/TIS-RP/TM/97-29, CERN, Geneva (1997).
- [17] S. Agosteo, Radiation protection constraints for use of proton and ion accelerators in medicine, Radiation Protection Dosimetry 137 (1-2) (2009) 167–186. doi:10.1093/rpd/ncp187.

List of Tables

2.1	Cross sections for high-energy particle	23
2.2	Radionuclides identified in accelerators environment	24
2.3	Activation products in concrete and barytes concrete	28
4.1	Composition of the barite concrete wall	49
4.2	A04 sample from 0 to 10 cm depth	54
4.3	A04 sample from 10 to 20 cm depth	55
4.4	A04 sample from 20 to 30 cm depth	55
4.5	A04 sample from 30 to 40 cm depth	55
4.6	A04 sample from 40 to 50 cm depth	56
4.7	A04 sample from 50 to 60 cm depth	56
4.8	A05 sample from 0 to 5 cm depth	56
4.9	A05 sample from 5 to 15 cm depth	57
4.10	A05 sample from 15 to 25 cm depth	57
4.11	A05 sample from 25 to 30 cm depth	57
4.12	A05 sample from 30 to 40 cm depth	58
4.13	A05 sample from 40 to 50 cm depth	58
4.14	A06 sample from 0 to 5 cm depth	58
4.15	A06 sample from 5 to 15 cm depth	59
4.16	A06 sample from 15 to 25 cm depth	59
4.17	A06 sample from 25 to 30 cm depth	59
4.18	A06 sample from 30 to 40 cm depth	60
4.19	A06 sample from 40 to 50 cm depth	60

5.1	Results of the Al foil activation experiment	75
5.2	Foil surface atomic densities	77
5.3	Raw calibration factors for each Al foil	78
5.4	Raw calibration factors for each Cu foil	79
5.5	IC calibration factor	80
5.6	Foil surface atomic densities for iron foils	82
5.7	Cross sections of the spallation reactions on ^{nat}Cu	85
5.8	Cross sections of the spallation reactions on ^{nat}Fe	85
5.9	Chemical composition of dried soil sample	87
5.10	Specific activities of radionuclides in soil and water	91
5.11	Radioactivity measured in the leached water for the soil-water mixing system	97
5.12	Radioactivity measured in the leached water for the soil-water flowing system	97
5.13	Fraction of radioactivity leached into the water in the mixing system	99
5.14	Fraction of radioactivity leached into the water in the flowing system	99
5.15	Fraction of tritium activity leached out from soil bulk and moisture for both systems	100
6.1	Linac4 main accelerating structures	103
6.2	Beam loss assumptions along the main accelerating structures.	105
6.3	Main radionuclides found in the Linac4 components.	112

List of Figures

1.1	Schematic diagram of the drift-tube type of linear accelerator .	8
1.2	Schematic diagram of the cyclotron	10
1.3	Basic layout of the synchrotron	13
2.1	Radioisotope build-up and decay over time	18
2.2	Mass-yield curves	21
2.3	The nuclear inelastic cross section	21
2.4	Isotopes having half-lives up to a given half-life	26
2.5	Build-up in concrete	28
3.1	Flow of information within the JEREMY code	36
4.1	The CERN synchro-cyclotron	38
4.2	Concrete core sampling at level 0	41
4.3	Sample of concrete core 50 cm deep and 5 cm in diameter . . .	42
4.4	Comparison between "heavy" and "light" concrete samples . . .	43
4.5	Depth profile of COR-A04 core	44
4.6	Depth profile of COR-A02 and COR-A03 cores	45
4.7	Depth profile of COR-A05 and COR-A06 cores	46
4.8	View of the SC geometry	48
4.9	Ratios of FLUKA an JEREMY over measured specific activities in concrete samples	51
4.10	Depth profile of the measured and calculated activity of ^{133}Ba in the North wall	53

4.11	Depth profile of the measured and calculated activity of ^{133}Ba in the East wall	54
5.1	Schematic view of the SPS North Experimental Area	63
5.2	Schematic view of the IC	64
5.3	Scheme of the geometry employed in the FLUKA simulations	65
5.4	Summary of the literature cross sections for the $^{27}\text{Al}(p,3pn)^{24}\text{Na}$ reaction	69
5.5	Recoil nuclei reaction scheme	73
5.6	Summary of the literature cross sections for the $^{nat}\text{Cu}(p,x)^{24}\text{Na}$ reaction	74
5.7	Experimental set-up for the foil activation	76
5.8	Foil activation experiment set-up	77
5.9	Plot of the calibration factors as calculated via the activation of the Al foils	78
5.10	Soil and water samples used in the activation experiment	87
5.11	Irradiation profile of the samples	88
5.12	H4IRRAD target area	89
5.13	Detail of the irradiation set-up used in the FLUKA geometry	92
5.14	Particle spectral fluences	92
5.15	Soil-water mixing system	93
5.16	Soil-water flowing system	94
5.17	Specific activity of the leached water as a function of the mixing time for the soil-water mixing system	96
5.18	Specific activity of the leached water as a function of the filtration steps for the water-soil flowing system.	98
5.19	Fraction of ^3H and ^{22}Na activities leached into the water	100
6.1	Schematic view of the Linac4	103
6.2	Beam loss profile in the DTL section	106
6.3	Beam loss profile in the CCDTL section	107
6.4	Beam loss profile in the PIMS section	107

6.5	Comparison of the neutron fluence spectra at the three beam impact points	109
6.6	Comparison of the neutron fluence spectra in DTL	110
6.7	Half section of a full-scale DTL prototype	110
6.8	Specific radioactivity in the main DTL components	113
6.9	Fraction of Swiss exemption limits for the DTL components	113
6.10	Fraction of CERN design exemption limits for the DTL components	114
6.11	Specific radioactivity in the main CCDTL components	115
6.12	Fraction of Swiss exemption limits for the CCDTL components	117
6.13	Fraction of CERN design exemption limits for the CCDTL components	117
6.14	Specific radioactivity in the main PIMS components	118
6.15	Fraction of Swiss exemption limits for the PIMS components	118
6.16	Fraction of CERN design exemption limits for the PIMS components	119
6.17	Profile of the total radioactivity in the third DTL tank	119
6.18	Profile of the total radioactivity in the fifth CCDTL module	120
6.19	Profile of the total radioactivity in the 12th and 13th PIMS tank	120
6.20	Ambient dose equivalent rate inside the DTL tank	122
6.21	Ambient dose equivalent rate at 10 cm from the DTL tank	122
6.22	Ambient dose equivalent rate in the DTL section	123
6.23	Ambient dose equivalent rate inside the CCDTL tank	124
6.24	Ambient dose equivalent rate at 10 cm from the CCDTL tank	124
6.25	Ambient dose equivalent rate in the CCDTL section	125
6.26	Ambient dose equivalent rate inside the PIMS tank	126
6.27	Ambient dose equivalent rate at 10 cm from the PIMS tank	126
6.28	Ambient dose equivalent rate in the PIMS section	127

Bibliography

- [1] US Department of Energy, Accelerators for america's future, June 2010.
- [2] R. Jayakumar, Particle accelerators colliders and the story of high energy physics, Springer, 2012.
- [3] E. Persico, E. Ferrari, S. E. Segre, Principles of particle accelerators, W.A. Benjamin, 1968.
- [4] K. Wille, The physics of particle accelerators, Oxford, 2000.
- [5] A. Wu Chao, Handbook of Accelerator Physics and Engineering, World Scientific, 2013.
- [6] W. Scharf, Particle accelerators and their uses, Harwood Academic Publishers, 1986.
- [7] H. Wiedemann, Particle accelerator physics, Springer-Verlag, 1993.
- [8] J. D. Cossairt, Radiation Physics for Personnel and Environmental Protection, Revision 9B, Tech. Rep. FERMILAB-TM-1834, 2007.
- [9] W. E. Meyerhof, Elements of Nuclear Physics, McGraw-Hill, New York, 1967.
- [10] Radiation protection for particle accelerator facilities: recommendations of the National Council on Radiation Protection and Measurements, no. 144 in NCRP Reports, NCRP, Bethesda, MD, 2005.

-
- [11] J. D. Cossairt, Induced radioactivity at accelerators, Professional Development School: Topics in Accelerator Health Physics, 31 Jan - 2 Feb 2008, Oakland, California, 2008.
- [12] H. W. Patterson, R. H. Thomas, Accelerator Health Physics, Academic Press, New York, NY, 1973.
- [13] A. H. Sullivan, A guide to radiation and radioactivity levels near high energy particle accelerators, Nuclear Technology Publishing, Ashford, Kent, 1992.
- [14] G. P. Yost, et al., Review of particle properties, Physics Letters B 204 (1988) 1.
- [15] M. Barbier, Induced Radioactivity, North-Holland, Amsterdam, 1969.
- [16] J. J. Bevelacqua, Health Physics in the 21st Century. Health Physics in the Twenty-First Century, Wiley, Weinheim, 2008.
- [17] L. R. Carroll, Predicting long-lived, Neutron-induced activation of concrete in a cyclotron vault, 16th International Conference on the Application of Accelerators in Research and Industry, Denton, USA, 2000.
- [18] Evaluation of the Radiological and Economic Consequences of Decommissioning Particle Accelerators, no. Report Eur 19151, European Commission - Nuclear Safety and the Environment, 1999.
- [19] W. L. Dunn, J. K. Shultis, Exploring Monte Carlo methods, Elsevier, Amsterdam, 2012.
- [20] A. Ferrari, P. R. Sala, A. Fasso', J. Ranft, FLUKA: a multi-particle transport code, CERN-2005-10, INFN/TC-05/11, SLAC-R-773, 2005.
- [21] G. Battistoni, S. Muraro, P. R. Sala, F. Cerutti, A. Ferrari, S. Roesler, A. Fasso', J. Ranft, The FLUKA code: Description and benchmarking,

- proceedings of the Hadronic Shower Simulation Workshop 2006, Fermilab 6–8 September 2006, M. Albrow, R. Raja eds., AIP Conference Proceeding 896, 31-49, 2007.
- [22] G. Battistoni, et al., The application of the Monte Carlo code FLUKA in radiation protection studies for the Large Hadron Collider, *Progress in Nuclear Science and Technologies*, Vol. 2, 358 - 364, 2011.
- [23] M. Brugger, A. Ferrari, S. Roesler, L. Ulrici, Validation of the FLUKA Monte Carlo code for predicting induced radioactivity at high-energy accelerators, *Nuclear Instruments and Methods in Physics Research A* 562 (2006) 814 – 818.
- [24] M. Brugger, Y. Donjoux, W. A. Mitaroff, S. Roesler, Measurements and simulation of induced activity at the CERN-EU high-energy reference field facility, In: *Proceedings of 6th International Meeting on Nuclear Applications of Accelerator Technology*, San Diego, CA, USA, 1 - 5 Jun 2003, 391-398, 2003.
- [25] M. Brugger, H. Khater, S. Mayer, A. Prinz, S. Roesler, L. Ulrici, H. Vincke, Benchmark studies of induced radioactivity produced in LHC materials, part I: specific activities, *Radiation Protection Dosimetry* 116 (1 - 4) (2005) 6 – 11.
- [26] M. Brugger, H. Khater, S. Mayer, A. Prinz, S. Roesler, L. Ulrici, H. Vincke, Benchmark studies of induced radioactivity produced in LHC materials, part II: remanent dose rates, *Radiation Protection Dosimetry* 116 (1 - 4) (2005) 12 – 15.
- [27] R. Froeschl, JEREMY: a code for radiological characterization of accelerator components including detailed uncertainty estimation, *Second International Workshop on Accelerator Radiation Induced Activation ARIA2011*, Israel, 2011.

-
- [28] A. Santamarina, et al., The JEFF-3.1.1 Nuclear Data Library, Technical Report JEFF Report 22, Nuclear Energy Agency, Paris, 2009.
- [29] R. Froeschl, Use of FLUKA for the analytical calculation of induced radioactivity in the CERN accelerator complex with the JEREMY code, In: 1st Fluka Advanced Course and Workshop, Ericeira, Portugal, October 4-8, 2010.
- [30] P. Carbonez, F. P. La Torre, R. Michaud, M. Silari, Residual radioactivity at the CERN 600 MeV Synchro-Cyclotron, Tech. Rep. CERN-SC-2011-026-RP-TN, Geneva, 2011.
- [31] F. P. La Torre, M. Silari, Residual radioactivity at the CERN 600 MeV Synchro-Cyclotron, Second International Workshop on Accelerator Radiation Induced Activation ARIA2011, Ma'ale Hachamisha, Israel, May 15-19, 2001.
- [32] S. Lindbäck, Study of the present extraction system for the CERN Synchro-Cyclotron, Tech. Rep. CERN-73-08, Geneva, 1973.
- [33] M. Morpurgo, Improvements to the CERN Synchro-Cyclotron Extraction System, in: Proceeding of the Conference on High Energy Cyclotron Improvement, Williamsburg, CERN report MSC/26/68, 1964.
- [34] L. Dick, L. di Lella, L. Feuvrais, M. Spighel, Preliminary Investigation of Factors Affecting External Beams from the CERN Synchrocyclotron, in: Proceeding of the Conference on High Energy Cyclotron Improvement, Williamsburg, CERN report MSC-24-30/80, 1964.
- [35] C. Theis, K. H. Buchegger, M. Brugger, D. Forkel-Wirth, S. Roesler, H. Vincke, Interactive three dimensional visualization and creation of geometries for Monte Carlo calculations, Nuclear Instruments and Methods in Physics Research A 562 (2006) 827 – 829.

-
- [36] G. Brianti, E. G. Michaelis, Summary of the seminar on SC improvements programme, Tech. Rep. MSC/M-la/13 M53, CERN, Geneva, 1966.
- [37] H. Beger, et al., Summary of the seminar on SC improvements programme, in: Proceedings of 7th International Conference on Cyclotrons and their Applications, Zurich, 1975.
- [38] R. Deltenre, J. W. N. Tuyn, Flux density measurements inside and behind the B-pipe with a proton beam hitting the wall of the SC proton room, Tech. Rep. CERN HS-RP/TM/76-11, Geneva, 1976.
- [39] B. W. Allardyce, et al., Performance and prospects of the reconstructed CERN 600 MeV Synchro-Cyclotron, in: Proceedings of 7th IEEE Particle Accelerator Conference, Chicago, USA, IEEE Trans. Nucl. Sci. 24, 1977.
- [40] B. W. Allardyce, et al., Status report on CERN SC, Tech. Rep. IEEE Trans. Nucl. Sci. 26, Geneva, 1979.
- [41] B. W. Allardyce, The CERN Synchrocyclotron today, CERN/PS-COP/81-30, in: Proceedings of 9th International Conference on Cyclotrons and their Applications, GANIL - Caen, 1981.
- [42] F. P. La Torre, M. Silari, Analytical and Monte Carlo calculations of the residual radioactivity in the walls of the 600 MeV synchrocyclotron vault, Tech. Rep. CERN-SC-2012-012-RP-TN, 2012, Geneva.
- [43] F. P. La Torre, Residual Radioactivity at the CERN 600 MeV Synchrocyclotron, Master Thesis, IUSS Pavia - Institute for Advanced Study, Academic year 2009 - 2010.
- [44] M. Silari, A. Mitaroff, The CERN-EU high-energy Reference Field (CERF) facility for dosimetry at commercial flight altitudes and in space, Radiation Protection Dosimetry 102 (2002) 7–22.

- [45] H. Atherton, et al., CERN Yellow Report 80-07, 1980.
- [46] SPS North Area Operation, Shutdown Lectures, CERN, Geneva, 2006.
- [47] F. P. La Torre, G. P. Manessi, F. Pozzi, C. T. Severino, M. Silari, A new verification of the calibration factor of the CERF beam monitor, Tech. Rep. CERN-RP-2013-083-REPORTS-TN, Geneva, 2013.
- [48] A. Porret, Radiographic Testing Report: Chambre Ionisation/F.P. La Torre (DGS/RP), Tech. Rep. EDMS 1282807, CERN, Geneva, 2012.
- [49] IAEA, Absorbed dose determination in external beam radiotherapy: an internal code of practice for dosimetry based on standards of absorbed dose to water, Tech. Rep. Series No. 398, 2000.
- [50] A. Ferrari, Private communication, 2013.
- [51] B. Biskup, et al., Commissioning and Operation of the H4IRRAD Mixed-Field Test Area, Tech. Rep. CERN-ATS-Note-2011-121-PERF, Geneva, 2011.
- [52] J. B. Cumming, Monitor reactions for high energy proton beams, *Annu. Rev. Nucl. Sci.* 13 (1963) 261–286.
- [53] EXFOR, Nuclear reaction database: <http://cdfc.sinp.msu.ru/>, 2013.
- [54] S. B. Kaufman, et al., Spallation of aluminum by 300 GeV protons, *Physical Review C* 19 (1979) 962–964.
- [55] J. P. Butler, D. C. Santry, Excitation curves for the reactions $^{27}\text{Al}(n,\alpha)^{24}\text{Na}$ and $^{24}\text{Mg}(n,p)^{24}\text{Na}$, *Canadian Journal of Physics* 41 (1963) 372.
- [56] A. F. Stehney, E. P. Steinberg, The effect of thick targets on some nuclear reactions commonly used to monitor high energy proton beams, *Nuclear Instruments and Methods* 59 (1968) 102–108.

- [57] J. B. Cumming, et al., $^{27}\text{Al}(p,3\text{pn})^{24}\text{Na}/^{12}\text{C}(p,\text{pn})^{11}\text{C}$ Cross-Section Ratio in the GeV Region, *Physical Review* 128 (1962) 2392–2397.
- [58] R. Brandt, et al., Some remarks concerning the proton flux monitor reaction $^{27}\text{Al}(p,3\text{pn})^{24}\text{Na}$, *Nuclear Instruments and Methods* 62 (1968) 109–111.
- [59] R. J. Grover, Nuclear Reactions of Tantalum with 5.7 GeV Protons, *Physical Review* 126 (1962) 1540–1554.
- [60] F. P. La Torre, G. P. Manessi, F. Pozzi, C. T. Severino, M. Silari, The June 2011 CERF run, Tech. Rep. CERN-DGS-2011-055-RP-TN, Geneva, 2011.
- [61] F. P. La Torre, G. P. Manessi, F. Pozzi, S. Puddu, C. T. Severino, M. Silari, The May 2012 CERF run, Tech. Rep. CERN-DGS-2012-045-RP-TN, Geneva, 2012.
- [62] F. P. La Torre, G. P. Manessi, F. Pozzi, C. T. Severino, M. Silari, The June 2012 CERF run, Tech. Rep. CERN-DGS-2011-055-RP-TN, Geneva, 2012.
- [63] F. P. La Torre, G. P. Manessi, F. Pozzi, S. Puddu, C. T. Severino, M. Silari, The December 2012 CERF run, Tech. Rep. CERN-DGS-2011-121-RP-TN, Geneva, 2012.
- [64] D. Filges, F. Goldenbaum, *Handbook of spallation research*, Wiley-VCH, Weinheim, 2009.
- [65] S. I. Baker, R. Allen, P. Yurista, $\text{Cu}(p,x)^{24}\text{Na}$ cross section from 30 to 800 GeV, *Physical Review C* 43 (1991) 6.
- [66] Goodfellow Corporation, see online catalogue, available at <http://www.goodfellow.com>, 2013.
- [67] Korea Atomic Energy Research Institute (KAERI), Photon cross sections and attenuation coefficients, <http://atom.kaeri.re.kr>, 2013.

- [68] M. C. Hopper, et al., Beam Monitoring in the May 1993 CERN-CEC Experiment, Tech. Rep. CERN/TIS/RP/TM/93-21, 1993.
- [69] G. R. Stevenson, J. C. Liu, K. O'Brien, J. Williams, Beam Intensity Measurements using ^{11}C Activation for the CERN-CEC Experiments., Tech. Rep. CERN/TIS/RP/TM/94-15, 1994.
- [70] H. Vincke, et al., Accurate PIC calibration by the use of a coincidence of two scintillators, Tech. Rep. CERN/SC/RP/TN/2004-090, 2004.
- [71] M. Calviani, F. Cerutti, F. P. La Torre, G. P. Manessi, F. Pozzi, C. T. Severino, M. Silari, Beam monitoring of high energy proton flux by the activation foil technique, progress in Nuclear Science and Technology, 23-05, In: Proc. of the 12th Intern. Conf. on Radiation Shielding, ICRS-12, 2-7 September 2012, Nara, Japan, 2012.
- [72] L. Sihver, et al., Total reaction and partial cross section calculations in proton-nucleus ($Z_t \leq 26$) and nucleus-nucleus reactions (Z_p and $Z_t \leq 26$), Physical Review C 47 (1993) 1225–1236.
- [73] H. Crannell, et al., Interaction lengths of energetic pions and protons in iron, Physical Review D 7 (1973) 730–740.
- [74] W. R. Nelson, Radioactive groundwater produced in the vicinity of beam dumps, Tech. Rep. SLAC-TN-65-16, Stanford, 1965.
- [75] F. Hoyer, Induced radioactivity in the earth shielding on top of high-energy particle accelerators, Tech. Rep. SLAC-TN-65-16, Stanford, 1965.
- [76] G. J. Warren, R. C. Busick, D.D. and McCall, Radioactivity produced and released from water at high energies, in: Proceedings of Second Int. Conf. in Accelerator Dosimetry, Stanford, November 1969.

- [77] J. Ranft, K. Goebel, Estimation of induced radioactivity around high-energy accelerators from hadronic cascade star densities obtained from Monte Carlo calculations, Tech. Rep. CERN HP-70-92, Geneva, 1970.
- [78] R. H. Thomas, Possible contamination of groundwater system by high-energy acceleration, Tech. Rep. UCRL-20131, Lawrence Berkley Laboratory, 1970.
- [79] G. B. Stapleton, R. H. Thomas, Estimation of the induced radioactivity of the groundwater system in the neighbourhood of a proposed 300 GeV high-energy accelerator situated on a chalk site, *Health Physics* 23 (1972) 689.
- [80] A. Rindi, Induced radioactivity in the cooling waters of the CERN 300 GeV SPS, Tech. Rep. RA/Note/72-71, CERN, Geneva, 1972.
- [81] T. B. Borak, The underground migration of radionuclides produced in soil near high-energy protons accelerators, *Health Physics* 23 (1972) 679–687.
- [82] S. I. Baker, Soil activation measurements at Fermi Laboratory, Tech. rep., Fermi National Accelerator Laboratory, 1975.
- [83] S. I. Baker, Fermilab Soil Activation Experience, in: *Proceedings of the Fifth DOE Environmental Protection Information Meeting*, Albuquerque, New Mexico, November 1984.
- [84] A. H. Sullivan, Groundwater activation around the AA and ACOL target areas, Tech. Rep. CERN/TIS-RP/IR/87-34, Geneva, 1987.
- [85] A. J. Malensek, et al., Groundwater Migration of Radionuclides at Fermilab, Tech. Rep. FERMILAB-TM-1851, Fermi National Accelerator Laboratory, 1993.
- [86] S. I. Baker, J. Bull, D. Gross, Leaching of accelerator produced radionuclides, *Health Physics* 73 (1997) 912–918.

-
- [87] K. Tesch, Production of radioactive nuclides in soil and groundwater near dump of a linear collider, Tech. Rep. D3-86, DESY, 1997.
- [88] B. Racky, Radiation environment of the linear collider TESLA, in: Proceedings of the Fourth Workshop on Simulating Accelerator Radiation Environments (SARE-4), Knoxville, Tennessee, U.S.A., 1998.
- [89] A. Wehmann, S. Childress, Tritium production in the Dolomitic rock adjacent to NuMI beam tunnels, Tech. Rep. FERMILAB-TM-2083, Fermi National Accelerator Laboratory, 1999.
- [90] H. Vincke, G. R. Stevenson, Production of radioactive isotopes in molasse, in: 5th Meeting of the Task Force on Shielding Aspects of Accelerators, Targets and Irradiation Facilities, Paris, France, 2000.
- [91] S. Rokni, J. C. Liu, S. Roesler, Initial estimates of the activation concentration of the soil and groundwater around the NLC Beam Delivery System tunnel, Tech. Rep. RP-00-04, SLAC, 2000.
- [92] S. Agosteo, M. Magistris, M. Silari, Radiological considerations on multi-MW targets Part I: Induced radioactivity, Nucl. Instrum. Methods Phys. Res. A 545 (2005) 813–822.
- [93] EMPA - Swiss Federal Laboratories for Material Science and Technology, Laboratory for Solid State Chemistry and Catalysis, Test Report n. 459595, Überlandstrasse 129, CH-8600 Dübendorf, 2001.
- [94] F. P. La Torre, M. Magistris, M. Silari, Irradiation of soil samples at H4IRRAD to study radioisotope leaching into groundwater: preliminary study, Tech. Rep. CERN-DGS-2012-047-RP-TN, Geneva, 2012.
- [95] F. P. La Torre, M. Silari, Leaching of radionuclides from activated soil into groundwater, Tech. Rep. CERN-DGS-2014, Geneva, 2014.

- [96] F. P. La Torre, G. P. Manessi, F. Pozzi, C. T. Severino, M. Silari, Cu and Al activation experiments for beam monitoring in H4IRRAD, Tech. Rep. CERN-DGS-2012-022-RP-TN, Geneva, 2012.
- [97] M. Vretenar, et al., The Linac4 project: overview and status, in: Proceedings of HHH-2008 Follow Up Meeting, CERN, Geneva, 2008.
- [98] M. Vretenar, et al., Linac4 Technical Design Report, Tech. Rep. CERN-2006-AB-084, Geneva, 2006.
- [99] M. Vretenar, et al., The Linac4 Project at CERN, Tech. Rep. CERN-ATS-2011-041, Geneva, 2011.
- [100] E. Mauro, M. Silari, Radiation protection studies for a high-power 160 MeV proton linac, Nuclear Instruments and Methods in Physics Research A 605 (3) (2009) 249–265.
- [101] P. A. Thonet, Linac4 inter-tank permanent magnet quadrupoles, Tech. Rep. Linac4 Project Document L4-MQM-ES-0002 rev.1.0, CERN, Geneva, 2012.
- [102] S. Maury, et al., Linac4 safety file, Tech. Rep. L4-S-SR-0002, EDMS 905423, CERN, Geneva, 2008.
- [103] M. Vretenar, Private communication, CERN, Geneva, 2013.
- [104] F. P. La Torre, M. Silari, Predictions of induced radioactivity and residual dose rates in Linac4, Tech. Rep. CERN-RP-2013-062-REPORTS-TN, Geneva, 2013.
- [105] Ordonnance du 22 juin 1994 sur la radioprotection (ORaP), 814.501, Etat: 1er janvier 2013.
- [106] S. Roesler, C. Theis, Exemption and Clearance of Material at CERN, Tech. Rep. EDMS 942170 v.5, CERN, Geneva, 2012.

- [107] M. Vretenar, J. Blaha, F. P. La Torre, C. Maglioni, M. Silari, Decommissioning of Linac4, Tech. Rep. L4-PM-MR-0001, CERN, Geneva, 2014.

- [108] F. P. La Torre, M. Silari, Induced radioactivity in the CERN Linac4: a new 160 MeV proton linac, in: Proc. of the Eleventh Intern. Topical Meeting on Nuclear Applications of Accelerators, AccApp'13, 5 - 8 August 2013, Bruges, Belgium, 2013.

Acknowledgements

I would like to express my gratitude to Dr. Marco Silari for his guidance, encouragement and constant help during my PhD work. It was my great pleasure to have him as a supervisor at CERN.

I gratefully acknowledge Prof. Dr. Antonio Ereditato for the advice, the support and the supervision of my PhD thesis. He gave me the opportunity to work in a very interesting scientific environment such as LHEP.

I am so grateful to Dr. Saverio Braccini for his excellent scientific support and very friendly collaboration. He spent extra time helping me with my PhD thesis.

I want to thank Prof. Paola Scampoli for the interesting discussions and very valuable inputs during my time at LHEP. I would also like to thank my committee members, Prof. Stefano Agosteo for serving as external referee and Prof. Peter Wurz, for accepting to chair my PhD defense.

I warmly thanks the entire CERN RP/SP team for the support and friendly working atmosphere. In particular I would like to acknowledge my colleagues Giacomo Manessi and Fabio Pozzi for their fundamental contribution to the activation experiments and the help on the paper works. I wish to extend my thanks and gratitude to all my colleagues and friends at LHEP. I owe special thanks to my colleague and flatmate Clizia Severino for the support and her understanding in stressful times.

Finally, I thank my family for the great support in all these years.

Erklärung

gemäss Art. 28 Abs. 2 RSL 05

Name/Vorname: La Torre / Francesco Paolo

Matrikelnummer: 10-129-443

Studiengang: Physik

Bachelor Master Dissertation

Titel der Arbeit: Study of induced radioactivity in proton accelerator facilities

LeiterIn der Arbeit: Prof. Dr. Antonio Ereditato

..... Dr. Marco Silari

Ich erkläre hiermit, dass ich diese Arbeit selbständig verfasst und keine anderen als die angegebenen Quellen benutzt habe. Alle Stellen, die wörtlich oder sinngemäss aus Quellen entnommen wurden, habe ich als solche gekennzeichnet. Mir ist bekannt, dass andernfalls der Senat gemäss Artikel 36 Absatz 1 Buchstabe r des Gesetzes vom 5. September 1996 über die Universität zum Entzug des auf Grund dieser Arbeit verliehenen Titels berechtigt ist.

.....
Ort/Datum

.....
Unterschrift

Curriculum Vitae

Name: Francesco Paolo La Torre

Birthday: June 26th, 1980

Place of Birth: San Giovanni Rotondo, Italy

February 2014 Ph.D. thesis defense under the co-supervision of Prof. Dr. Antonio Ereditato at the Albert Einstein Center for Fundamental Physics at the Laboratory for High Energy Physics of the University of Bern and Dr. Marco Silari at the European Center for Nuclear Research (CERN).

December 2013 CERN Fellowship award starting from April 2014.

February 2011 Master of Advanced Studies at the European School on Nuclear and Ionising Radiation Technology (TNRI) of the University Institute for Advanced Studies (IUSS) of Pavia.

December 2010 Internship under the supervision of Dr. Marco Silari at the European Center for Nuclear Research (CERN).

March 2010 Master's Degree in Physics under the co-supervision of Prof. Elio Rosato at the University of Naples "Federico II" and Dr. Jean-Pierre Wieleczko at GANIL (Grand Accélérateur National d'Ions Lourds), Caen, France.

December 2009 Internship under the supervision of Dr. Jean-Pierre Wieleczko at GANIL (Grand Accélérateur National d'Ions Lourds), Caen, France.